STUDIES OF TURBULENT FLOWS IN CONTINUOUS CASTING OF STEEL WITH AND WITHOUT MAGNETIC FIELD

BY

RAJNEESH CHAUDHARY

DISSERTATION

Submitted in partial fulfillment of the requirements
for the degree of Doctor of Philosophy in Mechanical Engineering
in the Graduate College of the
University of Illinois at Urbana-Champaign, 2011

Urbana, Illinois

Doctoral Committee:

Professor Brian G. Thomas, Chair and Director of Research
Professor Pratap S. Vanka, Contingent Chair
Professor Rizwan Uddin
Assistant Professor Carlos A. Pantano-Rubino

ABSTRACT

This thesis develops and tests various transient and steady-state computational models such as direct numerical simulation (DNS), large eddy simulation (LES), filtered unsteady Reynolds-averaged Navier-Stokes (URANS) and steady Reynolds-averaged Navier-Stokes (RANS) with and without magnetic field to investigate turbulent flows in canonical as well as in the nozzle and mold geometries of the continuous casting process.

The direct numerical simulations are first performed in channel, square and 2:1 aspect rectangular ducts to investigate the effect of magnetic field on turbulent flows. The rectangular duct is a more practical geometry for continuous casting nozzle and mold and has the option of applying magnetic field either perpendicular to broader side or shorter side. This work forms the part of a graphic processing unit (GPU) based CFD code (CU-FLOW) development for magnetohydrodynamic (MHD) turbulent flows. The DNS results revealed interesting effects of the magnetic field and its orientation on primary, secondary flows (instantaneous and mean), Reynolds stresses, turbulent kinetic energy (TKE) budgets, momentum budgets and frictional losses, besides providing DNS database for two-wall bounded square and rectangular duct MHD turbulent flows.

Further, the low- and high-Reynolds number RANS models (k-ε and Reynolds stress models) are developed and tested with DNS databases for channel and square duct flows with and without magnetic field. The MHD sink terms in k- and ε-equations are implemented as proposed by Kenjereš and Hanjalić using a user defined function (UDF) in FLUENT. This work revealed varying accuracies of different RANS models at different levels. This work is useful for industry to understand the accuracies of these models, including continuous casting.

After realizing the accuracy and computational cost of RANS models, the steady-state k-ε model is then combined with the particle image velocimetry (PIV) and impeller probe velocity measurements in a $1/3^{rd}$ scale water model to study the flow quality coming out of the well- and mountain-bottom nozzles and the effect of stopper-rod misalignment on fluid flow. The mountain-bottom nozzle was found more prone to the longtime asymmetries and higher surface velocities. The left misalignment of stopper gave higher surface velocity on the right leading to significantly large number of vortices forming behind the nozzle on the left.

Later, the transient and steady-state models such as LES, filtered URANS and steady RANS models are combined with ultrasonic Doppler velocimetry (UDV) measurements in a GaInSn model of typical continuous casting process. LES-CU-LOW is the fastest and the most accurate model owing to much finer mesh and a smaller timestep. This work provided a good understanding on the performance of these models. The behavior of instantaneous flows, Reynolds stresses and proper orthogonal decomposition (POD) analysis quantified the nozzle bottom swirl and its importance on the turbulent flow in the mold.

Afterwards, the aforementioned work in GaInSn model is extended with electromagnetic braking (EMBr) to help optimize a ruler-type brake and its location for the continuous casting process. The magnetic field suppressed turbulence and promoted vortical structures with their axis aligned with the magnetic field suggesting tendency towards 2-d turbulence. The stronger magnetic field at the nozzle well and around the jet region created large scale and lower frequency flow behavior by suppressing nozzle bottom swirl and its front-back alternation. Based on this work, it is advised to avoid stronger magnetic field around jet and nozzle bottom to get more stable and less defect prone flow.

To my parents

ACKNOWLEDGEMENTS

I express my sincere gratitude to my advisers Professor Brian G. Thomas and Professor Pratap S. Vanka for their continuous guidance and support during the course of my doctoral study.

The financial support from Continuous Casting Consortium for my doctoral research is gratefully appreciated. The experimental data for model validation in water model was supplied by Seong-Mook Cho, Dr. Go-Gi Lee and Professor Seon-Hyo Kim from POSTECH, South Korea and in GaInSn model by Klaus Timmel, Dr. Sven Eckert and Dr. Gunther Gerbeth from FZD, Dresden, Germany. The computations for this research were performed at Computational Fluid Dynamics Laboratory, Metals Processing Simulation Laboratory and at National Center for Supercomputing Application at University of Illinois at Urbana-Champaign. The FLUENT CFD package was provided by ANSYS Inc. This thesis would not have been possible without the support of the aforesaid individuals and organizations.

I would like to thank Aaron Shinn for providing basic non-magnetohydrodynamic (non-MHD) version of CU-FLOW. Special thanks to my colleagues (Rui Liu, Lance Hibbeler, Varun Kumar Singh, Chuanbo Ji, Kun Xu, Seong-Mook Cho and Go-Gi Lee) and visiting researchers (Seong-Yeon Kim, POSCO, South Korea and Junya Iwasaki, Nippon Steel, Japan) at Metals Processing Simulation Laboratory who made my work enjoyable. It is a pleasure to thank all my friends (Manas Ranjan Gartia, Suneet Singh, Hitesh Bindra, Arpit Tiwari, Surya Kumar Saripella, Deep Gupta, Varun Gupta and Naveen Fogla) for making my stay at UIUC memorable.

I am thankful to my family, especially my parents and wife. Without their continuous encouragement, this work would not have been possible.

TABLE OF CONTENTS

LIST OF TABLES

LIST OF FIGURES

NOMENCLATURE

$\vec{B}_0$	Externally applied magnetic field vector (Tesla, T)
$\vec{b}$	Induced magnetic field vector (Tesla, T)
$D_h,\ D$	Hydraulic diameter or diameter (m)
$\vec{F}_L$	Lorentz force (N/m^3)
$\mathrm{Ha} = DB_0\sqrt{\frac{\sigma}{\rho\nu}}$	Hartmann number
$\vec{J}$	Current density vector (A/m^2)
$k = \overline{u_i' u_i'} / 2$	Turbulent kinetic energy (TKE) (m^2/s^2)
p	Pressure (N/m^2)
p'	Pressure fluctuations (N/m^2)
$\mathrm{Re} = \frac{DW_b}{\nu}$	Bulk Reynolds number
$\mathrm{Re}_\tau = \frac{Du_\tau}{\nu}$	Friction Reynolds number
$\mathrm{Re}_T = \frac{\rho k^2}{\mu\varepsilon}$	Turbulent Reynolds number
$\mathrm{Re}_y = \frac{\rho\sqrt{k}y}{\mu}$	Kinetic energy Reynolds number
t	Time (sec)
u_τ	Friction velocity (m/s)
$\overline{u'_i u'_j}$	Reynolds stresses (m^2/s^2)
$\vec{\mathrm{u}}$ $(u,\ v,\ w)$	Instantaneous/filtered velocity vector with components (m/s)
$\vec{\bar{\mathrm{u}}}$ $(\bar{u},\ \bar{v},\ \bar{w})$	Time-average/ensemble velocity vector with components (m/s)
$\vec{u}'(u-\bar{u},\ v-\bar{v},\ w-\bar{w})$	Fluctuation velocity vector with components (m/s)
$V_{casting}$	Casting speed (m/s)

W_b	Bulk axial velocity (m/s)
x, y, z	x-, y-, z-coordinates (m)
$y^+ = yu_\tau / \nu$	Normalized distance from wall
δ	Half duct height or half channel width
Δx^+, Δy^+, Δz^+	Normalized grid spacing in x-, y- and z-directions
$\varepsilon = \nu \overline{\frac{\partial u_i'}{\partial x_j} \frac{\partial u_i'}{\partial x_j}}$	Rate of dissipation (m^2/s^3)
μ / ν	Dynamic/Kinematic viscosity (kg/m-s/m^2/s)
$\mu_{eff} = \mu + \mu_t$	Effective viscosity (kg/m-s)
ν_s	Subgrid scale (SGS) viscosity (m^2/s)
$\nu_t = \frac{\mu_t}{\rho} = C_\mu k^2 / \varepsilon$	Eddy/Turbulent viscosity (m^2/s)
ρ	Density (kg/m^3)
σ	Standard deviation (CHAPTER 6) Electrical conductivity ($1/\Omega m$) at other places
$\tau_w = \rho u_\tau^2 = \mu \left. \frac{\partial \overline{w}}{\partial n} \right\|_{wall}$	Wall stress (N/m^2)
ϕ	Electric potential (Volts)
$\omega_i = \frac{\partial u_k'}{\partial x_j} - \frac{\partial u_j'}{\partial x_k}$	Fluctuation vorticity (sec^{-1})
$\overline{\Omega}_z = \left(\frac{\partial \overline{v}}{\partial x} - \frac{\partial \overline{u}}{\partial y} \right)$	Mean streamwise vorticity (sec^{-1})
$\frac{\partial}{\partial t}$	Derivative with respect to time (sec^{-1})
$\nabla = \frac{\partial}{\partial x} i + \frac{\partial}{\partial y} j + \frac{\partial}{\partial z} k$	Gradient operator (m^{-1})
$\nabla \cdot$ / $\times$	Divergence / Cross-product

Subscripts

$i = 1,2,3(x,y,z)$, $j = 1,2,3(x,y,z)$, $k = 1,2,3(x,y,z)$

CHAPTER 1. INTRODUCTION

The continuous casting process solidifies over 95% of the steel worldwide [1]. Continuous casting of steel requires turbulent flow patterns in the nozzle and mold to be maintained within an optimum window to minimize defects [2]. Excessive meniscus velocities and surface turbulence lead to inclusion defects due to slag entrainment and level fluctuations in the mold [2-3]. Insufficient surface flows lead to meniscus freezing which in turn leads to hook formation and other surface defects [2-3].

These important flow parameters in nozzle and mold of continuous casting process are governed by the flow control system (stopper rod or slide gate), nozzle geometry, submerged entry nozzle (SEN) depth, casting speed, strand cross-section dimensions, argon gas injection rate, slag behavior, and the application of electromagnetics [2]. Among these, electromagnetic braking (EMBr) is one of the widely used methods to non-intrusively control the flow in nozzle and mold to maximize inclusion floatation and minimize slag entrainment and other surface related defects.

Numerical simulation of turbulent flow in continuous casting when combined with measurements is a powerful method for such studies. However, the computational models need to go through rigorous validation and assessment against measurements or direct numerical simulation databases before their confident usage in continuous casting nozzle and mold to understand important physics and analyze some of issues involved with these systems.

The current thesis develops and tests different transient and steady-state models such as direct numerical simulation (DNS), large eddy simulation (LES), filtered unsteady Reynolds-averaged Navier-Stokes (URANS) and steady Reynolds-averaged Navier-Stokes (RANS) with

and without electromagnetic braking effects. This thesis considered both transient and steady models due to the importance of both time-average and fluctuation velocities in defect formation. The models are used in canonical geometries such as channel, square duct and rectangular duct and in continuous casting nozzle and mold. The extensive validation of these models has been carried out with DNS databases in canonical geometries and with measurements in physical water and GaInSn models of continuous casting before using them to learn important physics associated with turbulent flows in these systems. A final objective of this thesis is to gain practical insights to help improve the continuous casting process.

1.1. Continuous Casting of Steel

Continuous casting of steel is a process involving complex turbulent flow physics. Figure 1.1(a) and (b) respectively show the side and front views of the schematic of the continuous casting process [4]. Here the molten steel flows from the tundish through a SEN into the copper mold. The mold is continuously cooled from the side walls and the solidification of shell starts at the meniscus. This shell holds the molten steel and is continuously removed from the bottom of the mold. To provide thermal and chemical protection to the steel from atmosphere, the free surface of the mold is covered with an oxide-based slag.

A close-up of the molten steel flow behavior with the solidifying shell in the upper part of the mold is shown in Figure 1.2 [4]. High speed jet comes out of the SEN port at an angle. This jet hits the shell at the narrow face and splits into upper and lower recirculation zones. Since, this jet carries superheat and if it gets more focused at shell under unstable conditions it may lead to shell erosion and ”break-out”. The molten steel flow which comes on the top free surface after hitting the narrow face is very important to the steel quality. The flow on the surface decides the initial solidification by controlling the heat transfer. If the surface flow is too fast then it may

cause slag entrainment by shearing off the slag layer. This entrained slag may be carried by the steel deep down into the mold cavity leading to entrapment in the shell forming defects. The flow which returns towards the upper side along narrow face on the surface causes a standing wave and thinning of the slag layer. This thinned slag layer may expose steel to the atmosphere leading to detrimental effects such as reoxidation and inclusions. Molten steel also contains alumina particles which can possibly get attached to the shell. Argon gas is injected in the SEN to avoid nozzle clogging and encourage inclusion floatation towards the molten slag layer. In addition to the defects caused by slag and alumina particles, argon gas can also be carried deep into mold cavity and thus causing defects.

The transient turbulent flow is responsible for transient level fluctuations and surface waves which are highly critical to the steel quality. The mold flow pattern should be optimized to achieve a flat surface profile with stable meniscus velocities of the desired magnitude and optimum turbulence. Due to the severe environment with molten steel being at 1500^{o} C in these systems, plant measurements are very difficult and limited. Few previous studies considered plant measurements of surface velocity using nail-boards [5], Sub-meniscus velocity control (SVC) [6] probe and electromagnetic [7] sensors combined with computational models to investigate turbulent flows. These techniques are limited to the surface velocities and suffer from limited number of data points, spatially and sometimes temporally.

Due to the limitations of the plant measurements, the use of measurements in physical models such as in water or liquid-metal models at the same or smaller scales is the most logical approach to thoroughly validate computational models. The validated computational models can then be used with higher degree of confidence to understand complex physics and related issues with continuous casting process.

1.2. Contributions of the Current Work

Researchers have carried out various studies to understand complex physics and associated issues in continuous casting process [8]. Studies using transient models such as DNS/LES with electromagnetic braking in continuous casting process are limited in the scope and depth and therefore have been the focus of the current thesis. In the current thesis, initially, transient and steady state turbulence models are employed and validated in canonical geometries before their evaluation and usage in more complicated continuous casting nozzle and mold geometries. The various contributions of the current thesis are outlined step by step below:

CHAPTER 2 presents DNS of the effect of magnetic field in the canonical geometries such as channel and square duct. This work is part of development and validation of the graphic processing unit (GPU) based CFD code (CU-FLOW) before its usage in more complex continuous casting geometries. The original non-magnetohydrodynamic (non-MHD) version of the code was provided by Aaron Shinn which was further augmented with MHD formulations, vorticity budgets, and turbulent kinetic energy budgets. The instantaneous velocities, time/ensemble average velocities, Reynolds stresses, streamwise vorticity budgets and turbulent kinetic energy budgets are given. The effects of magnetic fields are extensively investigated in a square duct to understand their usage in more practical material processing applications for controlling fluid flow, heat transfer, and frictional losses. This work also provides DNS database in two-wall bounded magnetohydrodynamic (MHD) turbulent flow for RANS and LES model development to incorporate the effect of magnetic field on turbulence in these models.

This work has been published in "Physics of Fluids":

R. Chaudhary, S. P. Vanka and B. G. Thomas, Direct Numerical Simulations of magnetic field effects on turbulent flow in a square duct, Physics of Fluids, 22, 075102, 2010.

CHAPTER 3 extends the aforementioned MHD channel and square duct DNS work to a 2:1 aspect ratio rectangular duct. The rectangular duct is a more practical geometry for application in continuous casting. The direct numerical simulations with transverse and spanwise magnetic fields are performed to study the effect of magnetic field orientations and strength on corner anisotropic turbulent flows. The instantaneous velocities, time/ensemble average velocities, Reynolds stresses, wall stresses, streamwise vorticity transport budgets, turbulent kinetic energy budgets, momentum equations budgets are given. The important details on the two orientations of magnetic field in controlling various mixing and frictional loss characteristics are presented. This work provides more versatile DNS databases for a corner anisotropic two-wall bounded MHD turbulent flow.

This work has been submitted to "Computers & Fluids":

R. Chaudhary, A. F. Shinn, S. P. Vanka and B. G. Thomas, Direct Numerical Simulations of Transverse and Spanwise Magnetic Field Effects on Turbulent Flow in a 2:1 Aspect Ratio Rectangular Duct , Computers & Fluids, Submitted, Nov. 2010.

CHAPTER 4 presents the validation of various steady-state RANS turbulence models for their usage in industrial application, including in continuous casting. Several low- and high-Reynolds number versions of k-ε and Reynolds stress turbulence models have been evaluated in a channel and a square duct flow with and without a magnetic field by comparing the predictions with our DNS data presented in CHAPTER 2 and previous DNS databases. The additional source terms for magnetic field effects on turbulence have been included through user-defined functions. A systematic assessment of the predicted mean flow, turbulence quantities, frictional losses and computational costs of the various turbulence models is also presented. The guidelines

on the usage and performance of these models to help interpret their predictions and associated inaccuracies are presented for industrial applications, including continuous casting.

This work has been documented as a "Continuous Casting Consortium report":

R. Chaudhary, B.G. Thomas and S.P. Vanka, Evaluation of turbulence models in MHD channel and square duct flows, CCC report 201011, Department of Mechanical Science & Engineering, University of Illinois at Urbana-Champaign, IL.

CHAPTER 5 presents first practical application of steady-state RANS model (Standard k-ε) combined with measurements to understand the mold flow quality produced by the nozzle with well- and mountain-type bottom wells. The instantaneous velocity measurements in a $1/3^{rd}$ scale water model using particle imaging velocimetry (PIV) and impeller velocity probe were provided by Go-Gi Lee and Seon-Hyo Kim, POSTECH, South Korea. The standard k-ε model was selected in this study due to it being computational cheap on coarse meshes with reasonable accuracy, as confirmed in CHAPTER 4. The model was customized to simulate the solidification effects by incorporating mass and momentum sink terms in the fluid cells at the shell interface. The flow patterns, surface velocities, free surface levels, jet characteristics produced by two nozzle bottoms were analyzed. The spectral analysis on the measured instantaneous surface and jet velocities was performed. The computational model was then extended to a real caster with Froude similarity. The different aspects on the turbulent flow in the nozzle and mold of the two nozzles were presented with pros and cons towards their usage in continuous casting.

This work has been published in "Metallurgical and Materials Transactions B":

R. Chaudhary, G.-G. Lee, B. G. Thomas, S.-H. Kim, Transient mold fluid flow with well- and mountain- bottom nozzles in continuous casting of steel, Metallurgical and Materials Transactions B, Vol. 39, 6, Dec. 2008, pp. 870-884.

CHAPTER 6 extends the standard k-ε model used in CHAPTER 5 to investigate the effect of stopper-rod misalignment on nozzle and mold flow in a conventional continuous casting process. The velocity and vortex formation frequency measurements for this work in a 1/3rd scale water model were provided by Seong-Mook Cho, Go-Gi Lee, Seon-Hyo Kim, POSTECH South Korea and Oh-Duck Kwon, POSCO, South Korea. Three stopper-rod configurations are studied (aligned, front-misaligned by 2 mm, and left-misaligned by 2 mm). The model predictions of surface velocity and turbulence matched reasonably well with measurements. The effect of misalignment on flow patterns, velocities, turbulence and vortex formation in difference regions of the nozzle and mold was presented. The importance of alignment of stopper-rod in continuous casting to avoid expensive defects is outlined.

This work has been published in "Metallurgical and Materials Transactions B":

R. Chaudhary, G.-G. Lee, B. G. Thomas, S.-M. Cho, S.-H. Kim and O.-D. Kwon, Effect of stopper rod misalignment on fluid flow in continuous casting of steel, Metallurgical and Materials Transactions B, Vol. 42, 2, April 2011, pp. 300-315.

CHAPTER 7 is part of the model evaluation, besides investigating the physics associated with turbulence in the nozzle and mold of a liquid-metal model of continuous casting process. The predictions of two RANS models, a filtered unsteady RANS model, and two LES models are combined with ultrasonic Doppler velocimetry (UDV) measurements. in a small scale GaInSn model of the continuous casting mold region fed by a bifurcated well-bottom nozzle with horizontal ports. The instantaneous horizontal velocity measurements for this work in GaInSn model were provided by K. Timmel, S. Eckert and G. Gerbeth, FZD, Dresden, Germany [9]. Chuanbo Ji helped in post processing some of results for this work. A thorough investigation of turbulent flow through a liquid-metal model of continuous casting process based upon

instantaneous and time-average flow patterns, Reynolds stresses, and proper orthogonal decomposition (POD) analysis is presented.

This work has been published in "Metallurgical and Materials Transactions B":

R. Chaudhary, C. Ji, B. G. Thomas, and S. P. Vanka, Transient Turbulent Flow in a Liquid-Metal Model of Continuous Casting, Including Comparison of Six Different Methods, Metallurgical and Materials Transactions B, In-Press, April, 2011.

CHAPTER 8 uses LES along with measurements performed using UDV to investigate the effects of single/double ruler type electromagnetic braking (EMBr) on turbulent flows in GaInSn model. The velocity measurements in two EMBr cases (92 mm and 121mm from free surface) were provided by K. Timmel, S. Eckert and G. Gerbeth, FZD, Dresden, Germany [10-11]. The transient and time-average flow features of turbulent flow under the influence of different strengths and locations of the EMBr are investigated. The detailed analysis based on Reynolds stresses, turbulent kinetic energy budgets and POD is presented.

This work will be submitted to "Metallurgical and Materials Transactions B":

R. Chaudhary, B. G. Thomas and S. P. Vanka, Effect of Electromagnetic Ruler Braking (EMBr) on Transient Turbulent Flow in Continuous Slab Casting Using Large Eddy Simulations, Metallurgical and Materials Transactions B, In Write-Up.

CHAPTER 9 summarizes the findings on each chapter and concludes overall thesis by providing a detailed discussion of the contributions. The models used in current work are extensively tested before using them to learn important physics associated with related issues. Overall, this thesis addresses several issues such as flow quality with well- and mountain-bottom nozzles, stopper-rod misalignment effects on steel quality and studies related to the effect of

magnetic field on turbulent flows in canonical as well as continuous casting nozzle and mold geometries. The recommendations are made on the future direction of research.

Other Publications during PhD:

1. **R. Chaudhary**, A. F. Shinn, S. P. Vanka and B. G. Thomas, Direct numerical simulation of turbulent MHD flow in a 2:1 aspect ratio rectangular duct subjected to transverse and span-wise magnetic fields, 63rd Annual Meeting of the APS Division of Fluid Dynamics, Vol. 55, No. 16, Nov. 21-23, 2010, Long Beach, CA.
2. S-M Cho, G-G Lee, S-H Kim, **R. Chaudhary**, O-D Kwon and B.G. Thomas, Effect of stopper rod misalignment on asymmetric flow and vortex formation in steel slab casting, Jim Evans Honorary Symposium, 2010 TMS Annual Meeting & Exhibition, Feb. 14-18, 2010, Seattle, WA.
3. **R. Chaudhary**, S. P. Vanka and B. G. Thomas, Direct Numerical Simulations of Magnetic Field Effects on Turbulent Duct Flows, ASME-IMECE, Nov. 13-19 2009, Lake Buena Vista, FL.
4. **R. Chaudhary**, B. T. Rietow and B. G. Thomas, Differences between Physical Water Models and Steel Continuous Casters: A Theoretical Evaluation, Material Science & Technology, Oct. 25-29, 2009, Pittsburgh, PA.
5. B. G. Thomas and **R. Chaudhary**, State of the Art in Electromagnetic Flow Control in Continuous Casting of Steel Slabs: Modeling and Plant Validation: Plenary Lecture, 6th International Conference on Electromagnetic Processing of Materials, Oct. 19-23 2009, Dresden, Germany.

1.3. Figures

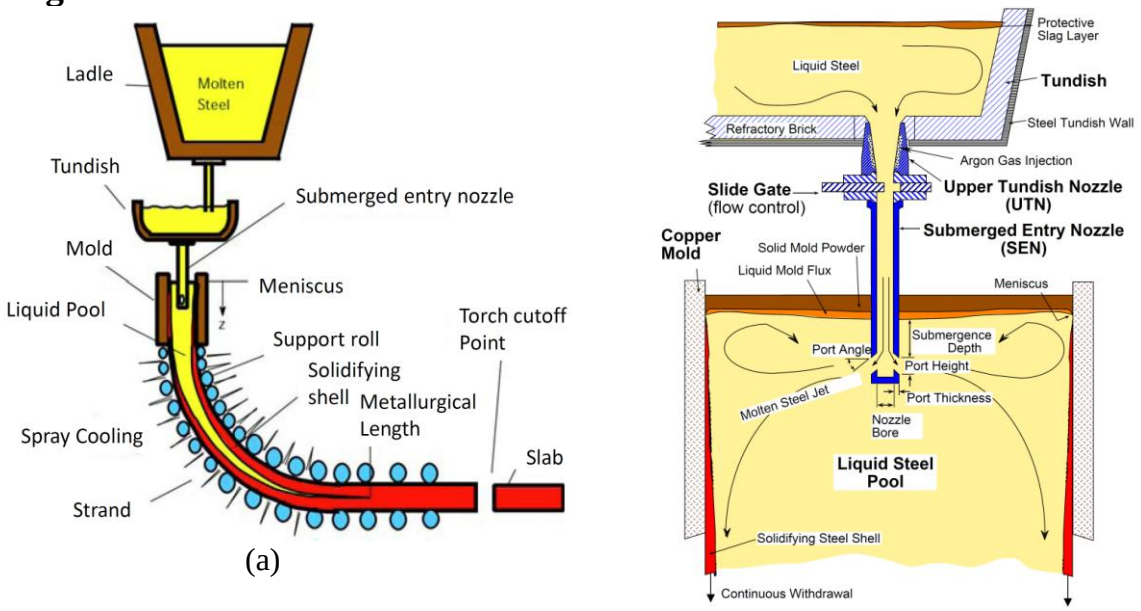

Figure 1.1 Continuous casting process (a) side-view (b) front-view [4]

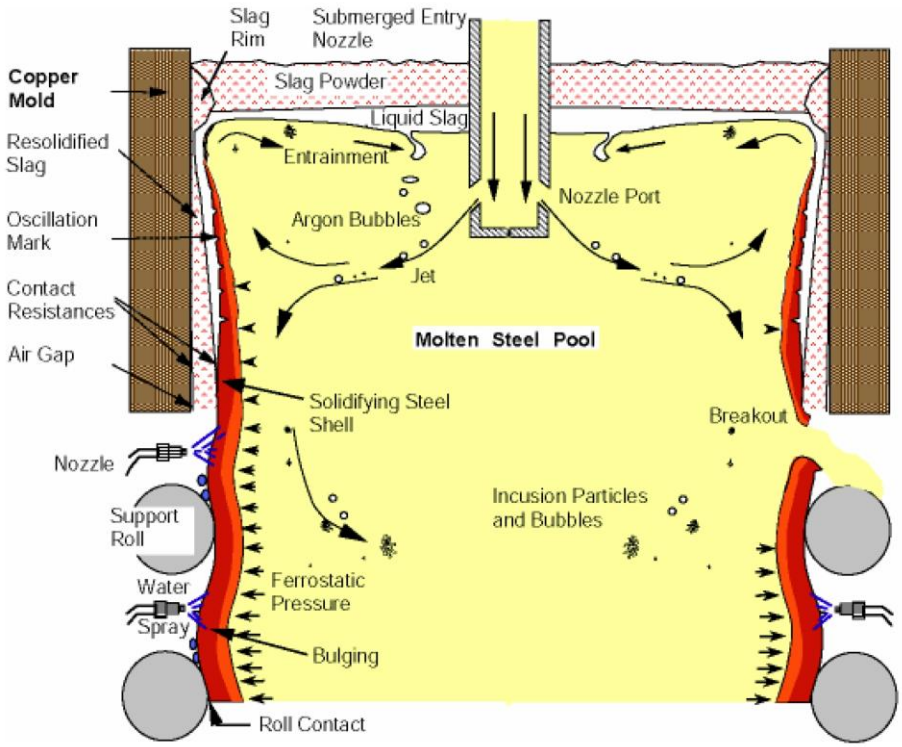

Figure 1.2 Close up at the fluid flow and shell solidification in continuous casting process [4]

1.4. References

1. *World Steel in Figures*. 2007, International Iron and Steel Institute: Brussels, Belgium, www.worldsteel.org.
2. B. G. Thomas, Fluid flow in the mold, Chapter 14 in Making, Shaping and Treating of Steel, 11th Edition, vol. 5, Casting Volume, Editor: A. Cramb, AISE Steel Foundation, Oct. 2003, Pittsburgh, PA, pp. 14.1-14.41.
3. J. Kubota, et al. *Meniscus Flow Control in the Mold by Travelling Magnetic Field for High Speed Slab Caster*. in *Steelmaking Conf. Proceedings*. 1991.
4. Continuous Casting Consortium, Department of Mechanical Science & Engineering, University of Illinois at Urbana-Champaign, IL, USA, http://ccc.illinois.edu/
5. K. Cukierski and B. G. Thomas, Flow Control with Local Electromagnetic Braking in Continuous Casting of Steel Slabs, Metall. Mat. Trans. B, 39, 1, 2007, pp. 94-107.
6. J. Sengupta, R. Liu, D. Crosbie, S. Chung, M. Trinh, B. G. Thomas, Measurement of Molten Steel Surface Velocity with SVC and Nail Dipping during Continuous Casting Process, TMS annual meeting and Exhibition, San Diego, 2011.
7. B. G. Thomas, Q. Yuan, S. Sivaramakrishnan, T. Shi, S. P. Vanka, and M. B. Assar, "Comparison of Four Methods to Evaluate Fluid Velocities in a Continuous Slab Casting Mold", ISIJ International, 2001, Vol. 41, No. 10, pp. 1266-1276.
8. B. G. Thomas, and L. Zhang, Review: Mathematical Modeling of Fluid Flow in Continuous Casting of Steel, ISIJ International, 2001, Vol. 41, No. 10, pp. 1181-1193.
9. K. Timmel, S. Eckert, G. Gerbeth, F. Stefani, and T. Wondrak, Experimental modeling of the continuous casting process of steel using low melting point alloys – the LIMMCAST program, ISIJ International, 2010, 50, No. 8, pp. 1134-1141.

10. K. Timmel, S. Eckert, and G. Gerbeth, Experimental investigation of the flow in a continuous-casting mold under the influence of a transverse, direct current magnetic field, Metall. Mat. Trans. B, 2011, vol. 42, 1, pp. 68-80.

11. K. Timmel, X. Miao, S. Eckert, D. Lucas, and G. Gerbeth, Experimental and numerical modeling of the steel flow in a continuous casting mould under the influence of a transverse DC magnetic field, Magnetohydrodynamics, 2010, vol. 46, 4, pp. 337-448.

CHAPTER 2. DIRECT NUMERICAL SIMULATIONS OF MAGNETIC FIELD EFFECTS ON TURBULENT CHANNEL AND SQUARE DUCT FLOWS

2.1. Introduction

Magnetic fields are commonly used to control flows in metal processing, MHD pumps, plasma and fusion technology, to name a few [1]. Continuous casting is one process using different types of magnetic fields in the mold to minimize defects in the final product [2]. When a magnetic field is applied to a flow field, it induces a current and the interaction of this current with the magnetic field generates a Lorentz force. This Lorentz force brakes the flow and alters the velocity field [3]. In case of turbulent flows, magnetic fields can relaminarize the flow and alter the structure of the turbulent flow significantly [4]. Consequently the friction characteristics and mixing phenomena in turbulent flows subjected to magnetic fields can be significantly different from those without a magnetic field. Tailoring the magnetic field to alter the flow in the mold of the continuous caster of steel is a topic of significant practical interest [2].

The common methodology used in most previous studies to simulate effects of magnetic field on turbulent flows has been the Reynolds-averaged approach [4-8]. However, the fundamental difficulty with such an approach is the modeling of the effects of the magnetic field on the Reynolds stresses [4]. Specifically, it is difficult to predict the suppression of turbulence and modification of the flow structures through the time-averaged approach [4]. Since the magnetic field directly acts on the turbulent fluctuations, a more rigorous method with solution of equations for the time-dependent three-dimensional turbulent flow is required. Recently, with the significant improvement in computer speed, Direct Numerical Simulations (DNS) have

become feasible as a complementary tool to experiments [9]. In the present work, the effects of a magnetic field on turbulent flow through a square duct are studied using the DNS approach.

Extensive studies exist on DNS, Large Eddy Simulations (LES) and experiments of turbulence in a planar two-dimensional channel flow (Moin and Kim [10], Kim, Moin and Moser [11], Moser, Kim and Mansour [12], Moser and Moin [13], and Monty and Chong [14]). Relatively, a smaller number of studies have considered flow in a duct with two inhomogeneous directions [15-18]. The first DNS with two inhomogeneous directions was performed by Gavrilakis [15]. A finite difference scheme with 16 million nodes and a moderate Reynolds number of 4410 were used to study turbulent flow in a square duct. The turbulence-driven secondary flows along with the bulging of the mean streamwise velocity field were accurately predicted. The turbulent statistics at the wall bisectors were seen to agree with data in a planar channel. Huser and Biringen [16] used a time-splitting method with spectral/higher-order finite difference discretization on a staggered mesh to simulate a similar flow but in their study, the Reynolds number based upon friction velocity was higher (600 with 96x101x101 grid points). Madabhushi and Vanka [17, 18] performed LES and DNS of turbulent flow in a square duct using a mixed spectral-finite difference method. DNS at Re_τ (Du_τ / ν, $(\rho u_\tau^2 = \tau_w$ (wall stress)) of 260 and LES at 360 were found to predict secondary flows and turbulence statistics accurately.

The turbulent flow subjected to a magnetic field has been the subject of many previous studies [19-30]. Brouillette and Lykoudis (1967) carried out experiments in a high aspect ratio (5:1) duct and predicted laminarization under a uniform and strong magnetic field [19]. Reed and Lykoudis (1978) reinvestigated effects of magnetic field on turbulence in a 5.8:1 aspect ratio duct and studied the effect of magnetic field on friction factor [20]. Satake, Kunugi and Smolentsev (2002) performed DNS to investigate turbulent pipe flow in a transverse magnetic

field at a moderate Reynolds number of 5300 and three Hartmann numbers of 5, 10, and 20 [21]. The skin friction, velocity profiles, turbulent intensities and turbulent kinetic energy budget were studied at different circumferential directions in the pipe. At locations close to wall on the horizontal axis, the velocity profile was observed to become more rounded with Hartmann flattening seen at the top and bottom of the pipe. Lee and Choi (2001) performed DNS of flow in a channel to study the effect of magnetic field orientation on the pressure drop [22]. They considered streamwise, wall-normal and span-wise magnetic fields and found increased drag due to the Hartmann effect in the case of wall normal magnetic field. Kobayashi (2006) performed LES in a channel flow under a wall normal magnetic field [23]. Results with a Coherent Structure Smagorinsky Model (CSM) were compared with those using the Smagorinsky Model (SM) and Dynamic Smagorinsky Model (DSM). Satake, Kunugi, Kazuyuki and Yasuo (2006) studied the effect of magnetic field on wall bounded turbulence in a channel using DNS at a high Re of 45818 and Hartmann numbers of 32.5 and 65 [24]. A uniform magnetic field was applied normal to the wall and various turbulence quantities were analyzed. Large scale structures were found to decrease in the core of the channel. Therefore, the difference between production and dissipation in the turbulent kinetic energy was found to decrease upon increase of Hartmann number in the central region of the channel. Boeck et al [25] performed DNS studies of the effect of the wall normal magnetic field on a turbulent flow in a channel at different Reynolds and Hartmann numbers. The three-layer near wall structure consisting of viscous region, logarithmic layer and plateau were reported at higher Hartmann numbers. These structures were reported signifying the importance of viscous, turbulent and electromagnetic stresses on the streamwise momentum equation. The turbulent stresses were found decaying more rapidly away from the wall than predicted by mixing-length models. Noguchi and Kasagi [26] also conducted the DNS

in MHD channel flow under transverse magnetic field at Re_τ=150 and Ha=6. The DNS databases of this as well as other calculations are maintained at http://www.thtlab.t.u-tokyo.ac.jp/. Krasnov et al. [27] performed DNS and LES in a channel flow under span-wise magnetic field at two Reynolds numbers (10,000 and 20,000) and Hartmann numbers varying over a wide range. The main effect of the magnetic field was seen in turbulence suppression and reduction in the momentum transfer in the wall normal direction. The centerline velocity increased while the mean velocity gradient close to wall reduced and thus reducing the drag. The coherent structures were found to be enlarged in the horizontal direction upon increasing the Hartmann number. From comparison of LES with the DNS, the dynamic Smagorinsky model was found to reproduce the changes in the flow more accurately.

Zikanov and Thess [28, 29] studied the effect of magnetic field on turbulence using DNS in a classical 3-D cube with all directions having periodic boundary conditions. At a low magnetic interaction (Stuart) number, turbulence was found to be three-dimensional and approximately isotropic while turbulence suppression was seen at large Stuart numbers (strong magnetic field).

Very recently, Kobayashi (2008) performed LES of the flow in a square duct with a transverse magnetic field. Two Reynolds numbers (Re=5300 and Re=29000) with 64x64x64 and 128x128x128 grids respectively were used [30]. At Re=5300, the Hartmann layer as well as side-wall layers were found to laminarize together at nearly the same Hartmann number. At the higher Reynolds number (Re=29000), the top and bottom Hartmann layers laminarized first, followed by laminarization of the side-wall layers.

In the present work, Direct Numerical Simulations of turbulent flow in a square duct subjected to various Hartmann numbers are conducted. The flow structures and mean velocities

are studied for a nominal Reynolds number around 5000. The computer code is initially validated for turbulent flow in a channel at Re_τ=178.12 without applying a magnetic field with previous work of Moser et al [12]. Subsequently, simulations in a non-MHD square duct are performed at Re=4547 and Re=5368 and results from Re=4547 calculation are compared with Gavrilakis (Re=4410) [15]. Further on, the simulation of laminar flow in a square duct with a transverse magnetic field is performed and the results are compared with previously known series solutions [31]. As a last validation, simulation of a turbulent MHD channel flow is performed at Re_τ=150 and Ha=6 and compared with Noguchi and Kasagi [26]. A magnetic field was then applied in the vertical direction of a square duct and computations with 64x64x128, 80x80x256 and 128x128x512 cells and 1x1x2π and 1x1x16 domain sizes were performed. Mean and RMS velocities, Reynolds shear stresses, turbulent kinetic energy budgets, and streamwise vorticity budgets are collected and analyzed. The effects of magnetic field on friction losses in the duct are also evaluated.

2.2. Governing Equations for a Magnetohydrodynamic Flow

It is well-known that when an electrically conducting material moves through a magnetic field, an electric current is induced. This induced electric current interacts with the magnetic field and produces a force (J x B) on the flow field, called the Lorentz force. This Lorentz force brakes the flow and therefore opposes the very mechanism that created it. The following equations mathematically describe the flow evolution for an incompressible MHD flow [32, 3].

Continuity equation:

$$\nabla \cdot \vec{v} = 0 \tag{2.1}$$

Momentum equations (x-, y- and z-)

$$\rho\left(\frac{\partial \vec{v}}{\partial t} + \nabla \cdot \left(\vec{v}\vec{v}\right)\right) = -\nabla p + \nabla \cdot \mu \nabla \vec{v} + \vec{F}_L \tag{2.2}$$

Since magnetic Reynolds number (Re_m) is less than unity in liquid metals, the induced magnetic field due to the induced electric current can be neglected. After neglecting the induced magnetic field, the electric potential method can be used to determine the current and the Lorentz force by the following equations [3].

$$\vec{F}_L = \vec{J} \times \vec{B}_0 \tag{2.3}$$

$$\vec{J} = \sigma\left(-\nabla\phi + \vec{v} \times \vec{B}_0\right) \tag{2.4}$$

$$\nabla \cdot \vec{J} = 0 \tag{2.5}$$

By inserting current from Eq.(2.4) into the conservation of charge Eq.(2.5), a Poisson equation for electric potential can be derived as,

$$\nabla^2\phi = \nabla \cdot \left(\vec{v} \times \vec{B}_0\right) = \vec{B}_0 \cdot \nabla \times \vec{v} = \vec{B}_0 \cdot \vec{\omega} \tag{2.6}$$

Where $\vec{\omega}$ is vorticity and external magnetic field is given as: $\vec{B}_0 = \left(B_{0x}, B_{0y}, B_{0z}\right)$. Above given governing equations can be non-dimensionalized as follows:

$$\vec{x}^* = \left(x^*, y^*, z^*\right) = \left(\frac{x}{D_h}, \frac{y}{D_h}, \frac{z}{D_h}\right), t^* = \frac{t}{\left(D_h / W_b\right)}$$

$$\vec{v}^* = \left(u^*, v^*, w^*\right) = \left(\frac{u}{W_b}, \frac{v}{W_b}, \frac{w}{W_b}\right) \quad , \quad p^* = \frac{p}{\rho W_b^2} \quad \vec{B}_0^* = \left(\frac{B_{0x}}{B_0}, \frac{B_{0y}}{B_0}, \frac{B_{0z}}{B_0}\right) \quad , \qquad \phi^* = \frac{\phi}{\left(D_h W_b B_0\right)} \quad ,$$

$$\nabla^* = \frac{\partial}{\partial x^*} i + \frac{\partial}{\partial y^*} j + \frac{\partial}{\partial z^*} k$$

The non-dimensionalized continuity and momentum equations can be written as;

$$\nabla \cdot \vec{v}^* = 0 \tag{2.7}$$

$$\frac{\partial \vec{v}^*}{\partial t^*} + \nabla^* \cdot \left(\vec{v}^* \vec{v}^*\right) = -\nabla^* p^* + \frac{1}{\mathrm{Re}} \nabla^* \cdot \nabla^* \vec{v}^* + \frac{\mathrm{Ha}^2}{\mathrm{Re}} \left(\vec{J}^* \times \vec{B}^*\right) \tag{2.8}$$

$$\nabla^{*2}\phi^* = \nabla^* \cdot \left(\vec{v}^* \times \vec{B}_0^*\right) \tag{2.9}$$

$$\vec{J}^* = -\nabla^* \phi^* + \vec{v}^* \times \vec{B}_0^* \tag{2.10}$$

There are essentially two independent non-dimensional parameters (Reynolds and Hartmann numbers) that govern the flow field and are defined based upon hydraulic diameter (D_h) and bulk axial velocity (W_b) as,

$$\mathrm{Re} = \frac{D_h W_b}{\nu} \qquad \mathrm{Ha} = D_h B_0 \sqrt{\frac{\sigma}{\rho \nu}} \tag{2.11}$$

2.3. Physical Domain and Boundary Conditions

Initially, for the validation purpose, the turbulent channel flows with and without MHD have been simulated and compared with previous DNS work [12, 26]. Figure 2.1 shows the physical and computational domain for the turbulent channel flow with other details (the mesh and domain sizes, mesh stretching, averaging time and Reynolds and Hartmann numbers etc.) on the runs given in Table 2.1. The non-uniform mesh was used in the wall normal direction as per the stretching factor given below Table 2.1. The streamwise and span-wise directions were considered periodic with top and bottom walls as no-slip and insulated. In MHD channel, the magnetic field is applied in vertical direction, as given in Figure 2.1. In addition to the above mentioned boundary conditions, in the MHD channel, the span-wise direction requires one more additional condition on mean electric potential gradient. For this purpose, the open-circuit condition in span-wise direction was assumed and the mean electric potential gradient as proposed by Lee and Choi [22] was implemented. In channel flow runs, a constant streamwise pressure gradient ($\partial \overline{p} / \partial z$) was fixed corresponding to the given Re_τ (178.12 and 150) and bulk Reynolds number was allowed to change.

Figure 2.2 presents the physical and computational domains considered for square duct in this study. Two directions of the domain are bounded by walls, whereas the main flow direction

is considered to be periodic. The size of the domain is 1x1x2π and 1x1x16 for the different meshes. For periodic boundary conditions, domain size should be at least twice the distance for which two-point velocity fluctuation correlation is zero [10]. Domain length of 2π or more seems adequate for the current case as proposed by Madabhushi and Vanka [17]. The preceding domain requirement still needs verification in MHD duct flow and therefore is also a subject of current study. The domain is discretized with 64x64x128, 80x80x256 and 128x128x512 cells for the different cases studied. Table 2.2 presents various cases simulated for square duct flow in the current study with various details (like domain and mesh sizes, grid stretching, Reynolds and Hartmann number etc.) given. The non-uniform grids were used in wall normal directions with stretching factors given below Table 2.2. A constant and uniform magnetic field is applied in the vertical (y-) direction. In all the runs the streamwise pressure gradient ($\partial\overline{p}/\partial z$) was fixed and the bulk Reynolds number was allowed to change. In all the square duct MHD runs, the streamwise pressure gradient was fixed corresponding to Re_τ=361. No-slip and insulated wall boundary conditions have been used for the side and top and bottom walls. Thus,

$$\vec{v}^* = 0,\ J_y^* = 0 \Rightarrow \frac{\partial \phi^*}{\partial y^*} = 0 \quad \text{(top and bottom walls)}$$

$$\vec{v}^* = 0,\ J_x^* = 0 \Rightarrow \frac{\partial \phi^*}{\partial x^*} = 0 \quad \text{(right and left walls)} \tag{2.12}$$

2.4. Numerical Method

The above coupled equations have been discretized using the Finite Volume Method (FVM) on a structured Cartesian staggered grid. Pressure-velocity coupling is resolved through the fractional step method [33] with explicit formulation of the diffusion and convection terms in the momentum equations. The method consists of the following steps.

x-momentum equation:

$$\left(\frac{\hat{u}^* - u^{*n}}{\Delta t^*}\right) = \left(\frac{3}{2}\left(H_{u^*}\right)^n - \frac{1}{2}\left(H_{u^*}\right)^{n-1}\right) - \left(\frac{\partial \overline{p}^*}{\partial x^*}\right) \tag{2.13}$$

$$\left(H_{u^*}\right)^n = \left(-\frac{\partial\left(u^* u^*\right)}{\partial x^*} - \frac{\partial\left(v^* u^*\right)}{\partial y^*} - \frac{\partial\left(w^* u^*\right)}{\partial z^*} + \frac{1}{\mathrm{Re}}\left(\frac{\partial^2 u^*}{\partial x^{*2}} + \frac{\partial^2 u^*}{\partial y^{*2}} + \frac{\partial^2 u^*}{\partial z^{*2}}\right)\right)^n$$

y-momentum equation:

$$\left(\frac{\hat{v}^* - v^{*n}}{\Delta t^*}\right) = \left(\frac{3}{2}\left(H_{v^*}\right)^n - \frac{1}{2}\left(H_{v^*}\right)^{n-1}\right) - \left(\frac{\partial \overline{p}^*}{\partial y^*}\right) \tag{2.14}$$

$$\left(H_{v^*}\right)^n = \left(-\frac{\partial\left(u^* v^*\right)}{\partial x^*} - \frac{\partial\left(v^* v^*\right)}{\partial y^*} - \frac{\partial\left(w^* v^*\right)}{\partial z^*} + \frac{1}{\mathrm{Re}}\left(\frac{\partial^2 v^*}{\partial x^{*2}} + \frac{\partial^2 v^*}{\partial y^{*2}} + \frac{\partial^2 v^*}{\partial z^{*2}}\right)\right)^n$$

z-momentum equation:

$$\left(\frac{\hat{w}^* - w^{*n}}{\Delta t^*}\right) = \left(\frac{3}{2}\left(H_{w^*}\right)^n - \frac{1}{2}\left(H_{w^*}\right)^{n-1}\right) - \left(\frac{\partial \overline{p}^*}{\partial z^*}\right) \tag{2.15}$$

$$\left(H_{w^*}\right)^n = \left(-\frac{\partial\left(u^* w^*\right)}{\partial x^*} - \frac{\partial\left(v^* w^*\right)}{\partial y^*} - \frac{\partial\left(w^* w^*\right)}{\partial z^*} + \frac{1}{\mathrm{Re}}\left(\frac{\partial^2 w^*}{\partial x^{*2}} + \frac{\partial^2 w^*}{\partial y^{*2}} + \frac{\partial^2 w^*}{\partial z^{*2}}\right)\right)^n$$

$$\left(\frac{\partial}{\partial x^*}\left(\frac{\partial p'^*}{\partial x^*}\right)^{n+1} + \frac{\partial}{\partial y^*}\left(\frac{\partial p'^*}{\partial y^*}\right)^{n+1} + \frac{\partial}{\partial z^*}\left(\frac{\partial p'^*}{\partial z^*}\right)^{n+1}\right) = \frac{1}{\Delta t^*}\left(\frac{\partial\left(\hat{u}^*\right)}{\partial x^*} + \frac{\partial\left(\hat{v}^*\right)}{\partial y^*} + \frac{\partial\left(\hat{w}^*\right)}{\partial z^*}\right) \tag{2.16}$$

$$u^{*n+1} = \left(\hat{u}^*\right) - \Delta t^*\left(\frac{\partial p'^*}{\partial x^*}\right)^{n+1} \tag{2.17}$$

$$v^{*n+1} = \left(\hat{v}^*\right) - \Delta t^*\left(\frac{\partial p'^*}{\partial y^*}\right)^{n+1} \tag{2.18}$$

$$w^{*n+1} = \left(\hat{w}^*\right) - \Delta t^*\left(\frac{\partial p'^*}{\partial z^*}\right)^{n+1} \tag{2.19}$$

where $p^* = \bar{p}^* + p'^*$.

Convection and diffusion terms have been discretized using the second order central differencing scheme in space. Time integration has been achieved using explicit second order Adams-Bashforth scheme. A multigrid solver is used to solve the Pressure Poisson Equation (PPE). Neumann boundary conditions are used at the walls for the pressure fluctuations (p'^*). The Electric Potential Poisson Equation (EPPE) is solved for ϕ^* also using a geometric multigrid solver. The Lorentz force $\left(\vec{J}^* \times \vec{B}^*\right)$ is then calculated and added as an explicit source term in momentum equations. All the calculations have been performed on a CPU (1.6 Ghz Itanium processor) based code written in FORTRAN except the finest calculations which have been performed by extending CU-FLOW (A Graphic processing Units (GPUs) based code) [34] with MHD modules [35] and vorticity, turbulent kinetic energy (TKE) budgets routines.

2.5. Results and Discussion

2.5.1. Results Without the Magnetic Field

We now present the results of the various calculations performed in this study. First, without a magnetic field, results at Re_τ=178.12 with 128x128x512 grid are compared with those of Moser et al [12]. Figures 2.3(a) and 2.3(b) give the comparisons of normalized mean axial velocity and RMS of velocity fluctuations respectively. The mean axial velocity and the RMS of velocity fluctuations are found to match very closely with the DNS of Moser et al [12].

Subsequently, the results in a square duct without a magnetic field for Re=4547 and 80x80x256 grid are compared with those of Gavrilakis [15] for a Reynolds number of 4410. Figures 2.4(a) and 2.4(b) give (snapshots) the instantaneous and the time-averaged flow fields, shown through contours of the streamwise velocity and cross-sectional velocity vectors. The

secondary flows generated by the anisotropic turbulence stresses are clearly captured. These secondary velocities are directed from the center towards the corners and cause bulging in contours of the streamwise velocity. Figure 2.4(c) shows an instantaneous picture of the flow at a y+ of 15. Regions of high and low speed streaks are clearly visible signifying the near wall sweeps and bursts in the x-z plane.

Figure 2.5(a) shows a comparison of the normalized mean axial velocity with results of Gavrilakis [15] at Re=4410. The mean axial velocity along the horizontal bi-sector from the current simulation is found to match well with results of Gavrilakis. Figure 2.5(b) shows a comparison of the normalized axial velocity along the diagonal of the duct. Again, normalized velocity matched with Gavrilakis [15] closely. Figure 2.5(c) presents comparison of RMS of axial velocity fluctuations with Gavrilakis [15] which also match closely with each other except for a minor disagreement probably due to the slightly different Reynolds number.

2.5.2. Results With a Magnetic Field

Figure 2.6 shows comparisons of the normalized axial velocity with analytical series solution of Muller and Buhler [31] for a laminarized square duct flow in the presence of a strong transverse magnetic field. Here the flow was initiated with a mean axial pressure gradient ($\partial\overline{p}/\partial z$) corresponding to Re_τ=372 (corresponds to bulk Re ~ 5368 with 64x64x128 grids) (calculated based upon hydraulic diameter) and a perturbation (1% of the mean) in the three directional velocities was applied for the initial 1500 timesteps to initiate turbulence. A strong magnetic field corresponding to Ha=60 was then applied. The strong magnetic field was found to annihilate turbulence followed by flattening of the velocity profile close to top and bottom walls. The suppression of turbulence reduces the frictional losses but subsequent velocity flattening close to top and bottom walls supersedes this reduction and increases friction losses, thus

reducing the bulk Reynolds number from ~5368 to 3900. The axial velocity along the horizontal bisector showed dampening of turbulence with a parabolic profile (hydrodynamic laminar profile) but the effect of velocity flattening is relatively smaller at this location. The velocity along the vertical bisector showed strong turbulence dampening followed by the velocity flattening. The axial velocity profiles match closely with the series solutions.

Figures 2.7(a) and 2.7(b) present comparisons of normalized mean axial velocity and RMS of velocity fluctuations with the DNS results of Noguchi and Kasagi (1994) at Re_τ=150 and Ha=6 in a channel. The current mean as well as RMS of velocity fluctuations matched closely with the results of Noguchi and Kasagi [26].

Figure 2.8(a) shows mean axial velocities along the horizontal bisector for three grid sizes at Ha=21.2 and their comparison with Kobayashi's LES results (Re=5300, Ha=21.2) [30]. In these cases, flow was initiated with a mean $\partial\overline{p}/\partial z$ corresponding to Re_τ=361 (calculated based upon hydraulic diameter) with a perturbation (1% of mean axial velocity) to the three directional velocities. The different grids, for the same Re_τ=361, resolved magnetic field-turbulence interaction slightly differently thus causing a slight difference in frictional losses and the bulk Reynolds numbers. The mean axial velocity along horizontal bisector achieved grid independence with the 80x80x256 grid. Figure 2.8(b) presents the mean axial velocity for the same cases along the vertical bisector. Axial velocity along this bisector with grid refinement has asymptotically approached grid independence on the finest mesh. The velocity along this bisector is seen to be more round than along the horizontal bisector. The main reason for this effect is the strong suppression of turbulence without velocity flattening at this Hartmann number close to top and bottom walls than near the side walls. Figures 2.8(c) and 2.8(d) respectively show the axial velocity along horizontal and vertical bisectors for various Hartmann

numbers. Along both bisectors, mean axial velocity initially becomes more round (at Ha=21.2 and Ha=22.26) compared to the non-magnetic field case. Upon further increasing the Hartmann number (to Ha=24.38), the turbulence is completely suppressed. The velocity along the vertical bisector flattens and closely follows the laminar parabolic profile along the horizontal bisector.

Figures 2.9(a) and 2.9(b) respectively show the instantaneous and time-averaged velocities in a representative cross-section for Re=5602 and Ha=21.2 case. With the magnetic field, the instantaneous velocities suggest weaker fluctuations close to the top and bottom walls and in the core than closer to side walls. It can be seen that the secondary flows are significantly modified in the presence of the magnetic field. Rather than going into the corners as in the non-MHD case, the secondary flows are now directed towards the top and bottom walls close to the corners, thus lifting axial velocity contours in these regions. After impinging on the walls in the corner regions, the secondary flows return towards the center of the top and bottom walls before heading to the core of the duct from top and bottom walls. This effect due to strong secondary flow from top and bottom walls towards the core causes strong sagging in mean axial velocity close to top and bottom walls. The effect of the magnetic field on the time-mean primary and secondary velocities is weaker close to the side walls.

Figure 2.9(c) shows the streaky structures at a transverse plane at Y^+=15 for the MHD case. Streaky structures in the presence of a magnetic field are more concentrated and elongated in the streamwise direction. A similar observation of the streaky structures in a MHD pipe flow was reported by Satake et al. [21].

Figure 2.9(d) gives the instantaneous current density lines plotted in the cross-section for laminar and turbulent MHD duct flows. The qualitative behavior of the current density in both flows is quite similar with current being parallel to magnetic field close to side walls and

perpendicular to magnetic field in the core and close to top and bottom walls. The magnitude and direction of the Lorentz force at different locations at the cross-section are mainly controlled by the current density magnitude and direction of current density with respect to applied magnetic field. The higher current perpendicular to magnetic field causes strong Lorentz force assisting the flow close to top and bottom walls. Weak current in the opposite direction and perpendicular to the magnetic field in the core gives retarding Lorentz force in the core region. At this Hartmann number (Ha=21.2) in the turbulent MHD duct, although the effect of the Lorentz force is small near the side walls (because of current being almost parallel to the magnetic field), the turbulence causes the current to fluctuate and become locally perpendicular to the magnetic field, resulting in slight turbulence suppression in this region as well.

Figure 2.10 presents the autocorrelation (as given in APPENDIX E2) of streamwise velocity fluctuations at front-mid (0.96D, 0.5D) and low-mid (0.5D, 0.08D) locations for Re=5602 and Ha=21.2 case. Direct spatial fluctuations as well as the temporal fluctuations (after converting them from time to length using Taylor's frozen turbulence hypothesis) have been used for calculating the spatial auto-correlations. Auto-correlations from both methods match closely within the approximation of a statistically stationary turbulent flow with turbulence intensity (w') small compared to the mean velocity. It can be seen in this figure that for both locations turbulence is de-correlated after ~2.4D. This provides an estimate of the characteristics length of the longest turbulence structure. Hence a domain length greater than twice this value (~2x2.4D=4.8D) is sufficient to capture the longest scales of turbulence. At the locations of strong Lorentz force (i.e. low-mid (0.5D, 0.08D)), the auto-correlation suggests a somewhat longer domain. A domain length of 2π is seen to be sufficient for both MHD and non-MHD cases.

Figures 2.11(a) and 2.11(b) present the RMS of axial velocity fluctuations along the horizontal and the vertical bisectors at Ha=21.2 respectively. As seen for the mean velocity, the grid-independence of the axial velocity fluctuations has also been obtained. Our results agree in general with Kobayashi's LES results but values in Kobayashi's LES showed underpredictions along the vertical bisector and overpredictions along the horizontal bisector. We believe that the difference may be caused by the use of the SGS model in LES calculations of Kobayashi [30].

Figures 2.12(a) and 2.12(b) show the RMS of axial velocity fluctuations for different Hartmann numbers along horizontal and vertical bisectors respectively. The effect of the magnetic field in suppressing turbulence is clearly visible in the core of the duct and close to the top wall along the vertical bisector. At this Hartmann number, axial velocity fluctuations close to the top wall are suppressed by approximately 40% from the non-MHD case with a slight shift of the location of peak towards the core of the duct. The magnetic field has relatively smaller turbulence suppression in the core of the duct compared to the region close to the top wall. In a laminar duct flow, the current is purely parallel to the magnetic field close to side walls. Hence the magnetic field has no effects. However, in a turbulent duct flow, a small effect is seen close to side walls because the current can be sometimes locally perpendicular to the magnetic field due to fluctuations in the current. The effect of the magnetic field is not much different at a Hartmann number of 22.26. However, around Ha=24, the turbulence along both bisectors is suppressed. This finding of simultaneous suppression of turbulence along both bisectors is consistent with Kobayashi's LES calculations (at Ha=5300 and Ha=21.2) [30].

Figures 2.13(a) and 2.13(b) show the RMS of horizontal and vertical velocity fluctuations along horizontal and vertical bisectors for the various Hartmann numbers. Since the magnetic field acts strongly close to the top and the bottom walls where the current is strong and

perpendicular to the field, the horizontal and vertical velocity fluctuations are suppressed strongly at these locations as well. However, close to side walls, both velocity fluctuations show weaker suppression. The variation of horizontal velocity fluctuations close to top and bottom walls is quite similar to the variation of vertical velocity fluctuations close to side walls. In the core of the duct, both horizontal and axial velocity fluctuations attain similar values.

Figures 2.14(a) and 2.14(b) show the Reynolds shear stresses ($\overline{w'u'}$, and $\overline{w'v'}$) along horizontal and vertical bisectors. Similar to the effects of the magnetic field on Reynolds normal stresses ($\overline{w'^2}$, $\overline{u'^2}$, $\overline{v'^2}$), the Reynolds shear stress ($\overline{w'v'}$) is also suppressed significantly close to top and bottom walls along the vertical bisector. Near the side walls, the suppression of $\overline{w'u'}$ is weak. Increasing Ha from 21.2 to 22.26 gives small additional suppression, especially in the region between the core and the wall.

2.6. Streamwise Vorticity Transport

Streamwise vorticity is caused by the secondary velocities in the transverse plane in a turbulent non-circular duct flow [15]. Several researchers have studied the mechanism of its transport in a non magnetic duct flow with source/sinks to determine the origin of the secondary flow [15-17].

They suggested that the Reynolds stresses are responsible for the production of mean streamwise vorticity in a non-MHD duct [15-17]. Gessner and Jones [36] were the first to propose that the difference in the second derivatives of Reynolds normal and shear stresses is responsible for the vorticity generation. Lee and Choi [22] extended the above analysis for a MHD flow. The streamwise vorticity in the case of a MHD flow has two additional terms. The first one is a second derivative of the electric potential and the second is a first derivative of a velocity component [22]. Contribution of these two additional terms is mainly decided by the

magnetic field orientation and flow type. For a wall normal or span-wise magnetic field in fully developed flow, the second derivative term of the electric potential has no contribution and only the first derivative of velocity acts as an additional sink. For a streamwise directed magnetic field, only the second derivative term of the electric potential contributes to the vorticity sink. In wall normal magnetic field in a developing flow, both terms have contribution to the vorticity sink.

The vorticity transport equation for fully developed turbulent square duct flow under a transverse magnetic field (B_{0y}) (after dropping superscript "*" from non-dimensional quantities) is written as,

$$\underset{\text{I}}{\bar{u}\frac{\partial\bar{\Omega}_z}{\partial x}+\bar{v}\frac{\partial\bar{\Omega}_z}{\partial y}}=\underset{\text{II}}{\frac{1}{\mathrm{Re}}\left(\frac{\partial^2\bar{\Omega}_z}{\partial x^2}+\frac{\partial^2\bar{\Omega}_z}{\partial y^2}\right)}+\underset{\text{III}}{\frac{\mathrm{Ha}^2}{\mathrm{Re}}\left(\frac{\partial\bar{u}}{\partial y}B_{0y}^2\right)}+\underset{\text{IV}}{\left(\frac{\partial^2}{\partial y^2}-\frac{\partial^2}{\partial x^2}\right)\overline{(u'v')}}+\underset{\text{V}}{\frac{\partial^2}{\partial x\partial y}\left(\overline{u'^2}-\overline{v'^2}\right)} \qquad (2.20)$$

where mean streamwise vorticity is $\bar{\Omega}_z=\left(\frac{\partial\bar{v}}{\partial x}-\frac{\partial\bar{u}}{\partial y}\right)$, I is the convection of streamwise vorticity, II is the viscous diffusion, III is the sink due to magnetic field, IV is the source/sink due to Reynolds shear stresses and V is the source/sink due to Reynolds normal stresses in the transverse plane.

Figure 2.15 presents the mean streamwise vorticity contours at a cross-section for a MHD and a non-MHD duct flow. Regions of positive and negative values signify the direction of rotation of secondary flows with mirror images on both sides of the diagonal bisectors signifying the secondary flows entering into the corners and exiting parallel to the side walls. The magnetic field is found to dampen the streamwise vorticity (secondary flows) across the whole cross-section and the dampening is proportional to the first derivative of horizontal velocity in vertical direction (Eq. 2.20). The regions of high vorticity close to top and bottom walls are elongated due to vertical magnetic field acting on a strong vertical derivative of horizontal velocity and

making vortices larger in this region. Exact contributions of the magnetic field to streamwise vorticity are presented in Figure 2.16 which gives various budgets of mean streamwise vorticity. Convection is mainly dominant in the regions of strong vorticity gradients and secondary velocities. Since diffusion is governed by the Laplacian of the vorticity it is seen to have larger values between regions of low and high vorticity close to the walls. Second derivatives of Reynolds shear and normal stresses give source/sink to the vorticity very close to walls in the corners. Source terms caused by Reynolds shear and normal stresses are of the same order but are of opposite sign. This finding is consistent with previous works of Gessner and Jones [36], and Madabhushi and Vanka [17] in a non-magnetic duct flow. The effect of shear stress is limited to small regions compared to those of normal stresses especially close to top and bottom walls. The magnetic field makes the Reynolds normal stress terms spread in the region of elongated vorticity to act as a source there and thus an indirect effect of magnetic field on vorticity production via Reynolds normal stresses in MHD duct. The magnetic field combined with the vertical derivative of horizontal velocity acts as a sink to dampen the vorticity close to the top and bottom walls. It is necessary to note that the vorticity source caused by the magnetic field is negatively correlated with the velocity derivative used to define vorticity (i.e. $\overline{\Omega}_z = \left(\frac{\partial \overline{v}}{\partial x} - \frac{\partial \overline{u}}{\partial y} \right)$ and $\frac{\partial \overline{u}}{\partial y}$ are negatively correlated). Thus the magnetic field produces a sink in streamwise vorticity.

2.7. Turbulent Kinetic Energy Budget

The turbulent kinetic energy budgets in MHD square duct flow under the transverse magnetic field can be derived by summing three momentum equations after multiplying with u',

v', w' and using averaging (again superscript "*" has been dropped from non-dimensional quantities). The balance can be written as the sum of various terms as:

$$\begin{aligned}0=&\text{Convection + Viscous Diffusion + Dissipation + Pressure Diffusion}\\&\text{+ Production + Turbulent Diffusion + MHD Source + MHD Sink}\end{aligned} \tag{2.21}$$

$$\text{Convection} = -\bar{u}\frac{\partial k}{\partial x} - \bar{v}\frac{\partial k}{\partial y} - \bar{w}\frac{\partial k}{\partial y} \tag{2.22}$$

$$\text{Viscous diffusion} = \frac{1}{\text{Re}}\left(\frac{\partial^2 k}{\partial x^2} + \frac{\partial^2 k}{\partial y^2} + \frac{\partial^2 k}{\partial z^2}\right) \tag{2.23}$$

$$\text{Dissipation} = -\frac{1}{\text{Re}}\left(\overline{\frac{\partial u'}{\partial x}\frac{\partial u'}{\partial x}} + \overline{\frac{\partial u'}{\partial y}\frac{\partial u'}{\partial y}} + \overline{\frac{\partial u'}{\partial z}\frac{\partial u'}{\partial z}} + \overline{\frac{\partial v'}{\partial x}\frac{\partial v'}{\partial x}} + \overline{\frac{\partial v'}{\partial y}\frac{\partial v'}{\partial y}} + \overline{\frac{\partial v'}{\partial z}\frac{\partial v'}{\partial z}} + \overline{\frac{\partial w'}{\partial x}\frac{\partial w'}{\partial x}} + \overline{\frac{\partial w'}{\partial y}\frac{\partial w'}{\partial y}} + \overline{\frac{\partial w'}{\partial z}\frac{\partial w'}{\partial z}}\right) \tag{2.24}$$

$$\text{Pressure Diffusion} = -\left(\frac{\partial\overline{(p'u')}}{\partial x} + \frac{\partial\overline{(p'v')}}{\partial y} + \frac{\partial\overline{(p'w')}}{\partial z}\right) \tag{2.25}$$

$$\text{Production} = -\left(\overline{u'^2}\frac{\partial\bar{u}}{\partial x} + \overline{u'v'}\frac{\partial\bar{u}}{\partial y} + \overline{u'w'}\frac{\partial\bar{u}}{\partial z} + \overline{v'u'}\frac{\partial\bar{v}}{\partial x} + \overline{v'^2}\frac{\partial\bar{v}}{\partial y} + \overline{v'w'}\frac{\partial\bar{v}}{\partial z} + \overline{w'u'}\frac{\partial\bar{w}}{\partial x} + \overline{w'v'}\frac{\partial\bar{w}}{\partial y} + \overline{w'^2}\frac{\partial\bar{w}}{\partial z}\right) \tag{2.26}$$

$$\text{Turbulent Diffusion} = -\frac{1}{2}\left(\begin{aligned}&\frac{\partial\overline{u'u'^2}}{\partial x} + \frac{\partial\overline{u'v'^2}}{\partial x} + \frac{\partial\overline{u'w'^2}}{\partial x} + \frac{\partial\overline{v'u'^2}}{\partial y} + \frac{\partial\overline{v'v'^2}}{\partial y}\\&+\frac{\partial\overline{v'w'^2}}{\partial y} + \frac{\partial\overline{w'u'^2}}{\partial z} + \frac{\partial\overline{w'v'^2}}{\partial z} + \frac{\partial\overline{w'w'^2}}{\partial z}\end{aligned}\right) \tag{2.27}$$

$$\text{MHD Source} = \frac{Ha^2}{\text{Re}}\left(\overline{u'\frac{\partial\phi'}{\partial z}} - \overline{w'\frac{\partial\phi'}{\partial x}}\right) \tag{2.28}$$

$$\text{MHD Sink} = -\frac{Ha^2}{\text{Re}}\left(\overline{w'^2} + \overline{u'^2}\right) \tag{2.29}$$

Figure 2.17 shows the turbulent kinetic energy along the horizontal and vertical bisectors for Re=5602 and Ha=21.2. The magnetic field dampens the turbulent kinetic energy more strongly close to the top wall along the vertical bisector than close to the side wall along the horizontal bisector. Figure 2.18(a) presents the budget of the turbulent kinetic energy along the horizontal bisector. Very close to the right and left walls, turbulent kinetic energy is diffused

from its peak region near the wall and is balanced by the viscous dissipation close to the wall. The diffusion of TKE also takes place towards the core but is weak in magnitude compared to the value towards the wall. Since production is governed by the mean velocity gradients and Reynolds stresses it has a maximum value in the region of peak axial normal stress. As expected, dissipation of TKE is the maximum close to the walls and falls off in the core. Most of the production of TKE is balanced by the dissipation term along the whole bisector. The source of turbulence due to MHD is caused by the correlation of velocity fluctuations with the derivative of electric potential, primarily the correlation of axial velocity fluctuations with the horizontal derivative of electric potential (i.e. both are perpendicular to applied magnetic field). The sink to turbulence by MHD is due to the Reynolds normal stresses in directions perpendicular to the field. The MHD sink term is qualitatively similar to the source but larger in magnitude thereby giving a net contribution in the reduction of TKE. This behavior of the MHD source and sink terms is consistent with the findings of Satake et al. [21] in the DNS of a MHD pipe flow. Convection and pressure diffusion terms have small contributions to the TKE budget. The qualitative behaviors of the non-magnetic terms in the budget are similar to those of a non-MHD duct but their magnitudes are different. Figure 2.18(b) gives the same budget along the vertical bisector. These terms have smaller magnitudes along the vertical bisector because of the suppression of turbulence. Along this bisector, the diffusion term exhibits the same variation but is weaker in magnitude. The convection term is relatively stronger along this bisector. The source and sink terms due to MHD act in the same way along both the bisectors but are weaker along the vertical bisector. The net effect of the magnetic field is the suppression of turbulence along both the bisectors.

2.8. Summary and Conclusions

The present study has described in detail, using a DNS, the effects of a magnetic field on the turbulent flow in a square duct at a nominal Reynolds number of 5500. First, the code is validated for a turbulent flow in a non-MHD channel (Re_τ=178.12) and a square duct (Re=4547 and Re=5368 (Re_τ=372)), followed by validation in a laminar MHD square duct (Re=3900(Re_τ=372), Ha=60) and a turbulent MHD channel (Re_τ=150 and Ha=6) flow. Subsequently, simulations were performed for turbulent MHD flow in a square duct. Two domain sizes (1x1x2π and 1x1x16) and three grids (64x64x128, 80x80x256, and 128x128x512) have been used and mean as well as Reynolds normal stresses have been shown to achieve grid independence. For all MHD square duct runs, the simulations were performed by fixing a constant streamwise mean pressure gradient corresponding to Re_τ=361 and varying the magnetic field for different Hartmann numbers. Thus the bulk Reynolds numbers varied slightly with Hartmann number depending upon the frictional losses and the effect of magnetic field on turbulence suppression and velocity flattening. Also, for different grid sizes, the resolved turbulence and magnetic field-turbulence interaction also contributed to the small changes in frictional losses and thus to the bulk Reynolds number.

The magnetic field affects the secondary flow significantly and shows strong bulging in the vertical direction close to top and bottom walls. Auto-correlation of axial velocity fluctuations suggested that a domain length of ~5D is enough for capturing the longest scales of turbulence. The velocity along the vertical bisector is found to be more round than along horizontal bisector at Ha=21.2 because of stronger turbulence suppression along this bisector. Further increase in Hartmann number (at Ha=24.38), makes velocity flattening dominant along the vertical bisector but the profile along the horizontal bisector becomes more round due to

complete turbulence suppression. Streaky structures get concentrated and elongated along streamwise direction under the influence of a transverse magnetic field. Because the electric current is strong and perpendicular to the magnetic field in the region close to top and bottom walls, the magnetic field suppresses the local turbulence. Close to the side walls the effect of magnetic field is weak due to the current being parallel to field. The Reynolds shear stress ($\overline{w'v'}$) shows strong suppression along vertical bisector than $\overline{w'u'}$ along the horizontal bisector.

Streamwise vorticity is suppressed directly by the magnetic field via the first derivative of horizontal velocity and indirectly via second derivatives of Reynolds normal and shear stresses, but more strongly via Reynolds normal stresses ($\overline{u'u'}, \overline{v'v'}$). The magnetic field produces a sink as well as a source to turbulent kinetic energy. Their variations along the bisectors are similar but the sink is stronger and causes a net reduction of turbulence due to a magnetic field.

2.9. Tables and Figures

Table 2.1. Computational details for non-MHD and MHD channel cases for validation

$Re_\tau(=\delta u_\tau/\nu)$ δ: half channel width, ($D=2\delta$)	Grid ($N_x x N_y x N_z$)	Comp. domain	Spatial resolution (Δx^+, Δy^+, Δz^+)*	Mag. field orientation	Ha $(=B_y\delta\sqrt{\frac{\sigma}{\rho\nu}})$	Averaging time**
178.12	128x128x512	$2/3\pi$x1x2π	5.82,1.40-4.86,4.37	-	0	631
150	128x128x512	2x1x6	4.68, 1.17-4.09, 3.51	B_y	6	537

* grids have 2% stretching in y-direction for 128x128x512 mesh and uniform in x- and z-direction.
** Averaging time given in convective units (δ/W_b or $0.5D/W_b$)

Table 2.2. Computational details for various cases

Re	Grid ($N_x x N_y x N_z$)	Comp. domain	Spatial resolution (Δx^+, Δy^+, Δz^+)***	Mag. field orientation	Ha	W_b	Averaging time****
4547	80x80x256	1x1x2π	2.53-5.49,2.53-5.49,3.76	-	0	1.031	1600
5368	64x64x128	1x1x2π	3.54-8.86, 3.54-8.86, 18.25	-	0	0.980	900
5457	64x64x128	1x1x2π	3.44-8.60, 3.44-8.60, 17.71	B_y	21.2	1.030	800
5681	80x80x256	1x1x2π	2.40-7.58, 2.40-7.58, 8.85	B_y	21.2	1.070	1600
3350	80x80x256	1x1x2π	2.40-7.58, 2.40-7.58, 8.85	B_y	24.38	0.630	720
5602	128x128x512	1x1x16	1.41-4.92, 1.41-4.92, 11.28	B_y	21.2	1.057	1600
5647	128x128x512	1x1x16	1.41-4.92, 1.41-4.92, 11.28	B_y	22.26	1.065	1600

*** grids have 2% stretching in x- and y-direction for all 80x80x256 and 128x128x512 meshes and 3% for 64x64x128 mesh with uniform in z-direction for all.
**** Averaging time given in convective units ($0.5D/W_b$)
Note: All MHD square duct runs are at Re_τ=361.
Note: Re and Ha in square duct are based upon hydraulic diameter.

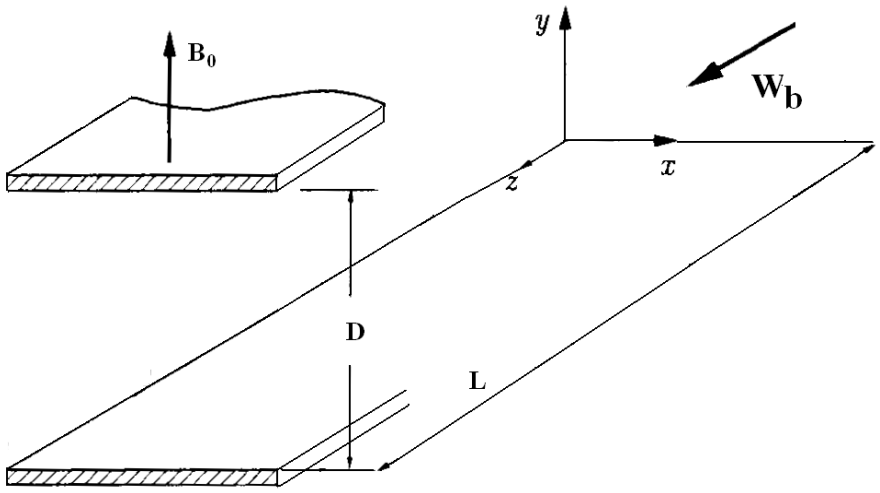

Figure 2.1 Physical and computational domain of MHD and non-MHD channel

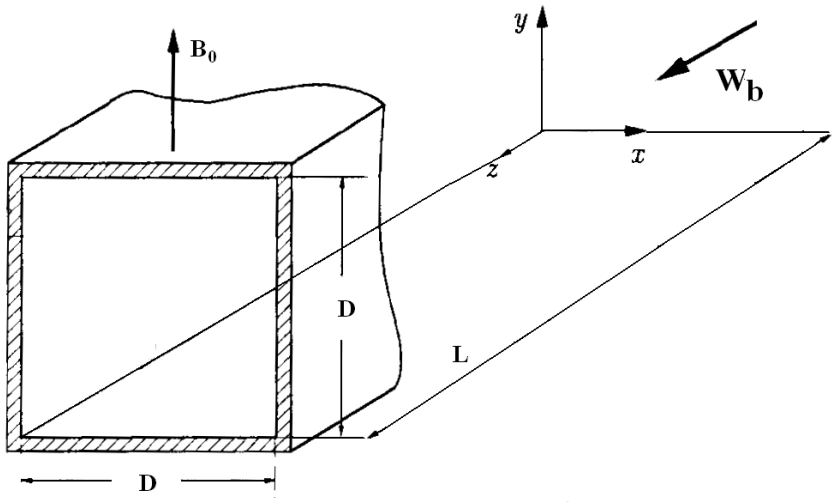

Figure 2.2 Physical and computational domain of MHD and non-MHD square duct

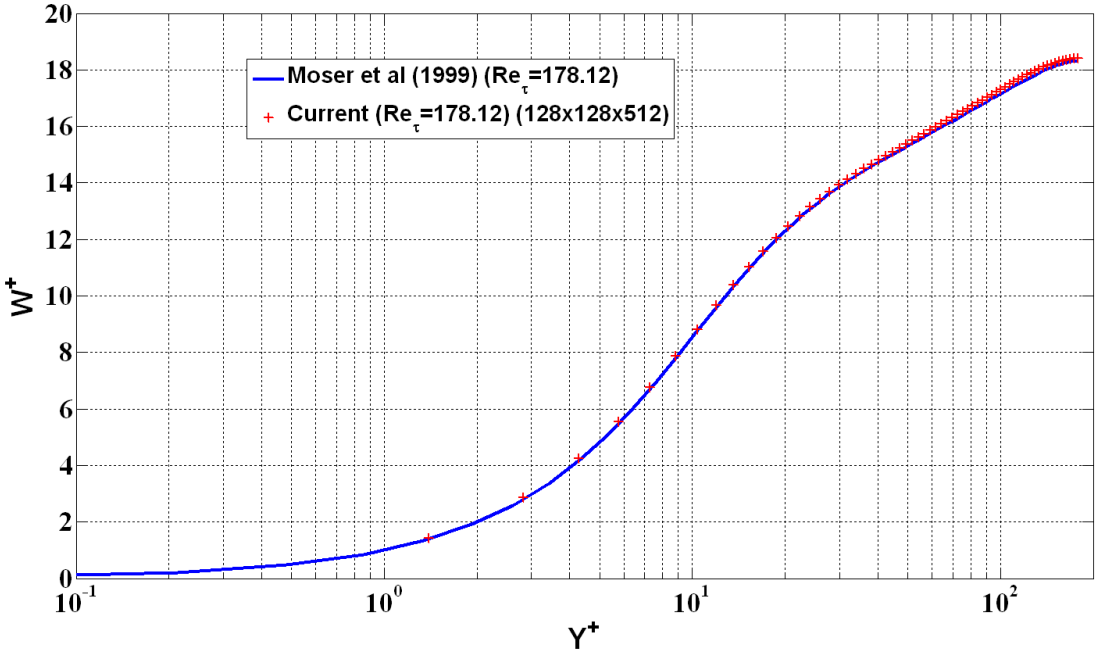

Figure 2.3(a) Comparison of normalized mean axial velocity in a turbulent channel flow with the previous DNS (Re_τ=178.12, Moser et al, 1999) [12]

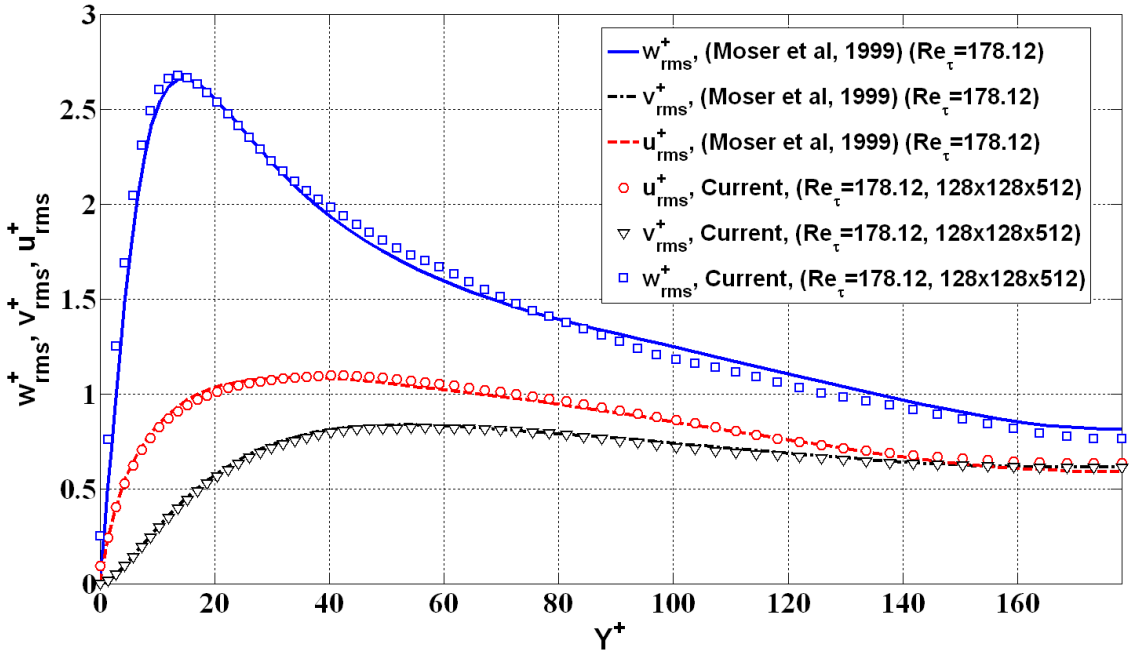

Figure 2.3(b) Comparison of normalized RMS of velocity fluctuations in a turbulent channel flow with the previous DNS (Re_τ=178.12, Moser et al, 1999) [12]

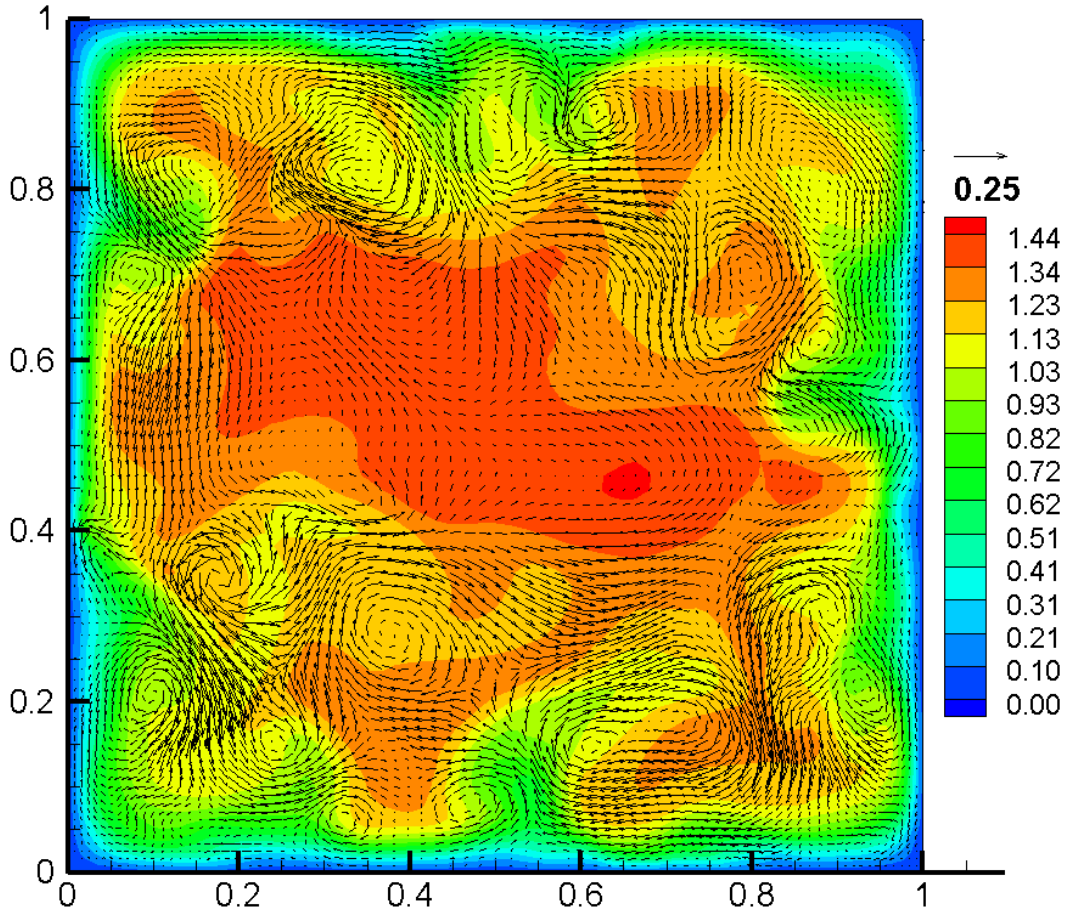

Figure 2.4(a) Instantaneous axial velocity contours with secondary velocity vectors (Re=4547, 80x80x256) for the case without a magnetic field

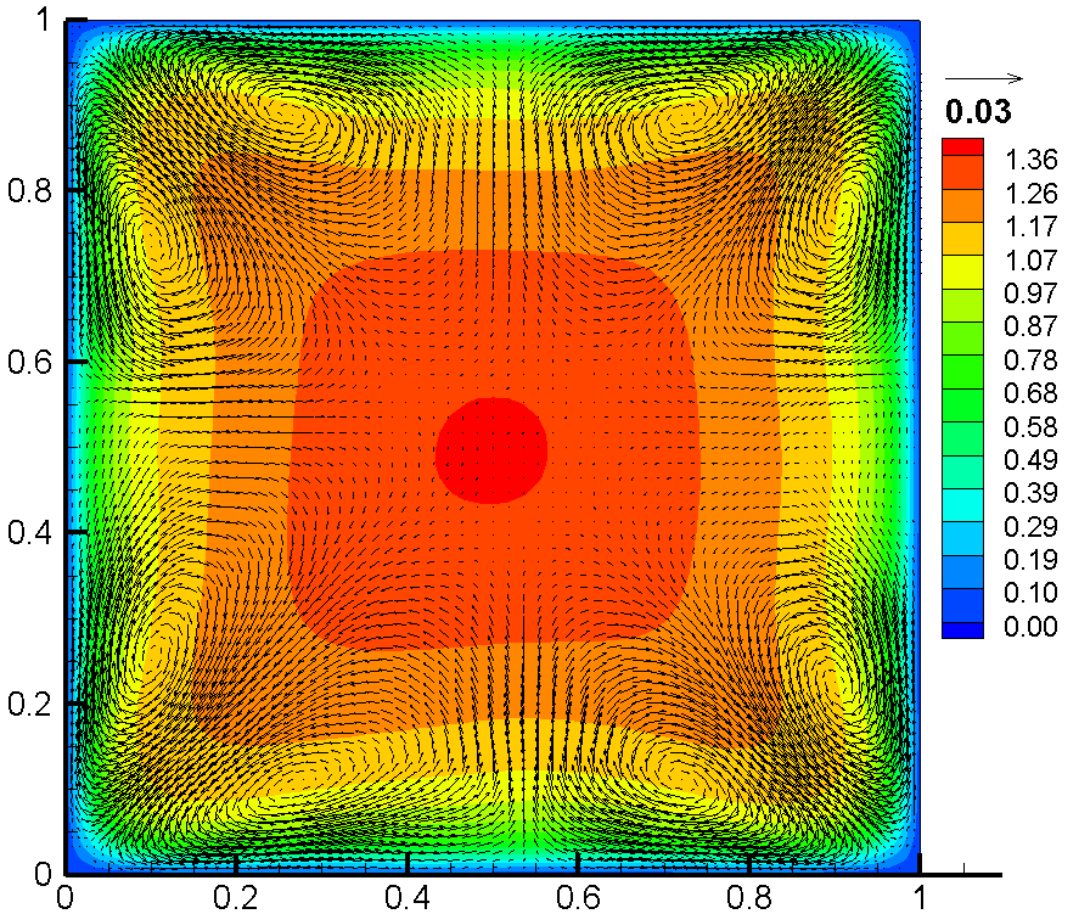

Figure 2.4(b) Mean axial velocity contours with secondary velocity vectors (Re=4547, 80x80x256) for the case without a magnetic field

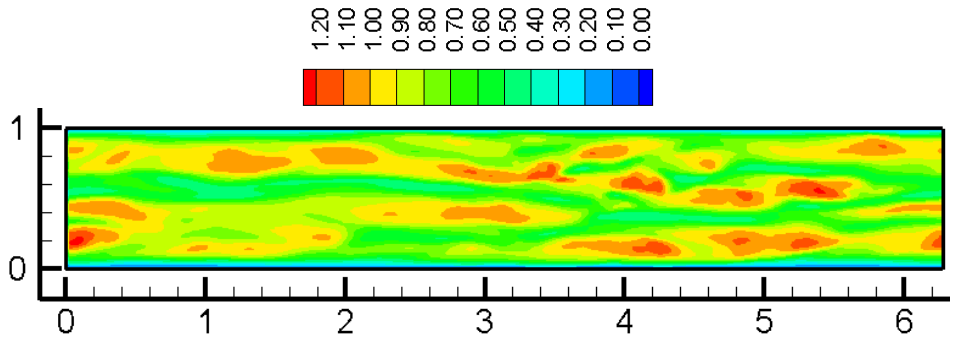

Figure 2.4(c) Instantaneous velocity contours at y^+=15 (Re=4547, 80x80x256)

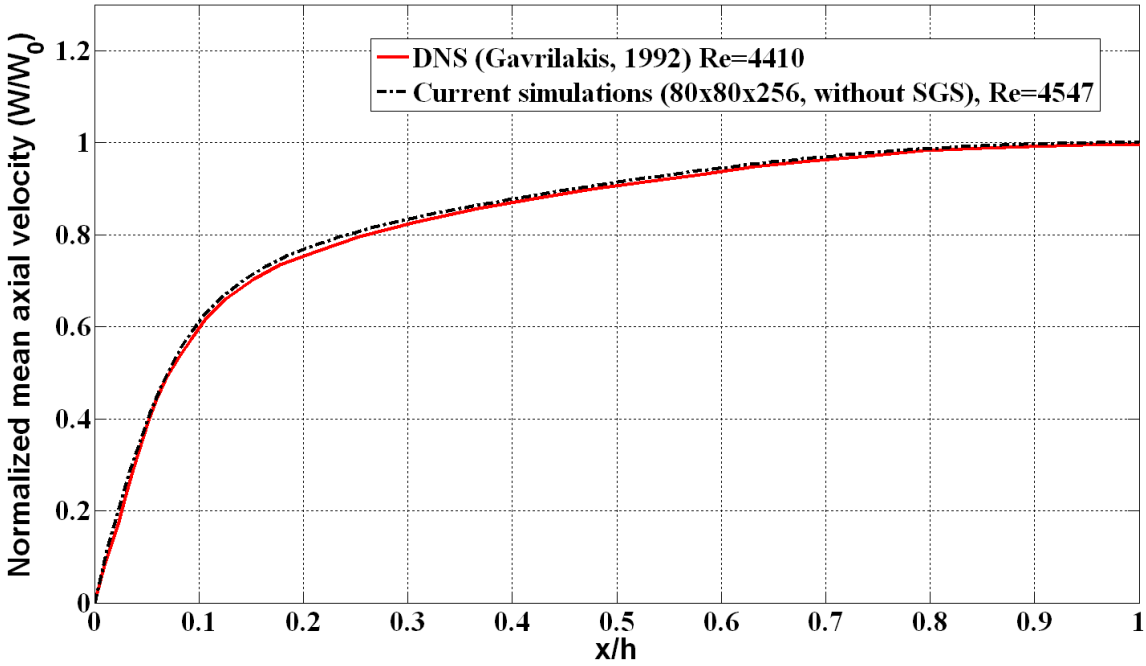

Figure 2.5(a) Mean velocity comparison along horizontal bisector with Gavrilakis [15]

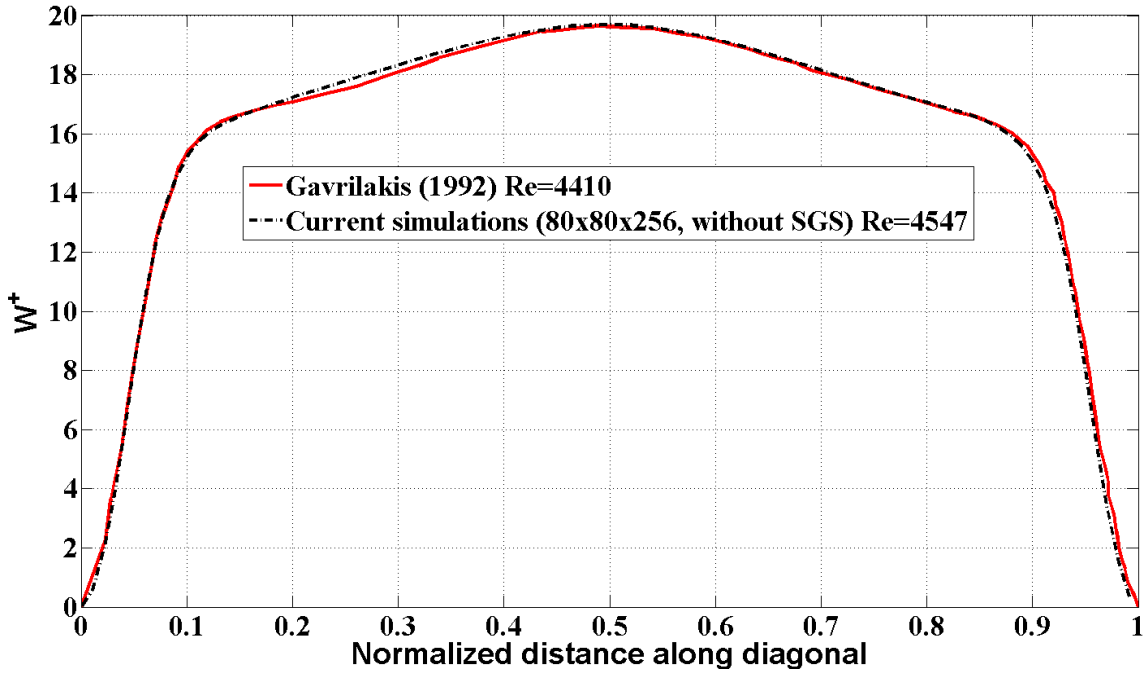

Figure 2.5(b) Mean velocity comparison along diagonal with Gavrilakis [15]

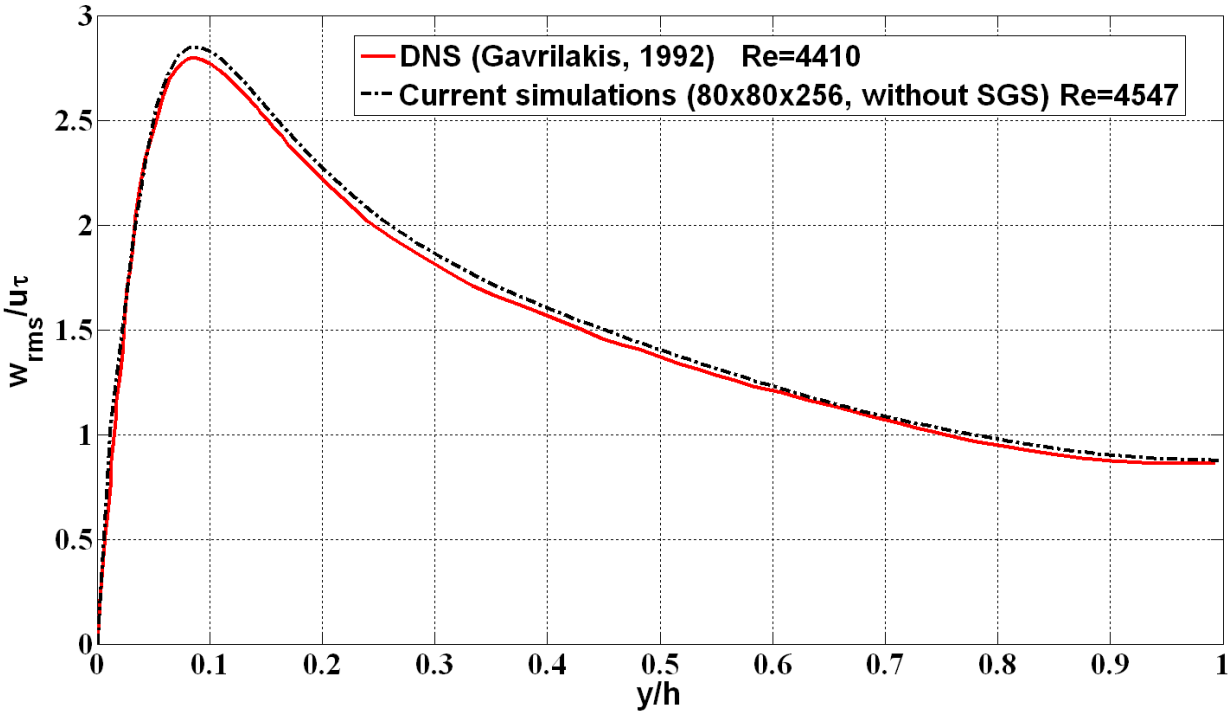

Figure 2.5(c) Comparison of RMS of axial velocity fluctuations along vertical bisector with Gavrilakis [15]

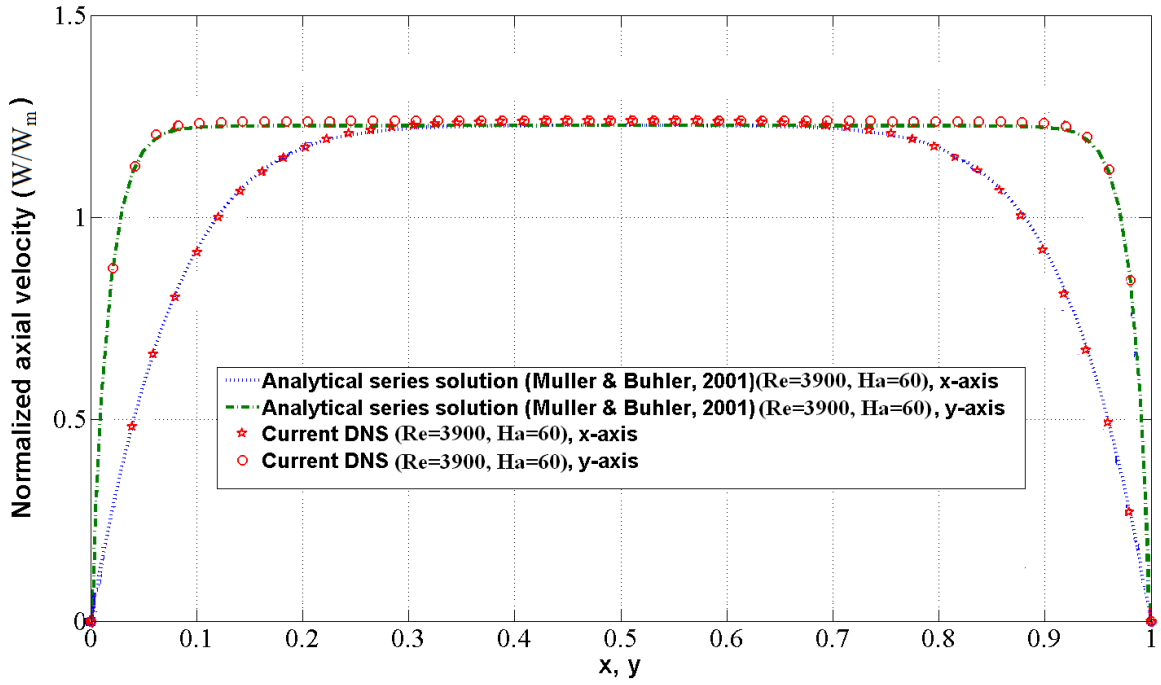

Figure 2.6. Comparison of laminarized results (64x64x128) with Muller & Buhler [31]

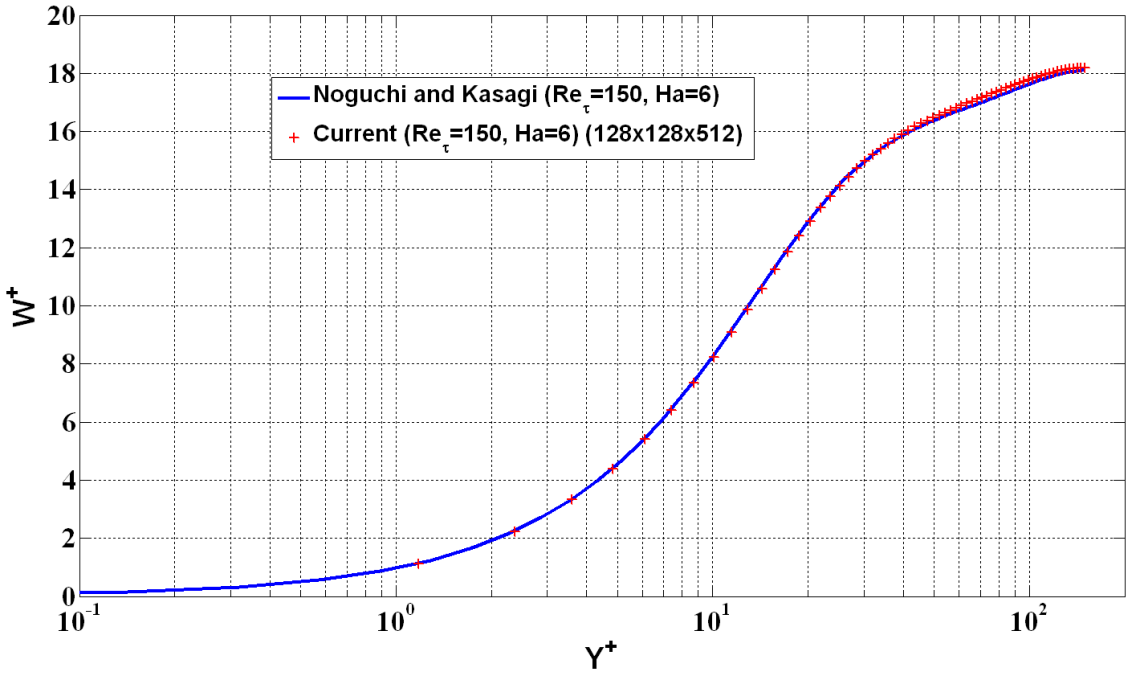

Figure 2.7(a) Comparison of mean axial velocity in MHD channel at Re_τ=150 and Ha=6 with Noguchi and Kasagi (1994) [26]

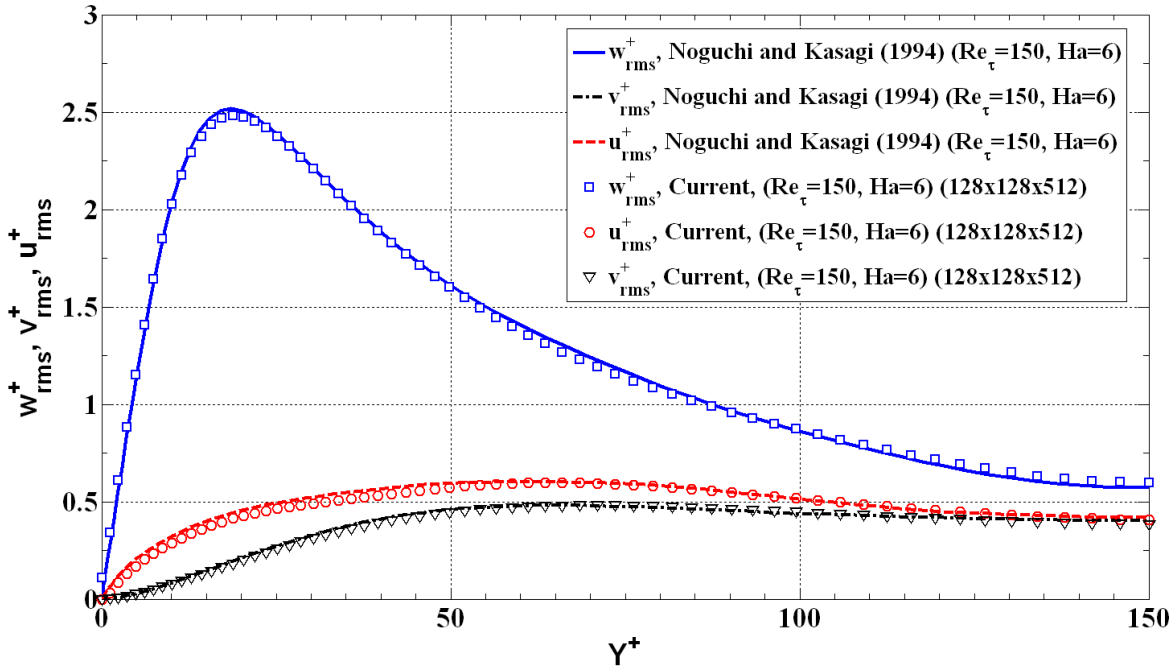

Figure 2.7(b) Comparison of RMS of velocity fluctuations in MHD channel at Re_τ=150 and Ha=6 with Noguchi and Kasagi (1994) [26]

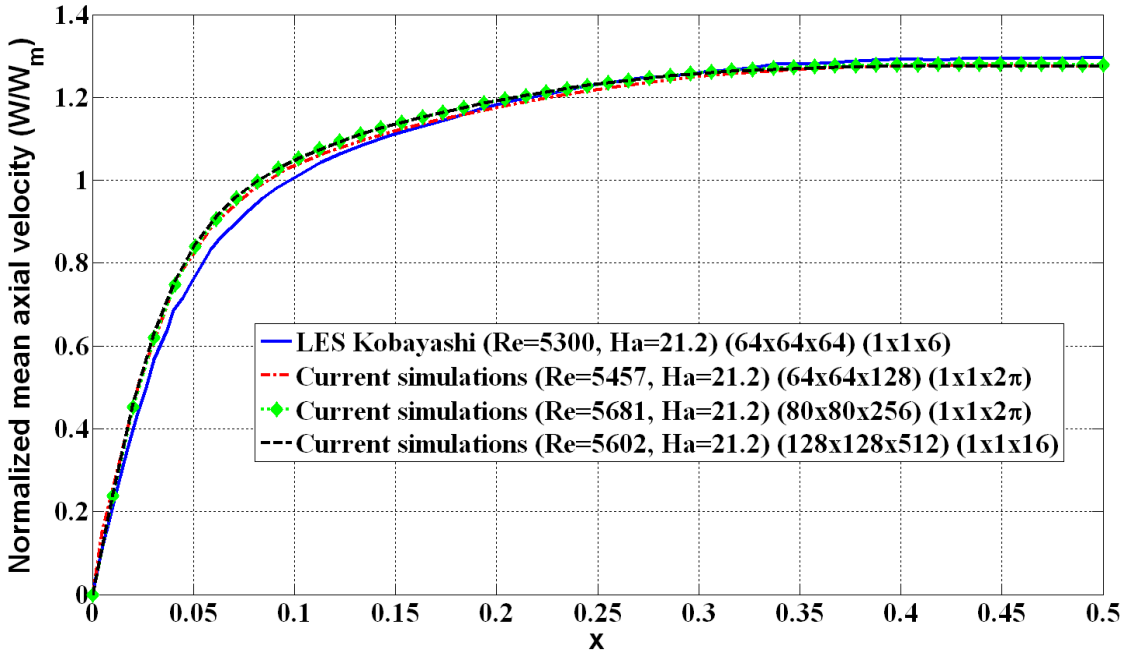

Figure 2.8(a) Mean axial velocity along horizontal bisectors with Kobayashi (2008) [30] at Ha=21.2

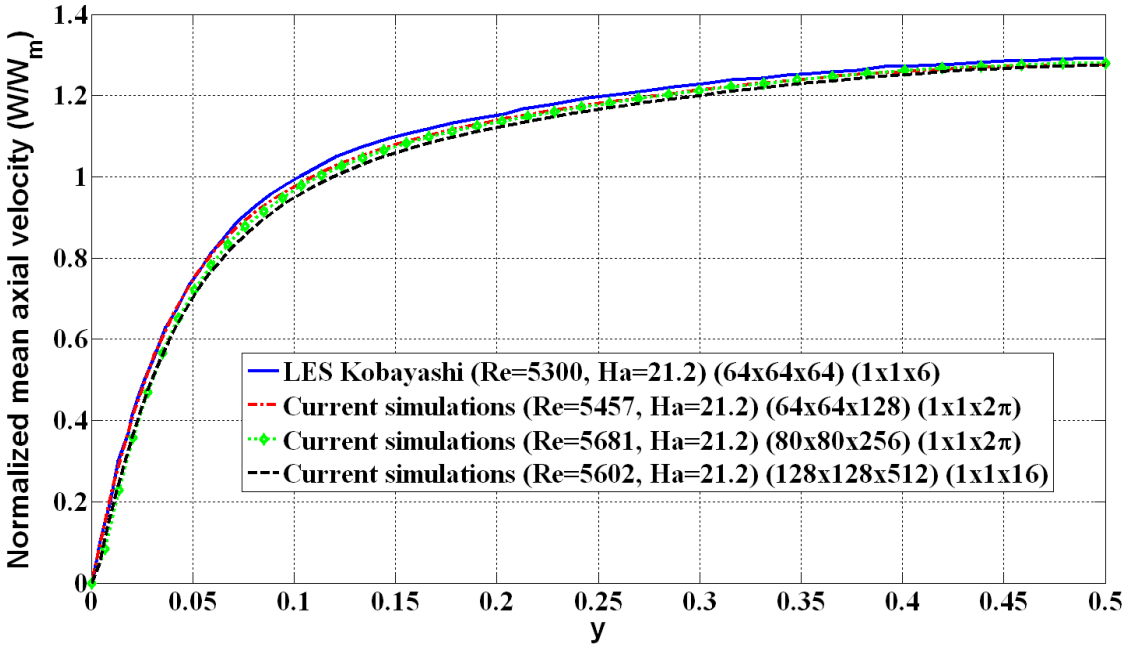

Figure 2.8(b) Mean axial velocity along vertical bisectors with Kobayashi (2008) [30] at Ha=21.2

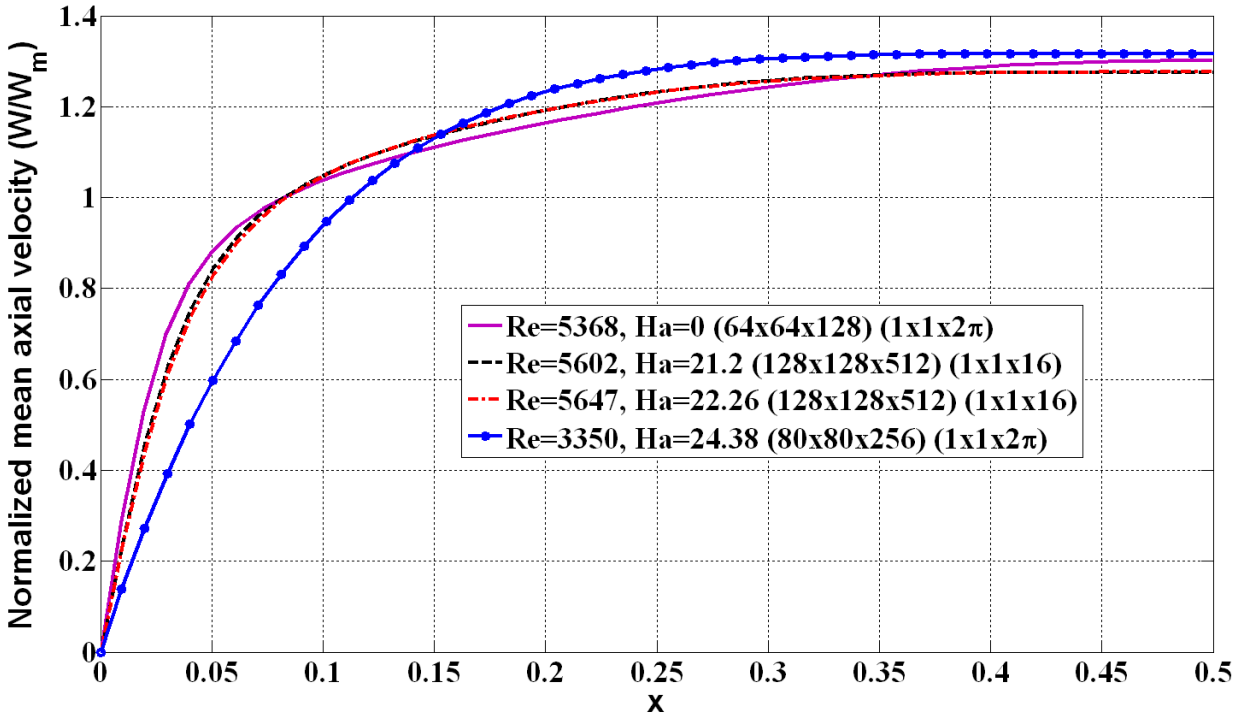

Figure 2.8(c) Mean axial velocity along horizontal bisectors in various cases

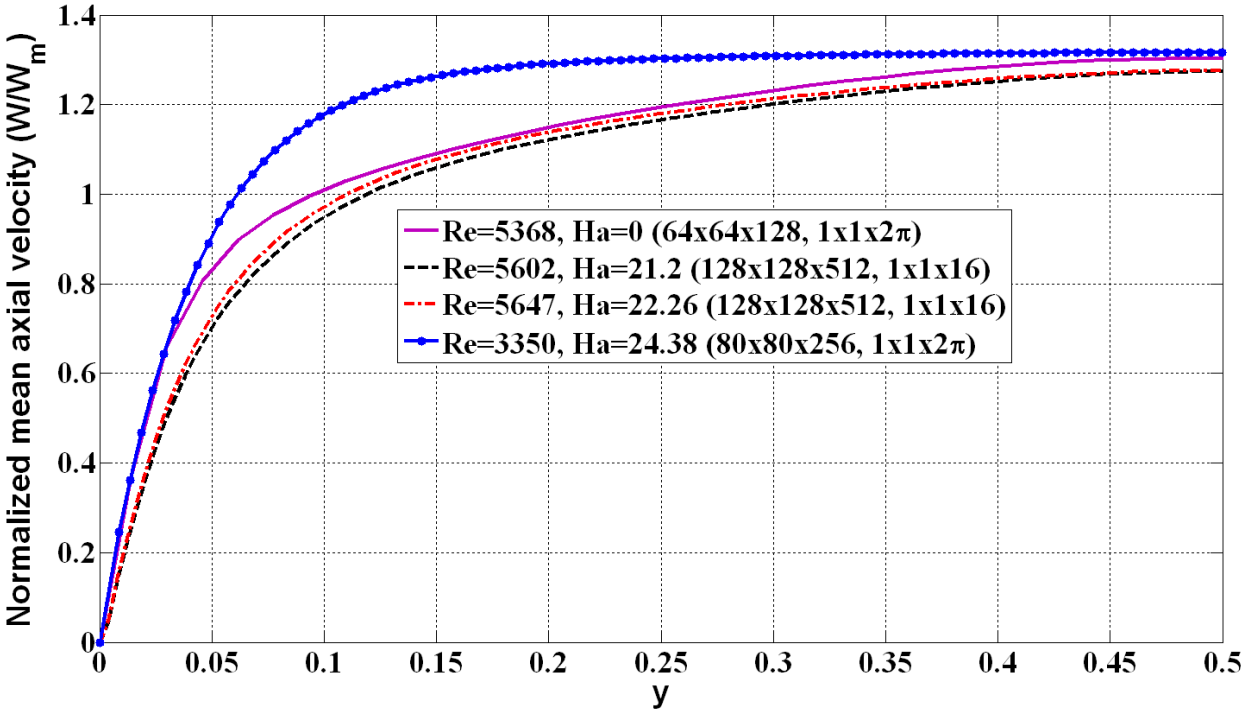

Figure 2.8(d) Mean axial velocity along vertical bisectors in various cases

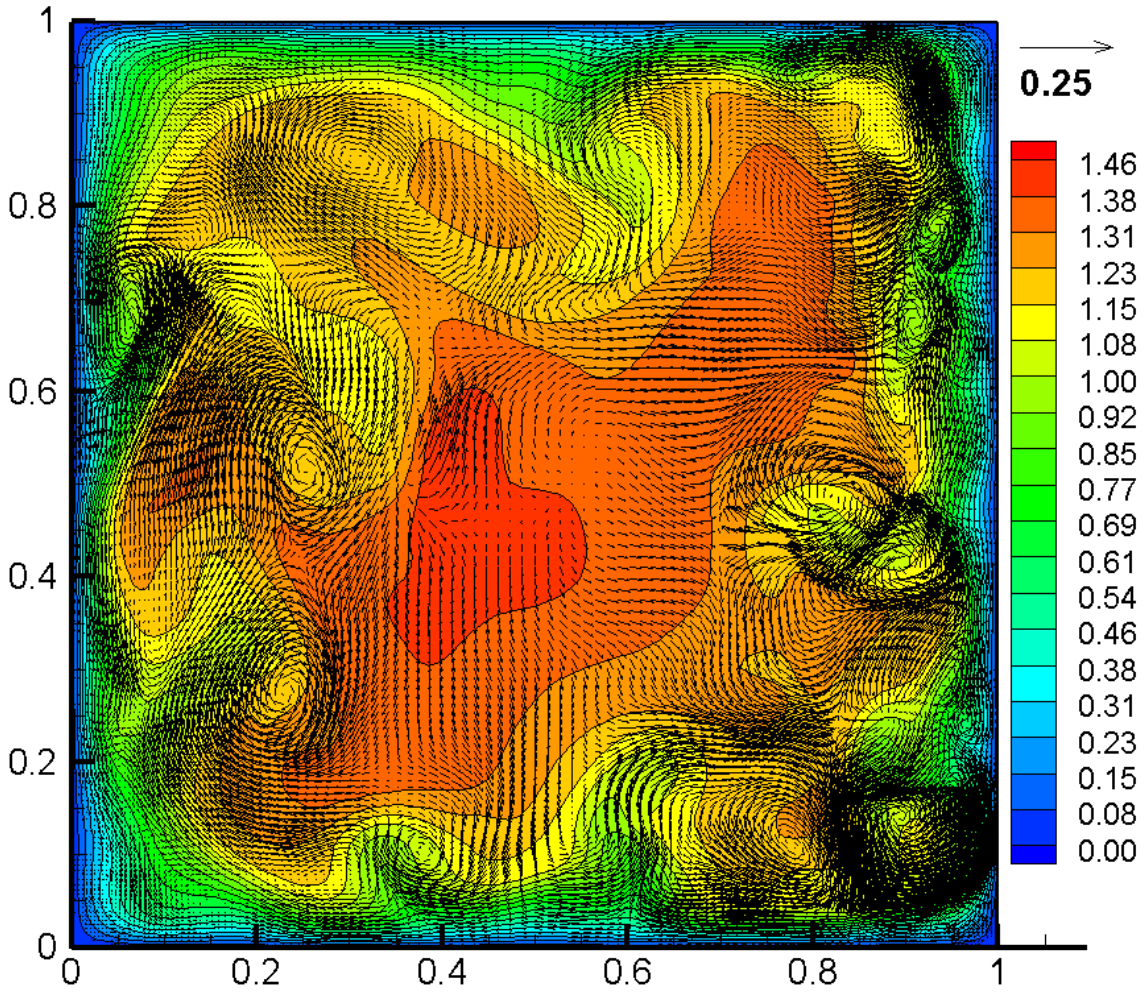

(Re=5602, Ha=21.2, 128x128x512)

Figure 2.9(a) Instantaneous axial velocity contours with secondary velocity vectors

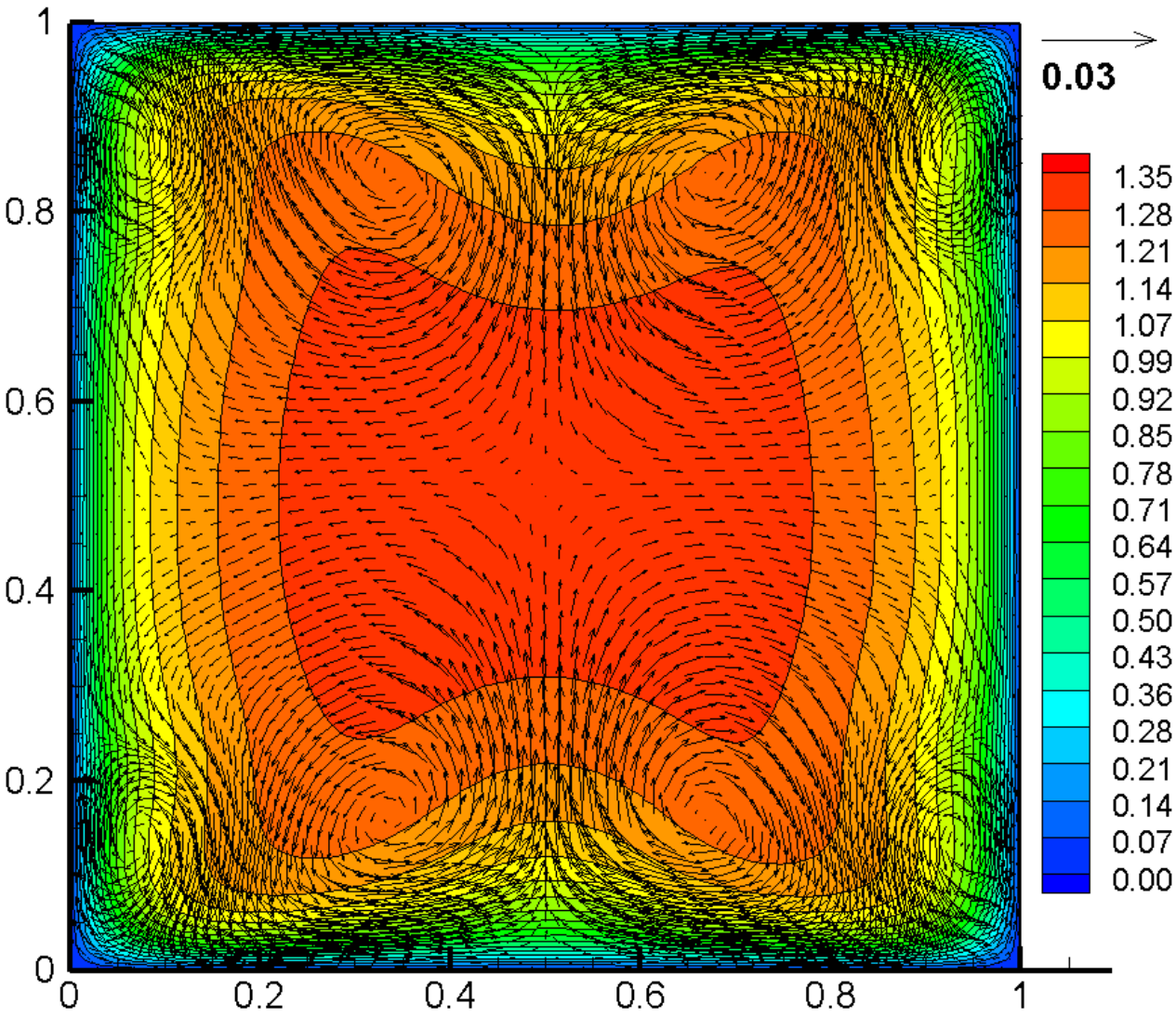

(Re=5602, Ha=21.2, 128x128x512)

Figure 2.9(b) Mean axial velocity contours with secondary velocity vectors.
(some vectors are skipped in mean secondary velocity for better visualization)

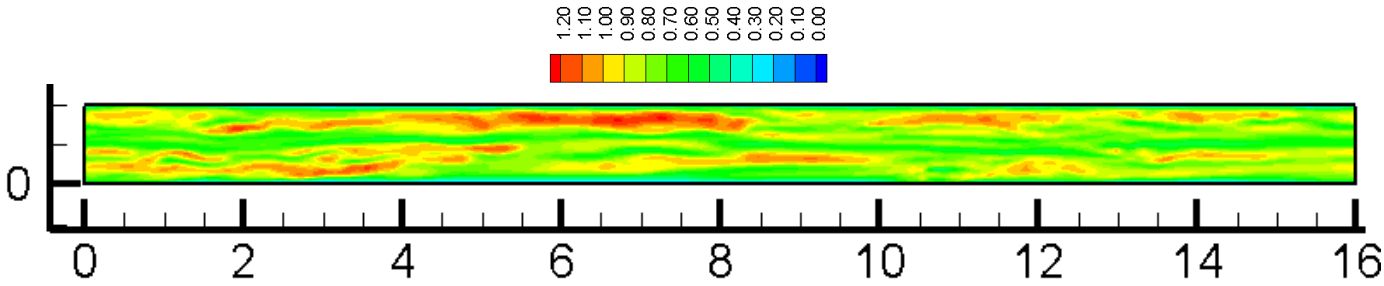

(Re=5602, Ha=21.2, 128x128x512)

Figure 2.9(c) Instantaneous velocity contours at y^+=15

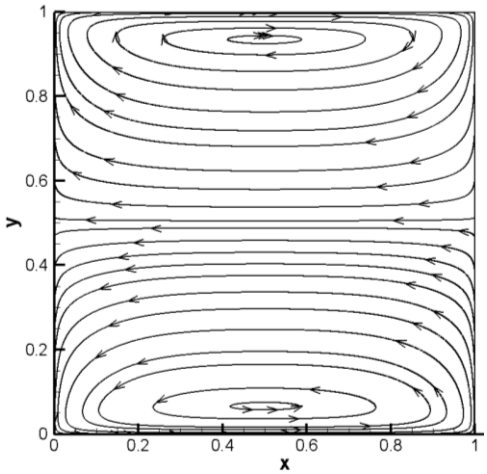

(Re=3350, Ha=24.38, 80x80x256)
(Laminar case)

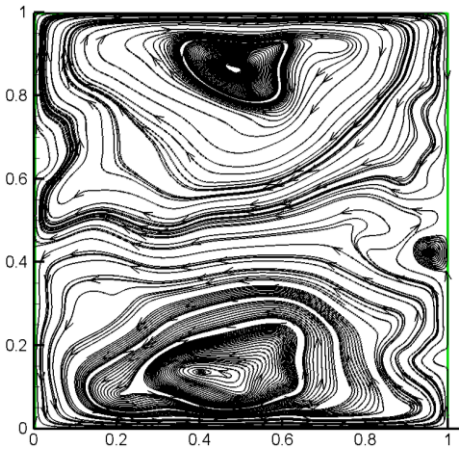

(Re=5602 Ha=21.2, 128x128x512)
(Turbulent case)

Figure 2.9(d) Instantaneous induced current lines across a cross-section

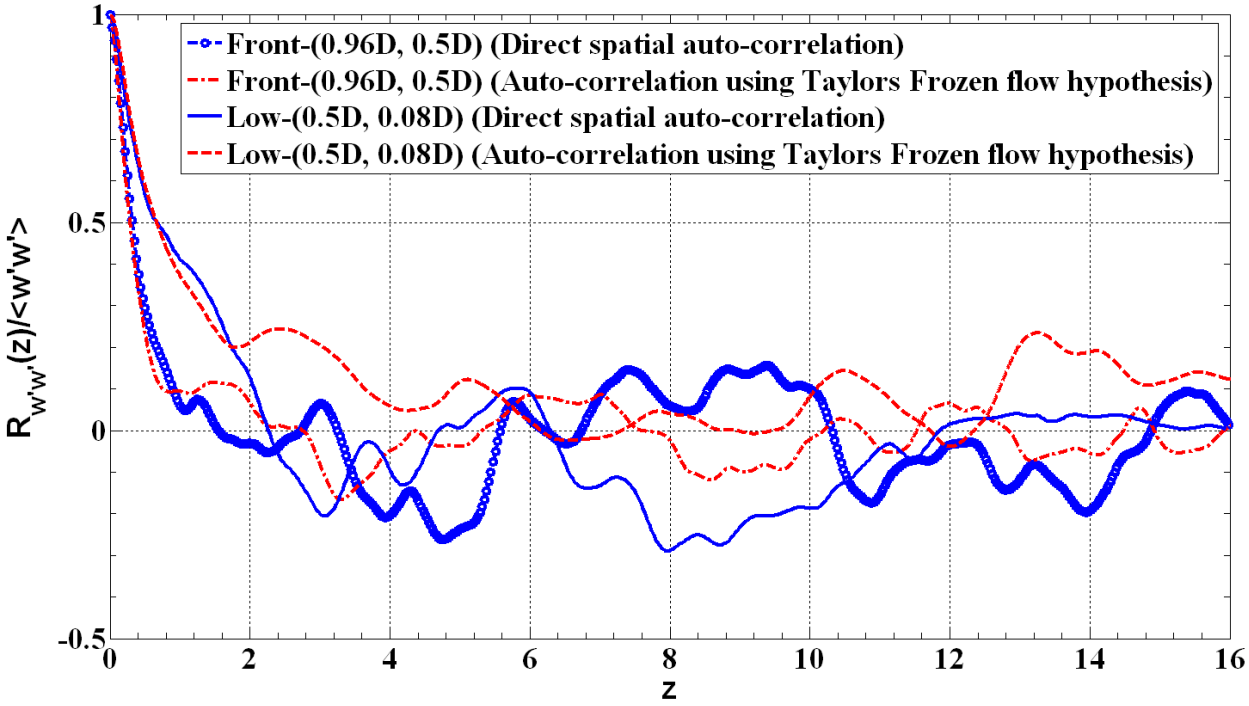

Figure 2.10 Auto-correlation of axial velocity fluctuations (Re=5602, Ha=21.2)

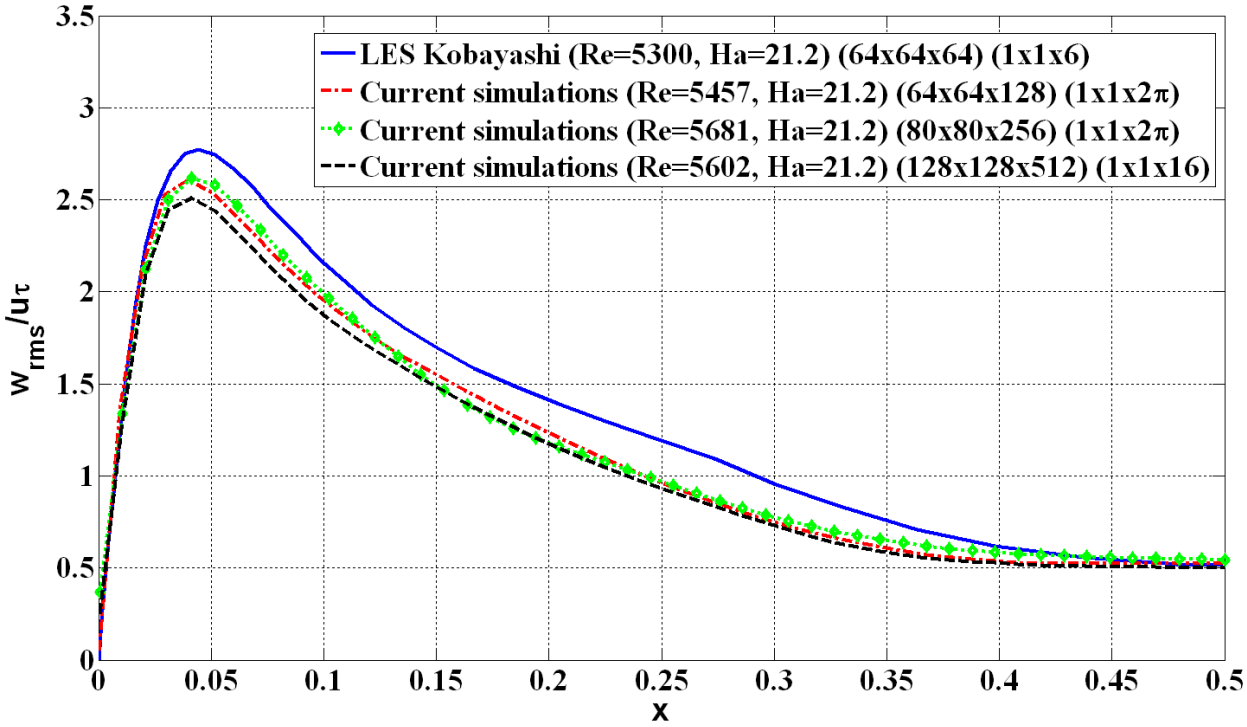

Figure 2.11(a) RMS of axial velocity fluctuations along horizontal bisector

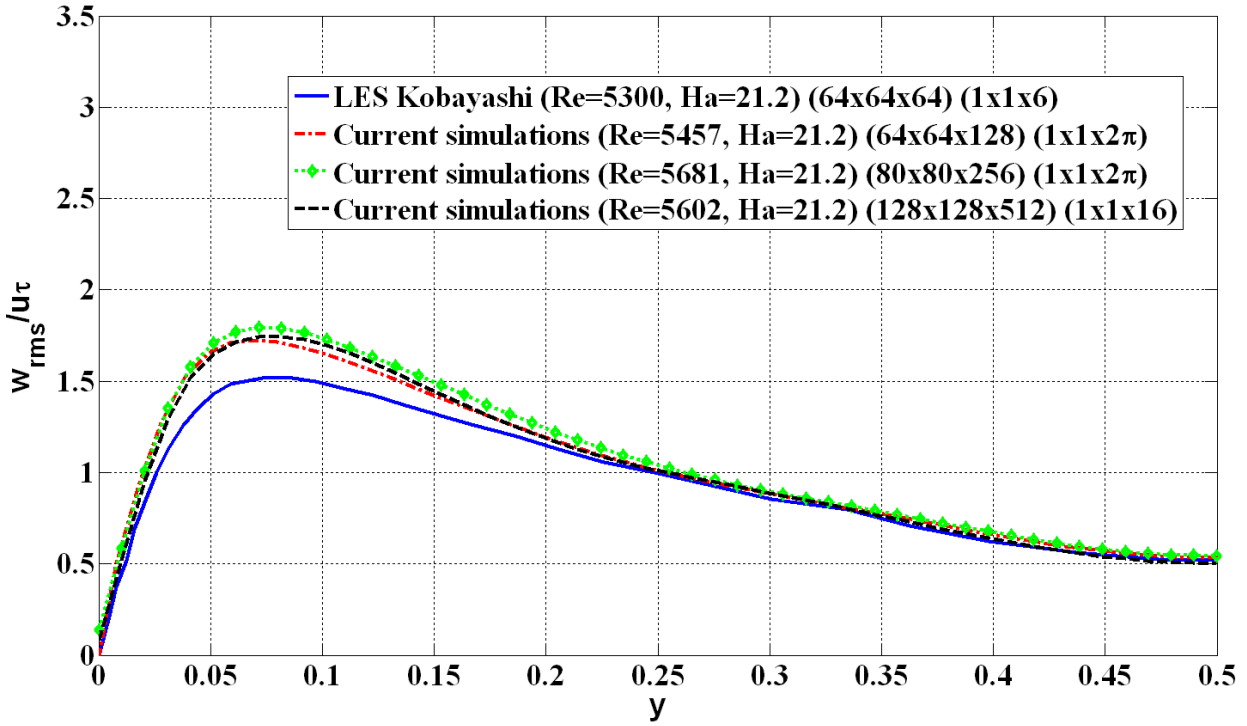

Figure 2.11(b) RMS of axial velocity fluctuations along vertical bisector

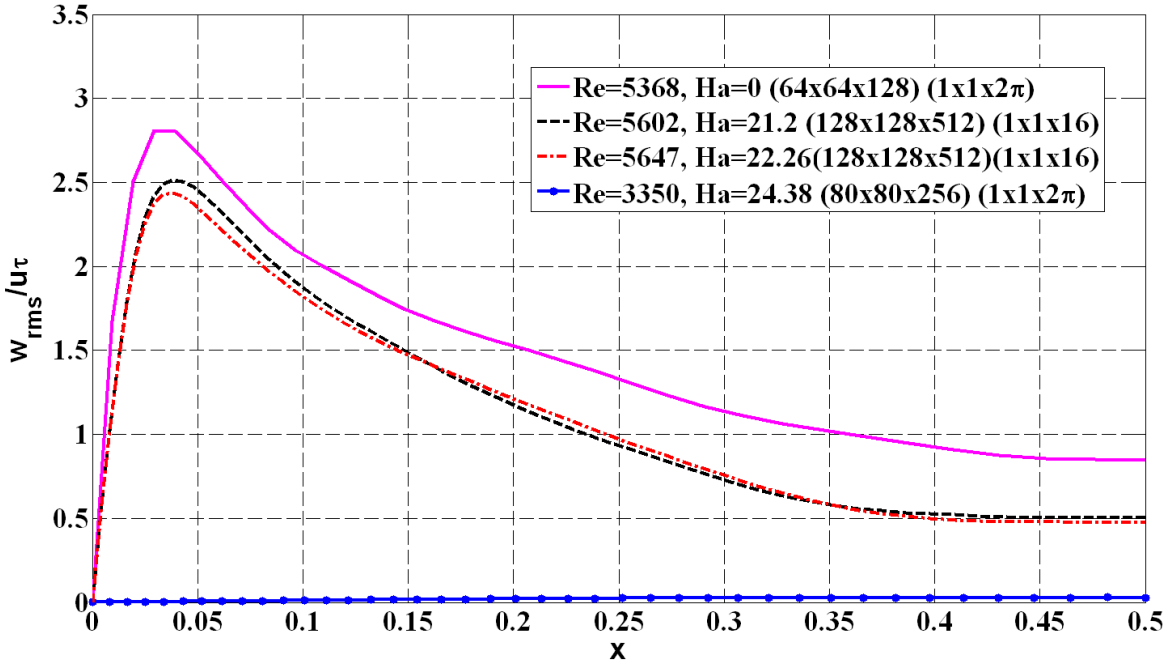

Figure 2.12(a) RMS of axial velocity fluctuations along horizontal bisector for various Ha

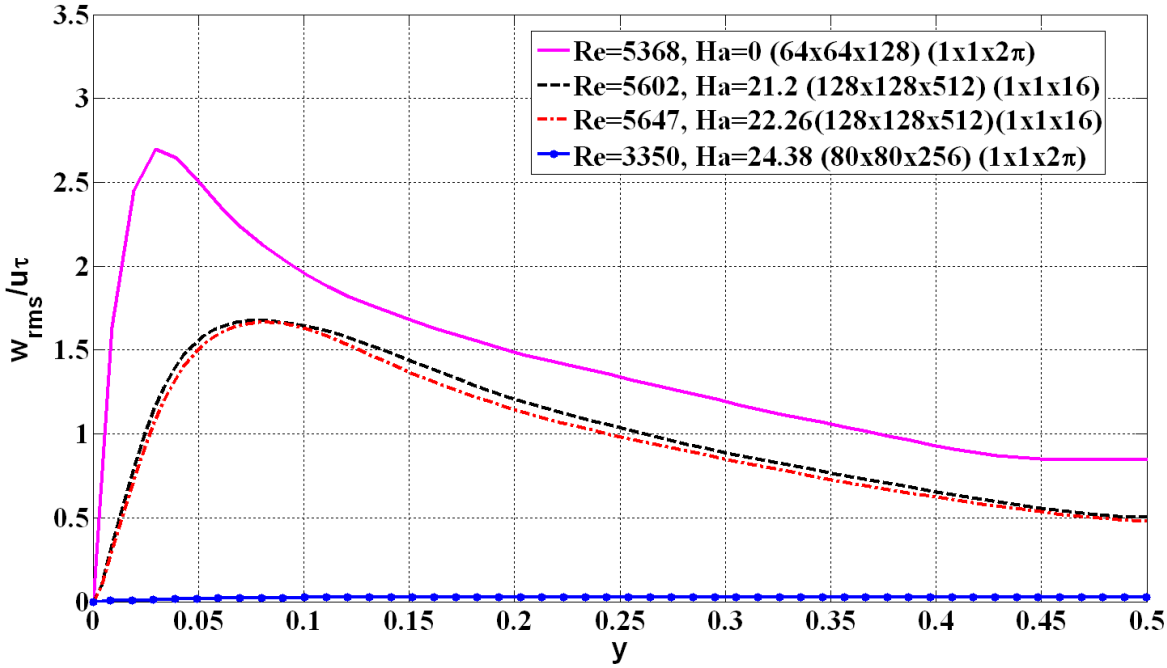

Figure 2.12(b) RMS of axial velocity fluctuations along vertical bisector for various Ha

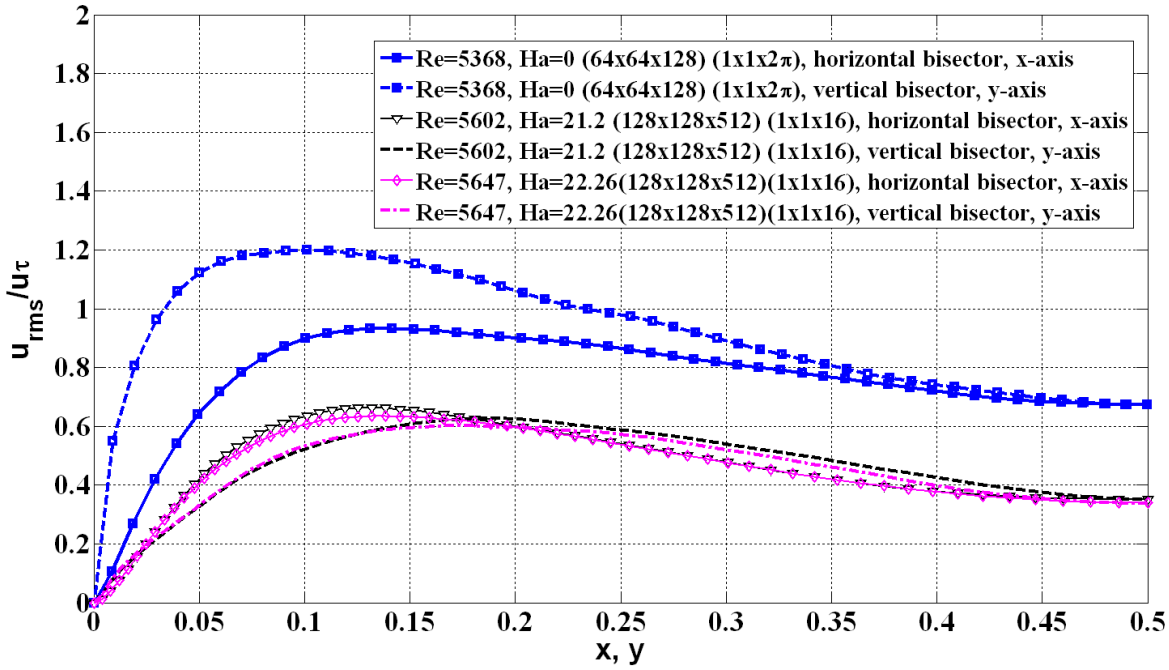

Figure 2.13(a) RMS of horizontal velocity fluctuations along horizontal (x-) and vertical (y-) bisectors

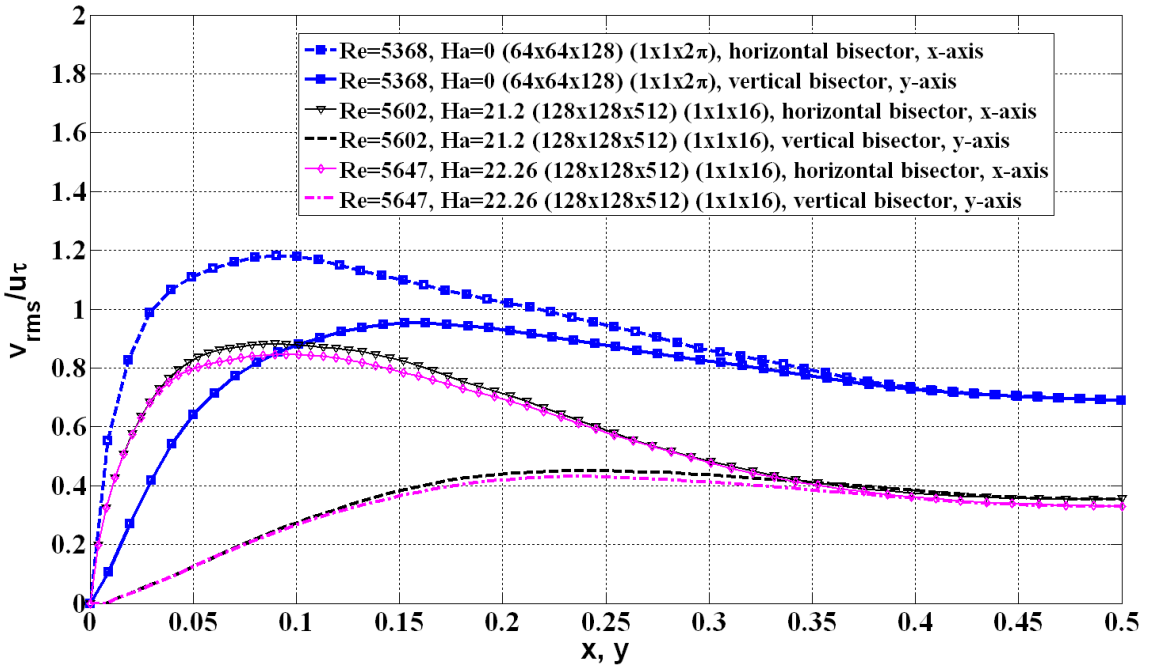

Figure 2.13(b) RMS of vertical velocity fluctuations along horizontal (x-) and vertical (y-) bisectors

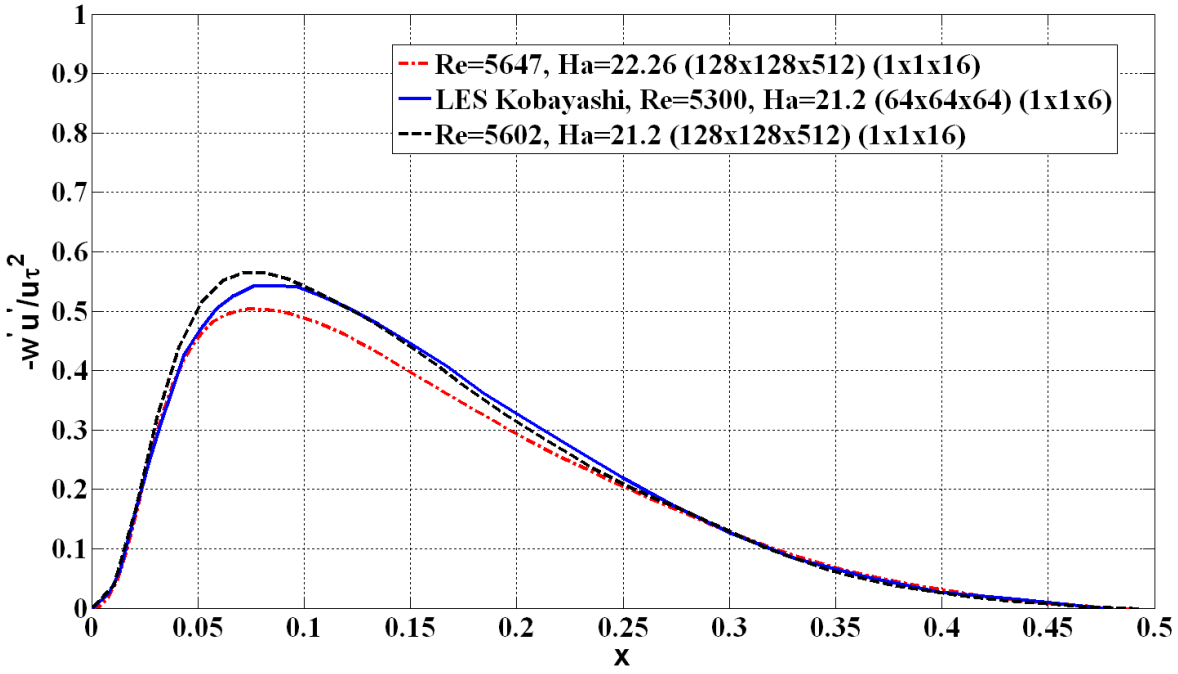

Figure 2.14(a) Reynolds shear stress along horizontal (x-) bisector

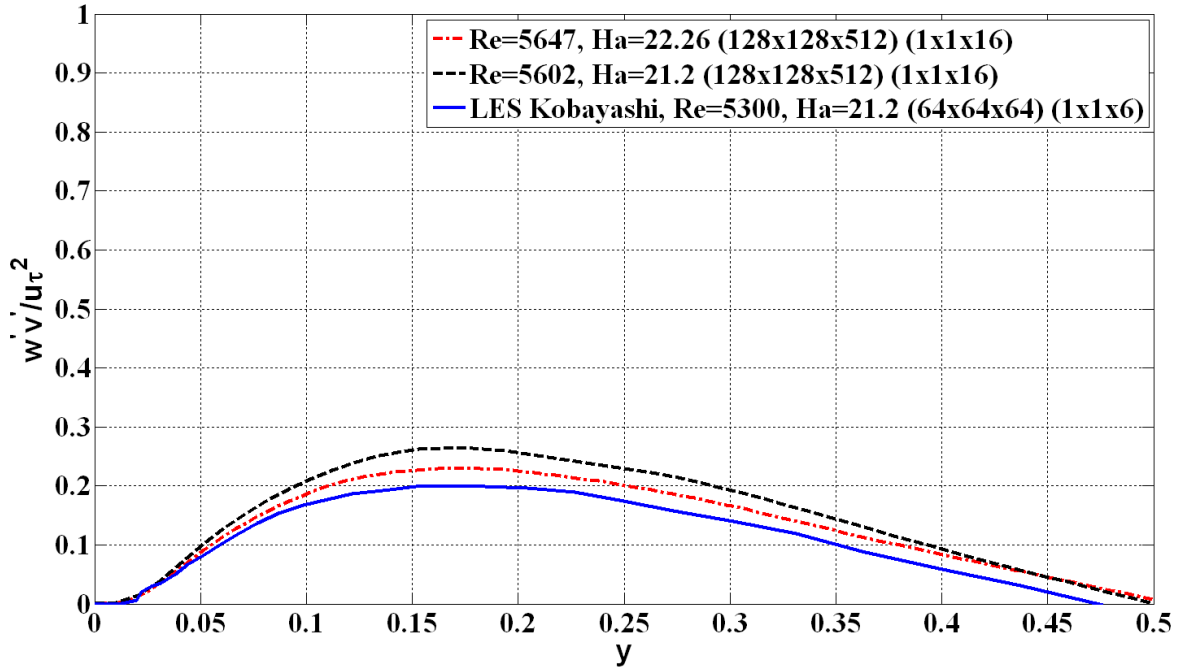

Figure 2.14(b) Reynolds shear stress along vertical (y-) bisector

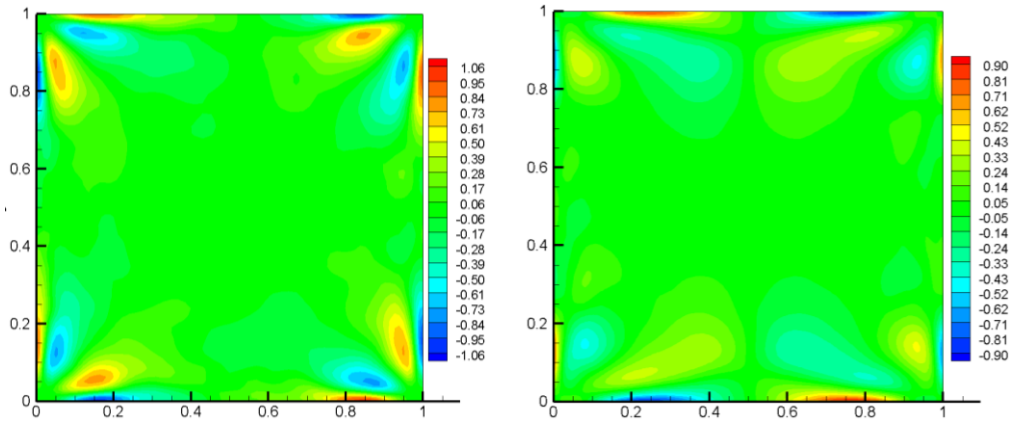

(a) (Re=5368, Ha=0, 64x64x128) (non-MHD)

(b) (Re=5602 Ha=21.2, 128x128x512) (MHD)

Figure 2.15 Mean streamwise vorticity, $\overline{\Omega}_z = \left(\frac{\partial \bar{v}}{\partial x} - \frac{\partial \bar{u}}{\partial y} \right)$

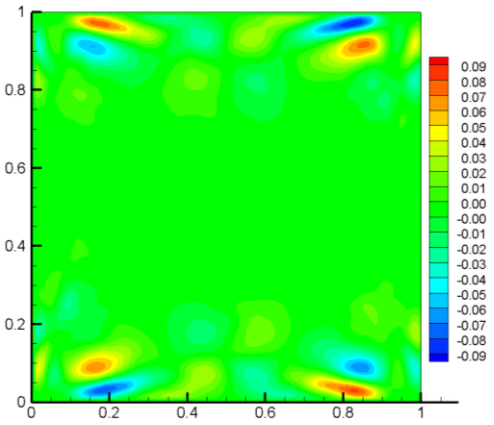

(a) $\bar{u}\frac{\partial\bar{\Omega}_z}{\partial x}+\bar{v}\frac{\partial\bar{\Omega}_z}{\partial y}$ (I)

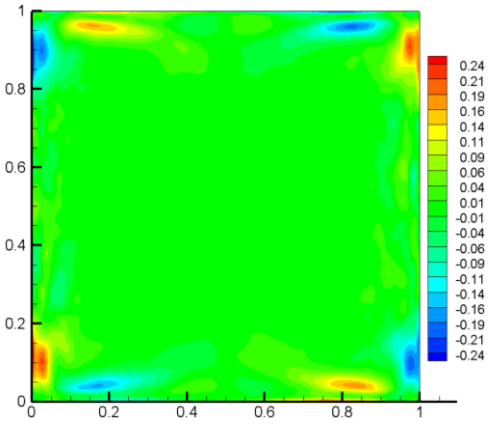

(b) $\frac{1}{\mathrm{Re}}\left(\frac{\partial^2\bar{\Omega}_z}{\partial x^2}+\frac{\partial^2\bar{\Omega}_z}{\partial y^2}\right)$ (II)

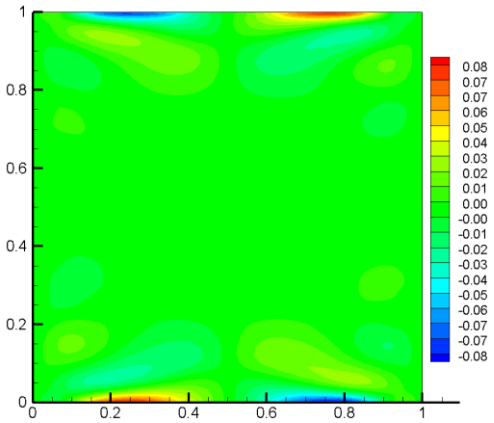

(c) $\frac{\mathrm{Ha}^2}{\mathrm{Re}}\left(\frac{\partial\bar{u}}{\partial y}B_{0y}^2\right)$ (III)， Magnetic source/sink

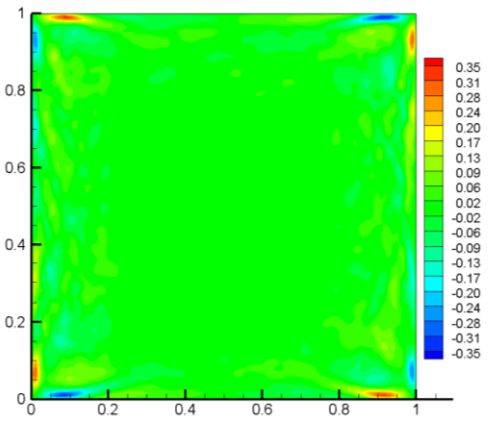

(d) $\left(\frac{\partial^2}{\partial y^2}-\frac{\partial^2}{\partial x^2}\right)\overline{(u'v')}$ (IV)

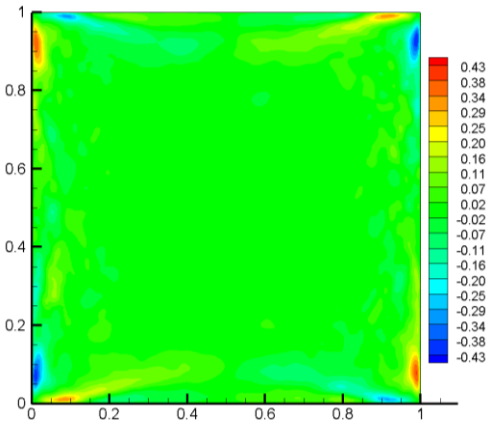

(e) $\frac{\partial^2}{\partial x\partial y}\left(\overline{u'^2}-\overline{v'^2}\right)$ (V)

(Re=5602 Ha=21.2, 128x128x512, 1x1x16)

Figure 2.16 Various budgets of streamwise vorticity ($\bar{\Omega}_z=\left(\frac{\partial\bar{v}}{\partial x}-\frac{\partial\bar{u}}{\partial y}\right)$) equation

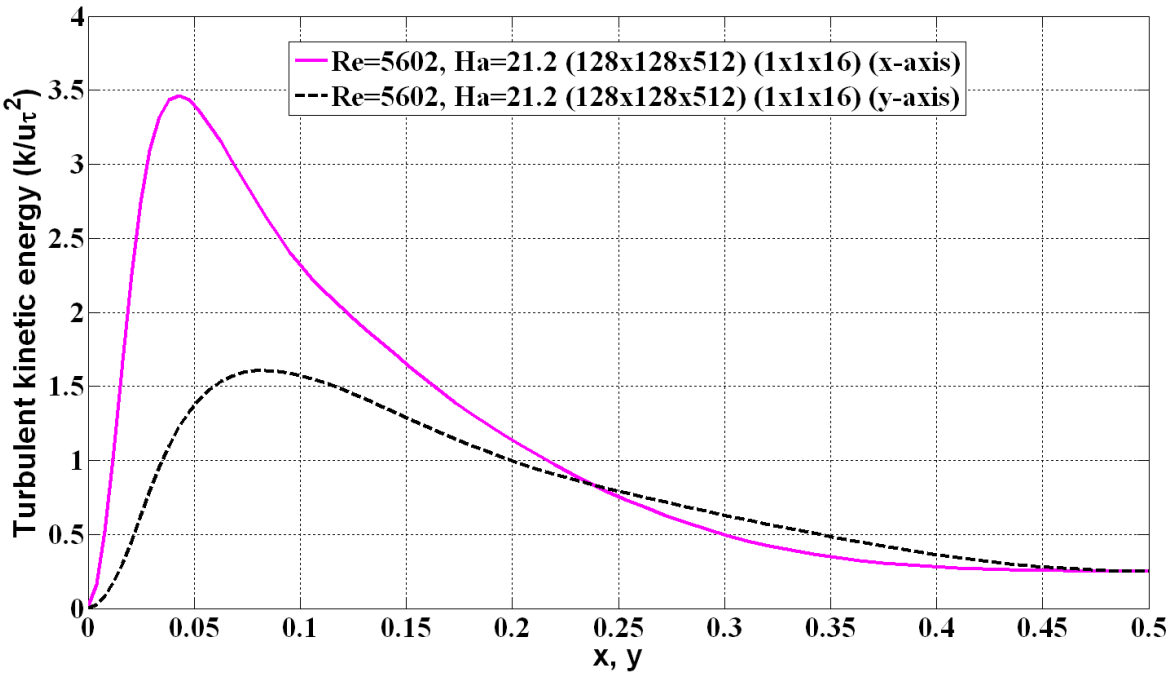

Figure 2.17 Turbulent kinetic energy along horizontal (x-) and vertical (y-) bisectors

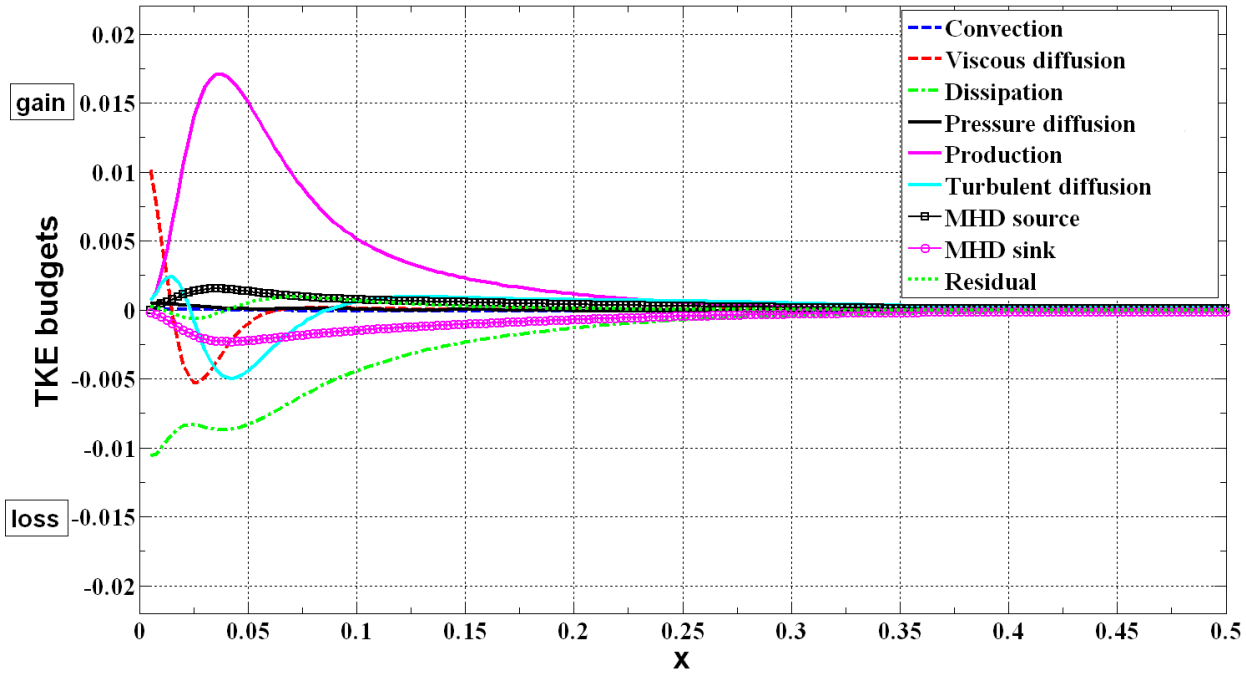

Figure 2.18(a) TKE Budgets along horizontal (x-) bisector

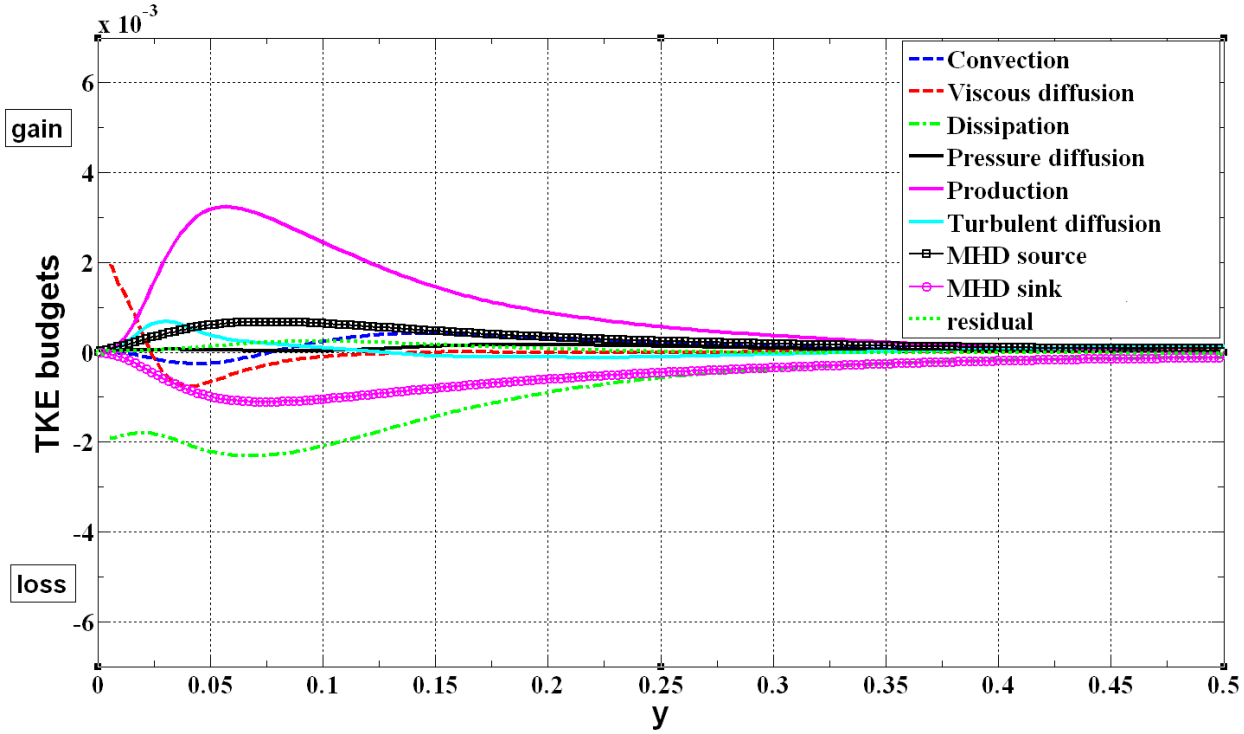

Figure 2.18(b) TKE Budgets along vertical (y-) bisector

2.10. References

1. P. A. Davidson, Magnetohydrodynamics in materials processing, Ann. Rev. Fluid Mech., 1999, 31, pp.273–300.
2. B. G. Thomas and Lifeng Zhang, Mathematical modeling of fluid flow in continuous casting: a review, ISIJ International, 2001, 41, 10, pp.1181-1193.
3. R. Moreau, Magnetohydrodynamics., Kluwer Academic Publishers, 1990.
4. B. Knaepen and R. Moreau, Magnetohydrodynamic turbulence at low magnetic Reynolds number, Ann. Rev. Fluid Mech., 2008, 40, pp. 25-45.
5. H. C. Ji and R. A. Gardner, Numerical analysis of turbulent pipe flow in a transverse magnetic field, Int. J. Heat Mass Transfer., 1997, 40, pp. 1839–1851.
6. S. Kenjereš and K. Hanjalić, On the implementation of effects of Lorentz force in turbulence closure models, Int. J. Heat Fluid Flow, 2000, 21, pp. 329–337.
7. S. Smolentsev, M. Abdou, N. Morley, A. Ying, T. Kunugi, Application of the "k-ε" model to open channel flows in a magnetic field., Int. J. Eng. Sci., 2002, 40, pp. 693–711.
8. S. Smolentsev and R. Moreau, Modeling quasi-two-dimensional turbulence in MHD duct flows. *Proc. 2006 Summer Program*, Stanford, CA: Cent. Turbul. Res., Stanford Univ. & NASA Ames Res. Cent, 2006, pp. 419–430.
9. P. Moin and K. Mahesh, Direct Numerical Simulation: A Tool in Turbulence Research, Ann. Rev. Fluid Mech., 1998, 30, pp. 539-578.
10. P. Moin, and J. Kim, Numerical investigation of turbulent channel flow, J. Fluid Mech., 1982, 118, pp. 341-377.
11. J. Kim, P. Moin, and R. Moser, Turbulence statistics in fully developed channel flow at low Reynolds number, J. Fluid Mech., 1987, 177, pp. 133-166.

12. R. Moser, J. Kim, and N. Mansour, Direct numerical simulation of turbulent channel flow up to Re_τ=590, Phys. Fluid, vol. 11, no. 4, pp. 943-945. http://turbulence.ices.utexas.edu/MKM_1999.html

13. R. Moser, and P. Moin, The effects of curvature in wall-bounded turbulent flows., J. Fluid Mech., 1987, 175, pp. 479-510.

14. J. P. Monty, and M.S. Chong, Turbulent channel flow: comparison of streamwise velocity data from experiments and direct numerical simulations, J. Fluid Mech., 2009, 623, pp. 461-474.

15. S. Gavrilakis, Numerical simulation of low Reynolds number turbulent flow through a straight square duct, J. Fluid Mech., 1992, 244, pp. 101-129.

16. A. Huser, and S. Biringen, Direct numerical simulation of turbulent flow in a square duct, J. Fluid. Mech., 1993, 257, pp. 65-95.

17. R. K. Madabhushi and S. P. Vanka, Large eddy simulation of turbulence driven secondary flow in a square duct, Phys. Fluid A, 1991, 3, pp. 2734-2745.

18. R. K. Madabhushi and S. P. Vanka, Direct numerical simulation of turbulent flow in a square duct at low Reynolds number, Near-wall Turbulent flows, RMC So. C.G. Speziale and B. E. Launder (Editors), 1993.

19. E. C. Brouillette and P. S. Lykoudis, Magneto-fluid-mechanic channel flow. I. Experiment, Phys. Fluids, 1967, 10, pp. 995-1001.

20. C. B. Reed and P. S. Lykoudis, The effect of a transverse magnetic field on shear turbulence, J. Fluid Mech., 1978, 89, pp. 147-171.

21. S. Satake, T. Kunugi and S. Smolentsev, Direct numerical simulations of turbulent pipe flow in a transverse magnetic field, J. of Turbulence, 2002, 3, 020.

22. D. Lee and H. Choi, Magnetohydrodynamic turbulent flow in a channel at low magnetic Reynolds number, J. Fluid Mech., 2001, 439, pp. 367–394.

23. H. Kobayashi, Large eddy simulation of magnetohydrodynamic turbulent channel flows with local subgrid-scale model based on coherent structures, Phys. Fluids, 2006, 18, 4, pp. 45107-1-11,.

24. S. Satake, T. Kunugi, T. Kazuyuki and O. Yasuo, Direct numerical simulation of turbulent channel flow under a uniform magnetic field for large-scale structures at high Reynolds number, Phys. Fluids, 2006, 18.

25. T. Boeck, D. Krasnov and E. Zienicke, Numerical study of turbulent magnetohydrodynamic channel flow, J. Fluid Mech., 2007, 572, pp. 179-188.

26. H. Noguchi, and N. Kasagi, Direct Numerical Simulation of Liquid Metal MHD Turbulent Channel Flows, (in Japanese), Preprint of JSME, No. 940-53, Nov. 1994, pp. 365-366.

27. D. Krasnov, O. Zikanov, J. Schumacher, and T. Boeck, Magnetohydrodynamic turbulence in a channel with spanwise magnetic field, Phys. Fluids, 20, 095105 (2008).

28. O. Zikanov and A. Thess, Direct numerical simulation of forced MHD turbulence at low magnetic Reynolds number, J. Fluid Mech., 1998, 358, pp. 299-333.

29. O. Zikanov, and A. Thess, Direct numerical simulation as a tool for understanding MHD liquid metal turbulence, Appl. Mathematical Modelling, 2004, 28, pp. 1-13.

30. H. Kobayashi, Large eddy simulation of magnetohydrodynamic turbulent duct flows, Phys. Fluids, 2008, 20, 4, pp 015102-1-13.

31. U. Muller and L. Buhler, Magneto Fluid Dynamics in Channels and Containers, Springer, Berlin, 2001, Sec. 4.2.1.

32. G. K. Batchelor, An Introduction to Fluid Dynamics, Cambridge University Press; ISBN:0521663962

33. F. Harlow and E. Welch., Numerical calculation of time-dependent viscous incompressible flow of fluid with free surface, Phys. of Fluids, 1965, 8, pp. 2182-2189.

34. A. F. Shinn, S. P. Vanka, and W. W. Hwu., Direct Numerical Simulation of Turbulent Flow in a Square Duct Using a Graphics Processing Unit (GPU), AIAA-2010-5029, 40th AIAA Fluid Dynamics Conference, June 2010.

35. R. Chaudhary, S.P. Vanka, and B.G. Thomas, Direct numerical simulations of magnetic field effects on turbulent duct flows, Proc. ASME Int. Mech. Eng. Congress (IMECE09), 2009, Nov. 13-19, Lake Buena Vista, FL.

36. B. F. Gessner, and J. B. Jones, On some aspects of fully developed turbulent flow in rectangular channels, J. Fluid Mech., 1965, 23, pp. 689-713.

CHAPTER 3. DIRECT NUMERICAL SIMULATIONS OF TRANSVERSE AND SPANWISE MAGNETIC FIELD EFFECTS ON TURBULENT FLOW IN A 2:1 ASPECT RATIO RECTANGULAR DUCT

3.1. Introduction

Magnetic fields have numerous applications in steering liquid metal flows [1]. Continuous casting of steel uses static and time varying magnetic fields to alter the flow and inclusion transport in order to reduce defects in the cast steel [2]. Magnetic field, when applied to a flowing liquid metal, induces a force which alters the velocity field [3]. A strong magnetic field can suppress turbulence significantly leading to a complete laminarization [4]. In the case of continuous casting, a magnetic field when used wisely across the mold can help in the transport of unwanted inclusions to the top slag surface where they can be captured and removed [2]. A variety of options exist on tailoring the magnetic field in order to accomplish the desired objective. These include local, single-ruler, and double-ruler static field brakes, oscillatory (cyclic) time varying magnetic fields and different orientations of the magnetic field [2].

It is not easy to get a fundamental understanding of the turbulence characteristics in a real-life continuous caster through measurements because of the high temperatures and non-intrusive nature of the medium. Hence, one is limited to simulations of the various processes through accurate mathematical models. However, mathematical modeling of turbulent flows is also not easy as several assumptions have to be made in constructing models for turbulence, multiphase flow and particle transport [2] if the flow is approximated by the traditional Reynolds-averaged Navier-Stokes (RANS) approach. Although Direct Numerical Simulations (DNS) of turbulent flows are currently feasible, they require large amounts of computer

resources and have to be restricted to low Reynolds numbers. Despite this constraint, valuable information on the flow is being obtained using DNS.

In a previous study [5], we presented results of several direct numerical simulations of turbulent flow in a square duct with a magnetic field imposed along one of the cross-stream directions. We had conducted well-resolved simulations using a finite volume code, CU-FLOW [6] extended to include magnetohydrodynamic (MHD) effects [5]. The main observations of this study were the suppression of turbulence along the direction of the magnetic field and alteration of the instantaneous and mean structure of the turbulence-driven secondary flows in the square duct. The magnetic field strength was gradually increased to the point where all the turbulent fluctuations were completely damped and the flow laminarized. The results of this study were then used to evaluate a number of RANS based turbulence models including low and high Reynolds number k-ε models, Reynolds stress models (RSM) and a number of their variants with different near-wall formulations [7]. Unfortunately, it was difficult to predict with accuracy many of the important turbulence quantities that were obtained by DNS.

The geometry we previously considered was a canonical problem of turbulence in a square duct modulated by the magnetic field. This study produced valuable information regarding the turbulence structures and the instantaneous flow. However, in a real-life caster, the geometry is rectangular and the magnetic field can be imposed on the wide or the narrow side. The resulting flow patterns can be quite different because of the asymmetry about the horizontal and vertical bisectors. Because of the differences in the secondary flow, the particle transport and capture can be quite different in the two cases.

In the present study, we have therefore considered a streamwise periodic flow in a duct with an aspect ratio of 2:1 and subjected it to a magnetic field either on the broad side or on the

narrower side. This problem is also of fundamental significance as it elucidates the differences resulting from imposing the magnetic field in two different orthogonal directions. We have conducted DNS of five different cases, with two magnetic field intensities in either direction and compared them with the case of no magnetic field. Calculations have been performed for Hartmann numbers (based upon half duct height) of 0, 6.0 and 8.25 at a friction Reynolds number (based on friction velocity and half duct height) of 170. The grid used consists of 224x120x512 control volumes with stretching in two cross-stream directions. Various turbulence and mean flow statistics have been computed to characterize the effects of the magnetic field. We believe these results can be valuable additions to the already existing databases in literature which are used for large eddy simulation (LES) and RANS turbulence model development.

This paper is organized as follows; Section 2 gives a brief overview of the previous research on non-MHD and MHD turbulent channel, pipe and duct flows, including our own recent DNS in MHD square duct. Section 3 presents the governing equations, boundary conditions and numerical method. Section 4 presents results of the current simulations. The results for the non-MHD duct are compared with the results for the two different orientations of the magnetic field and two different intensities. Section 5 summarizes the findings.

3.2. Previous Work

Several DNS and LES of turbulence in non-MHD flows have been previously published for pipes, jets, shear and mixing layers and for more complex situations relevant to practical engineering applications. A few DNS/LES relevant to the present geometrical configuration are the DNS/LES of annular square [8] and square [9-12] ducts. Gavrilakis [9] was the first to perform DNS of turbulent flow in a square duct at a Reynolds number of 4410. Soon after this study, Madabhushi and Vanka [10-11] performed LES and DNS of the same flow at nearly the

same Reynolds number ($Re_\tau = u_\tau D/\nu = 360$ for LES and 260 for DNS). For LES, a finite-difference-spectral code was used whereas for the DNS, a fully-spectral code with two Chebyshev and one Fourier (streamwise) expansions was used. The turbulence statistics and secondary flows were accurately predicted in both the simulations. Subsequent study of non-MHD turbulent duct flow was conducted by Huser and Biringen [12]. Recently Shinn et al [6] presented a simulation of square duct flow at $Re_\tau = 360$ with a GPU based finite volume code using 26 million nodes. The same base code has been used here and was validated against Gavrilakis's study for a turbulent square duct flow at the same Reynolds number [5].

Many DNS and LES of turbulent MHD channel flow with two periodic directions have been previously conducted [13-18]. Turbulent rectangular duct and pipe flows subjected to a magnetic field have been studied to a lesser extent [19-21]. Brouillette and Lykoudis (1967) [19] and Reed and Lykoudis (1978) [20] performed measurements in high aspect ratio (5:1 and 5.8:1) MHD rectangular ducts respectively. The effect of the magnetic fields on turbulence suppression and frictional losses was studied. Satake, Kunugi and Smolentsev (2002) performed DNS of a MHD pipe flow with transverse magnetic field at a moderate Reynolds number of 5300 and three Hartmann numbers of 5, 10, and 20 [21]. The effect of magnetic field on various flow parameters along the circumference was evaluated. The velocity profile close to the side walls on horizontal axis becomes more round and flat close to top and bottom along vertical axis.

Studies of square ducts subjected to a magnetic field are relatively few in number. These include LES of Kobayashi [22], and our own recent DNS study in a square duct [5], and recent DNS studies by Shatrov and Gerbeth [23] on marginally turbulent duct flow. Kobayashi (2008) performed LES of the turbulent flow in a square duct with a transverse magnetic field at two Reynolds numbers (Re=5300 and Re=29000) with 64x64x64 and 128x128x128 grids

respectively [22]. In our study [5], DNS computations at a nominal Reynolds number of ~5500 with 64x64x128, 80x80x256 and 128x128x512 cells and 1x1x2π and 1x1x16 domain sizes were performed. Mean and RMS velocities, Reynolds shear stresses, turbulent kinetic energy budgets, and streamwise vorticity budgets were collected and analyzed. Shatrov and Gerbeth [23] performed DNS studies in a marginally turbulent MHD square duct using a higher order finite difference method. The magnetic field was found to increase the required Reynolds number to maintain turbulence in the square duct.

The rectangular duct is a more realistic representation of the caster mold or nozzle region and the magnetic field direction. From a fundamental flow view point, it provides an opportunity to study the widely different effects generated by the asymmetric turbulence and magnetic field directions in turbulence modulation and suppression. To the best of our knowledge, there have been no numerical studies of the effect of aspect ratio and the orientation of the magnetic field on the turbulence structures and statistics. The present paper provides detailed data in this configuration both for fundamental understanding and turbulence model development.

3.3. Governing Equations

The equation set for an incompressible MHD flow in a duct consists of equations for conservation of mass, conservation of momentum in three directions and the equation governing the electric potential. The magnetic field induces an electric current, which is calculated from the electric potential field. Source terms are then added to the appropriate momentum equations to include the Lorentz forces. We first non-dimensionalize the equations with the following definitions.

$$\vec{x}^* = \left(x^*, y^*, z^*\right) = \left(\frac{x}{\delta}, \frac{y}{\delta}, \frac{z}{\delta}\right),\ t^* = \frac{t}{\left(\delta / W_b\right)},\ \vec{v}^* = \left(u^*, v^*, w^*\right) = \left(\frac{u}{W_b}, \frac{v}{W_b}, \frac{w}{W_b}\right),$$

$$p^* = \frac{p}{\rho W_b^2},\ \vec{B}_0^* = \left(\frac{B_{x0}}{B_0}, \frac{B_{y0}}{B_0}, \frac{B_{z0}}{B_0}\right),\ \phi^* = \frac{\phi}{\left(\delta W_b B_0\right)},\ \nabla^* = \frac{\partial}{\partial x^*} i + \frac{\partial}{\partial y^*} j + \frac{\partial}{\partial z^*} k$$

The non-dimensional equations can be written as [3]:

Continuity equation:

$$\nabla \cdot \vec{v}^* = 0 \tag{3.1}$$

Momentum equations:

$$\frac{\partial \vec{v}^*}{\partial t^*} + \nabla^* \cdot \left(\vec{v}^* \vec{v}^*\right) = -\nabla^* p^* + \frac{1}{\mathrm{Re}} \nabla^* \cdot \nabla^* \vec{v}^* + \frac{\mathrm{Ha}^2}{\mathrm{Re}} \left(\vec{J}^* \times \vec{B}^*\right) \tag{3.2}$$

$$\nabla^{*2} \phi^* = \nabla^* \cdot \left(\vec{v}^* \times \vec{B}_0^*\right) \tag{3.3}$$

$$\vec{J}^* = -\nabla^* \phi^* + \vec{v}^* \times \vec{B}_0^* \tag{3.4}$$

The Reynolds and Hartmann numbers are defined based upon half duct height (δ) and bulk mean axial velocity (W_b) as,

$$\mathrm{Re} = \frac{\delta W_b}{\nu} \qquad \mathrm{Ha} = \delta B_0 \sqrt{\frac{\sigma}{\rho \nu}} \tag{3.5}$$

3.4. Computational Domain, Boundary Conditions and Numerical Method

The schematic of the physical and computational domains is shown in Figure 3.1. The computational domain considered in the current simulations is 2x1x6 non-dimensional units. The horizontal (x-) and the vertical (y-) directions are bounded by electrically insulated no-slip walls whereas the streamwise (z-) direction is considered periodic. The boundary conditions for insulated non-slip walls were presented in previous work [5]. The computational domain is discretized with 224x120x512 cells. In all runs, the mean streamwise pressure gradient ($\frac{\partial \overline{p}}{\partial z}$) was fixed corresponding to $\mathrm{Re}_\tau = \frac{u_\tau \delta}{\nu} = 170$ (based upon half vertical height) and bulk Reynolds

number was allowed to change. For MHD cases, a constant and uniform magnetic field is applied in the vertical (y-, transverse) and horizontal (x-, span-wise) directions. Table 3.1 presents the flow parameters, domain, and grid sizes for the five cases simulated in the current study.

The above incompressible-MHD flow governing equations along with the boundary conditions have been discretized using the Finite Volume Method (FVM) on a structured Cartesian staggered grid with pressure-velocity coupling resolved through the fractional step method [24]. Convection and diffusion terms have been discretized using second order central differencing scheme. Time integration has been achieved using explicit second order Adams-Bashforth scheme. A multigrid solver is used for the solution of Pressure Poisson Equation (PPE) and Electric Potential Poisson Equation (EPPE). The current density ($\vec{J}^*$) is then calculated from electric potential and velocity field. Thereafter, the Lorentz force $\left(\vec{J}^* \times \vec{B}^*\right)$ is added as an explicit source term in momentum equations. All calculations have been performed on a Graphics Processing Unit (GPU) by extending CU-FLOW (a GPU-based code) [6] by including MHD equations [5], and balances/computations for vorticity and TKE budgets. More details about the numerical method and GPU implementations of CU-FLOW are given in Shinn et al. [6] and Chaudhary et al. [5].

The code has been validated for a number of flows including model problems like turbulent channel flow, turbulent channel flow with a magnetic field, turbulent square duct, laminar and turbulent square duct flows with a magnetic field [5]. In all cases, comparisons with previously published numerical results have been made satisfactorily. The grids selected in current study have comparable resolution to the finest grid used in the simulations of turbulent

flow in channel and square duct in our previous study [5]. Hence we believe that all the important structures are adequately resolved in our current simulations.

3.5. Results and Discussion

All computations were initiated from a fully-developed laminar duct velocity profile to which a sinusoidal divergent-free perturbation velocity field was added. The simulations were continued with the perturbation for 1500 time steps and the perturbation was then removed. A stationary state of turbulence was first achieved before the collection of time-mean velocities (u, v, w) was initiated. After the mean velocities became stable (~30,000 timesteps in different cases, $\Delta t = 0.0001$), the collection of turbulence statistics and turbulent kinetic energy budgets terms was initiated. Thereafter the means, turbulence statistics and turbulent kinetic energy budgets were together collected. The averaging times in convective units are given in Table 3.1.

3.5.1. Instantaneous Flow Fields

We first present the instantaneous flow fields for some of the cases studied. The magnetic field is imposed either on the broad side of the duct (in the vertical direction) or on the narrower side (in the horizontal direction). Computations were performed for two Hartmann numbers (Ha = 6.0 and 8.25) for each direction, in addition to the case with no magnetic field. The instantaneous fields were selected after integrating the flow fields to reach a stationary turbulent state. Figure 3.2 shows three plots of instantaneous cross-sectional velocity vectors, and contours of streamwise velocity for the no-magnetic field and the Ha=8.25 cases. Since the flow fields evolve in their own unique statistical manner, there is no correspondence in time among the three plots. Rather they show the qualitative features of the flow patterns in the three different cases. It can be seen that the maximum of instantaneous cross-stream velocity magnitude can be as large as ~30% of the maximum instantaneous stream-wise velocity in a non-MHD 2:1 aspect duct.

Although it is difficult to draw any precise conclusions from the instantaneous fields, there are some qualitative differences that can be noticed. First, the effect of the duct aspect ratio on the turbulence structures can be seen at the corners. The turbulence eddies are relatively more compressed and intense on the narrow faces (left and right) than on the top and bottom walls. This will further become clear in the time-averaged plots to be presented later. The application of a magnetic field dampens the turbulence fluctuations and also reduces the secondary velocities in the core region. The effect of a vertical magnetic field is however seen to be more pronounced than that of a horizontal field. When a vertical magnetic field is applied, the core region is widened due to flattening effects. Also, the turbulence close to the top and bottom walls is suppressed more strongly. This is due to the formation of Hartmann layer close to the walls perpendicular to the magnetic field direction. Based upon same argument as above, with horizontal magnetic field, the Hartmann layer close to side walls leads to more strong suppression of turbulence close to side walls. Interestingly, although a magnetic field causes stronger turbulence suppression close to the walls perpendicular to the magnetic field, weaker suppression is also seen close to the walls parallel to the field due to intermittent fluctuations in current density causing it to become locally perpendicular to the field with time. Additionally, in the case of vertical magnetic field, there is a greater region close to top and bottom walls where current becomes locally perpendicular thus leading to more turbulence suppression as compared to the region near left and right walls with horizontal magnetic field. The current density lines across the cross-section will be later outlined in greater detail. The results for a smaller Hartmann number (Ha=6.0) show a similar behavior but relatively weaker effects and therefore are not shown.

3.5.2. Time/Ensemble-Averaged Flows

Figure 3.3 shows the ensemble-averaged velocity fields in the cross-sectional plane after the instantaneous fields have been averaged in time and stream-wise direction. Also, since the fields are quadrant symmetric, they have been averaged about the vertical and horizontal bisectors, after appropriate mirror reflections. The streamwise and quadrant averaging is performed every 10,000 time steps during the computations. The top Figure 3.3(a) shows the case with no magnetic field. In comparison with the case of a square duct, for a rectangular duct, there is no octant symmetry in the secondary velocities as well as the streamwise velocity. This asymmetry in secondary flows is caused by the effect of aspect ratio on Reynolds stresses. The secondary flow eddies on the narrow face are more circular, while those on the wider face are elongated. Further, unlike the case of a square duct, the central region and regions close to top and bottom walls above central regions are relatively free of the secondary flows. The secondary velocities do not penetrate all the way into the duct center. When compared with square duct, the secondary flow does not go to the corners at a 45 degree angle, but it goes towards the longer sides thus giving asymmetric bulging in the axial velocity at the corners. The bulging in axial velocity is stronger on the wider sides than close to narrow sides. As compared to square duct which has only two symmetric vortices in every quadrant, in 2:1 aspect non-MHD duct three vortices are witnessed. The two of the primary vortices are similar to square duct but have anisotropic effects of the aspect ratio which gives rise to a third smaller vortex in between the weaker vortex and the horizontal bisector.

With the application of the magnetic field, different trends are seen with horizontal versus the vertical magnetic fields. Figures 3.3(b) and 3.3(c) show the mean flow fields for the horizontal magnetic fields (Ha=6.0 and Ha=8.25). It is seen that a horizontal magnetic field

pushes the flow to the central core. The region where the axial velocity is the greatest is elongated as the magnetic field is increased. Compared with Figure 3.3(a), the secondary flow on the narrow face has increased, while it has decreased on the broader side. The strong secondary flow close to narrow face upon returning to the core causes strong bulging in axial velocity profile at the middle of the right and the left walls. This bulging in axial velocity has also been witnessed previously in MHD square duct [5]. Even though secondary flows close to the broader side are reduced, the secondary flows remain attached to the top and bottom walls until the center where they return to the core. Upon increasing the magnetic field (Ha=8.25), the secondary flow separates close to the middle of the top and bottom walls. With a vertical magnetic field (Ha=6 and Ha=8.25) (Figure 3.3(d) and 3.3(e)), the secondary flow region is elongated near the top and bottom walls. The qualitative pattern of secondary flows with a vertical magnetic field is quite similar to the non-magnetic field case. However, the axial velocity is flattened close to top and bottom walls with the application of a strong vertical magnetic field.

The magnetic field reorganizes the mean secondary velocity vortices across the cross-section completely. With horizontal field, the strength of the primary vortices is flipped with stronger vortex now being close to side wall. In this case, the third bigger vortex is close to longer wall. With vertical magnetic field, the vortices are similar as in non-MHD case but weaker in strength. Interestingly, the stronger magnetic field (i.e. Ha=8.25, with both orientations), generates a fourth vortex close to longer walls and vertical bisector in every quadrant. The horizontal magnetic field is found to be suppressing and reorganizing secondary flows more strongly compared to vertical field. This will be confirmed in vorticity plots (Figure 3.10) which will be presented later. These features and pattern of flow with different orientation

of the magnetic field can be important for the continuous casting situation in deciding the optimal orientation of the magnetic field for transport and capture of the inclusions.

The variations of mean axial velocity along horizontal and vertical bisectors of the duct are presented in Figure 3.4(a) and 3.4(b) respectively. The axial velocity profiles along both the bisectors show the effects of aspect ratio and magnetic field. Along the longer bisector, a longer region of flat values is seen in the core. This effect is due to weaker effects of Reynolds shear stress ($\overline{u'w'}$) in this part of the domain. More on this region will be discussed with the following results. The strongest effects along both the bisectors is seen with a stronger magnetic field (Ha=8.25). The horizontal magnetic field makes the axial velocity profile more rounded whereas a vertical field makes the profiles more flat along both bisectors. This behavior is consistent at both Hartmann numbers.

Figure 3.5(a) and 3.5(b) respectively show the root mean square (RMS) of axial velocity fluctuations ($\sqrt{\overline{w'w'}}$) along horizontal and vertical bisectors. The effect of longer and shorter sides is clearly seen on the axial velocity fluctuations along the two bisectors. Similar to mean axial velocity, the axial Reynolds normal stress also has a longer region of flat and lower values in the core beyond x>0.5. In non-MHD case, the peak value of axial velocity fluctuations is slightly higher close to broader side than close to narrow side due to anisotropic effect of aspect ratio. It is interesting to note that axial velocity fluctuations close to the sidewalls are more strongly suppressed by strong horizontal magnetic field (B_x, Ha=8.25). The suppression close to top and bottom walls is stronger (suppressed by ~16% compared to non-MHD case) in stronger vertical magnetic field (B_y, Ha=8.25) case. Higher axial velocity fluctuations (w') around these locations when interacts with fluctuating current density perpendicular (j_x' or j_y' , Where

$\vec{J}' = \sigma\left(-\nabla\phi' + \vec{v}' \times \vec{B}_0\right)$) to magnetic field causes this suppression. More on the behavior of instantaneous current density at the cross-section with two orientations of magnetic field will be given later. In the core, the strongest suppression is seen with vertical magnetic field. Overall, across the whole domain, the strongest suppression of axial velocity fluctuations is seen with strong magnetic field parallel to shorter side (B_y, Ha=8.25) and therefore seems to be the best way to control turbulence in such flows. It is surprising to see that a weaker magnetic field in the horizontal direction (B_x, Ha=6.0) actually increased axial velocity fluctuations slightly close to the top and bottom walls when compared to the non-MHD case. This behavior is due to the interaction of v' with j_z' (i.e. $\overline{v' j_z'}$) which acts as a source term to axial Reynolds normal stress transport. This is consistent with the mean secondary flow staying attached to top and bottom walls and leading to higher values of $\bar{v}$ along vertical bisector in Figure 3.3(b). This behavior is also seen in $\overline{v'w'}$ and MHD source/sink terms which will be discussed later. The other MHD cases which have lower $\bar{v}$ in this region do not show this effect.

The RMS of horizontal velocity fluctuations ($\sqrt{\overline{u'u'}}$) along horizontal and vertical bisectors is presented in Figure 3.6(a) and 3.6(b), respectively. Similar to axial velocity fluctuations, here also the horizontal velocity fluctuations are more strongly suppressed by strong vertical magnetic field (B_y, Ha=8.25). Interestingly, very close to the side wall, again similar to axial velocity fluctuations, the horizontal velocity fluctuations are suppressed more by strong horizontal field (B_x, Ha=8.25). Although weaker but similar behavior along both bisectors is shown by horizontal velocity fluctuations at Ha=6.0. Very close to the top/bottom walls with strong vertical magnetic field, the effect of Hartmann flattening is clearly visible where

horizontal velocity fluctuations falls sharply within a small region to zero values at the wall. Again, horizontal velocity fluctuations give a longer flatter region in the core along longer horizontal (x-) bisector than along shorter vertical (y-) bisector. Also, in general for all cases except strong vertical field (B_y, Ha=8.25), the horizontal velocity fluctuations are weaker along horizontal (x-) bisector than along vertical (y-) bisector.

Figures 3.7(a) and 3.7(b) show the RMS of vertical velocity fluctuations ($\sqrt{\overline{v'v'}}$) along horizontal and vertical bisectors respectively. Qualitatively, the profiles of vertical velocity fluctuations are quite similar to horizontal velocity fluctuations along the two bisectors but their values are flipped along the two bisectors. Unlike square duct where these values match exactly, in 2:1 duct they are slightly different and thus signifying the effect of aspect ratio. Along the longer bisector a longer region of flat values can be seen. The magnetic field further increases asymmetry in these values. Close to side walls, the effect of Hartmann layer can be seen in vertical velocity fluctuations with strong horizontal magnetic field.

The Hartmann layer effects on horizontal and vertical velocity fluctuations clearly suggest the regions of stronger influence in two orientations of magnetic fields. To reinforce the regions of stronger Lorentz force effects/Hartmann flattening, the magnitude and current lines of instantaneous induced current density ($\vec{J} = \sigma\left(-\nabla\phi + \vec{v} \times \vec{B}_0\right)$) at a cross-section with two orientations of magnetic fields are presented in Figure 3.7(c) and 3.7(d). With horizontal magnetic field (B_x), current lines are perpendicular to the field in the core and close to the side walls. Close to side walls, the magnitude of current density is much higher than in the core and thus being the region of strong Lorentz force effects in this case followed by in the core. The regions where current is parallel to the magnetic field has weaker effects (close to top and bottom

walls). In case of vertical field (B_y), strong effect is close to top and bottom walls followed by in the core. As previously mentioned, a vertical magnetic field has a wider Hartmann layer leading to a large region of magnetic field influence with this orientation of the field. In addition, the vertical field gives higher current density magnitude than the horizontal field. For example, the maximum value of induced current density in the vertical magnetic field is ~5% (16.11 vs. 15.36) higher than the maximum value in the horizontal magnetic field.

The Reynolds shear stresses ($\overline{u'w'}$ and $\overline{v'w'}$) along horizontal and vertical bisectors are presented in Figure 3.8(a) and 3.8(b) respectively. Similar to axial, horizontal and vertical velocity fluctuations, the Reynolds shear stress ($\overline{u'w'}$) close to side wall is more strongly suppressed in the strong horizontal magnetic field case. Overall, with both horizontal and vertical magnetic fields, the strongest suppression is in $\overline{v'w'}$ with the strong vertical magnetic field. Again, a bigger flatter region with lower values of $\overline{u'w'}$ is seen in the core along the horizontal bisector.

It is interesting to note that although magnetic field suppresses turbulence but the peak values of $\sqrt{\overline{u'u'}}$, $\sqrt{\overline{v'v'}}$, $\sqrt{\overline{w'w'}}$, $\overline{u'w'}$ and $\overline{v'w'}$ stay at the same (x or y) position except in horizontal field where the peak values of $\sqrt{\overline{u'u'}}$, $\sqrt{\overline{v'v'}}$, $\sqrt{\overline{w'w'}}$ and $\overline{u'w'}$ close to side walls get shifted towards the core due to strong returning secondary flows.

The profiles of wall stress ($\tau_w = \mu \left.\frac{\partial \overline{w}}{\partial n}\right|_{wall}$) along the top horizontal and along left vertical walls are presented in Figures 3.9(a) and 3.9(b) respectively. Along the top horizontal wall, the wall stress shows more oscillations, suggesting the influence of fluctuating secondary flows along the longer side. The wall stress close to corners with vertical magnetic field gives higher values on both sides along top horizontal wall. These higher values are not seen in non magnetic

field case and even values are lowered in horizontal magnetic field around corners. The frictional losses along this wall (top-horizontal) are higher in vertical magnetic field than horizontal magnetic field. Along the left vertical wall, the profile is completely different and with less oscillations when compared with the top horizontal wall. The horizontal magnetic field gives higher frictional losses along left vertical wall. The friction factor along left vertical wall in vertical magnetic field follows a similar profile as in non magnetic field case. The vertical magnetic field gives stronger secondary flows towards broader side and horizontal field towards shorter side affecting axial velocity to give above trends in wall stresses. Overall, the behavior of friction factor with two orientations of magnetic fields is consistent with the Hartmann flattening close to top/bottom and side walls as discussed previously.

3.5.3. Streamwise Vorticity Transport

The mean streamwise vorticity transport equation for streamwise fully developed turbulent 2:1 aspect duct flow under horizontal (B_{x0}) and vertical (B_{y0}) magnetic fields (after dropping superscript "*" from non-dimensional quantities) can be written as [5],

For horizontal field (B_{x0}):

$$\underset{\text{I}}{-\bar{u}\frac{\partial\bar{\Omega}_z}{\partial x}+\bar{v}\frac{\partial\bar{\Omega}_z}{\partial y}}=\underset{\text{II}}{\frac{1}{\mathrm{Re}}\left(\frac{\partial^2\bar{\Omega}_z}{\partial x^2}+\frac{\partial^2\bar{\Omega}_z}{\partial y^2}\right)}\underset{\text{III}}{-\frac{\mathrm{Ha}^2}{\mathrm{Re}}\left(\frac{\partial\bar{v}}{\partial x}B_{x0}^2\right)}\underset{\text{IV}}{+\left(\frac{\partial^2}{\partial y^2}-\frac{\partial^2}{\partial x^2}\right)\overline{(u'v')}}\underset{\text{V}}{+\frac{\partial^2}{\partial x\partial y}\left(\overline{u'^2}-\overline{v'^2}\right)} \quad (3.6)$$

For vertical field (B_{y0}):

$$\underset{\text{I}}{-\bar{u}\frac{\partial\bar{\Omega}_z}{\partial x}+\bar{v}\frac{\partial\bar{\Omega}_z}{\partial y}}=\underset{\text{II}}{\frac{1}{\mathrm{Re}}\left(\frac{\partial^2\bar{\Omega}_z}{\partial x^2}+\frac{\partial^2\bar{\Omega}_z}{\partial y^2}\right)}\underset{\text{III}}{+\frac{\mathrm{Ha}^2}{\mathrm{Re}}\left(\frac{\partial\bar{u}}{\partial y}B_{y0}^2\right)}\underset{\text{IV}}{+\left(\frac{\partial^2}{\partial y^2}-\frac{\partial^2}{\partial x^2}\right)\overline{(u'v')}}\underset{\text{V}}{+\frac{\partial^2}{\partial x\partial y}\left(\overline{u'^2}-\overline{v'^2}\right)} \quad (3.7)$$

where mean streamwise vorticity is $\overline{\Omega}_z = \left(\frac{\partial \overline{v}}{\partial x} - \frac{\partial \overline{u}}{\partial y} \right)$, and term-III is the sink due to magnetic field. Details about other terms and their contour plots for MHD square duct have been previous presented in [5].

The mean streamwise vorticity for non-magnetic field, horizontal magnetic field (Ha=6.0) and vertical magnetic field (Ha=6.0) cases is presented in Figure 3.10(a), 3.10(b) and 3.10(c) respectively. Unlike the square duct, the 2:1 aspect duct does not have corner bisector symmetry and vortices close to broader sides are elongated. It is very interesting to note that the horizontal magnetic field elongates vortices close to narrow side walls and vertical field elongates vortices close to the broader top and bottom walls. The suppression and reorganization of secondary flows is stronger in horizontal magnetic field compared to vertical magnetic field. The maximum value of mean streamwise vorticity is reduced by ~17% in horizontal magnetic field and ~10% in vertical magnetic field compared to non magnetic field case.

The streamwise vorticity transport equation has five terms as given in Eq. 3.6 and 3.7 but only contours of the sources/sinks (term-III from Eq. (3.6) and (3.7)) due to magnetic field are presented in Figure 3.11(a) and 3.11(b) for horizontal and vertical magnetic fields (Ha=6.0) respectively. The horizontal magnetic field causes the sink to the streamwise vorticity close to the side walls whereas vertical field causes the sink close to top and bottom walls. It is quite fascinating to note that although the vertical field gives a stronger sink to vorticity, more suppression of vorticity is seen with the horizontal magnetic field. This behavior is due to combined effect of secondary flow suppression and reorganization of secondary flows across the cross-section.

3.5.4. Turbulent Kinetic Energy Budget and Streaky Structures

The TKE budget transport equation with the effect of magnetic field in a square duct has been presented previously by Chaudhary et al [5]. In the current work, all the terms of the TKE budget equation were collected but due to non-MHD terms being quite similar to as in MHD square duct, they are not presented. The terms having magnetic field effects are important because of their requirement in turbulence model development to incorporate the effect of the magnetic field on turbulence. Thus the magnetic field terms (source and sink) are presented for the two orientations of the magnetic field.

For horizontal field (B_{x0}):

$$\text{MHD Source} = \frac{Ha^2}{\text{Re}}\left(-\overline{v'\frac{\partial \phi'}{\partial z}} + \overline{w'\frac{\partial \phi'}{\partial y}}\right) \tag{3.8}$$

$$\text{MHD Sink} = -\frac{Ha^2}{\text{Re}}\left(\overline{w'^2} + \overline{v'^2}\right) \tag{3.9}$$

For vertical field (B_{y0}):

$$\text{MHD Source} = \frac{Ha^2}{\text{Re}}\left(\overline{u'\frac{\partial \phi'}{\partial z}} - \overline{w'\frac{\partial \phi'}{\partial x}}\right) \tag{3.10}$$

$$\text{MHD Sink} = -\frac{Ha^2}{\text{Re}}\left(\overline{w'^2} + \overline{u'^2}\right) \tag{3.11}$$

Figures 3.12(a) and 3.12(b) respectively present the MHD source and sink terms along horizontal and vertical bisectors for Ha=6.0. The profiles of the source and sink terms due to the magnetic field are quite similar, with the sink being stronger than the source thus causing net suppression of turbulence along both bisectors with both orientations of the magnetic field. This behavior of MHD source and sink terms is consistent with previous work on MHD square duct [5]. Source terms with both orientations of magnetic fields match closely in the core along both

bisectors. The mismatch increases in the sink terms in the core and in both source and sink terms close to peak values.

Figure 3.13(a), 3.13(b) and 3.13(c) respectively present the low-speed streaks in non magnetic field, horizontal magnetic field and vertical magnetic field cases for Ha=8.25. The low-speed streaky structures are reduced significantly with the application of magnetic field. With horizontal magnetic field, streaky structures are reduced close to side walls and in the core. Vertical magnetic field reduces streaky structures close to top and bottom walls and in the core. The reduction of low-speed streaks with the vertical magnetic field is stronger than with the horizontal field.

3.5.5. Mean Streamwise/Axial Momentum Equation Budget

The time-averaged axial momentum equations for streamwise (z-) fully developed MHD and non-MHD turbulent duct flows can be written along vertical (y-) bisectors as:

For horizontal field (B_{x0}):

$$\rho\overline{v}\frac{\partial\overline{w}}{\partial y}+\frac{\partial\left(\overline{\rho w'v'}\right)}{\partial y}-\underbrace{\left(-\frac{\partial\overline{p}}{\partial z}+\mu\left(\frac{\partial^2\overline{w}}{\partial y^2}\right)\right)}-\sigma B_{x0}\frac{\partial\overline{\phi}}{\partial y}+\sigma\overline{w}B_{x0}^2=0 \qquad (3.12)$$

I II III IV V

For vertical field (B_{y0}):

$$\rho\overline{v}\frac{\partial\overline{w}}{\partial y}+\frac{\partial\left(\overline{\rho w'v'}\right)}{\partial y}-\underbrace{\left(-\frac{\partial\overline{p}}{\partial z}+\mu\left(\frac{\partial^2\overline{w}}{\partial y^2}\right)\right)}+\sigma B_{y0}\frac{\partial\overline{\phi}}{\partial x}+\sigma\overline{w}B_{y0}^2=0 \qquad (3.13)$$

I II III IV V

The various budget terms of axial momentum equation, as given above, for non magnetic field, horizontal magnetic field and vertical magnetic field cases (Ha=8.25) are plotted in Figure 3.14(a), 3.14(b) and 3.14(c) respectively. The non magnetic field case does not have last two

terms of Eqs. (3.12) and (3.13). The comparison of other terms is made in Figure 3.14(a) for non MHD case. The term involving the derivative of Reynolds shear stress (II) is mainly balanced by the term (III) involving sum of applied mean pressure gradient and derivative of viscous stresses. The Reynolds shear stress (II) and sum of viscous stress and pressure gradient (III) terms show peak close to wall with flat and opposite sign values in the core. Effect of mean convective term (I) is small. Overall, the non-MHD turbulent flow in fully developed duct is sustained by the balance of Reynolds shear stress, viscous stress and externally applied mean pressure gradient.

In the case of a horizontal magnetic field (B_{x0}) (Figure 3.14(b), terms are given by Eq. (3.12)), the non-MHD terms remain qualitatively the same except some reduction in the peak and core values of terms involving Reynolds and viscous stresses. In this case, there are two additional terms (term IV and V of Eq. 3.12) which act opposite to each other. These two terms are almost balanced by each other and follow a profile similar to that of the mean axial velocity. The net effect of these terms is also attributed due to magnetic stresses. Unlike the non-MHD case, the MHD turbulent duct flow is sustained by the balance of Reynolds stresses, viscous stresses, magnetic stresses and the applied mean pressure gradient.

With a vertical magnetic field (B_{y0}), the axial momentum budget terms are represented by Eq. 3.13. The difference in the vertical magnetic field case is in the term IV (now it becomes horizontal derivative of the electric potential). Figure 3.14(c) presents different terms of Eq. 3.13 along the vertical bisector. The behavior of these terms (especially of term I and term IV) with the vertical magnetic field is quite different from the case of horizontal magnetic field. For example, term IV is almost constant across the whole bisector and only drops to low values sharply close to the wall. The strong effect of term IV very close to the wall is responsible for strong turbulence suppression in this region. In addition, there is a significant imbalance between

the Reynolds shear stress (term II) and viscous stress (term III) terms. The term due to Reynolds shear stress is weaker and has very low values in the core. This suggests the effect of strong turbulence suppression (especially on $\overline{v'w'}$) in the core and close to top/bottom walls in vertical magnetic field case. Interestingly, unlike non-MHD and horizontal magnetic field cases, the convection term (i.e. term I) has negative values close to the wall. This effect is caused by negative values of mean vertical velocity ($\overline{v}$) in very small region below y=0.05 along vertical bisector.

3.6. Summary and Conclusions

In this work, direct numerical simulations in a 2:1 aspect ratio rectangular duct have been carried out. Calculations have been performed for the case of no magnetic field, followed by horizontal and vertical magnetic fields corresponding to two Hartmann numbers (Ha) of 6.0 and 8.25. During calculations, the mean streamwise pressure gradient was fixed corresponding to Re_τ=170 (based upon half duct height) and the bulk Reynolds number was allowed to change. Interesting effects of magnetic field orientation on turbulent and mean flow properties have been observed.

Unlike the square duct, the non-MHD 2:1 aspect duct does not have corner bisector symmetry for secondary flows and axial velocity. The secondary flows are focused close to side walls. The vortices of secondary flows are more rounded close to narrow sides and are elongated in the vicinity of the broad sides. As compared to square duct that has two diagonal symmetric vortices, three vortices are observed in every quadrant in non-MHD 2:1 aspect duct.

In the case of a MHD flow in a 2:1 aspect ratio duct, the horizontal magnetic field suppresses turbulence close to side walls and in the core. The vertical magnetic field has an effect close to top and bottom walls and in the core. The effect of magnetic field is much

stronger in the case of a vertical magnetic field (i.e. field perpendicular to broader wall) and therefore can be a more effective orientation to suppress turbulence. Similar to non-MHD duct, with a weaker magnetic field, three vortices are observed in every quadrant. Increasing the magnetic field increases the number of vortices.

Both orientations of magnetic field suppress secondary flows with horizontal field giving elongation of the secondary flows close to the side walls and the vertical field giving elongation close to the top and bottom walls. The elongation close to the side walls causes bulging in axial velocity which is not observed close to top and bottom walls perhaps due to the larger width. This bulging in axial velocity was also seen previously in the MHD square duct with a magnetic field [5]. The horizontal magnetic field is more effective in suppressing and reorganizing secondary flows.

The MHD source and sink terms in the TKE budget equation have similar profiles but the sink term is stronger and thus the net effect is the suppression of the turbulence. These terms are of great importance as they can be used to formulate a model for the effect of magnetic field on turbulence for RANS and LES based turbulence models. Application of a magnetic field reduces the formation of the low-speed streaks with the vertical field having a greater effect as compared to the case of a horizontal magnetic field. Although, this work only considered 2:1 aspect duct but we expect similar behavior at higher aspect ratios perhaps with more secondary flow vortices across the cross-section.

Tailoring the magnetic field to control turbulence, secondary flows, and streaky structures can be of great practical importance in controlling mixing characteristics of the turbulent flow in different regions of a flow domain. Overall, this work gives an idea of the

behavior of turbulent flows with two orientations of magnetic fields and supplies a DNS database for future model development through a rectangular 2:1 aspect ratio duct.

3.7. Tables and Figures

Table 3.1. Various flow parameters in simulated cases

Re_τ / Re_b	Grid (N_xxN_yxN_z)	Comp. Domain (x,y,z)	Spatial resolution (Δx^+, Δy^+, Δz^+)*	Mag. field orientation	Ha	Averaging time**
170/5315	224x120x512	2x1x6	1.66-5.01,1.49-4.79,3.98	-	0	312
170/5405	224x120x512	2x1x6	1.66-5.01, 1.49-4.79,3.98	B_x	6.00	445
170/5520	224x120x512	2x1x6	1.66-5.01,1.49-4.79,3.98	B_x	8.25	454
170/5372	224x120x512	2x1x6	1.66-5.01,1.49-4.79,3.98	B_y	6.00	454
170/5455	224x120x512	2x1x6	1.66-5.01,1.49-4.79,3.98	B_y	8.25	452

Where,

$$\mathrm{Re}_\tau = \frac{\delta u_\tau}{\nu},\ \mathrm{Re}_b = \frac{2\delta W_b}{\nu} = 2\,\mathrm{Re},\ Ha = B_0\delta\sqrt{\frac{\sigma}{\rho\nu}}$$

δ is half duct height

W_b is bulk axial velocity

B_0 is externally applied magnetic field either in horizontal (x-) or vertical (y-) direction

σ is electrical conductivity

ν is kinematic viscosity

* grids have 1% stretching in x-direction, 2% in y-direction and uniform in z-direction.
** Averaging time given in convective units (δ/W_b)

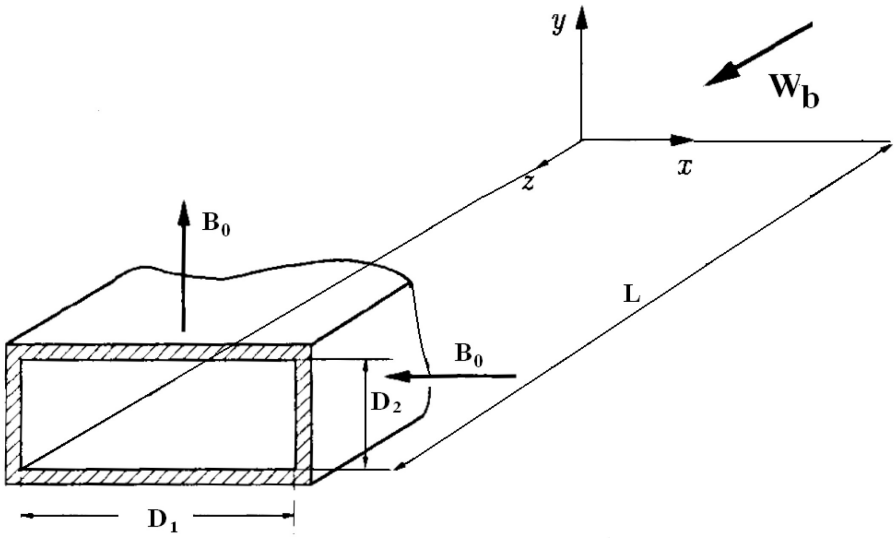

Figure 3.1. Physical and computational domain (where: $D_1 = 2D_2 = 2$ and $D_2 = 2\delta = 1$).

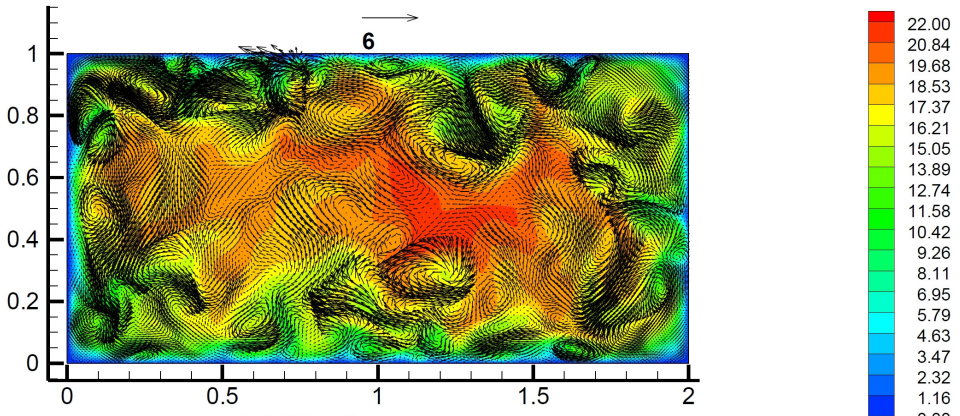

(a) Ha=0

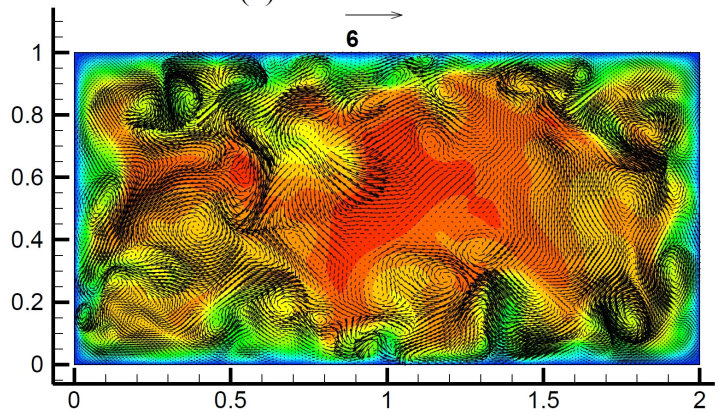

(b) Ha=8.25 (horizontal field, B_x)

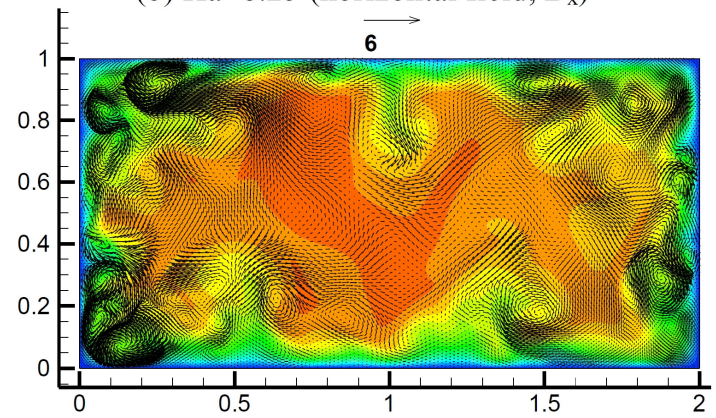

(c) Ha=8.25 (vertical field, B_y)

Figure 3.2. Instantaneous axial velocity contours and secondary velocity vectors (some vectors are skipped for clarity)

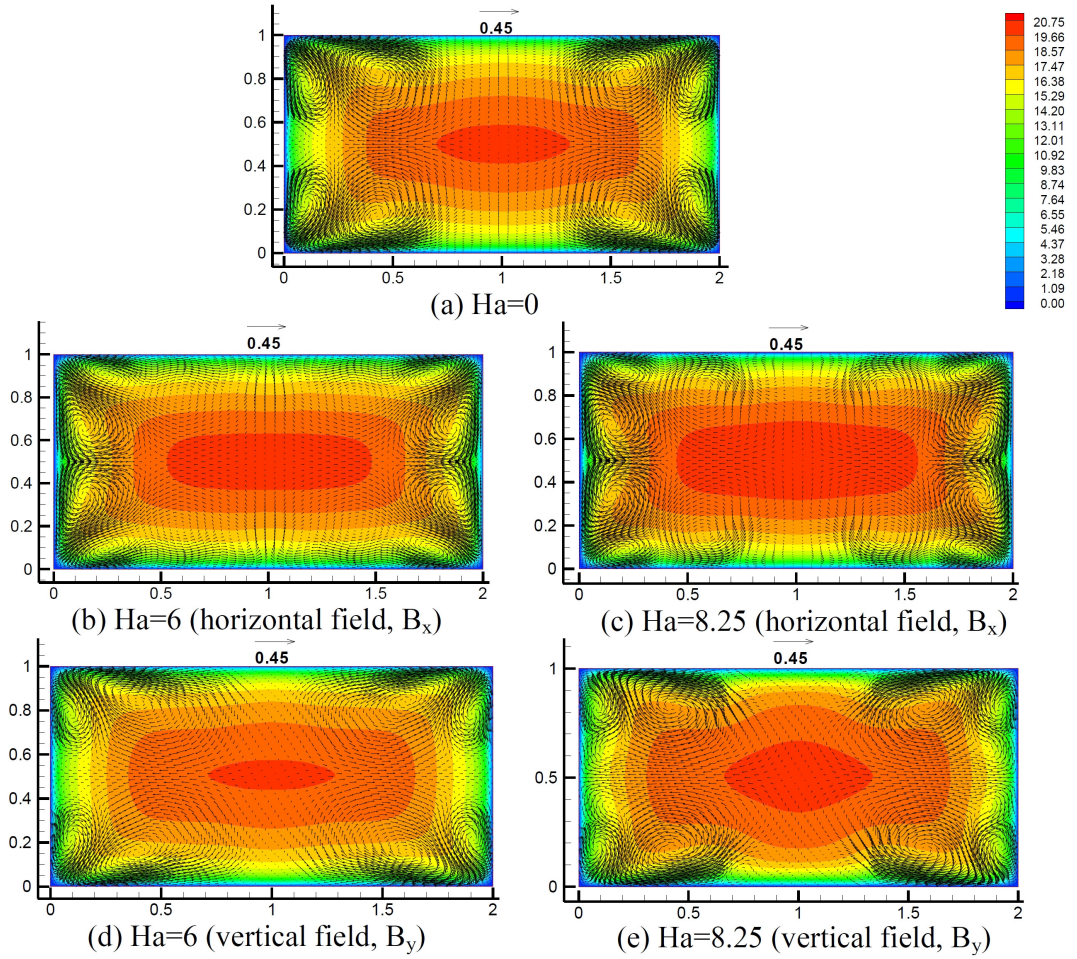

(a) Ha=0

(b) Ha=6 (horizontal field, B_x)

(c) Ha=8.25 (horizontal field, B_x)

(d) Ha=6 (vertical field, B_y)

(e) Ha=8.25 (vertical field, B_y)

Figure 3.3. Time/ensemble-averaged axial velocity contours and secondary velocity vectors (some vectors are skipped for clarity)

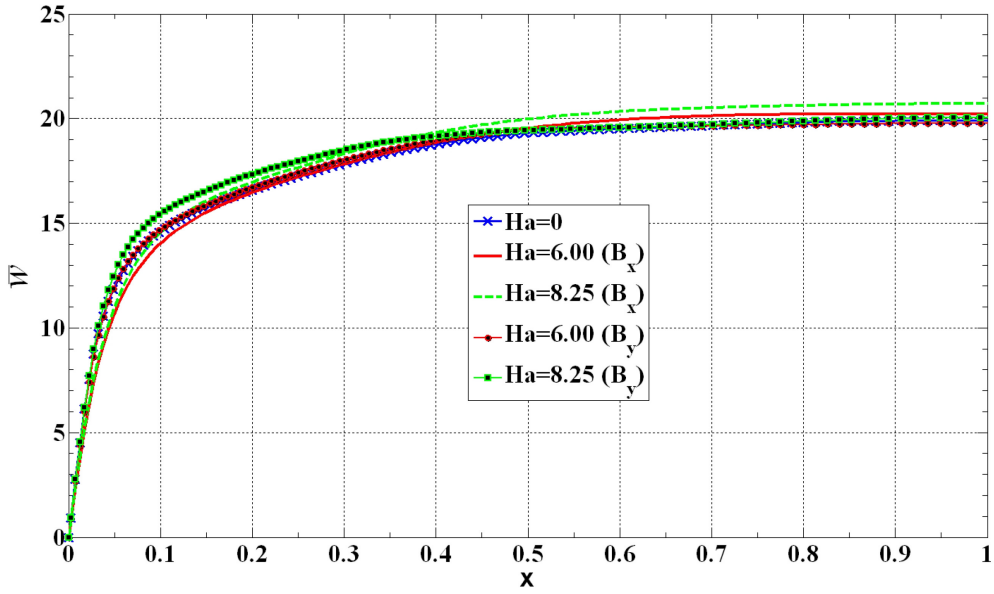

Figure 3.4(a) Time-averaged axial velocity ($\overline{w}$) along horizontal (x-) bisector

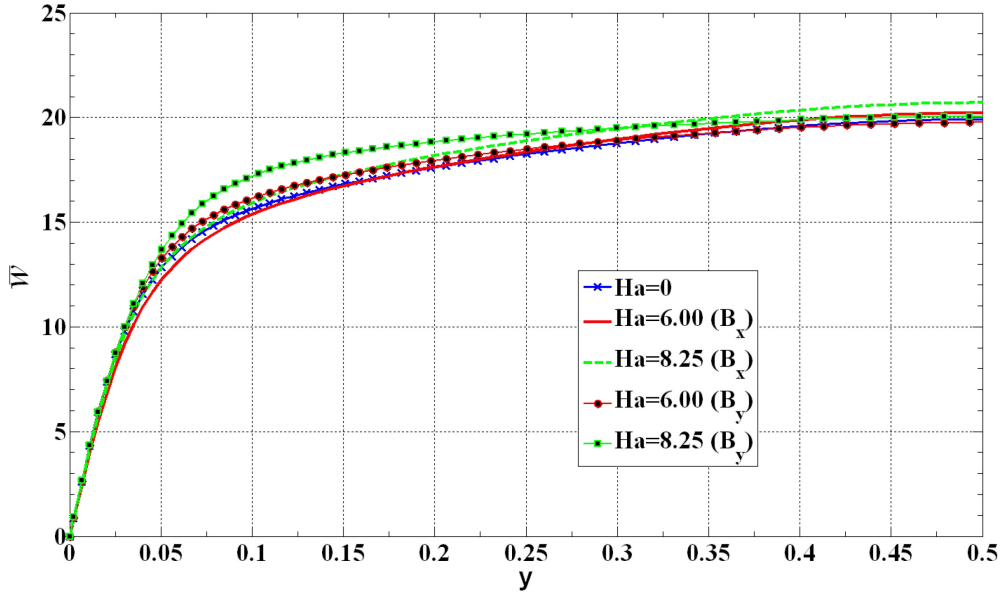

Figure 3.4(b) Time-averaged axial velocity ($\overline{w}$) along vertical (y-) bisector

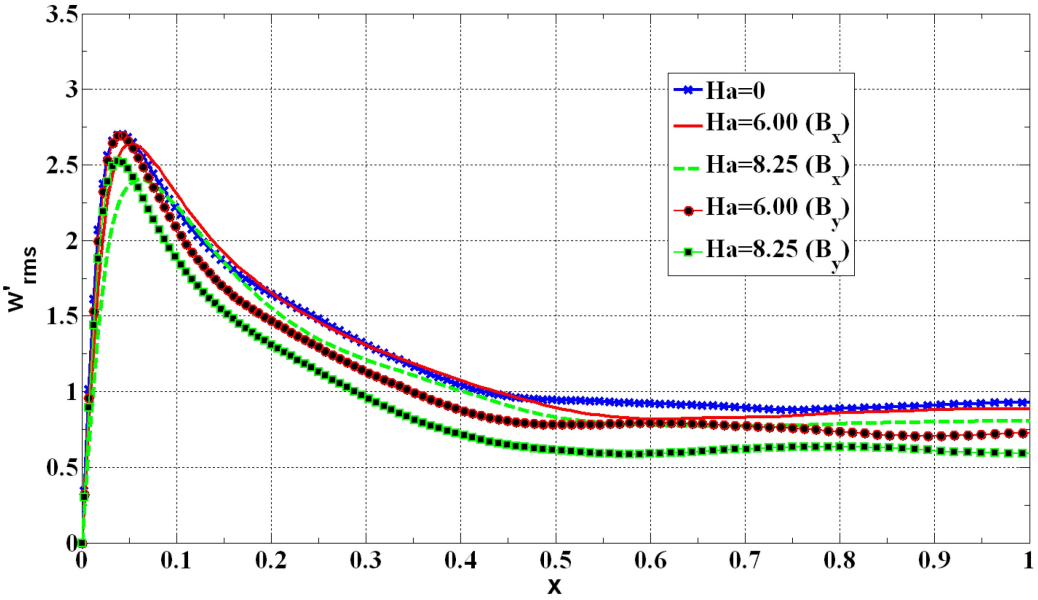

Figure 3.5(a) RMS of axial velocity fluctuations along horizontal (x-) bisector

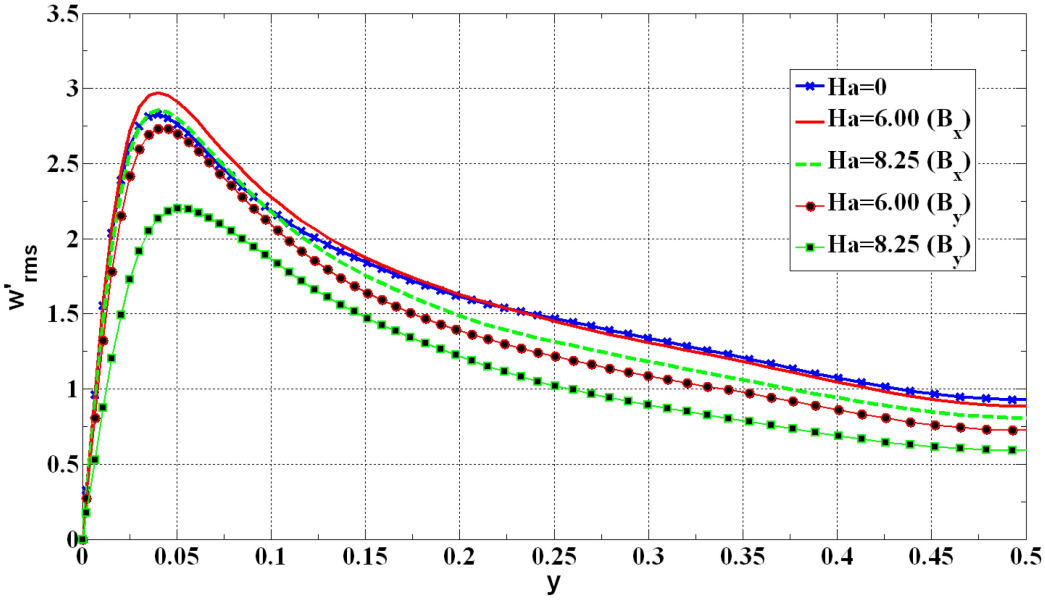

Figure 3.5(b) RMS of axial velocity fluctuations along vertical (y-) bisector

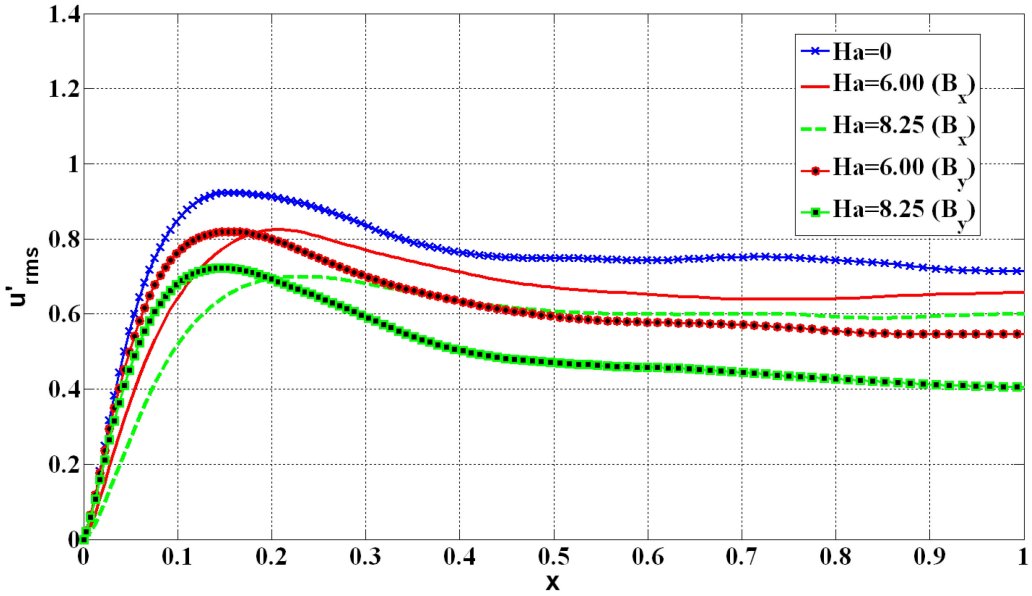

Figure 3.6(a) RMS of horizontal velocity fluctuations along horizontal (x-) bisector

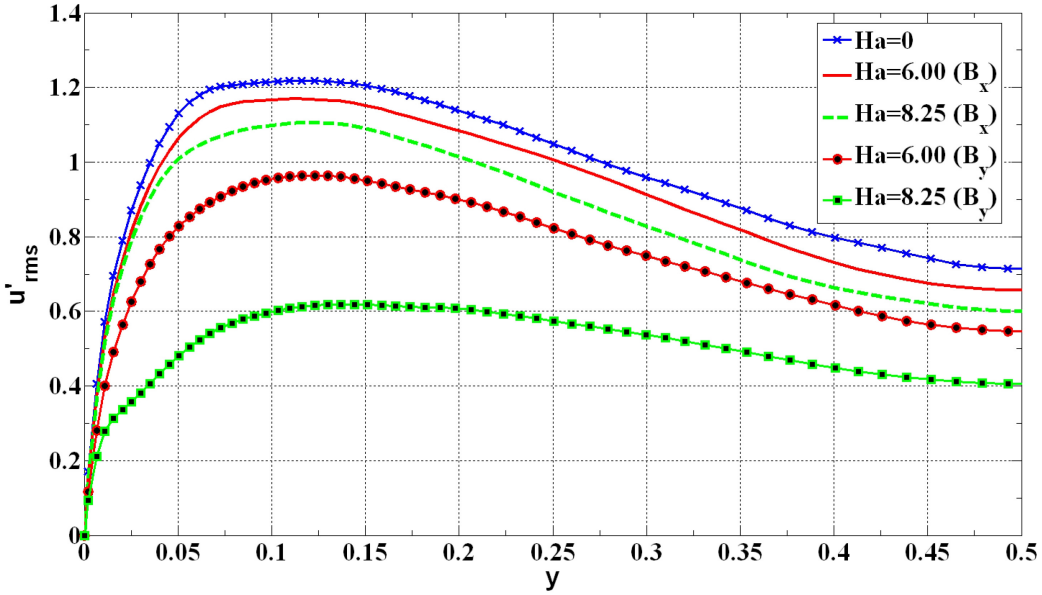

Figure 3.6(b) RMS of horizontal velocity fluctuations along vertical (y-) bisector

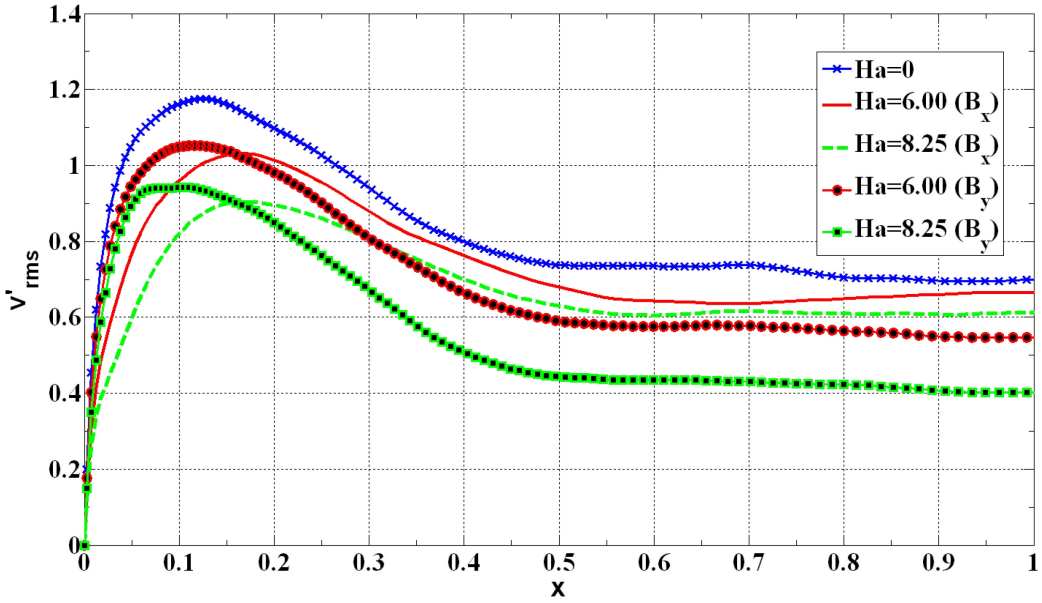

Figure 3.7(a) RMS of vertical velocity fluctuations along horizontal (x-) bisector

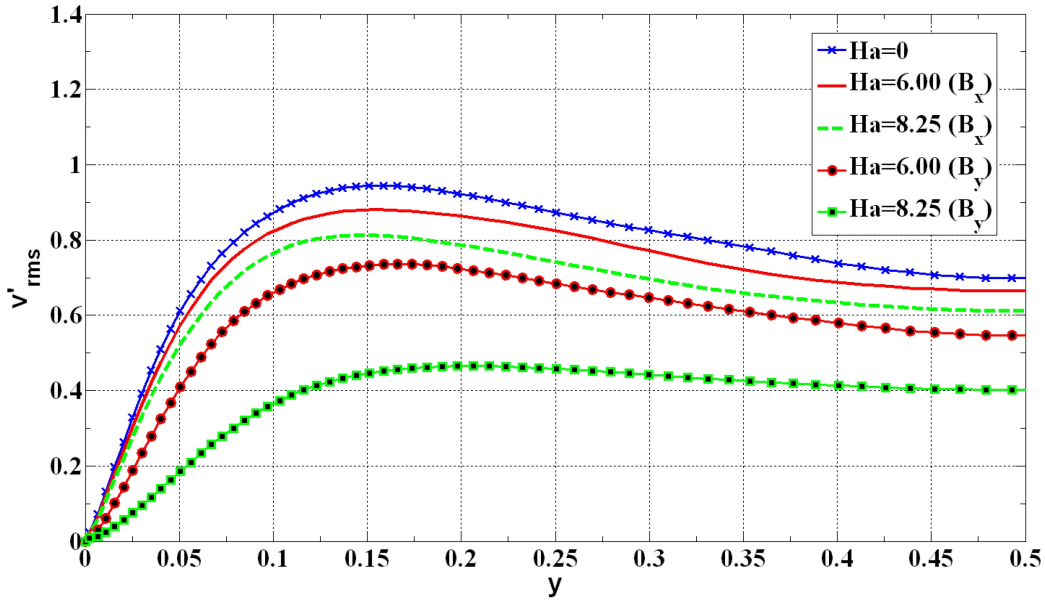

Figure 3.7(b) RMS of vertical velocity fluctuations along vertical (y-) bisector

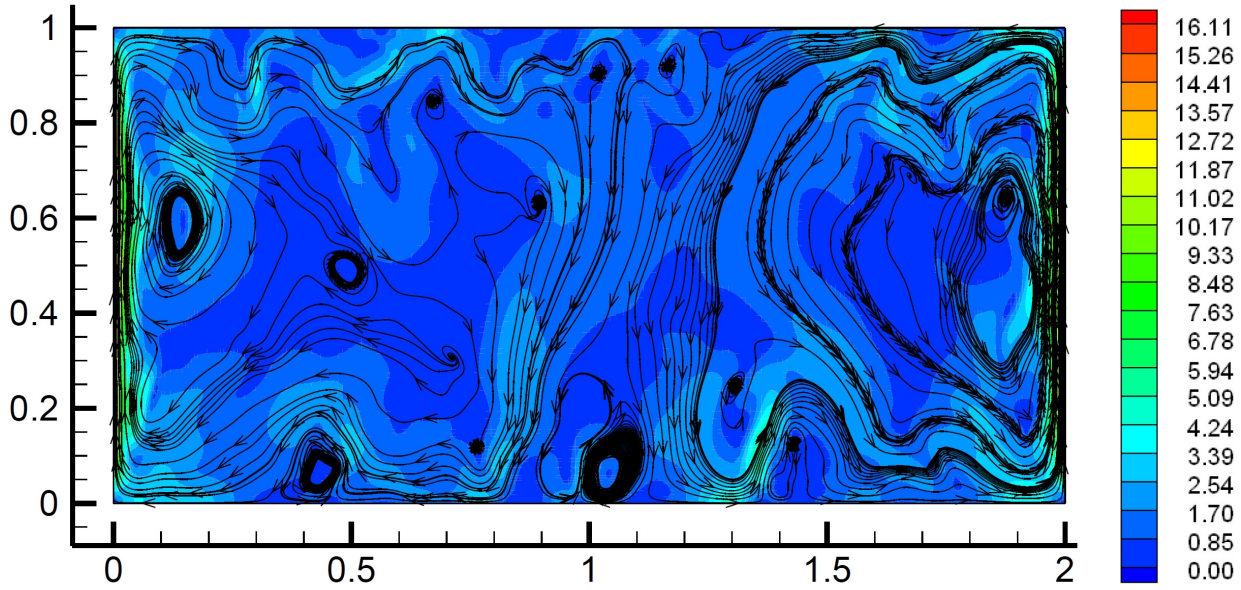

(c) Horizontal field, B_x (max value: 15.36)

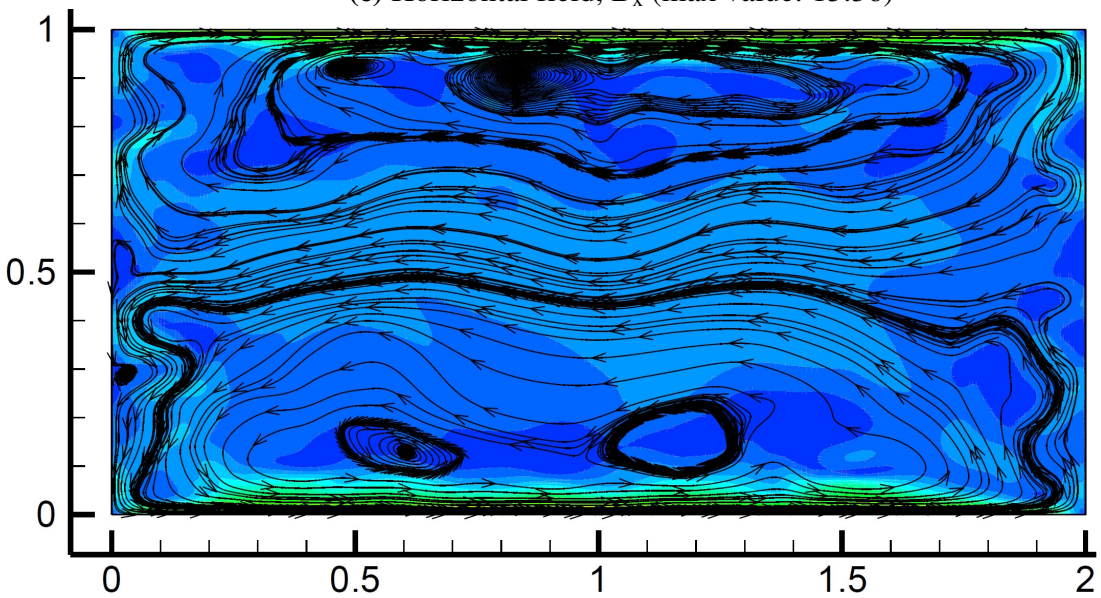

(d) Vertical field, B_y (max value:16.11)

Figure 3.7(c) & (d) Current density contours and lines at a cross-section with Ha=8.25

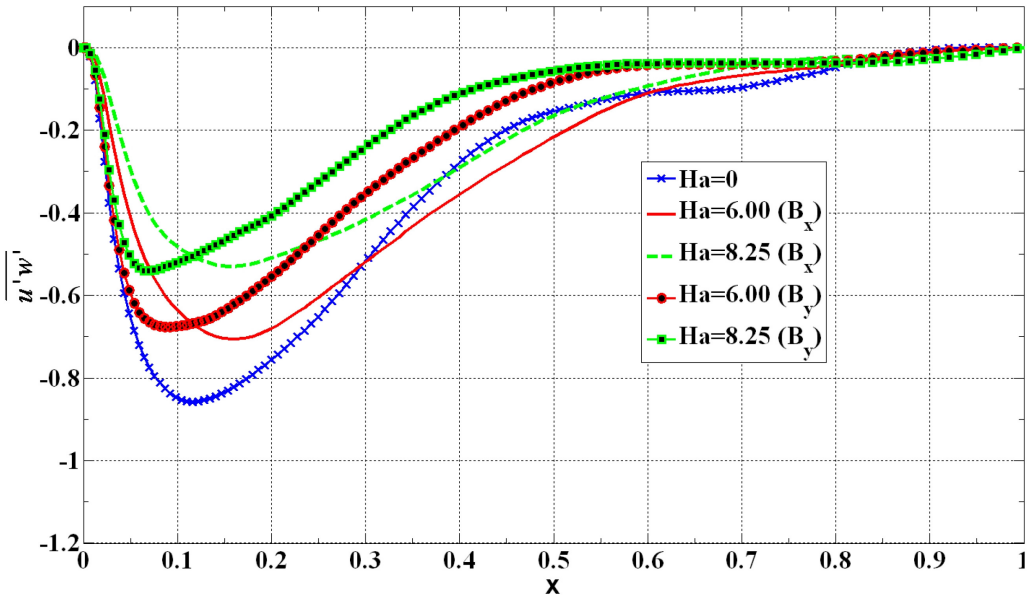

Figure 3.8(a) Reynolds shear stress ($\overline{u'w'}$) along horizontal (x-) bisector

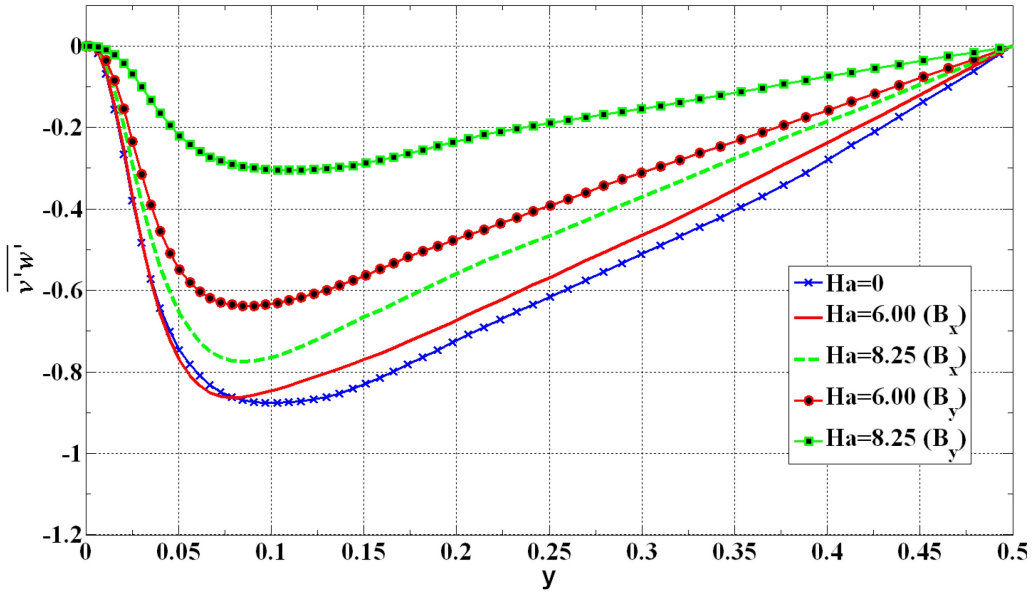

Figure 3.8(b) Reynolds shear stress ($\overline{v'w'}$) along vertical (y-) bisector

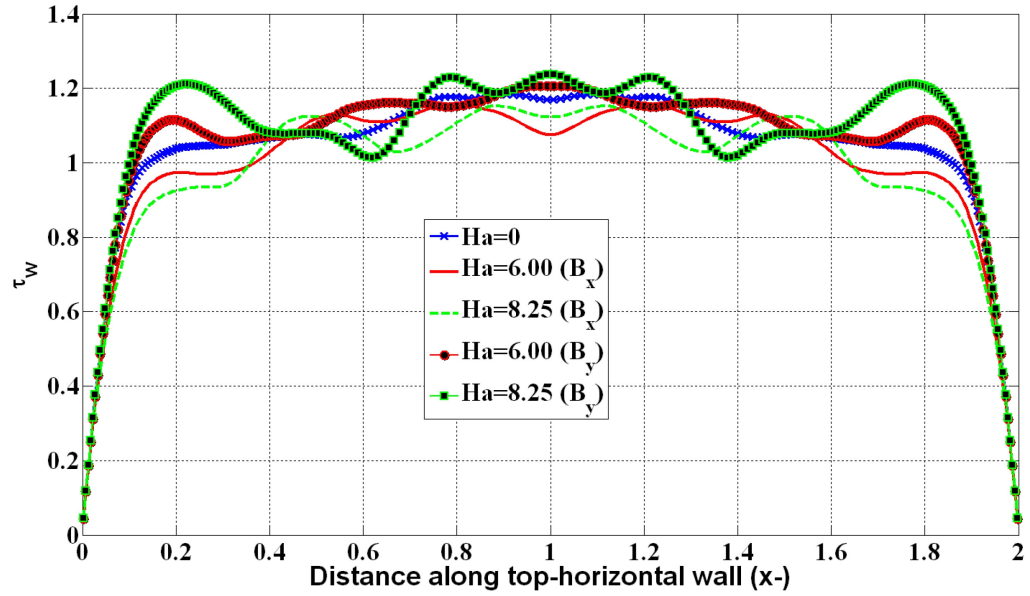

Figure 3.9(a) Wall stress along top-horizontal wall

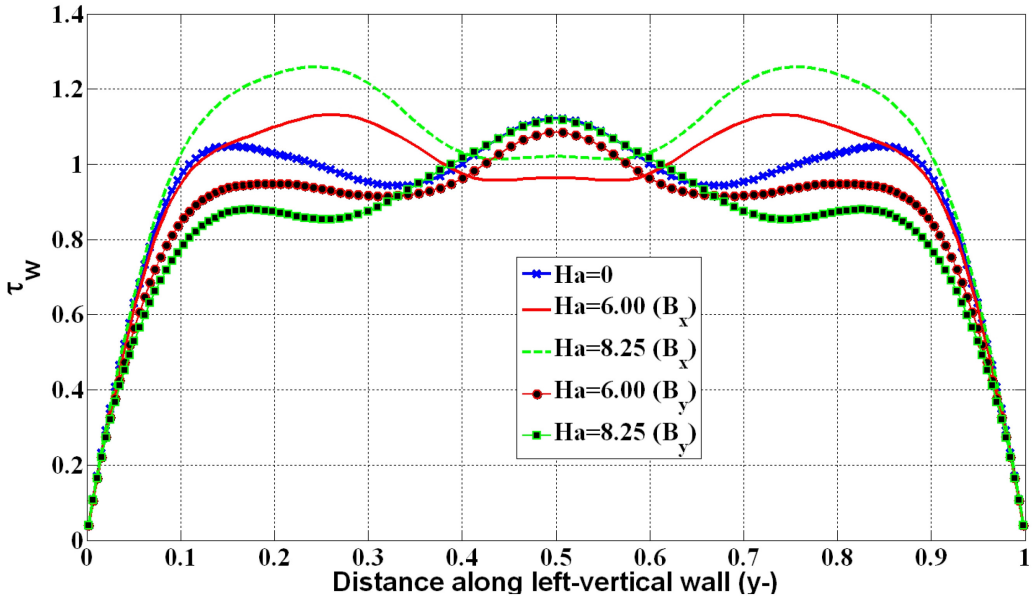

Figure 3.9(b) Wall stress along left-vertical wall

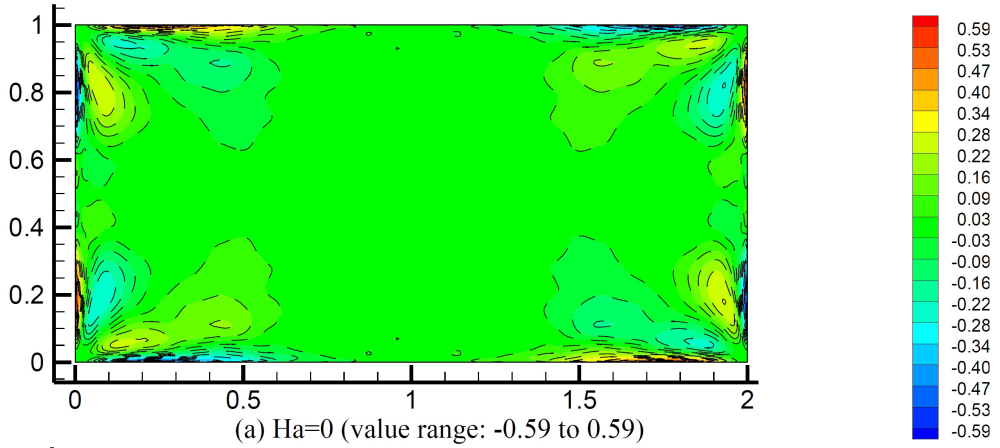

(a) Ha=0 (value range: -0.59 to 0.59)

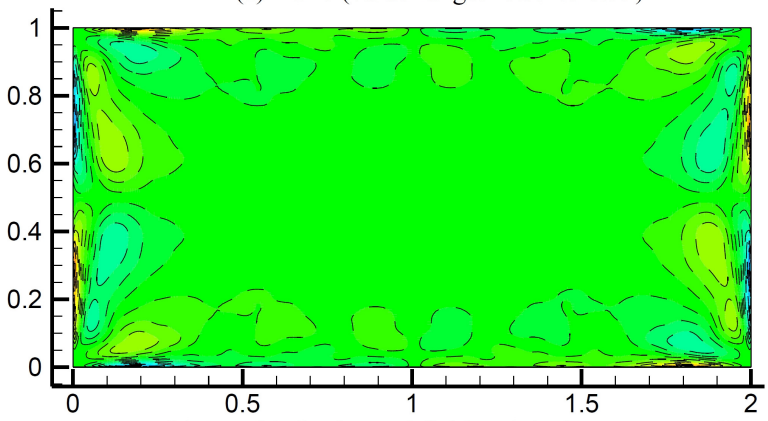

(b) Ha=6.0 (horizontal field, B_x) (value range: -0.49 to 0.49)

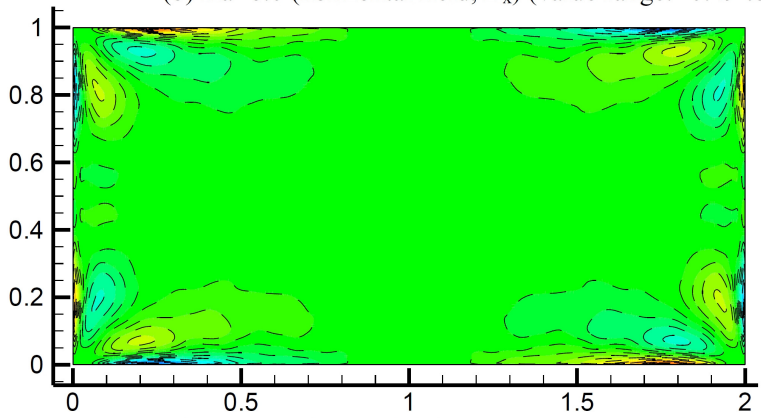

(c) Ha=6.0 (vertical field, B_y) (value range: -0.53 to 0.53)

Figure 3.10 Mean streamwise vorticity ($\overline{\Omega}_z = \left(\frac{\partial \overline{v}}{\partial x} - \frac{\partial \overline{u}}{\partial y} \right)$) contours

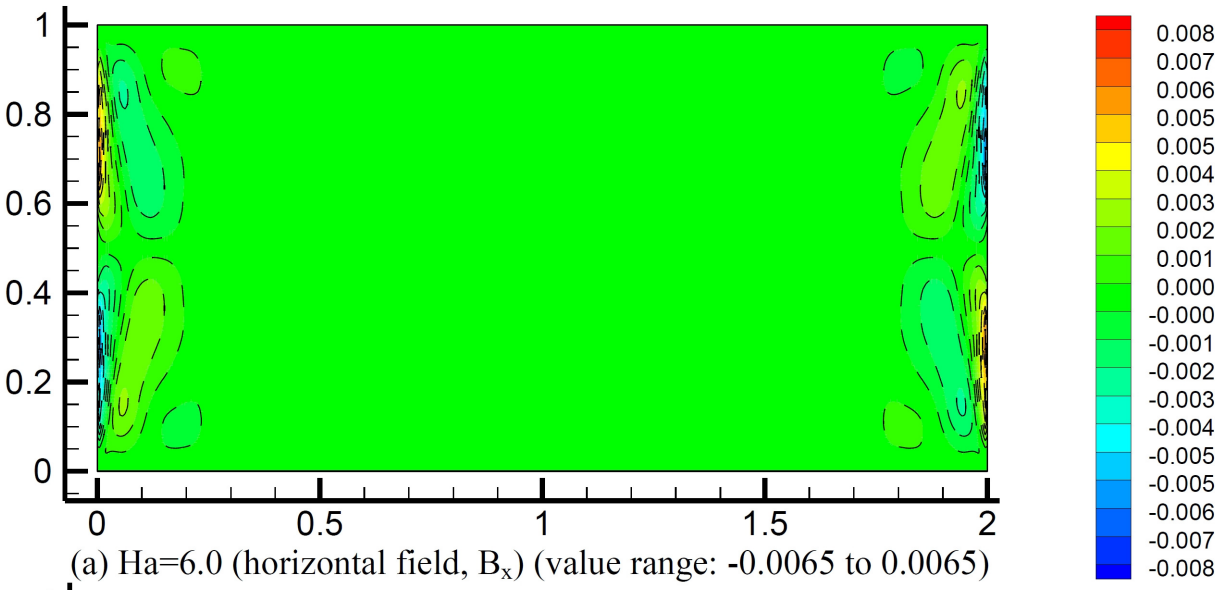

(a) Ha=6.0 (horizontal field, B_x) (value range: -0.0065 to 0.0065)

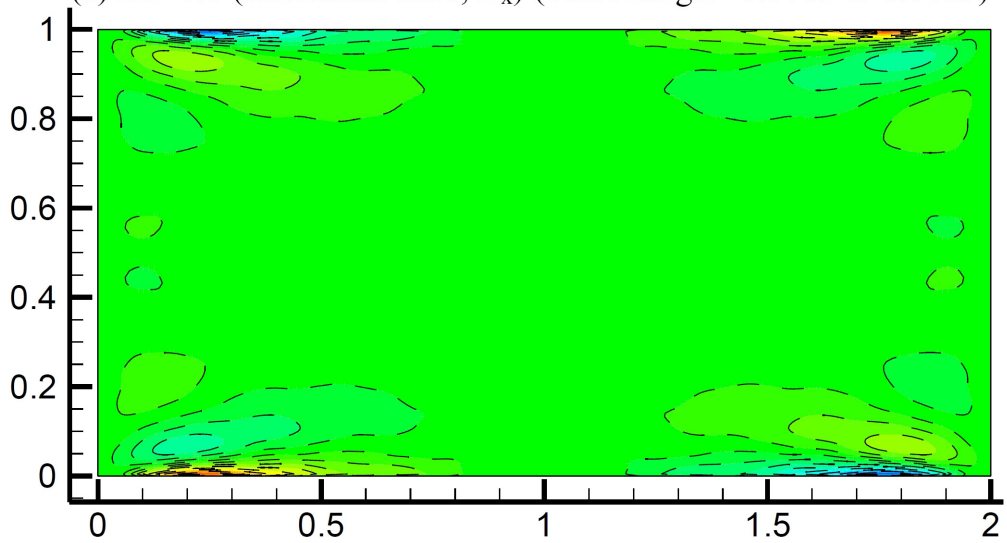

(b) Ha=6.0 (vertical field, B_y) (value range: -0.0072 to 0.0072)

Figure 3.11 MHD sink ($-\frac{\mathrm{Ha}^2}{\mathrm{Re}}\left(\frac{\partial \bar{v}}{\partial x}B_{x0}^2\right)$ and $\frac{\mathrm{Ha}^2}{\mathrm{Re}}\left(\frac{\partial \bar{u}}{\partial y}B_{0y}^2\right)$) to mean streamwise vorticity ($\bar{\Omega}_z = \left(\frac{\partial \bar{v}}{\partial x} - \frac{\partial \bar{u}}{\partial y}\right)$)

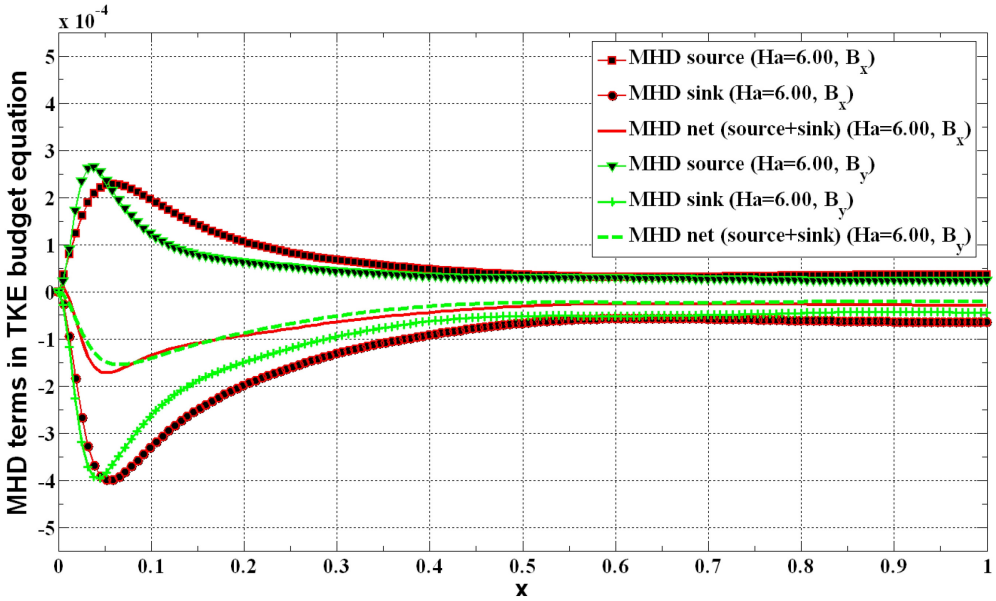

Figure 3.12(a) MHD source/sink terms in TKE budget equation along horizontal (x-) bisector

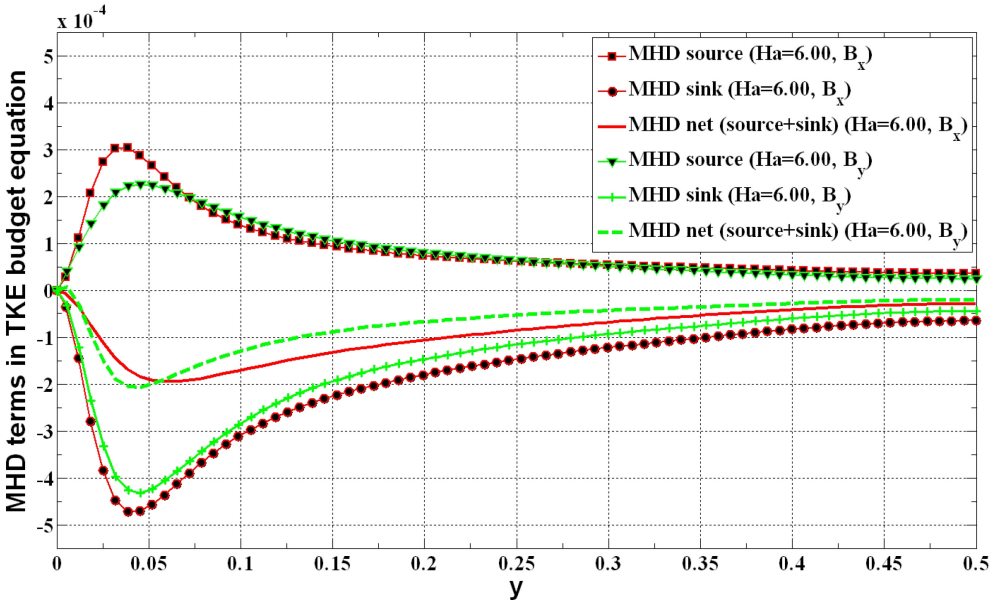

Figure 3.12(b) MHD source/sink terms in TKE budget equation along vertical (y-) bisector

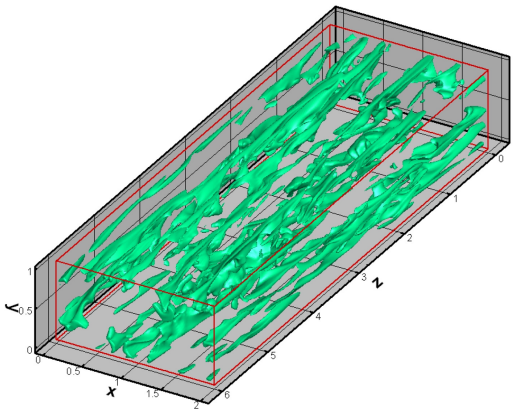

(a) Ha=0

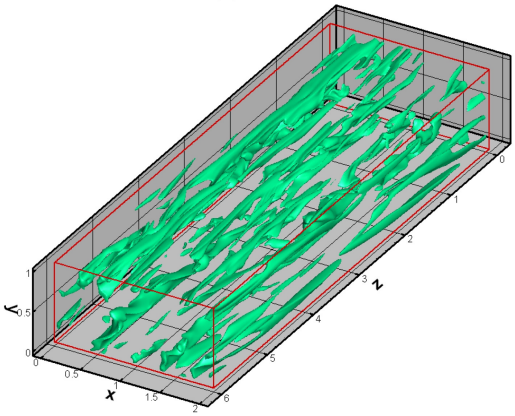

(b) Ha=8.25 (horizontal field, B_x)

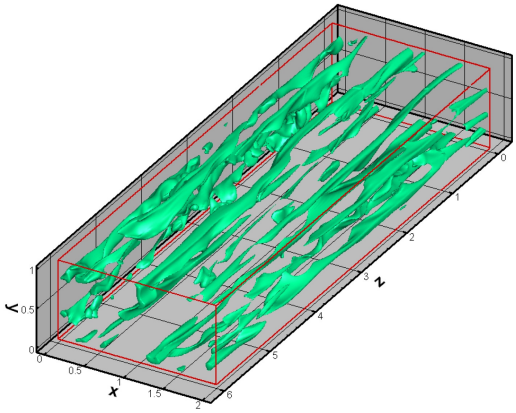

(c) Ha=8.25 (vertical field, B_y)

Figure 3.13 Low-speed streaks ($u'^{+} < -3$)

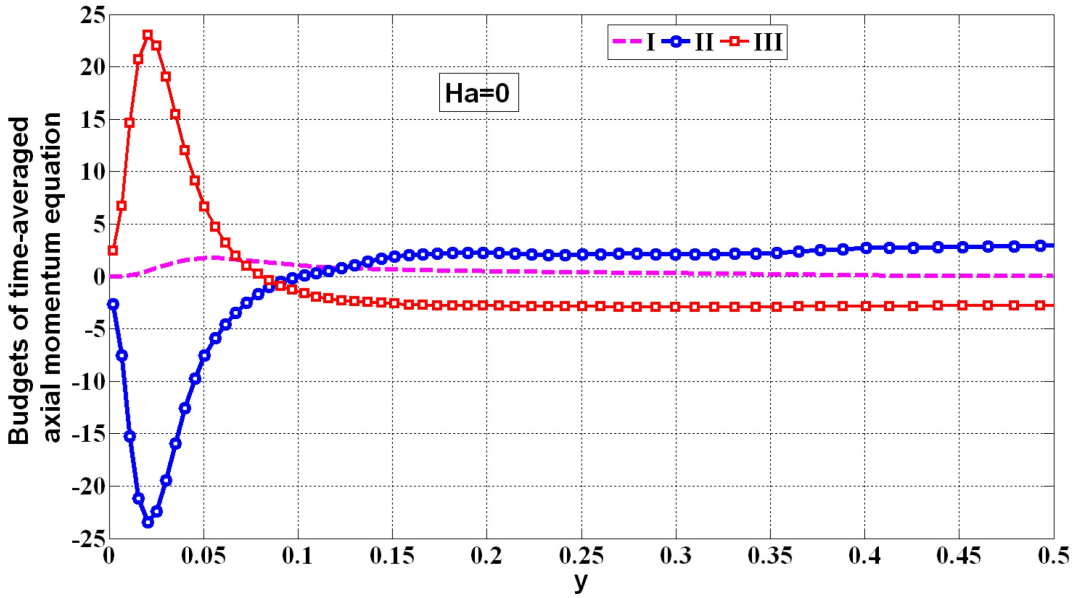

Figure 3.14(a) Various budget terms of time averaged axial momentum equation along vertical (y-) bisector in non-MHD 2:1 aspect duct

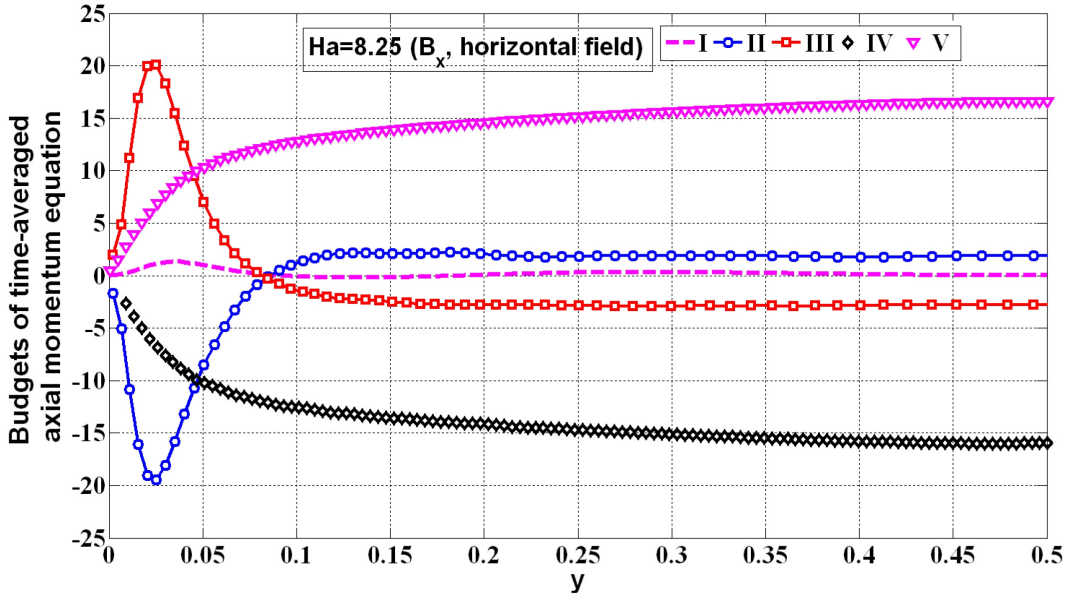

Figure 3.14(b) Various budget terms of time averaged axial momentum equation along vertical (y-) bisector in MHD (Ha=8.25, B_x (horizontal field)) 2:1 aspect duct

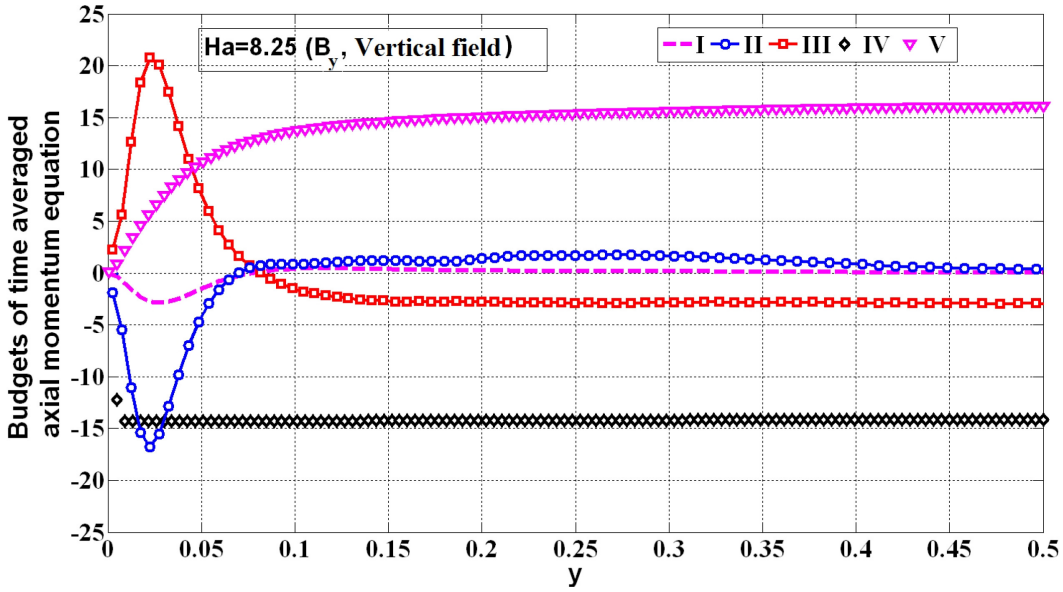

Figure 3.14(c) Various budget terms of time averaged axial momentum equation along vertical (y-) bisector in MHD (Ha=8.25, B_y (vertical field)) 2:1 aspect duct

3.8. References

1. P. A. Davidson, Magnetohydrodynamics in materials processing, Ann. Rev. Fluid Mech., 1999, 31, pp.273–300.
2. B. G. Thomas and Lifeng Zhang, Mathematical modeling of fluid flow in continuous casting: a review, ISIJ International, 2001, 41, 10, pp.1181-1193.
3. R. Moreau, Magnetohydrodynamics., Kluwer Academic Publishers, Boston, 1990.
4. B. Knaepen and R. Moreau, Magnetohydrodynamic turbulence at low magnetic Reynolds number, Ann. Rev. Fluid Mech., 2008, 40, pp. 25-45.
5. R. Chaudhary, S.P. Vanka and B.G. Thomas, Direct numerical simulations of magnetic field effects on turbulent flow in a square duct, Phys. of Fluids, 22, 075102, 2010.
6. A. F. Shinn, S. P. Vanka, and W. W. Hwu, Direct numerical simulation of turbulent flow in a square duct using a graphics processing unit (GPU), AIAA-2010-5029, 40th AIAA Fluid Dynamics Conference, June 2010.
7. R. Chaudhary, B.G. Thomas and S.P. Vanka, Evaluation of turbulence models in MHD channel and square duct flows, CCC report, 201011, Department of Mechanical Science & Engineering, University of Illinois at Urbana-Champaign, IL, USA.
8. H. Xu, Direct numerical simulation of turbulence in a square annular duct, J. Fluid Mech., 2009, 621, pp. 23-57.
9. S. Gavrilakis, Numerical simulation of low Reynolds number turbulent flow through a straight square duct, J. Fluid Mech., 1992, 244, pp. 101-129.
10. R. K. Madabhushi and S. P. Vanka, Large eddy simulation of turbulence driven secondary flow in a square duct, Phys. Fluid A, 1991, 3, pp. 2734-2745.

11. R. K. Madabhushi and S. P. Vanka, Direct numerical simulation of turbulent flow in a square duct at low Reynolds number, in *Near-Wall Turbulent Flows*, edited by R. M. C. So, C. G. Speziale, and B. E. Launder, Elsevier, New York, 1993, pp. 297–306.

12. A. Huser, and S. Biringen, Direct numerical simulation of turbulent flow in a square duct, J. Fluid. Mech., 1993, 257, pp. 65-95.

13. D. Lee and H. Choi, Magnetohydrodynamic turbulent flow in a channel at low magnetic Reynolds number, J. Fluid Mech., 2001, 439, pp. 367–394.

14. H. Kobayashi, Large eddy simulation of magnetohydrodynamic turbulent channel flows with local subgrid-scale model based on coherent structures, Phys. Fluids, 2006, 18, 4, pp. 45107-1-11.

15. S. Satake, T. Kunugi, T. Kazuyuki and O. Yasuo, Direct numerical simulation of turbulent channel flow under a uniform magnetic field for large-scale structures at high Reynolds number, Phys. Fluids, 18, 125106, 2006.

16. T. Boeck, D. Krasnov and E. Zienicke, Numerical study of turbulent magnetohydrodynamic channel flow, J. Fluid Mech., 2007, 572, pp. 179-188.

17. H. Noguchi, and N. Kasagi, Direct numerical simulation of liquid metal MHD turbulent channel flows, (in Japanese), Preprint of JSME, No. 940-53, Nov. 1994, pp. 365-366.

18. D. Krasnov, O. Zikanov, J. Schumacher, and T. Boeck, Magnetohydrodynamic turbulence in a channel with spanwise magnetic field, Phys. Fluids, 20, 095105 (2008).

19. E. C. Brouillette and P. S. Lykoudis, Magneto-fluid-mechanic channel flow. I. Experiment, Phys. Fluids, 1967, 10, pp. 995-1001.

20. C. B. Reed and P. S. Lykoudis, The effect of a transverse magnetic field on shear turbulence, J. Fluid Mech., 1978, 89, pp. 147-171.

21. S. Satake, T. Kunugi and S. Smolentsev, Direct numerical simulations of turbulent pipe flow in a transverse magnetic field, J. of Turbulence, 2002, 3, 020.

22. H. Kobayashi, Large eddy simulation of magnetohydrodynamic turbulent duct flows, Phys. Fluids, 2008, 20, 4, pp 015102-1-13.

23. Shatrov and Gerbeth, Marginal turbulent magnetohydrodynamic flow in a square duct, Phys. of Fluids, 22, 084101, 2010.

24. F. Harlow and E. Welch., Numerical calculation of time-dependent viscous incompressible flow of fluid with free surface, Phys. of Fluids, 1965, 8, pp. 2182-2189.

CHAPTER 4. EVALUATION OF TURBULENCE MODELS IN MHD CHANNEL AND SQUARE DUCT FLOWS

4.1. Introduction

Reynolds-Averaged Navier-Stokes (RANS) simulations are widely used to optimize various industrial flows because of their low computational cost. However, it is well-known that their accuracy in complex flows is limited by the difficulties in modeling the complex turbulence interactions through transport equations for the mean flow variables [1]. Significant effort has already been devoted to validation, improvement, and custom tailoring of these models of turbulent flows for different classes of flows [2-8]. This is usually done through comparisons with experimental data. However, with the availability of Direct Numerical Simulation (DNS) and Large Eddy Simulation (LES) computed flow fields, it has also become possible to evaluate the turbulence models using DNS / LES data [2, 9-11].

Despite the importance of magnetic fields in material processing, very limited work [12-15] exists on improving and testing turbulence models to include the effects of a magnetic field on the turbulence. A few modified models with magnetic field effects have been tested in channel flow/rectangular duct flow with a partial magnetic field (low-Re k-ε and Reynolds stress model (RSM)) [12-13], pipe flow (low-Re k-ε) [14] and free surface channel flow (k-ε) [15]. The modifications proposed in the latter two of these studies (pipe flow [14] and free surface channel flow [15]) were based upon bulk properties of the flow and cannot be generalized to other flows. The first two studies (k-ε and RSM, [12-13]) relate the magnetic field generated source terms in the turbulent transport equations to the local properties, and therefore can be generalized to other flows. However, these models have been so far tested only in a turbulent channel flow and in a rectangular duct with a partial magnetic field. For the rectangular duct with a partial magnetic

field only the mean velocity was compared. The mean velocity obtained with this model was reported to show better agreement with measurements but no comparisons are available for turbulence quantities [12].

The present work reports a systematic assessment of a number of turbulence models, and their variants, for magnetohydrodynamic (MHD) flow in two representative geometries: a) channel flow, and b) a square duct flow. Confined internal flows through long pipes and ducts are relevant in many commercial flows. The square duct flow is more complicated to predict because of the turbulence-driven secondary flows [16]. The various models considered are: a) 3 variants of high-Re two-equation models (Standard k-ε (SKE) [17], RNG k-ε (RNG) [18], Realizable k-ε (RKE) [19], b) 6 low-Re k-ε models (Abid [20], Lam-Bremhorst (LB) [21], Launder-Sharma (LS) [22], Yang-Shih (YS) [23], Abe-Kondoh-Nagano (AKN) [24], and Chang-Hsieh-Chen (CHC) [25-26]) and c) 2 second-momentum closure Reynolds Stress Models with Linear Pressure Strain (RSM-LPS) and Stress-Omega (RSM-Sω) [27-31]) models along with standard wall functions (SWF) [32], non-equilibrium wall functions (NEWF) [33], or two-layer wall treatment combined with single-blended wall function (enhanced wall treatment or EWT) [34-35, 30]. The simulations have been performed using FLUENT [30] and the effect of magnetic field on turbulence, as given by Kenjereš and Hanjalić [12-13], has been incorporated through additional source terms using user-defined functions (UDF). Mean velocities, turbulent kinetic energy (TKE), root mean square (RMS) of velocity fluctuations, MHD sources/sinks and frictional losses are compared against available DNS data in channel and square duct flows.

4.2. Turbulence Models Tested

The ensemble averaged continuity and Navier-Stokes equations are solved [36-37]:

$$\frac{\partial \overline{u}_i}{\partial x_i} = 0$$

$$\frac{\partial \overline{u}_i}{\partial t}+\frac{\partial \overline{u}_i \overline{u}_j}{\partial x_j}=-\frac{1}{\rho}\frac{\partial \overline{p}}{\partial x_i}+\frac{\partial}{\partial x_j}\left(\nu\frac{\partial \overline{u}_i}{\partial x_j}\right)+\frac{\partial R_{ij}}{\partial x_j}+\overline{F}_L \tag{4.1}$$

where, $R_{ij}=-\overline{u_i' u_j'}$: Reynolds Stresses, and $\overline{F}_L$ is the average Lorentz force due to magnetic field. The k-ε models use the Boussinesq hypothesis for Reynolds stresses (i.e. $R_{ij}=-\overline{u_i' u_j'}=\nu_t\left(\frac{\partial \overline{u}_i}{\partial x_j}+\frac{\partial \overline{u}_j}{\partial x_i}\right)-\frac{2}{3}k\delta_{ij}$). The base equations for the two equation k-ε models are:

$$\frac{\partial \rho k}{\partial t}+\frac{\partial}{\partial x_k}\left(\rho \overline{u}_k k\right)=\frac{\partial}{\partial x_j}\left[\left(A\right)\frac{\partial k}{\partial x_j}\right]+G_k-\rho\varepsilon+\rho D \tag{4.2}$$

$$\frac{\partial \rho \varepsilon}{\partial t}+\frac{\partial}{\partial x_k}\left(\rho \overline{u}_k \varepsilon\right)=\frac{\partial}{\partial x_j}\left[\left(B\right)\frac{\partial \varepsilon}{\partial x_j}\right]+C+\rho E \tag{4.3}$$

Where, $k=\overline{u_i' u_i'}/2$, $\varepsilon=\nu\overline{\frac{\partial u_i'}{\partial x_j}\frac{\partial u_i'}{\partial x_j}}$, and $G_k=-\rho\overline{u_i' u_j'}\frac{\partial \overline{u}_j}{\partial x_i}$

After defining A, B, C, D and E in the above equations for each k-ε model and the basic equations for RSM, modifications for the presence of a magnetic field are described.

4.2.1. Standard k-ε Model (SKE)

In this classic model [17], A, B, C, D and E in Eqs. 4.2-4.3 are given as follows;

$$A=\mu+\frac{\mu_t}{\sigma_k},\ B=\mu+\frac{\mu_t}{\sigma_\varepsilon},\ C=C_{\varepsilon 1}\frac{\varepsilon}{k}G_k-\rho C_{\varepsilon 2}\frac{\varepsilon^2}{k},\ D=0,\ E=0 \tag{4.4}$$

$\mu_t=\rho C_\mu k^2/\varepsilon$, $C_\mu=0.09$, $C_{\varepsilon 1}=1.44$, $C_{\varepsilon 2}=1.92$, $\sigma_k=1.0$, $\sigma_\varepsilon=1.3$,.

4.2.2. RNG k-ε Model (RNG)

The RNG k-ε turbulence model [18] includes an additional term (R_ε) in the ε equation, and uses different turbulent Prandtl numbers, so A, B, C, D and E in this model are as follows:

$$A=\alpha_k\mu_{eff}\,,B=\alpha_\varepsilon\mu_{eff}\,,\ C=C_{\varepsilon1}\frac{\varepsilon}{k}G_k-\rho C_{\varepsilon2}\frac{\varepsilon^2}{k}-R_\varepsilon\,,\ D=0\,,\ E=0 \tag{4.5}$$

where, $\mu_{eff}=\mu+\mu_t$, $C_{\varepsilon1}=1.42,\quad C_{\varepsilon2}=1.68$.

The inverse Prandtl numbers (α_k and α_ε) are calculated using formula derived from RNG theory,

$$\left|\left(\alpha-1.3929\right)/\left(\alpha_o-1.3929\right)\right|^{0.6321}\left|\left(\alpha+2.3929\right)/\left(\alpha_o+2.3929\right)\right|^{0.3679}=\mu/\mu_{eff}\,,\ \alpha_o=1 \tag{4.6}$$

The additional term (R_ε) is defined as, $R_\varepsilon=\dfrac{C_\mu\rho\eta^3\left(1-\eta/\eta_0\right)}{1+\beta\eta^3}\dfrac{\varepsilon^2}{k}\,,\ \eta=\dfrac{Sk}{\varepsilon}$ (4.7)

$$S=\sqrt{2s_{i,j}s_{i,j}}\,,\ s_{i,j}=\frac{1}{2}\left(\frac{\partial\overline{u}_i}{\partial x_j}+\frac{\partial\overline{u}_j}{\partial x_i}\right),\ \eta_0=4.38,\beta=0.012$$

The differential formulation for effective viscosity for low-Re effects is defined as;

$$d\left(\left(\rho^2k\right)/\left(\sqrt{\varepsilon\mu}\right)\right)=1.72\left(\hat{\nu}/\sqrt{\hat{\nu}^3-1+C_\nu}\right)d\hat{\nu}\text{, where, }\hat{\nu}=\mu_{eff}/\mu\text{ and }C_\nu=100 \tag{4.8}$$

This equation can be integrated for $\hat{\nu}$ and the integration constant can be calculated under the condition that $\hat{\nu}=1,\text{when }k=0$.

4.2.3. Realizable k-ε Model (RKE)

The RKE [19] has a realizable formulation to ensure positive normal Reynolds stresses and satisfy Schwarz inequality ($\overline{u'_a u'_b}^2\le\overline{u'^2_a}\,\overline{u'^2_b}$) in highly strained flows. This model has C_μ sensitized to the mean flow, k and ε. The new dissipation rate (ε) equation is derived from the exact mean-square vorticity fluctuation equation ($\varepsilon=\nu\overline{\omega_i\omega_i}$, $\omega_i=\partial u'_k/\partial x_j-\partial u'_j/\partial x_k$). The equations for $A,\ B,\ C,\ D$ and E in this model are as follows:

$$A=\mu+\frac{\mu_t}{\sigma_k}\,,\ B=\mu+\frac{\mu_t}{\sigma_\varepsilon}\,,\ C=\rho C_1S\varepsilon-\rho C_2\frac{\varepsilon^2}{k+\sqrt{\nu\varepsilon}}\,,\ D=0\,,\ E=0 \tag{4.9}$$

$C_2=1.9,\quad \sigma_k=1.0,\quad \sigma_\varepsilon=1.2\,,\ C_1=\max\left(0.43,\eta/\left(\eta+5\right)\right),\ \mu_t=\rho C_\mu k^2/\varepsilon$

$C_\mu = 1/\left(A_0 + A_s\left(kU^*/\varepsilon\right)\right)$, where $U^* = \sqrt{s_{i,j}s_{i,j} + \tilde{\Omega}_{i,j}\tilde{\Omega}_{i,j}}$, $\tilde{\Omega}_{i,j} = \Omega_{i,j} - 2\varepsilon_{ijk}\omega_k$ (4.10)

, $\bar{\Omega}_{i,j} = \frac{1}{2}\left(\frac{\partial \bar{u}_i}{\partial x_j} - \frac{\partial \bar{u}_j}{\partial x_i}\right)$, $\varepsilon_{ijk} = \begin{cases} 1 & \text{if(i, j, k) are cyclic} \\ -1 & \text{if(i, j, k) are anticyclic} \\ 0 & \text{otherwise} \end{cases}$

with constants $A_0 = 4.04$ and $A_s = \sqrt{6}\cos(\phi)$, $\phi = \frac{1}{3}\cos^{-1}\left(\sqrt{6}W\right)$, $W = \frac{s_{i,j}s_{j,k}s_{k,i}}{\tilde{S}^3}$, $\tilde{S} = \sqrt{s_{i,j}s_{i,j}}$

4.2.4. Low-Re k-ε Models

Six low-Re k-ε models [20-26] have been tested in the present work, with *A*, *B*, and *C* defined in all of these models as follows:

$$A = \mu + \frac{\mu_t}{\sigma_k},\ \mu + \frac{\mu_t}{\sigma_\varepsilon},\ C = f_1 C_1 \frac{\varepsilon}{k} G_k - \rho f_2 C_2 \frac{\varepsilon^2}{k},\ \text{and}\ \mu_t = \rho f_\mu C_\mu k^2/\varepsilon \quad (4.11)$$

The values of *D* and *E*, damping functions, wall boundary conditions and various constant for the different low-Re k-ε models are given in Table 4.1 and Table 4.2.

4.2.5. Reynolds Stress Model (RSM)

The exact transport equation for the six independent Reynolds stresses ($\overline{u_i'u_j'}$) in RSM can be written as [27-31]:

$$\frac{\partial}{\partial t}\left(\rho\overline{u_i'u_j'}\right) + \frac{\partial}{\partial x_k}\left(\rho \bar{u}_k \overline{u_i'u_j'}\right) = P_{ij} + D_{ij}^L + D_{ij}^T + \phi_{ij} - \varepsilon_{ij} \quad (4.12)$$

$P_{ij} = -\rho\left(\overline{u_i'u_k'}\frac{\partial \bar{u}_j}{\partial x_k} + \overline{u_j'u_k'}\frac{\partial \bar{u}_i}{\partial x_k}\right)$ (I: Production), $D_{ij}^L = \frac{\partial}{\partial x_k}\left(\mu\frac{\partial}{\partial x_k}\left(\overline{u_i'u_j'}\right)\right)$ (II: Molecular diffusion),

$D_{ij}^T = -\frac{\partial}{\partial x_k}\left(\rho\overline{u_i'u_j'u_k'} + \overline{p\left(\delta_{kj}u_i' + \delta_{ik}u_j'\right)}\right)$ (III: Turbulent diffusion), $\phi_{ij} = \overline{p\left(\frac{\partial u_i'}{\partial x_j} + \frac{\partial u_j'}{\partial x_i}\right)}$ (IV: Pressure strain), $\varepsilon_{ij} = 2\mu\overline{\frac{\partial u_i'}{\partial x_k}\frac{\partial u_j'}{\partial x_k}}$ (V: Dissipation), where $\delta_{ij} = 1$, if i=j, else 0.

Of these five terms, the last three (D_{ij}^T , ϕ_{ij} and ε_{ij} ,) require modeling, with the pressure strain (ϕ_{ij}) and dissipation (ε_{ij}) considered to be critical [28]. The turbulent diffusion term (i.e. D_{ij}^T , III) is modeled the same way as the molecular diffusion term [38]:

$$D_{ij}^T = \frac{\partial}{\partial x_k}\left(\frac{\mu_t}{\sigma_k}\frac{\partial}{\partial x_k}\left(\overline{u_i' u_j'}\right)\right), \text{ where } \mu_t = \rho C_\mu \frac{k^2}{\varepsilon},\ C_\mu = 0.09,\ \ \sigma_k = 0.82 \tag{4.13}$$

The dissipation tensor is defined from ε as: $\varepsilon_{ij} = (2/3)\delta_{ij}\rho\varepsilon$ (4.14)

The dissipation rate (i.e. ε) in the above equation is defined by same equations (with ($\sigma_\varepsilon = 1.0$)) as in SKE.

The main difference between RSM models is the handling of pressure strain (ϕ_{ij}) and many different ways have been proposed for high- and low- Re versions [27-28, 31, 39-41]. The current work tests low- and high-Re versions of the Linear Pressure Strain (LPS) model and low-Re stress omega model (RSM-Sω) formulations [30-31]. The high-Re version of LPS is used with SWF and NEWF. The low-Re version of LPS is used in conjunction with EWT.

In RSM-LPS, the pressure strain term is decomposed into three components,

$$\phi_{ij} = \phi_{ij1} + \phi_{ij2} + \phi_{ijw}, \phi_{ij1} = -C_1\rho\frac{\varepsilon}{k}\left(\overline{u_i' u_j'} - \frac{2}{3}\delta_{ij}k\right), \phi_{ij2} = -C_2\left(\left(P_{ij} - C_{ij}\right) - \frac{2}{3}\delta_{ij}\left(\frac{P_{kk}}{2} - \frac{C_{kk}}{2}\right)\right) \tag{4.15}$$

where, $C_1 = 1.8$, $C_2 = 0.6$ and $C_{ij} = \frac{\partial}{\partial x_k}\left(\rho\overline{u}_k\overline{u_i' u_j'}\right)$ (convection term)

$$\begin{aligned}\phi_{ijw} &= C_1'\frac{\varepsilon}{k}\left(\overline{u_k' u_m'}n_k n_m\delta_{ij} - \frac{3}{2}\overline{u_i' u_k'}n_j n_k - \frac{3}{2}\overline{u_j' u_k'}n_i n_k\right)\frac{C_l k^{3/2}}{\varepsilon d} \\ &+ C_2'\left(\phi_{km2}n_k n_m\delta_{ij} - \frac{3}{2}\phi_{ik2}n_j n_k - \frac{3}{2}\phi_{jk2}n_i n_k\right)\frac{C_l k^{3/2}}{\varepsilon d}\end{aligned} \tag{4.16}$$

$C_1^{'}=0.5,\ C_2^{'}=0.3,\ C_l=C_\mu^{3/4}/\kappa,\ C_\mu=0.09,\ \kappa=0.42,\ d$ is the normal distance to the wall. n_k is the x_k component of unit normal vector. In low-Re RSM-LPS with EWT, the constants (C_1, C_2, $C_1^{'}$ and $C_2^{'}$) are sensitized to Reynolds stress invariants and turbulent Reynolds number ($\mathrm{Re}_T=\rho k^2/\mu\varepsilon$) [41]. $C_1=1+2.58A\sqrt{A_2}\left(1-\exp\left(-\left(0.0067\,\mathrm{Re}_T\right)^2\right)\right),\ C_2=0.75\sqrt{A}$

$,C_1^{'}=-(2/3)C_1+1.67,\ C_2^{'}=\max\left(((2/3)C_2-1/6)/C_2,0\right)$,

Where, $A=1-\frac{9}{8}\left(A_2-A_3\right),\ A_2=a_{ik}a_{ki},\ A_3=a_{ik}a_{kj}a_{ji},\ a_{ij}=-\left(-\rho\overline{u_i'u_j'}+(2/3)\rho k\delta_{ij}/\rho k\right)$

In addition to RSM-LPS, the RSM with low-Re stress omega formulation (RSM-Sω) was used for one low-Re non-MHD channel flow calculation. Details of this model are given in [30-31].

4.2.6. Near-Wall Treatment

Near-wall treatment is very important in wall-bounded turbulent flows. Walls have high velocity gradients and thus are the main source of turbulence production. The wall regions are differently handled in different models. The low-Re models (i.e. Abid, LB, LS, YS, AKN, CHC, RSM-Sω with low Re-correction) use damping functions and need a fine grid to integrate up to viscous sublayer ($y^+=yu_\tau/\nu(\tau_w=\rho u_\tau^2)$ <=1) [42]. The high-Re models (i.e. RKE, SKE, RNG, RSM etc.), use two different near-wall treatments [30-33]: i) wall functions which do not resolve the buffer region or viscous sublayer (applicable for 30< y^+ <300: SWF and NEWF), ii) two-layer model for ε and μ_t with a single blended law of wall for mean velocity (EWT). Formulations for the different wall treatment methods (SWF, NEWF and EWT) are given below.

4.2.6.1. Standard Wall Function (SWF)

The standard "law of the wall" for mean velocity [30, 32] is:

$$U^* = (1/\kappa)\ln(Ey^*),\ \kappa = 0.418,\ E = 9.79,\ C_\mu = 0.09 \tag{4.17}$$

Where, $U^* = U_p C_\mu^{1/4} k_p^{1/2} / (\tau_w / \rho)$, $y^* = \rho C_\mu^{1/4} k_p^{1/2} y_p / \mu$, (in equilibrium boundary layer y^* and y^+ are approximately equal) (subscript p stands for the cell center next to wall). U_p and k_p, and y_p are the TKE, tangential velocity and distanced of cell center from wall in the cell next to the wall respectively. τ_w is the wall shear stress.

At the wall, the normal derivative of TKE is taken zero (i.e. $\partial k / \partial n = 0$) and assuming rate of TKE production equal to rate of dissipation, the value of dissipation in the cell next to the wall can be calculated as, $\varepsilon_p = C_\mu^{3/4} k_p^{3/2} / (\kappa y_p)$

4.2.6.2. Non-Equilibrium Wall Function (NEWF)

In this formulation, the log-law mean velocity of SWF is sensitized with pressure and a two layer approach for production and dissipation of turbulence is considered [30, 33].

$$\tilde{U} C_\mu^{1/4} k^{1/2} / (\tau_w / \rho) = (1/\kappa)\ln(E\rho C_\mu^{1/4} k^{1/2} y / \mu) \tag{4.18}$$

$$\tilde{U} = U - \frac{1}{2}\frac{\partial p}{\partial x}\left(\frac{y_v}{\rho\kappa\sqrt{k}}\ln\left(\frac{y}{y_v}\right) + \frac{y - y_v}{\rho\kappa\sqrt{k}} + \frac{y_v^2}{\mu}\right),\ y_v = \frac{\mu y_v^*}{\rho C_\mu^{1/4} k_p^{1/2}},\ y_v^* = 11.225.$$

y_v is viscous sublayer thickness. The two layer concept to calculate cell-average production (G_k) and dissipation rate (ε) is outlined below.

$$\tau_t = \begin{Bmatrix} 0, & y<y_v \\ \tau_w, & y>y_v \end{Bmatrix},\ k = \begin{Bmatrix} \left(\frac{y}{y_v}\right)^2 k_p, & y<y_v \\ k_p, & y>y_v \end{Bmatrix},\ \varepsilon = \begin{Bmatrix} \frac{2\nu k}{y^2}, & y<y_v \\ \frac{k^{3/2}}{C_l^* y}, & y>y_v \end{Bmatrix},\ C_l^* = \kappa C_\mu^{-3/4}$$

$$G_k = \frac{1}{y_n}\int_0^{y_n} \tau_t \frac{\partial U}{\partial y} dy = \frac{1}{\kappa y_n}\frac{\tau_w^2}{\rho C_\mu^{1/4} k_p^{1/2}}\ln\left(\frac{y_n}{y_v}\right), \text{ and } \varepsilon = \frac{1}{y_n}\int_0^{y_n} \varepsilon dy = \frac{1}{y_n}\left(\frac{2\nu}{y_v} + \frac{k_p^{1/2}}{C_l^*}\ln\left(\frac{y_n}{y_v}\right)\right)k_p$$

where, $y_n = 2y_p$. With G_k and ε, the TKE equation is solved in the domain with $\partial k / \partial n = 0$ at the wall.

4.2.6.3. Two-Layer Treatment with Blended Wall Function (EWT)

This technique uses a two layer approach for eddy viscosity and dissipation rate based upon turbulent Reynolds number ($\mathrm{Re}_y = \rho\sqrt{k}y/\mu$, y is the normal distance from cell center to the wall) [30]. In the viscous region (i.e. $\mathrm{Re}_y < \mathrm{Re}_y^*$, $\mathrm{Re}_y^* = 200$), the momentum equation and TKE equations are solved as usual but the eddy viscosity and dissipation rates are calculated as:

$$\mu_{t,2} = \rho C_\mu l_\mu \sqrt{k},\ l_\mu = yC_l^*\left(1-\exp(-\mathrm{Re}_y/A_\mu)\right) \tag{4.19}$$

$\varepsilon = k^{3/2}/l_\varepsilon$, $l_\varepsilon = yC_l^*\left(1-\exp\left(-\mathrm{Re}_y/A_\varepsilon\right)\right)$, where $C_l^* = \kappa C_\mu^{-3/4}$, $A_\mu = 70$, $A_\varepsilon = 2C_l^*$.

Further, the eddy viscosity of viscous region is blended with the fully turbulent viscosity to give smooth behavior in between viscous and fully turbulent regions:

$\mu_{t,enhanced} = \lambda_\varepsilon \mu_t + (1-\lambda_\varepsilon)\mu_{t,2}$ where, $\mu_t = \rho C_\mu k^2/\varepsilon$, $C_\mu = 0.09$. The same blending is performed for ε, where $\lambda_\varepsilon = 0.5\left(1+\tanh\left(\left(\mathrm{Re}_y - \mathrm{Re}_y^*\right)/A\right)\right)$, $A = \left|\Delta\mathrm{Re}_y/\tanh(0.98)\right|$, $\Delta\mathrm{Re}_y$ is assigned a value in between 5% to 20% of Re_y^* to give smooth behavior.

The blended single wall law is defined as [30, 34],

$$U^+ = e^\Gamma U^+_{\text{laminar}} + e^{1/\Gamma}U^+_{\text{turbulent}} \text{ and } dU^+/dy^+ = e^\Gamma dU^+_{\text{laminar}}/dy^+ + e^{1/\Gamma}dU^+_{\text{turbulent}}/dy^+ \tag{4.20}$$

$\Gamma = -a\left(y^+\right)^4/\left(1+by^+\right)$, $a = 0.01$, and $b = 5$. For turbulent region, the wall law with the effect of pressure is as follows [43-44]:

$$\frac{dU^+_{\text{turbulent}}}{dy^+} = \frac{1}{\kappa y^+}\left(S^{'}\right)^{1/2},\ S^{'} = \begin{Bmatrix} 1+\alpha y^+, & \mathrm{y}^+ < y_s^+ \\ 1+\alpha y_s^+, & \mathrm{y}^+ >= y_s^+ \end{Bmatrix},\ y_s^+ = 60, \text{ and } \alpha = \frac{\mu}{\rho^2 u_\tau^3}\frac{\partial p}{\partial x}$$

For laminar region, $dU^+_{\text{laminar}} / dy^+ = 1 + \alpha y^+$. Eq. 4.2 is solved for TKE in the whole domain with $\partial k / \partial n = 0$ at the wall, and the G_k term in TKE equation is calculated using the velocity gradient (Eq-4.20) consistent with single wall law as given above.

4.2.6.4. Wall Treatment in RSM Model for Reynolds Stresses

RSM model needs boundary conditions for Reynolds stresses in addition to the above wall treatment procedures. With SWF and NEWF, TKE is calculated using $k = 0.5\overline{u_i' u_i'}$ away from the wall and in the near wall cells, a transport equation, similar to as in SKE, for TKE (with $\sigma_k = 0.82$) is solved with $\partial k / \partial n = 0$ at the wall. Afterwards, the individual Reynolds stresses are calculated using equation given below in near wall cells (derived based upon equilibrium of Reynolds stresses, i.e. production=dissipation) [30].

$$\overline{u_t' u_t'} / k = 1.098,\ \overline{u_\eta' u_\eta'} / k = 0.247,\ \overline{u_\lambda' u_\lambda'} / k = 0.655,\ -\overline{u_t' u_\eta'} / k = 0.255 \tag{4.21}$$

where subscripts t, η and λ stand for local tangential, normal and binormal coordinates respectively. With EWT, the normal derivatives of Reynolds stresses are zero at the wall.

4.2.7. MHD Formulations

When the Magnetic Reynolds number, $\text{Re}_m = vL(\mu\sigma)$, is <1 (such as for liquid metals), the induced magnetic field is negligible relative to the applied field. Based on Ohm's law and conservation of charge, coupled equations for electric potential, ϕ, and Lorentz force, $\vec{F}_L$ can be solved as follows [45, 30].

$$\nabla^2 \phi = \nabla \cdot \left(\vec{v} \times \vec{B}_0 \right) \text{and } \vec{F}_L = \sigma \left(-\nabla \phi + \vec{v} \times \vec{B}_0 \right) \times \vec{B}_0 \tag{4.22}$$

In time varying fields, and when the induced current is significant, (i.e. Re_m >1), the Maxwell's equations are combined with Ohm's law to obtain a transport equation for the induced magnetic field, $\vec{b}$ [45, 30].

$$\frac{\partial \vec{b}}{\partial t}+(\vec{v}\cdot\nabla)\vec{b}=\frac{1}{\mu\sigma}\nabla^2\vec{b}+\left(\left(\vec{B}_o+\vec{b}\right)\cdot\nabla\right)\vec{v}-(\vec{v}\cdot\nabla)\vec{B}_o-\frac{\partial \vec{B}_0}{\partial t}+\frac{1}{\mu\sigma}\nabla^2\vec{B}_0 \qquad (4.23)$$

$$\vec{B}=\vec{B}_o+\vec{b}\,; \qquad \vec{J}=\nabla\times\vec{B}/\mu\,; \qquad \vec{F}_L=\vec{J}\times\vec{B}$$

In both above methods, the Lorentz force is applied as a source term in the momentum equations.

4.2.8. Effect of Magnetic Field on Turbulence in RANS Turbulence Models

Many researchers [12-15, 46] improved the conventional non-MHD RANS turbulence models for the effect of the magnetic field on the turbulence in low magnetic Reynolds number liquid metal MHD flows. Ji and Gardner [14] proposed and tested source terms for magnetic field damping effects on turbulence using a k-ε model on a turbulent conducting liquid flow in an insulated pipe. Velocity profiles, skin friction, temperature profiles, Nusselt numbers showed agreement with available experimental data for range of Re and Ha. The biggest shortcoming of this model is the dependence of the turbulence damping terms on bulk flow, making the model applicable only in problems where the bulk Stuart number (or interaction parameter, Ha^2/Re) is readily defined. Smolentsev et al [15] proposed different source terms for k-ε models but again based on bulk Stuart number. The model was found to match experiments closely in free surface channel flow.

Galperin [46] proposed a second-moment closure model for MHD turbulence, although this model was not numerically tested on conventional flows. Kenjereš and Hanjalić [12-13] proposed new source terms for k-ε and second-moment closure models (RSM). The improved k-ε model was validated with the DNS results in a channel flow under transverse magnetic field. After validation, the model was used in a 3-d developing rectangular duct flow with partial magnetic field and model was found performing well for mean velocities. No assessment for turbulence parameters was made in rectangular duct flow. Kenjereš and Hanjalić [12-13] also

proposed a similar closure for $\overline{u_i u_j}$ equations for MHD effects in RSM as proposed by Galperin [46]. This closure for RSM showed considerable improvement of results in a channel flow. The current study includes the models proposed by Kenjereš and Hanjalić's [12-13] for the channel and square duct flows. The following modifications were made to the models.

4.2.8.1. k-ε Model

k-equation: $$S_k^M = -\sigma B_0^2 k \exp\left(-C_1^M \left(\sigma/\rho\right) B_0^2 \left(k/\varepsilon\right)\right) \tag{4.24}$$

ε-equation: $$S_\varepsilon^M = -\sigma B_0^2 \varepsilon \exp\left(-C_1^M \left(\sigma/\rho\right) B_0^2 \left(k/\varepsilon\right)\right) \tag{4.25}$$

where, $C_1^M = 0.025$

4.2.8.2. Reynolds Stress Model (RSM) MHD Source Terms

After simplification for y-directional (vertical) magnetic field and some algebra the six independent Reynolds stress transport equations can be derived with the following MHD source terms;

$\overline{w'w'}$-equation: $$S_{w'w'}^M = \sigma\left(-2B_{y0}\overline{w'\partial\phi'/\partial x} - 2B_{y0}^2\overline{w'w'}\right) \tag{4.26}$$

$\overline{v'v'}$-equation: $$S_{v'v'}^M = 0 \tag{4.27}$$

$\overline{u'u'}$-equation: $$S_{u'u'}^M = \sigma\left(2B_{y0}\overline{u'\partial\phi'/\partial z} - 2B_{y0}^2\overline{u'u'}\right) \tag{4.28}$$

$\overline{u'v'}$-equation: $$S_{u'v'}^M = \sigma\left(B_{y0}\overline{v'\partial\phi'/\partial z} - B_{y0}^2\overline{u'v'}\right) \tag{4.29}$$

$\overline{w'u'}$-equation: $$S_{w'u'}^M = \sigma\left(-B_{y0}\overline{u'\partial\phi'/\partial x} + B_{y0}\overline{w'\partial\phi'/\partial z} - 2B_{y0}^2\overline{w'u'}\right) \tag{4.30}$$

$\overline{w'v'}$-equation: $$S_{w'v'}^M = \sigma\left(-B_{y0}\overline{v'\partial\phi'/\partial x} - B_{y0}^2\overline{w'v'}\right) \tag{4.31}$$

Source term for scalar dissipation rate (ε) is defined as [13]; $S_\varepsilon^M = 0.5 S_{ii}^M \varepsilon/k$ (4.32)

It can be seen that all the source terms due to the magnetic field are negatively correlated with the corresponding Reynolds stress therefore sinks to the Reynolds stresses. It is interesting to note that the magnetic field causes no direct sink to the Reynolds normal stress parallel to magnetic field (i.e. $\overline{v'v'}$). The indirect suppression effect on $\overline{v'v'}$ is via Reynolds shear stresses. In the above sinks, the terms involving correlation of velocity fluctuation with electric potential gradient require modeling and cannot be incorporated directly in RSM. Kovner and Levin [47] suggested a way to model electric potential-velocity correlation. Galperin [46] and later Kenjereš and Hanjalić [12-13] followed their method and came up with following formulation for the correlation;

$$\partial\phi'/\partial x_k = \beta\varepsilon_{kmn}u_m' B_{n0} \Rightarrow \overline{u_i'\partial\phi'/\partial x_k} = \beta\varepsilon_{kmn}\overline{u_i'u_m'}B_{n0} \tag{4.33}$$

Galperin [46] proposed $0<\beta<1$. Kenjereš and Hanjalić [13] proposed $\beta = 0.6$ via MHD channel flow. In the current work, the value of β as proposed by Kenjereš and Hanjalić is used.

The above discussed two formulations for k-ε and RSM for the effect of magnetic field on turbulence have been implemented using a UDF with the magnetic induction and the electric potential methods [30]. More details on various turbulence models, wall treatment approaches, magnetic induction and electric potential method for MHD calculations can be found in [30].

4.3. DNS Databases

Five DNS databases were used to assess the above models. The conditions for various DNS databases are given in Table 4.3.

4.3.1. High-Reynolds Number Non-MHD Channel Flow

Satake et al [48] performed DNS calculations in a non-MHD channel at a bulk Reynolds number of ~45818 using 800 million nodes. The mean velocities, RMS of velocity fluctuations and TKE budgets were reported. This non-MHD case was used as a base case to first evaluate the purely hydrodynamic models.

4.3.2. Low-Reynolds Number MHD and Non-MHD Channel Flows

The non-MHD channel flow data of Iwamoto et al [49] has been used to test performance of RANS models at lower Reynolds numbers. In his case, Re_τ (=$\delta u_\tau/\nu$)=150, corresponding to bulk Re (=$2\delta W_b/\nu$, δ: half channel height)=4586 was used. To test the models for MHD turbulence, the MHD channel case of Noguchi et al [50] (Re_τ (=$\delta u_\tau/\nu$)=150, bulk Re (=$2\delta W_b/\nu$)=4710, Ha (=sqrt($\sigma/\rho\nu$)$B_0\delta$)=6), δ: half channel height) was used.

4.3.3. Low-Reynolds Number MHD and Non-MHD Square Duct Flows

A GPU based code (CU-FLOW) [51] that has been previously used for DNS calculations in a non-MHD square duct has been extended for DNS calculations of a MHD square duct [52]. For the non-MHD case, (Re_τ(=Du_τ/ν)=360, bulk Re (=DW_b/ν)=5466), a duct of size of 1x1x8 non-dimensional units and 160x160x1024 control volumes (with 1% grid stretching in wall normal directions) were used. For the MHD case, (Re_τ(=Du_τ/ν)=361, bulk Re (=DW_b/ν)=5602, Ha (=sqrt($\sigma/\rho\nu$)B_0D)=21.2)) a duct of size of 1x1x16 non-dimensional units with 128x128x512 control volumes (with 2% grid stretching in wall normal directions) were used. Both these simulations were shown to give grid-independent solutions to the relevant equations.

4.4. Computational Details

4.4.1. Computational Domain, Boundary Conditions and Numerical Method

Taking advantage of fully-developed flow with RANS models, the domain size was taken as 1x1x1 non-dimensional units for both the channel and the square duct. For the channel, the top and the bottom walls were electrically insulated with no-slip velocity conditions while the streamwise (z-) and spanwise (x-) directions were considered periodic. In the square duct, the four walls (top, bottom, right and left) were electrically insulated with no-slip velocity conditions whereas the streamwise direction (z-) is periodic. For the MHD calculations, the magnetic field

was applied in the vertical (y-) direction. The simulations were carried out by fixing the bulk mean flow Reynolds number as given in Table 4.3 with the mean streamwise pressure gradient free to change. All the calculations were performed using FLUENT's steady-state segregated solver with SIMPLE algorithm for pressure-velocity coupling with either magnetic induction or electric potential methods for MHD calculations [30]. For each case, the results were ensured to be grid-independent by systematically increasing the number of control volumes until a grid-independent solution is obtained. All cases were converged such that the unscaled absolute residuals reached below 10^{-3} to stagnant values.

4.4.2. Grids

For the high-Re calculations (case 1, Re=45818) with EWT, five grids with ten control volumes each in streamwise (z-) and spanwise (x-) directions were used. In the wall-normal (y-) direction, three uniform grids (consisting of 50, 80 and 130 control volumes) and two non-uniform grids (near-wall y+ = 1) were used. Figure 4.1 compares the TKE along the wall normal direction in the case of the RKE model with EWT. The results show grid independence as y^+ approached a value of one in the cells adjacent to the wall. The coarse grids produced peaks in k near the wall that appear closer to the true DNS solution. This occurs if the cell next to the wall is in the buffer region for the models with EWT. However, the trend is better-matched with the fine grids. Similar behavior was seen for the other high-Re models (RNG, SKE and RSM-LPS); hence grid independence plots for other models are not presented. All models obtained grid independence with a 139(non-uniform)x10x10 grid, so this grid was used for evaluation of these models. For the models using the SWF and NEWF approaches, the first cell center next to the wall should be placed in the range of $30 \le y^+ \le 300$ and, arbitrary grid refinement close to the

wall is not appropriate. Hence, only uniform grids of 30x10x10 with y^+ in cells next to the wall being in the range of 35-40 are used for models with these wall functions.

For low-Reynolds number flows (cases 2-5), the number of cells required to satisfy near-wall $y^+>30$ is too small to be accurate. Hence, SWF and NEWF were not evaluated for low-Re flows. Only low-Re models (Abid, LB, LS, YS, AKN, and CHC) or high-Re models (like SKE, RNG (with low-Re differential viscosity model), RKE, and RSM-linear pressure-strain) with EWT are considered. Two uniform (50x10x10 and 80x10x10) and one non-uniform (100x10x10) grids were used for RKE, SKE, RNG, and RSM-LPS models with EWT to ascertain grid independency. The same grids were also used for the RSM-Sω (with low-Re correction) model. Figure 4.2 shows the TKE for different grids predicted by SKE with EWT. Similar behavior was seen by other models as well. As the grid is refined to 100 non-uniformly-spaced cells, the results show very good grid independence. Hence this grid is used in all subsequent computations of low-Re cases with these models. For the square duct, the same grid is used in both the wall-normal directions (i.e. 100 x 100 x 10 cells).

Grid-convergence tests were also systematically done for each of the six low-Re k-ε models. Figure 4.3 shows one plot of TKE in the Abid model for three different grids. All low-Re k-ε models were observed to achieve grid independence with 120 cells in the wall normal direction (giving a near-wall y^+ between 0.55-0.9). Hence this grid is used in all subsequent computations of low-Re cases with these models. In square duct flows, the same grid resolution of 120 cells is used in both wall-normal directions (i.e. 120x120x10).

4.4.3. Computational Costs

Due to their varying complexities and convergence rates, both the total and per-iteration computational times for each model were different. Table 4.4 summarizes the time per iteration

and total number of iterations to final convergence required by FLUENT (using 6 cores of a Dell Precision T7400 workstation with 2.66 GHz Intel Xeon processor and 8 GB RAM) with different models. As expected, the two equation models RKE, RNG and SKE with EWT require nearly the same time (per iteration as well as total time). On a per-iteration basis, the various two equations models are 5-30% less expensive than RSM-LPS (which solves 7 transport equations) with EWT. However, to obtain final converged results, RSM-LPS model is ~13-26 times more expensive. With SWF and NEWF, the two equation models are about 20-30% less expensive than RSM-LPS when compared on a per iteration basis but the time required to final convergence by RSM-LPS model reduces and it is only slightly more expensive. It seems that with finer grids, RSM-LPS model becomes increasingly expensive to achieve final convergence relative to two equation models. The EWT and SWF/NEWF are almost equally expensive for the same grid, but the grid required for EWT is much higher. In all models tested, the computational requirement increases almost linearly with the grid size. Surprisingly, low-Re RSM-Sω model, which also solves 7 equations, is only about twice as expensive as the two equation models. All low-Re k-ε models take nearly the same time per iteration, but the total times for LB and LS models are smaller. YS model took five times more time than LB and LS.

4.5. Results and Discussion

Results are first presented for non-MHD flows to show the accuracy of the various models without magnetic field. From these, models giving the best agreement are evaluated for the MHD flows after incorporating the changes due to the magnetic field effects.

4.5.1. High-Reynolds Number Non-MHD Channel Flow (Re=45818)

Figure 4.4 compares the TKE predicted by the various models with the DNS data of Satake et al. [48] for the grid independent mesh with EWT. It is seen that all models (RKE, RNG,

SKE, and RSM-LPS) give nearly the same distribution of the TKE. They underestimate the DNS peak values near the wall by 22-27%. Error decreases with distance from the wall, and TKE in the central core is predicted within 10%. Figure 4.5 shows similar behavior comparing models with SWF. As theoretically required, the near-wall y^+ has been maintained around 36-37. The results with SWF were nearly the same as with the NEWF probably because of the lack of flow separation or pressure gradient effects in a channel flow. As seen with the EWT, the peak value of TKE was again under-predicted, this time by a larger amount (42%). The agreement in the core region is much better with all the models, except RKE giving slightly lower predictions.

The non-dimensionalized mean axial velocities predicted with the SKE and RSM-LPS models using EWT and SWF are presented in Figure 4.6. The velocity profiles with NEWF are not presented as they were nearly the same as with SWF. It is seen that the EWT with $y^+=1$ resolves velocity accurately all the way up to the viscous sublayer and matches best with the DNS results across the whole channel. Both models performed equally well with EWT, with errors consistently within 3%. With SWF, as y^+ is maintained ~36, the cell next to the wall stays in log-law region. Again both models predicted mean velocities well, although error with the RSM-LPS model increased to ~5% in the central core.

The Reynolds normal stresses predicted by the RSM-LPS model with all 3 wall treatments are compared with the DNS data in Figures 4.7(a) and (b). With SWF and NEWF, the predictions matched closely with the DNS data in the core region except for the wall normal velocity fluctuations, which were underpredicted. The errors increased towards the wall especially in the axial and wall normal velocity fluctuations. Both wall functions performed equally but both missed the peak values close to the wall in all the three velocity fluctuations. The peak value of the RMS of axial velocity fluctuations is underpredicted by ~36% while the

error in transverse and spanwise velocity fluctuations is smaller. The RMS of spanwise velocity fluctuations matched best with the DNS. The RSM-LPS model with EWT performed better than with SWF or NEWF in predicting all three velocity fluctuations, as expected. Again, the spanwise velocity fluctuations were predicted most accurately followed by wall normal fluctuations. The error in predicting peak value of axial velocity fluctuations reduced from ~36% to ~12% by using the EWT. Overall, RSM-LPS with EWT predicted the anisotropy of Reynolds normal stresses reasonably well.

The mean streamwise pressure gradient predicted by various models is compared with the DNS data in Table 4.5. Overall, all models predicted the frictional losses within 10% error. The predictions with EWT were better than with SWF and NEWF.

4.5.2. Low-Reynolds Number Non-MHD Channel Flow (Re=4586)

We next consider the low-Re non-MHD channel flow for which the various low-Re turbulence models are first evaluated. Figure 4.8 compares the TKE predicted by various low-Re k-ε models with the DNS. The LS model greatly overpredicted throughout the domain, while the CHC model underpredicted near the wall and matched in the core. This huge overprediction by LS model is not reported previously [53]. This is perhaps due to the fact that all previous work compared normalized k (i.e. k^+ after normalizing with u_τ^2, where u_τ is calculated from RANS predictions of frictional losses) or may be due to implementation issues in this model in FLUENT and therefore needs further investigation. The 4 remaining models predicted similar values, matching the DNS data within 15% error near the wall but over-predicting (by ~60%) in the core. Overall, the LB model performed the best of all the models. The YS model gave the correct trend across the whole domain, consistently overpredicting by 7-30%. The best low-Re k-ε models (LB, AKN, and YS) are evaluated for mean axial velocity predictions in Figure 4.9. All

three models predicted the mean axial velocity profile across the channel very well (within 5% error).

In addition to the low-Re k-ε models, the high-Re k-ε models with EWT (RKE, RNG with differential viscosity, and SKE) and RSM models (RSM-LPS with EWT and RSM-Sω low-Re) also have been evaluated in this low-Re non-MHD channel flow. Figure 4.10 compares TKE predicted by these models. All models, except RNG and RSM-Sω, performed similarly by matching the peak values but over-predicting the values significantly (by ~120%) in the core. The RNG model overpredicted slightly more in the core than other models. RSM-Sω model matched TKE better in the core. Figure 4.11 compares the RMS of velocity fluctuations predicted by low-Re RSM-Sω and RSM-LPS model with the DNS. The RSM-Sω model, although it predicted the TKE best in the core, did not capture the anisotropy of Reynolds stresses even qualitatively. Because it was outperformed by the RSM-LPS model, the RSM-Sω model was not considered further in this study. The RSM-LPS model with EWT captured anisotropy qualitatively in all velocity fluctuations but overpredicted in the core. Figure 4.12 shows the comparison of the mean axial velocities given by RKE, SKE, and RSM-LPS models. All matched the DNS data closely except for some underprediction in the core.

Table 4.5 presents the mean streamwise pressure gradient predicted by various models for this flow. The best prediction of pressure gradient is by low-Re LB model (within 2% error) followed by the RSM-Sω model (3% error). All high Reynolds number k-ε models with EWT overpredicted the pressure gradient by ~10%. The LS and CHC models were unreasonable, with frictional loss errors of ~95% and -16%. The other low-Re models predicted friction loss within 7%.

4.5.3. Low-Reynolds Number MHD Channel Flow (Re=4710, Ha=6)

The models (LB, SKE, and RSM-LPS) which performed better in low-Re non-MHD channel flow were then tested in low-Re MHD channel flow at a Reynolds number of 4710 and Ha = 6.0. Comparison of the computed TKE using the selected turbulence models with and without inclusion of the MHD sources/sinks is shown in Figure 13. The LB low-Re k-ε model with MHD sources/sinks matches the DNS computed turbulent kinetic energy quite well in the core but underpredicts the high values close to the wall calculated by the DNS. This match in the core seems to be fortuitous when overall trend is not predicted that well by this model. The peak TKE is seen to be better predicted by LB without the MHD sources. The effect of the MHD sources/sinks on suppressing turbulence is clearly seen. SKE and RSM with EWT matched the peak values closely but overpredicted greatly (by 300-500%) in the core. The models using EWT show very little effect of MHD source terms. This is likely due to the lack of magnetic field effects in wall treatment method. This contrasts with the strong effect observed in the low-Re LB model, where the source terms are applied throughout the domain.

Figure 4.14 compares the axial velocity in wall coordinates. The LB low-Re k-ε model with MHD sources gives the best agreement with DNS data. However, part of profile in between $15<y^+<80$ is under-predicted. The second best prediction is from the LB model without MHD sources. The predictions of RSM and SKE are similar, with the RSM-LPS performing slightly better. The underprediction of the normalized velocity in the core is mainly due to the higher frictional losses leading to higher friction velocity. The SKE and RSM models with EWT do not show much effect of MHD sources in the mean velocity. Figure 4.15 compares the axial velocity, as in Figure 4.14, but this time non-normalized mean velocity as a function of distance from the wall in the wall normal direction. The close match of predictions from all models with the DNS

reinforces the assertion that the higher frictional losses are causing the differences in predictions in Figure 4.14.

We next examine the MHD source/sink terms in the k-equation and compare their magnitude with those extracted from the DNS budgets (Figure 4.16). The trends predicted by all 3 models are reasonable, but the LB low-Re k-ε model matches best with the DNS (within 20%). Although, the SKE model predicts the peak closely, it overpredicts the values in the core by ~300%. Interestingly, none of the models capture the small positive peak very close to the wall.

Figure 4.17 presents the sink term due to magnetic field in the turbulent dissipation rate (ε) equation. All 3 models correctly predict the asymptotic decay of source to dissipation to zero in the core. The LB low-Re model correctly predicts the profile qualitatively across the whole channel but underestimates the values. The SKE and RSM models predict qualitatively similar profiles with negative peaks at y^+~10. The SKE model gives the closest match although errors approach 50% near the wall.

Figures 4.18 and 4.19 give comparisons of the magnetic field source/sink terms in Reynolds normal stresses obtained by RSM-LPS. For S^{M+}_{ww}, RSM behaves similar to the TKE source. It underpredicts the peak value and overpredicts in the core. The positive values, which indicate a source in S^{M+}_{ww} below y^+<5, are again missed by the model. The MHD sink in S^{M+}_{uu} is qualitatively captured but the values are over-predicted across the whole length.

For this case, the LB model with MHD sources predicts the pressure gradient closest to the DNS (within 2.5%) followed by LB without MHD sources (Table 4.5). The SKE and RSM models overpredict the pressure gradient by about 20%. Adding the MHD sources improves the predictions only slightly.

4.5.4. Low-Reynolds Number Non-MHD Square Duct Flow (Re=5466)

The models are next evaluated for the fully-developed turbulent flow in a square duct bounded by four walls. For this case, it is well-known that the anisotropy in the Reynolds stresses generates cross-stream flows [16], which are not present in the laminar case. Turbulence models based on isotropic eddy-viscosity cannot predict such secondary flows [16]. To predict the secondary flows, it is necessary to use either non-linear/anisotropic two equation models [54-57], RSMs [58], or algebraic stress models [59-60]. Hence, models other than the above are not expected to be accurate. However, they have been considered in this study to assess their inaccuracy and to evaluate their relative performance against the more expensive RSM. Figure 4.20 presents the comparison of TKE along vertical bisector in a non-MHD square duct using LB, RKE, SKE and RSM-LPS models. The grid in all models resolved the flow up to the viscous sublayer (y^+~1). The LB model predicts the TKE better than other models. However, all models give excessive TKE in the core region by over 100%. Figure 4.21 compares the predicted RMS of velocity fluctuations by the RSM model along vertical bisector of the duct. RSM-LPS model with EWT, even when used with near wall spacing of y^+<1.1, over-predicts all the components of Reynolds normal stresses in the core by 40-75%. The agreement is however better in the near-wall region.

Figure 4.22 compares the mean axial velocity along the vertical bisector obtained by the different models. The RKE, SKE and LB models show similar reasonable behavior, as they agree with the DNS within ~8%. All 3 models overpredict in-between the wall and the core and underpredict in the core region. The RSM model expectedly is slightly better but matches the other models in underpredicting the core region. Compared to the channel, the square duct flow is predicted with less accuracy, probably as a result of the inability to predict the secondary flows.

Figure 4.23(a) and (b) compare the mean axial velocity contours and secondary velocity vectors of the RSM-LPS model with the DNS. Bulging of axial velocity is underpredicted. The other models cannot predict secondary flows so are not shown.

Table 4.5 compares the mean streamwise pressure gradient predictions with the DNS. The LB model is best with an error of only ~7%. The RSM overpredicts pressure gradient by ~25% which is worst. SKE and RKE overpredict by ~12.0%.

4.5.5. Low-Reynolds Number MHD Square Duct Flow (Re=5602, Ha=21.2)

The final test case is MHD square duct flow, which is an appropriate geometry for the industrial application of electromagnetic, such as control of nozzle flow in the continuous casting of steel. The magnetic field causes different flow profiles along the vertical and the horizontal bisectors in the square duct. Both the magnetic induction and electric potential methods in FLUENT were tested. Both methods gave virtually identical result, which was expected because the maximum induced magnetic field is only 0.039% of the externally applied field.

Figures 4.24 and 4.25 compare TKE along vertical and horizontal bisectors respectively. The DNS shows that MHD suppresses turbulence more along the vertical bisector. Only the LB model with MHD sources predicts this trend, matching with DNS generally within 50%. Without MHD sources, the LB model overpredicts DNS by 100-500%. The MHD sources/sinks [12-13] provide significant improvement by predicting the correct trend of turbulence suppression, especially using the LB model. Both the RKE and RSM models over-predict the turbulence energy in the core along both the bisectors by ~500%. Moreover they do not capture the strong differential suppression of turbulence along the two bisectors, as was seen in the DNS and in the results of LB model with MHD sources. On the horizontal bisector close to the side walls, turbulence is not suppressed much because the induced current is parallel to the magnetic

field in this region. The RKE and RSM models predict the peak TKE better along the horizontal bisector. Surprisingly, the RSM model is found to perform the worst among the tested models for suppressing turbulence by magnetic field effects.

Figures 4.26 and 4.27 give the mean axial velocity predictions from various models compared with the DNS along vertical and horizontal bisectors respectively. The DNS solution shows less flattening along the vertical bisector, which shows the importance of the secondary flows and the anisotropic suppression of turbulence by the magnetic field. All tested models predict about the same velocity profile along both bisectors. They match the DNS within ~4% along the horizontal bisector and overpredict velocity flattening along the vertical bisector by ~30%. The LB and RSM-LPS models are no better than the other models. MHD sources produce higher velocities, due to suppressing turbulence somewhat, but the agreement with DNS is not improved.

Figure 4.28 presents mean axial velocity contours and mean secondary velocity vectors in the cross-section. As shown by the DNS, the mean axial velocity contours and the secondary flows are significantly altered in the presence of the transverse magnetic field. The secondary velocities, rather going into corners, now go towards the top and bottom walls, thus lifting the axial velocity contours in these regions towards the top and the bottom walls. After hitting the walls, these secondary flows move parallel to the top and bottom walls before turning towards the core at the center and thus cause a strong bulging in mean axial velocity there. This effect of strong bulging is not seen close to the side walls. It can be seen that none of the models is able to capture this effect. Although RSM predicts secondary flows, the differential effect of the magnetic field close to the top /bottom walls and the right/left side walls is missing. RSM predicts almost symmetric mean secondary and axial velocities except for a slight elongation of

mean axial velocity (i.e. flattening) in the vertical direction. As mentioned earlier, LB and RKE do not predict secondary flows at all and over-predict the velocity flattening in the vertical direction, as also seen in the line plots of Figure 4.26. Both the k-ε models (LB and RKE) predict similar axial velocity across the cross-section.

Figures 4.29 and 4.30 show the MHD sources/sinks in the TKE equation computed by the various models. The velocity-electric potential gradient correlation acts as a source whereas the Reynolds normal stresses perpendicular to the magnetic field act as sinks, as shown in the DNS data. The sink is stronger than the source giving a net effect of suppressing the turbulence. It can be seen that the LB model predicts this source reasonably correctly, followed by RKE and then RSM-LPS. The predictions are better along the stronger Lorentz force bisector. Both the RKE and the RSM-LPS over-predict the MHD sources to TKE along both bisectors.

The friction factor along bottom horizontal and left vertical walls is presented in Figure 4.31. Along the bottom horizontal wall, the friction factor shows two side peaks with a large dip at the center. Along left-vertical wall, the friction factor shows a central flat region with two side dips. None of the models is seen to predict these trends correctly. Both the k-ε models (LB and RKE) give similar profiles, with a central overpredicted peak. The RSM-LPS model predicts the side peaks with a central dip along both walls but does not completely agree with the DNS results. RSM suggests larger frictional losses, especially in the corners. The best agreement is seen with LB model with MHD sources. The LB model, without MHD sources, overpredicts friction along both walls.

Finally, a comparison of mean streamwise pressure gradients computed by the various models again shows (Table 4.5) that the LB low-Re model with MHD sources performs best by matching within ~2% error with the DNS predictions. LB model without MHD sources is next,

followed by RKE with EWT. The performance of these models is similar in the non-MHD and the MHD cases.

4.6. Conclusions

In this study several turbulence models of k-ε and Reynolds stress transport category are evaluated for their ability to predict turbulent flow fields subjected to a magnetic field. Five test cases of flows in a channel and square duct have been computed and the results are compared with DNS data. The MHD sources/sinks in k- and ε- equations for k-ε models and in Reynolds stresses for RSM, as proposed by Kenjereš and Hanjalić [12-13], were implemented through UDFs in the FLUENT code. The performance of these models, on the basis of their predictions of mean velocities, RMS of velocity fluctuations, TKE, MHD sources and frictional losses can be summarized as follows:

In both high- and low-Re channel flows, all of the models predicted mean axial velocity reasonably well (within 5% error), given fine-enough grids for grid-independence (EWT and low-Re) or satisfaction of the y+ requirements (SWF and NEWF). However, the TKE was much less accurate, often exceeding 60% overprediction in the core. In high-Re channel flows, models underpredicted near-wall peak turbulence energy whereas in low-Re channel flows, they showed better agreement near the wall but over-predicted values in the core. For the MHD flows, the implementation of the MHD sources improved predictions for low-Re k-ε models. The high-Re models which use the wall treatments did not show much improvement with MHD sources, perhaps due to the lack of MHD effects in the wall formulations.

In the case of low-Re square duct flows, the models tested did not predict the mean axial velocities to a good accuracy (error ranging ~8-30%) because of the secondary flows generated due to turbulence anisotropy. The TKE was overpredicted in the core, often exceeding ~60%, by

all models except LB in MHD duct. The effect of turbulence suppression by magnetic field was not properly captured on mean velocity, Reynolds stresses/turbulent kinetic energy and frictional losses by any single model in a MHD duct, even after inclusion of the MHD sources of turbulence.

For problems involving high-Re, the SKE model offers reasonable accuracy at low computational cost. Adding EWT improves accuracy slightly over standard wall laws, but significantly increases cost. For flows with low-Re number, the Lam-Bremhorst (LB) low-Re k-ε model performed better than the others in both hydrodynamic and magnetic field influenced turbulent flows. Given the need to compute complex industrial flows with efficient computational use, using these 2 models with appropriate changes for magnetic field effects provides a reasonable compromise of accuracy and speed. Finally, the RSM-LPS model with EWT offers similar accuracy with the added ability of capturing turbulence anisotropy and secondary flows, but its computational cost is very high.

4.7. Tables and Figures

Table 4.1. Damping functions and wall boundary conditions for different low-Re k-ε models*

Model	f_1	f_2	f_μ	ε_w (wall BC)
Abid	1.0	$\left(1-\frac{2}{9}\exp(-\mathrm{Re}_T^2)/36\right)^2$ $\left(1-\exp\left(-\mathrm{Re}_y/12\right)\right)$	$\tanh\left(0.008\,\mathrm{Re}_y\right)\left(1+4\,\mathrm{Re}_T^{-3/4}\right)$	$\varepsilon_w=\nu\frac{\partial^2 k}{\partial y^2}$
LB	$1+\left(0.05/f_\mu\right)^3$	$\left(1-\exp(-\mathrm{Re}_T^2)\right)$	$\left(1-\exp(-0.0165\,\mathrm{Re}_y)\right)^2\left(1+20.5/\mathrm{Re}_T\right)$	$\frac{\partial\varepsilon}{\partial y}=0$
LS	1.0	$\left(1-0.3\exp(-\mathrm{Re}_T^2)\right)$	$\exp(-3.4/\left(1+\mathrm{Re}_T/50\right)^2)$	$\varepsilon_w=0$
YS	$\frac{\sqrt{\mathrm{Re}_T}}{1+\sqrt{\mathrm{Re}_T}}$	$\frac{\sqrt{\mathrm{Re}_T}}{1+\sqrt{\mathrm{Re}_T}}$	$\left(1+1/\sqrt{\mathrm{Re}_T}\right)$ $\left(1-\exp\left(\begin{array}{l}-1.5x10^{-04}\,\mathrm{Re}_y\\ -5x10^{-07}\,\mathrm{Re}_y^3-10^{-10}\,\mathrm{Re}_y^5\end{array}\right)\right)^{1/2}$	$\varepsilon_w=2\nu\left(\frac{\partial\sqrt{k}}{\partial y}\right)^2$
AKN	1.0	$\left(1-0.3\exp(-\left(\mathrm{Re}_T/6.5\right)^2)\right)$ $\left(1-\exp\left(-\mathrm{Re}_\varepsilon/3.1\right)\right)^2$	$\left(1+5.0/\mathrm{Re}_T^{3/4}\exp(-\left(\mathrm{Re}_T/200\right)^2)\right)$ $\left(1-\exp\left(-\mathrm{Re}_\varepsilon/14\right)\right)^2$	$\varepsilon_w=\nu\frac{\partial^2 k}{\partial y^2}$
CHC	1.0	$\left(1-0.01\exp(-\mathrm{Re}_T^2)\right)$ $\left(1-\exp\left(-0.0631\,\mathrm{Re}_y\right)\right)$	$\left(1-\exp\left(-0.0215\,\mathrm{Re}_y\right)\right)^2$ $\left(1+31.66/\mathrm{Re}_T^{5/4}\right)$	$\varepsilon_w=\nu\frac{\partial^2 k}{\partial y^2}$

* wall BC, $k_w=0$, and $\mathrm{Re}_T=\frac{\rho k^2}{\mu\varepsilon}$, $\mathrm{Re}_y=\frac{\rho\sqrt{k}\,y}{\mu}$ and $\mathrm{Re}_\varepsilon=\frac{\rho\left(\mu\varepsilon/\rho\right)^{1/4}y}{\mu}$

Table 4.2. Various terms and constant of low-Re k-e models

Model	D	E	C_1	C_2	σ_k	σ_ε	C_μ
Abid	0	0	1.45	1.83	1.0	1.4	0.09
LB	0	0	1.44	1.92	1.0	1.3	0.09
LS	$2\nu\left(\frac{\partial\sqrt{k}}{\partial y}\right)^2$	$2\nu\nu_t\left(\frac{\partial^2\bar{u}}{\partial y^2}\right)^2$	1.44	1.92	1.0	1.3	0.09
YS	0	$\nu\nu_t\left(\frac{\partial^2\bar{u}}{\partial y^2}\right)^2$	1.44	1.92	1.0	1.3	0.09
AKN	0	0	1.5	1.9	1.4	1.4	0.09
CHC	0	0	1.44	1.92	1.0	1.3	0.09

Table 4.3 Various parameters in different DNS calculations considered during evaluation [48-52]

Geometry	Re	Grid (N_xxN_yxN_z)	Comput. Domain (XxYxZ)	Spatial resolution (Δx^+, Δy^+, Δz^+)	Ha	$W_b / d\bar{p}/dz$
Channel (Case-1)	45818 (Re_τ=1120) (Satake et al)	1024x1024x768	πx1x2.5π	9.16, 0.163-4.25, 17.2	0	20.45 / 2.0
Channel (Case-2)	4586 (Re_τ=150) (Iwamoto et al)	128x97x128	πx1x2.5π	7.36, 0.08-4.91, 18.4	0	15.28 / 2.0
Channel (Case-3)	4710 (Re_τ=150) (Noguchi et al)	64x128x64	0.5πx1x1.25π	7.36, 0.08-4.9, 9.2	6.0	15.7 / 2.0
Square duct (Case-4)	5466 (Re_τ=360) (Shinn et al)	160x160x1024	1x1x8	1.47-3.24, 1.47-3.24, 2.81 (1% stretching in x- and y-)	0	15.187 / 4.0
Square duct (Case-5)	5602 (Re_τ=361) (Chaudhary et al)	128x128x512	1x1x16	1.41-4.92, 1.41-4.92, 11.28 (2% stretching in x- and y-)	21.2	1.057/0.01857

Where, $\mathrm{Re}_\tau = \frac{D_1 u_\tau}{\nu}$, $\mathrm{Re} = \frac{D_2 W_b}{\nu}$, and $Ha = B_y D_1 \sqrt{\frac{\sigma}{\rho \nu}}$.

Channel: $D_1 = \delta$, $D_2 = 2\delta$ ($\delta = 0.5$ is half channel height)

Square duct: $D_1 = D_2 = D$, ($D = 1$ is the side of the square duct)

Table 4.4 Time taken per iteration (sec) / # of iterations in final convergence by FLUENT with various models, wall treatment methods and Reynolds numbers in non-MHD channel flow for final grids

Turbulence Model	Wall treatment method	Re=4586	Re=4586	Re=45818	
		120x10x10	100x10x10	139x10x10	30x10x10
RKE	En wall treatment	-	0.19 / 2289	0.22 / 3818	-
	Non-eq wall fn	-	-	-	0.11 / 1227
	Std wall fn	-	-	-	0.11 / 1227
SKE	En wall treatment	-	0.19/ 2289	0.23 / 3195	-
	Non-eq wall fn	-	-	-	0.11 / 954
	Std wall fn	-	-	-	0.11 / 954
RNG	En wall treatment	-	0.20 / 2700	0.24 / 3125	-
	Non-eq wall fn	-	-	-	0.11 / 954
	Std wall fn	-	-	-	0.11 / 954
RSM-LPS	En wall treatment	-	0.21 / 55033	0.29 / 38689	-
	Non-eq wall fn	-	-	-	0.14 / 2464
	Std wall fn	-	-	-	0.13 / 3115
RSM-Sω	Low-Re RSM model	-	0.22 / 4568	-	-
Abid	Low-Re k-ε model	0.20 / 5400	-	-	-
LB	Low-Re k-ε model	0.20 / 3150	-	-	-
LS	Low-Re k-ε model	0.20 / 3075	-		
YS	Low-Re k-ε model	0.20 / 17700	-	-	-
AKN	Low-Re k-ε model	0.21 / 4571	-	-	-
CHC	Low-Re k-ε model	0.21 / 5214	-	-	-

Table 4.5 Mean streamwise pressure gradient in different flows predicted by various models

	Channel (Re=45818)	Channel (Re=4586)	Channel (Re=4710, Ha=6) Mag-Ind Method		Square duct (Re=5466)	Square duct (Re=5602, Ha=21.2) Mag-Ind/Elec Pot Methods	
			With MHD sources	Without MHD sources		With MHD sources	Without MHD sources
DNS	2.0	2.0	2.0		4.0	0.01857	
RKE-EWT	1.97	2.20	-	-	4.46	0.0228/0.0228	-
SKE-EWT	2.02	2.20	2.40	2.47	4.46	-	-
RNG-EWT	1.99	2.20	-	-	-	-	-
RSM-LPS-EWT	2.08	2.16	2.37	2.42	5.0	0.0244	-
RKE-NWF	1.83	-	-	-	-	-	-
SKE-NWF	1.90	-	-	-	-	-	-
RNG-NEWF	1.83	-	-	-	-	-	-
RSM-LPS-NEWF	1.84	-	-	-	-	-	-
RKE-SWF	1.85	-	-	-	-	-	-
SKE-SWF	1.94	-	-	-	-	-	-
RNG-SWF	1.89	-	-	-	-	-	-
RSM-LPS-SWF	1.85	-	-	-	-	-	-
RSM-Sω	-	1.94	-	-	-	-	-
Abid	-	2.07	-	-	-	-	-
LB	-	1.97	2.04	2.18	4.28	0.0190	0.0215
LS	-	3.87	-	-	-	-	-
YS	-	2.13	-	-	-	-	-
AKN	-	2.11	-	-	-	-	-
CHC	-	1.68	-	-	-	-	-

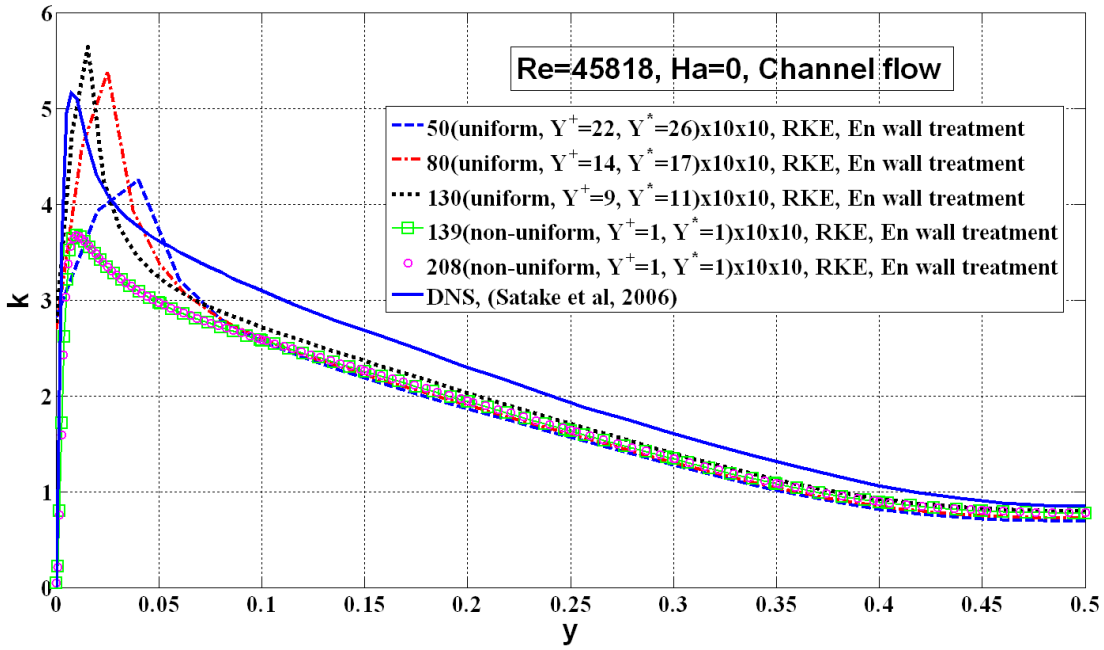

Figure 4.1 Grid independence study in high-Re channel flow for RKE with EWT

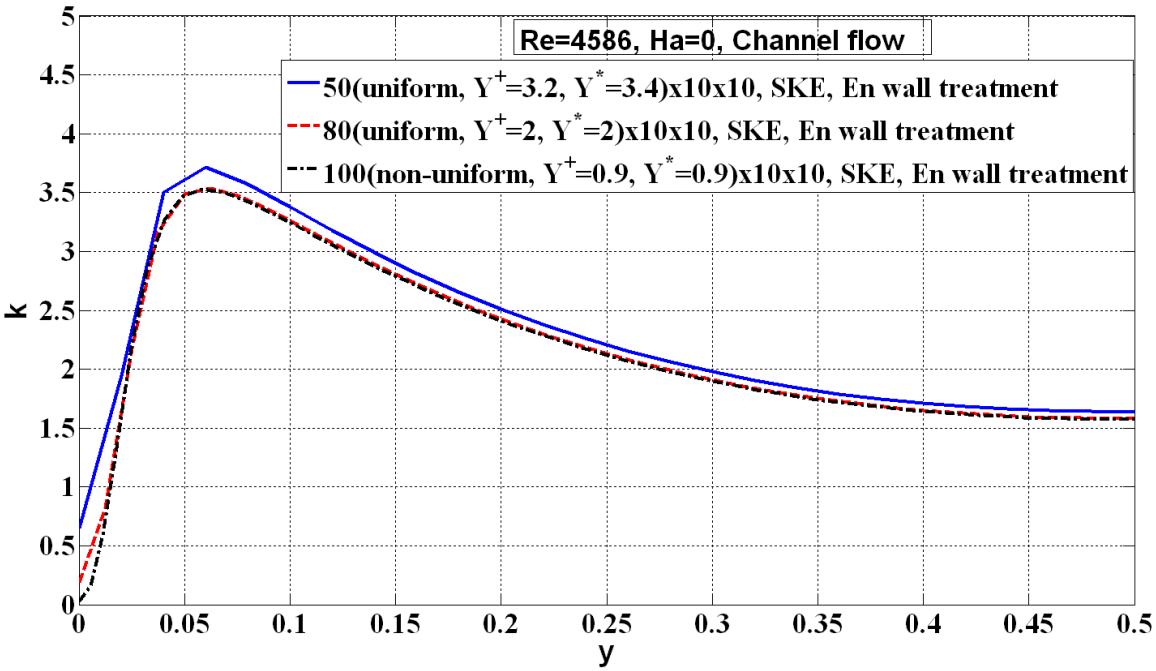

Figure 4.2 Grid independence study in low-Re channel flow for SKE with EWT

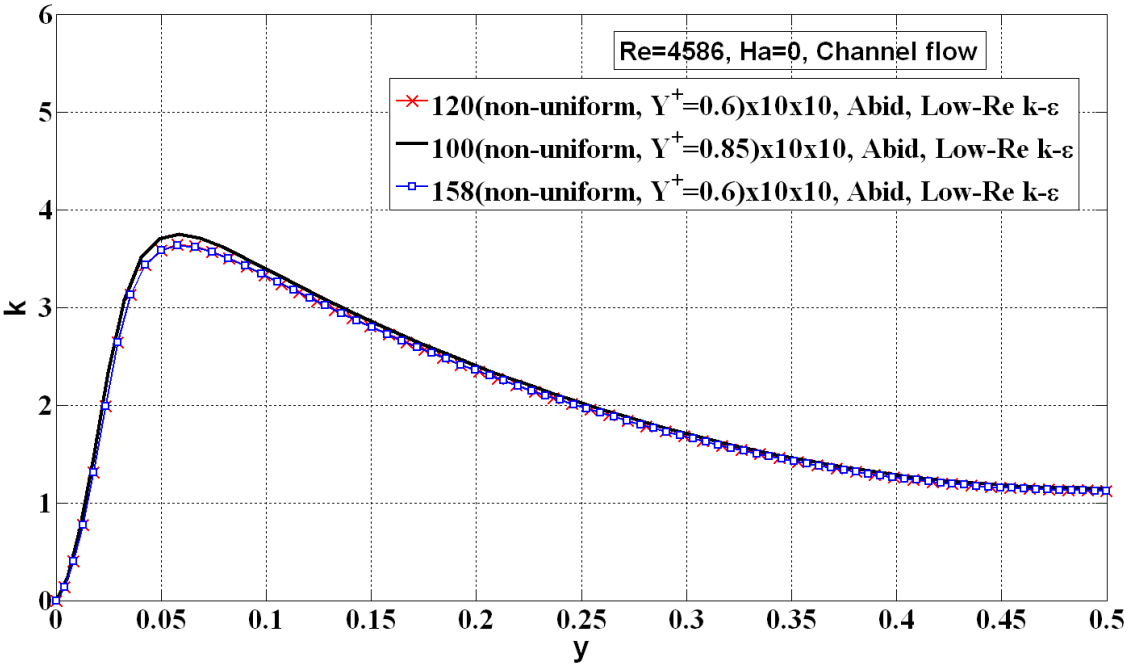

Figure 4.3 Grid independence study in low-Re channel flow for Abid low-Re k-ε model

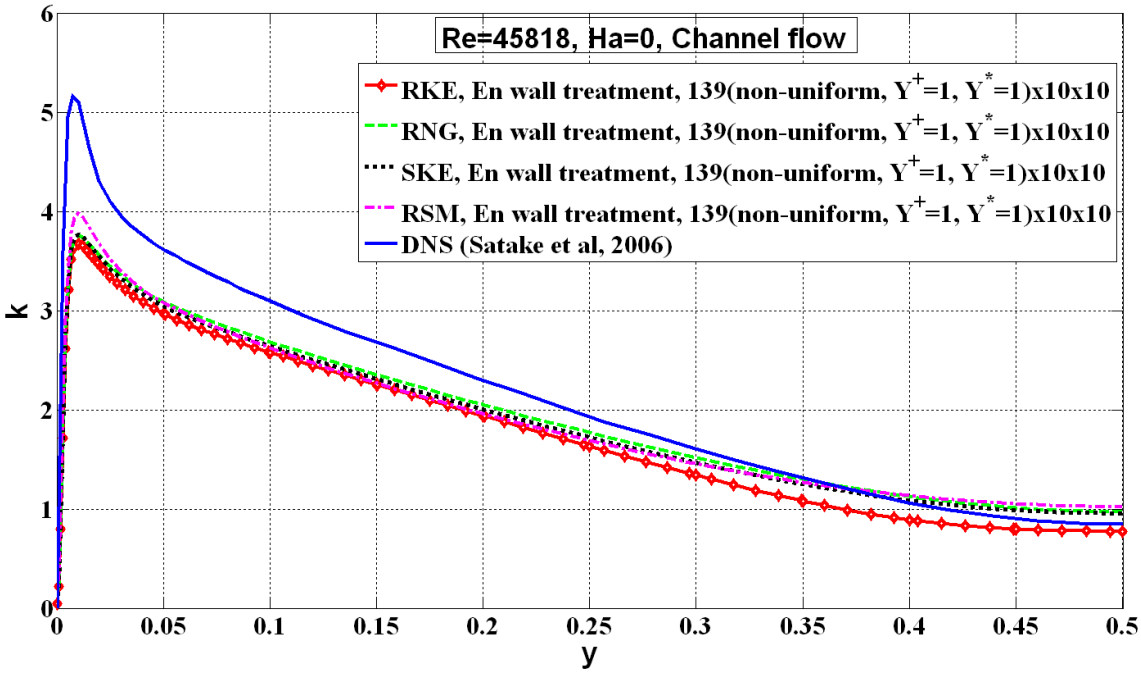

Figure 4.4 Comparison of TKE in various models with EWT in high-Re channel flow

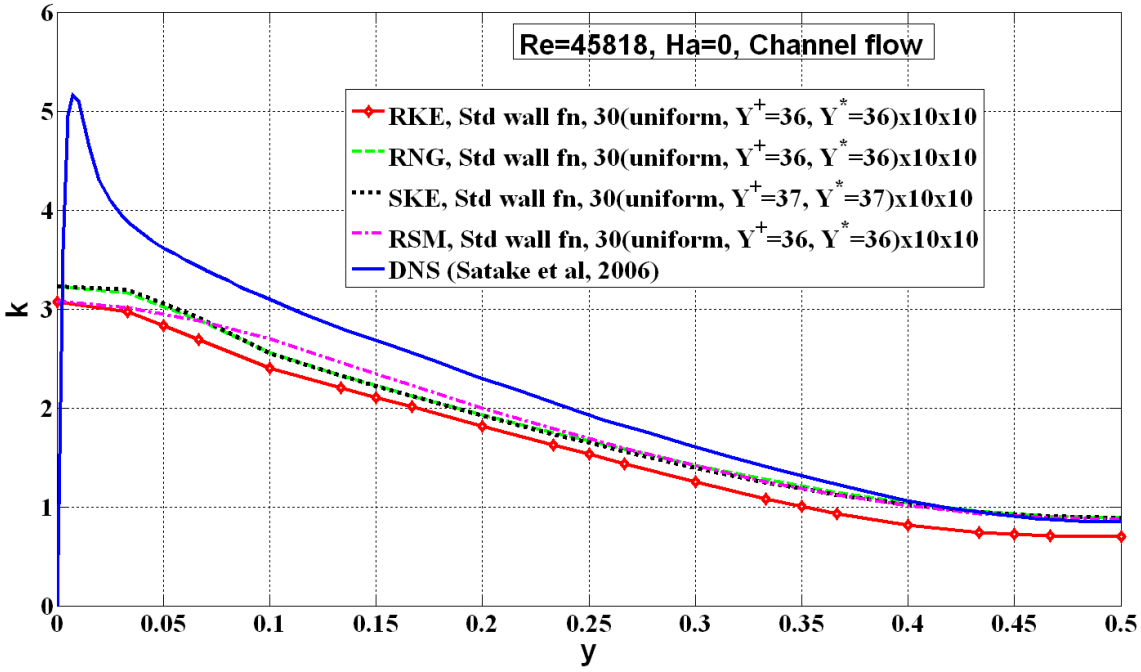

Figure 4.5 Comparison of TKE in various models with SWF approach in high-Re channel flow

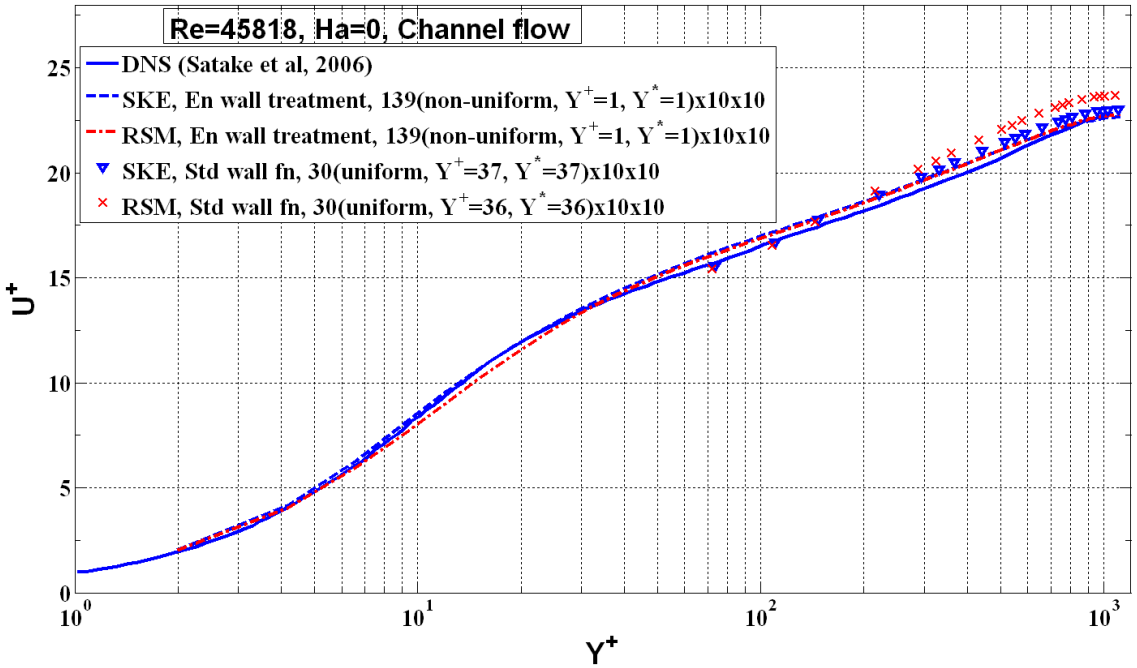

Figure 4.6 Comparison of normalized mean axial velocity in SKE and RSM-LPS with SWF and EWT in high-Re channel flow

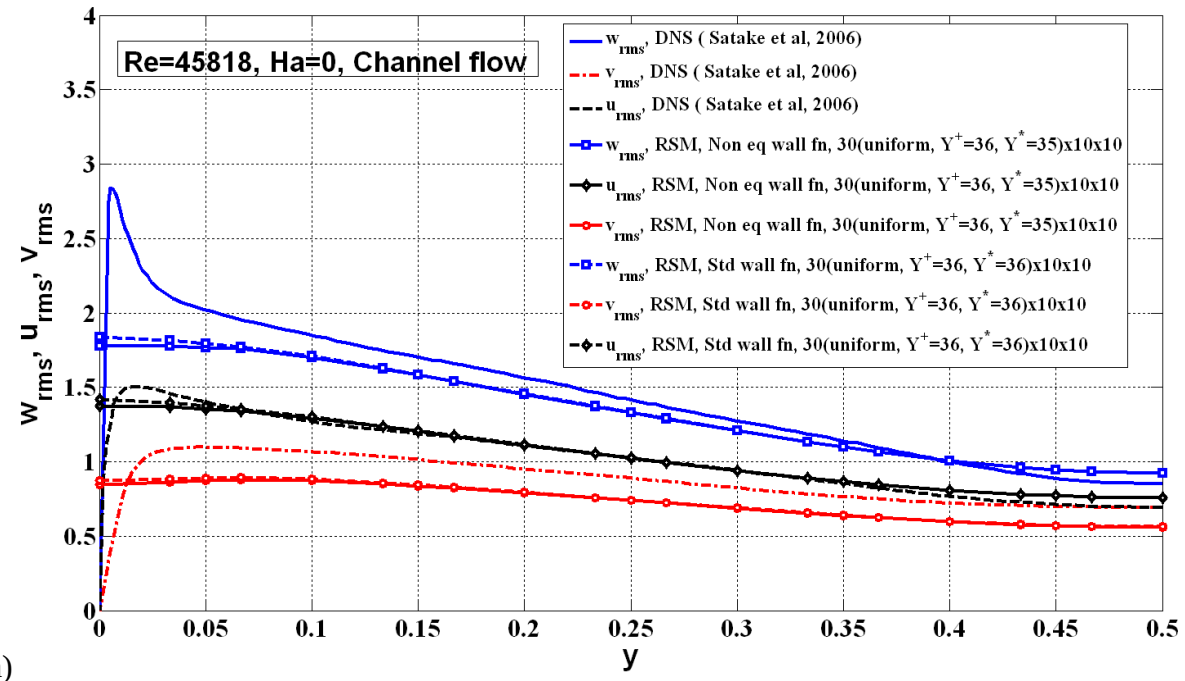

(a)

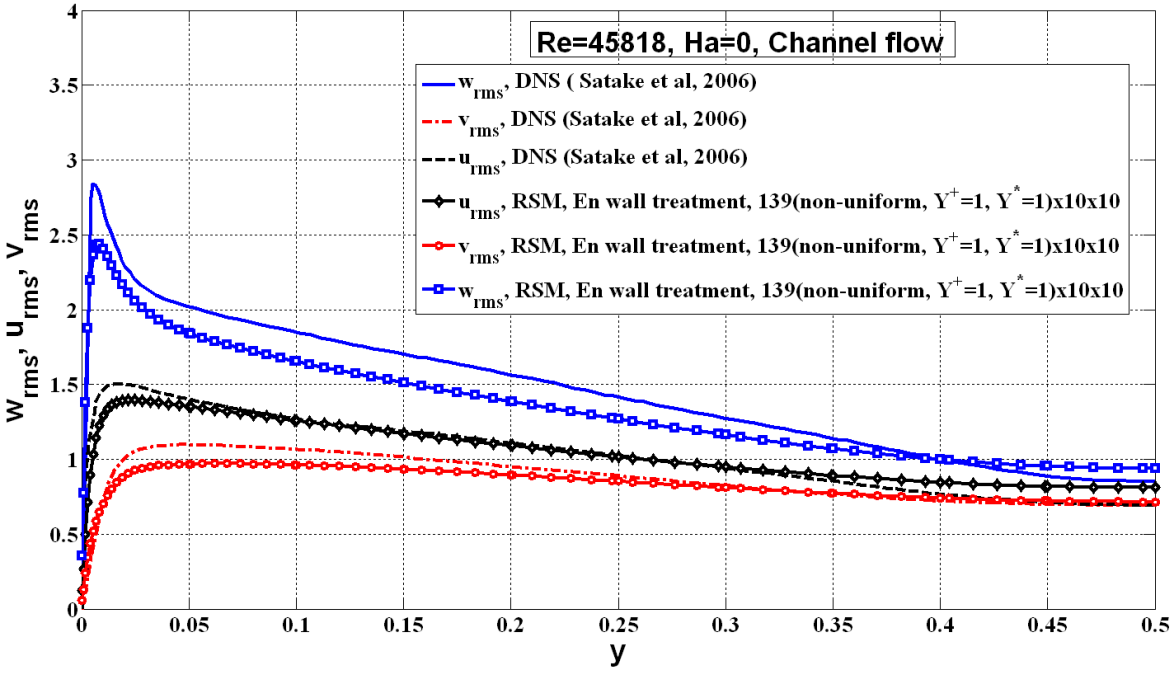

(b)

Figure 4.7 Comparison of RMS of velocity fluctuations in RSM-linear-pressure-strain with (a) NEWF and SWF (b) EWT in high-Re channel flow

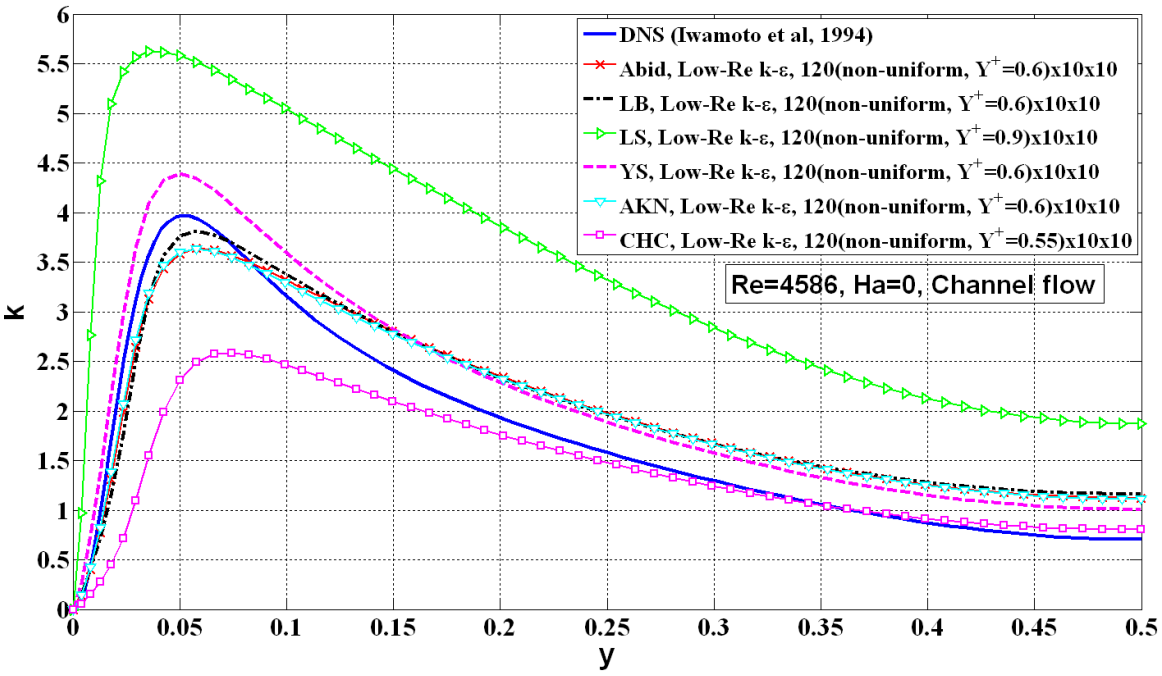

Figure 4.8 Comparison of TKE predicted by low-Re k-ε models with the DNS in low-Re channel flow

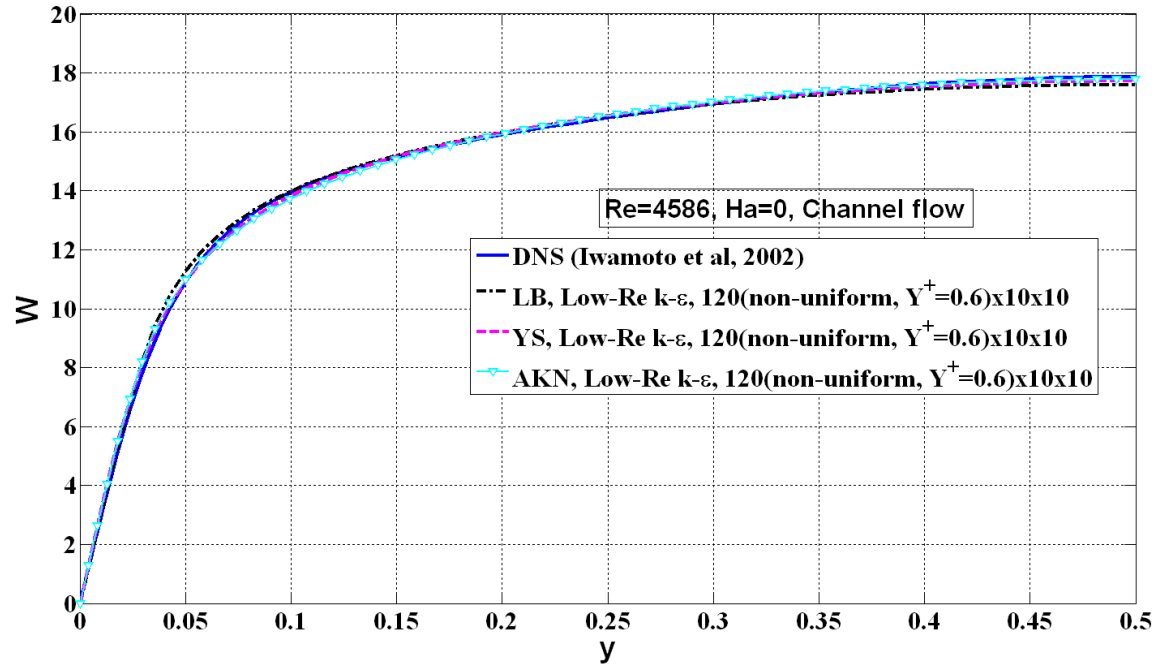

Figure 4.9 Comparison of the mean axial velocity predicted by low-Re k-ε models with the DNS in low-Re channel flow

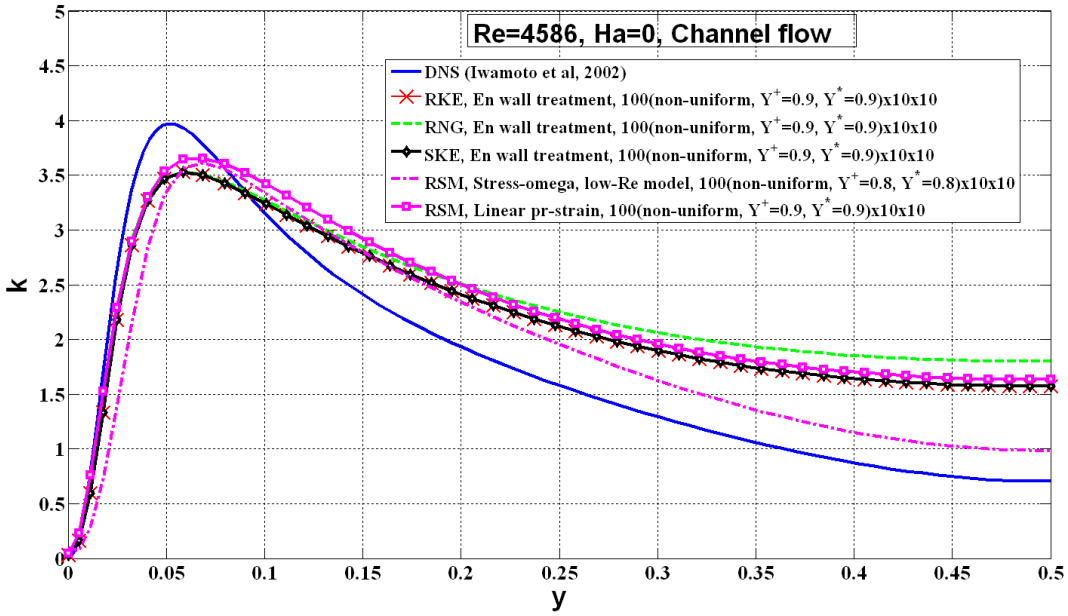

Figure 4.10 Comparison of TKE predicted by RKE, RNG, SKE and RSM-LPS with EWT and low-Re RSM-Sω turbulence models with the DNS in the low-Re channel flow

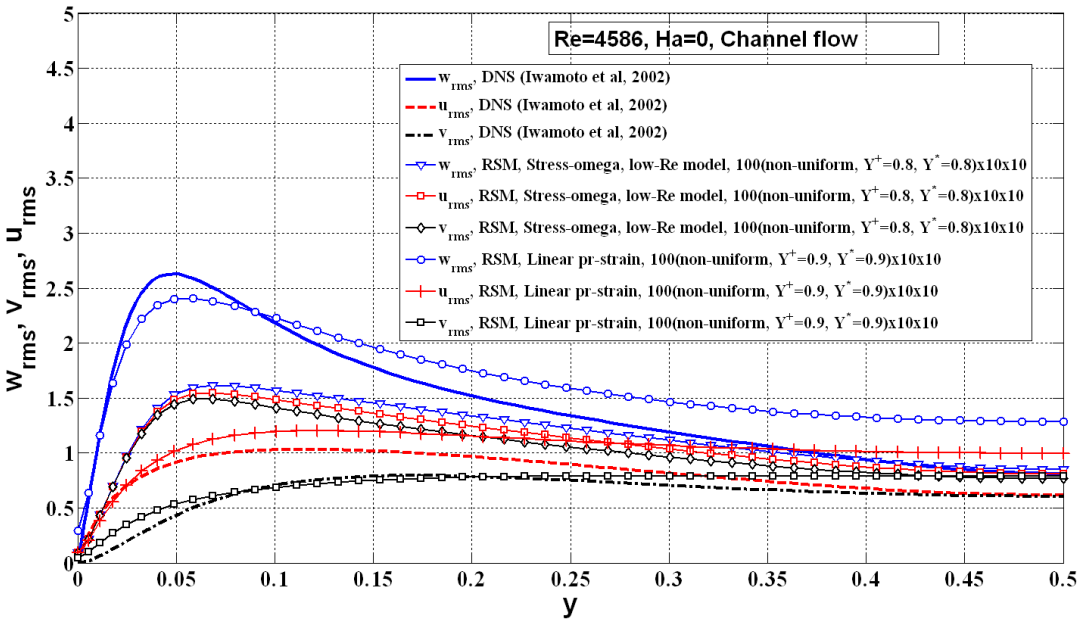

Figure 4.11 Comparison of RMS of velocity fluctuations by RSM models with the DNS in low-Re channel flow

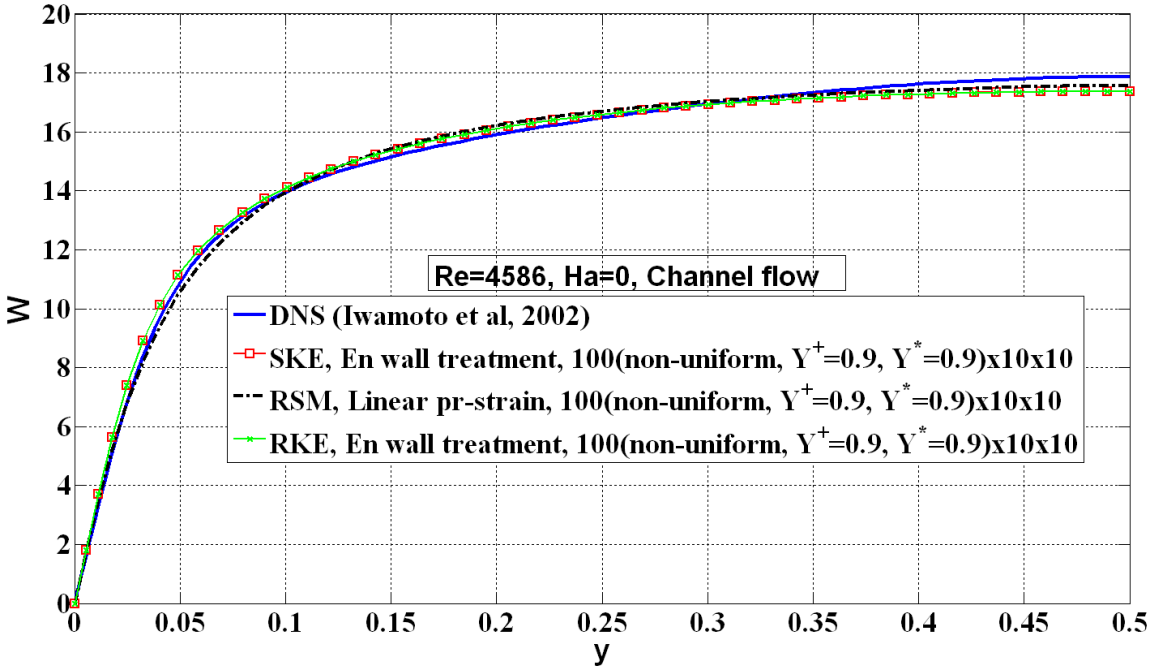

Figure 4.12 Comparison of mean axial velocity by SKE, RKE, RSM-LPS models with EWT with the DNS in low-Re channel flow

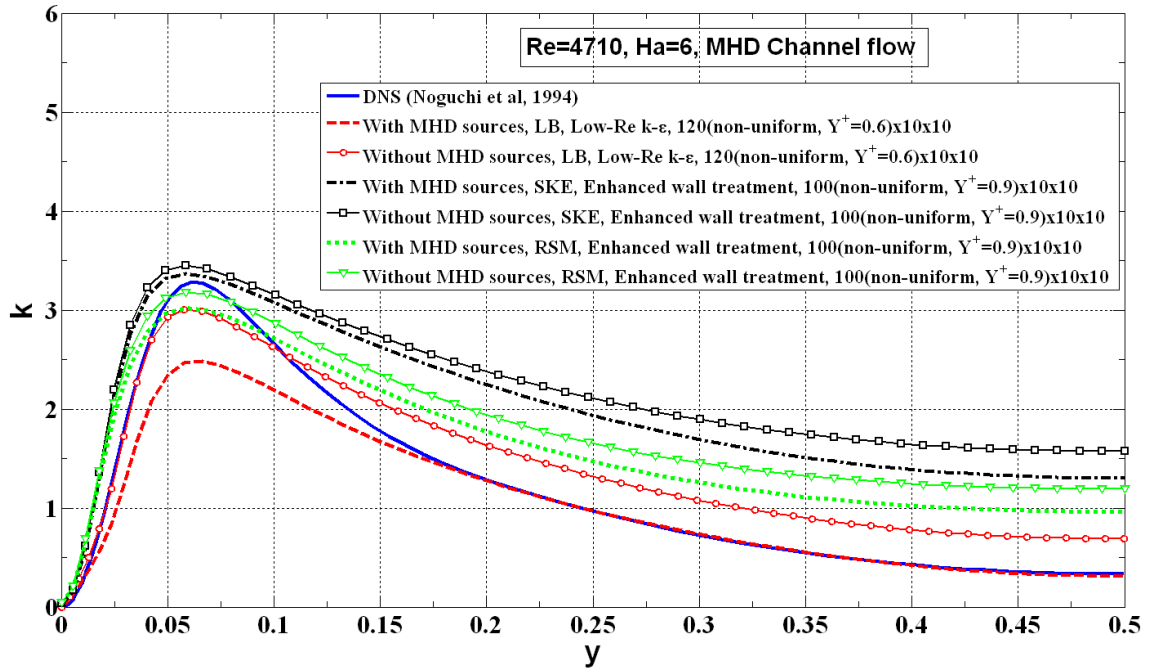

Figure 4.13 Comparison of TKE in low-Re MHD channel flow with various models

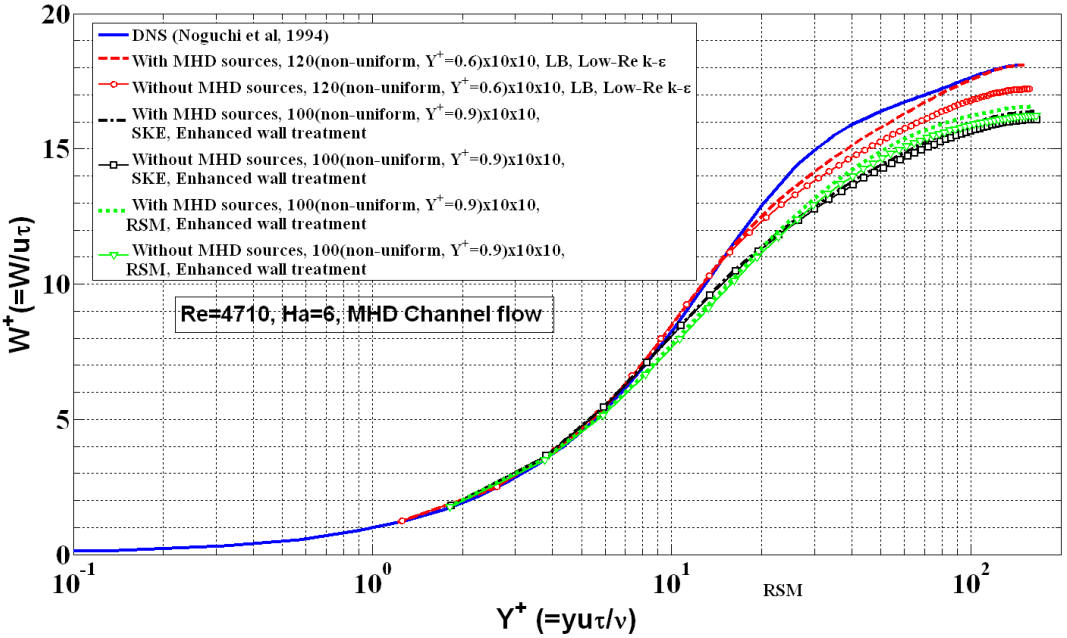

Figure 4.14 Comparison of normalized mean axial velocity vs. normalized wall distance in wall units in low-Re MHD channel flow in various models

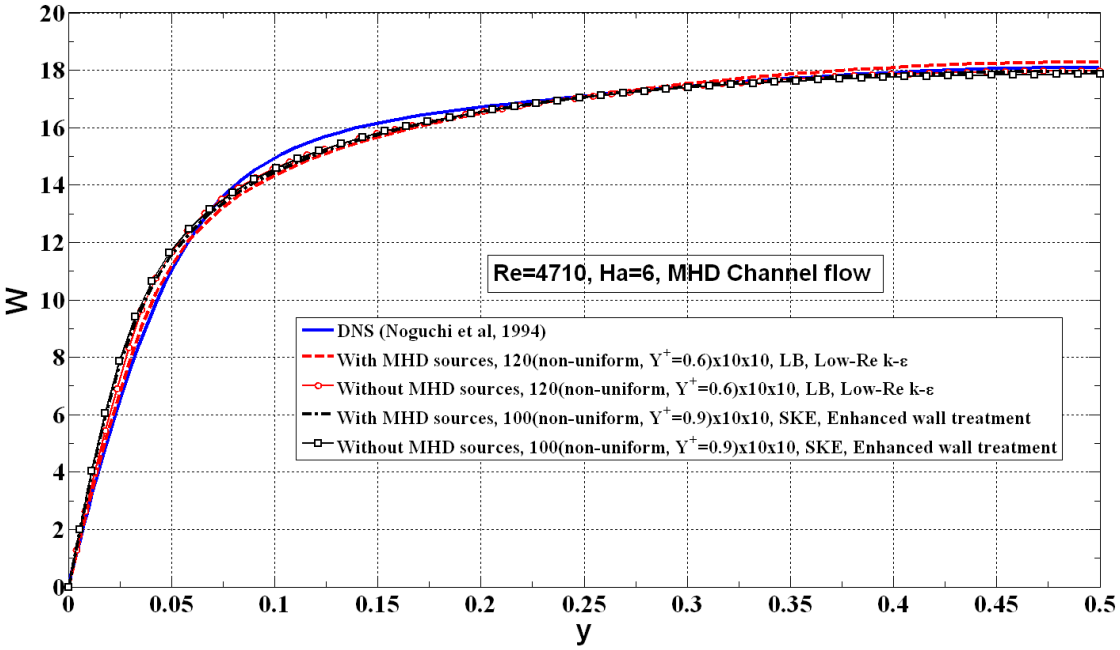

Figure 4.15 Comparison of mean axial velocity vs. distance from the wall in low-Re MHD channel flow in LB and SKE models

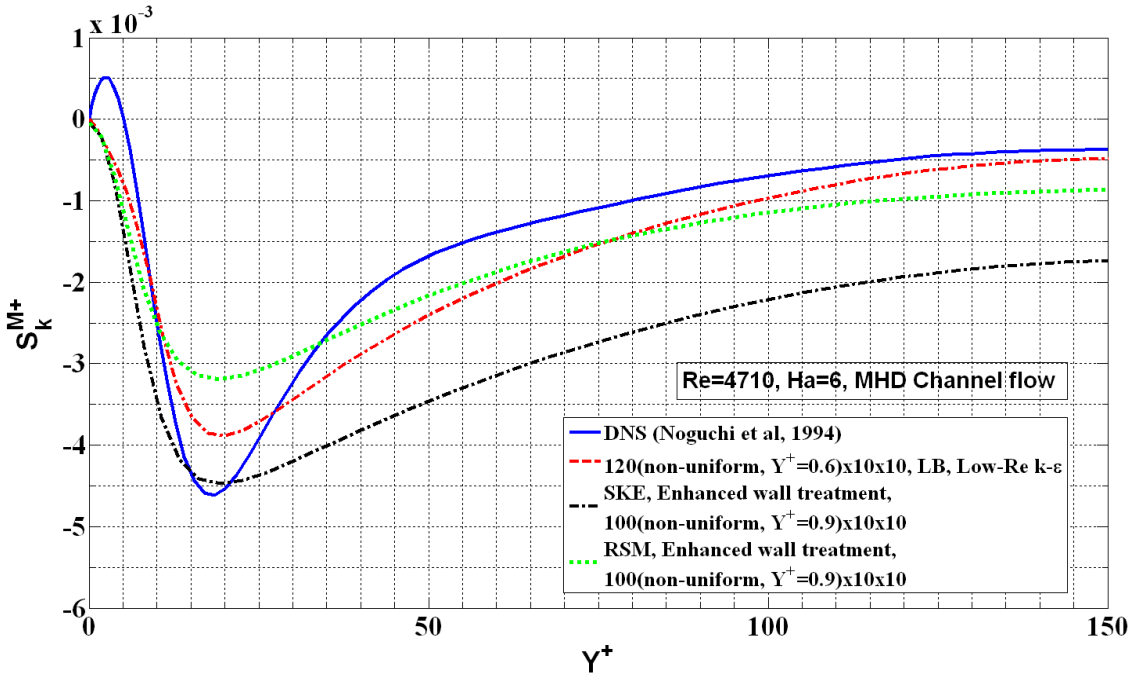

Figure 4.16 Comparison of the MHD source/sink in the k-equation / budget (DNS) in low-Re MHD channel flow in various models with the DNS

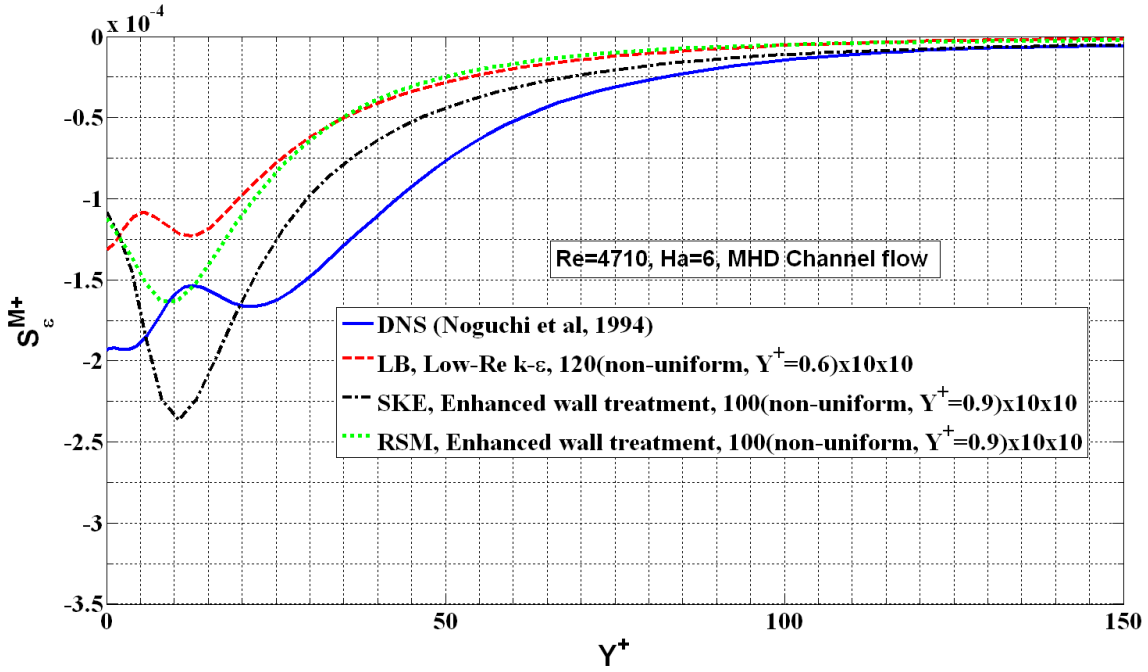

Figure 4.17 Comparison of MHD sink in ε-equation / budget (DNS) in low-Re MHD channel flow in various models with the DNS

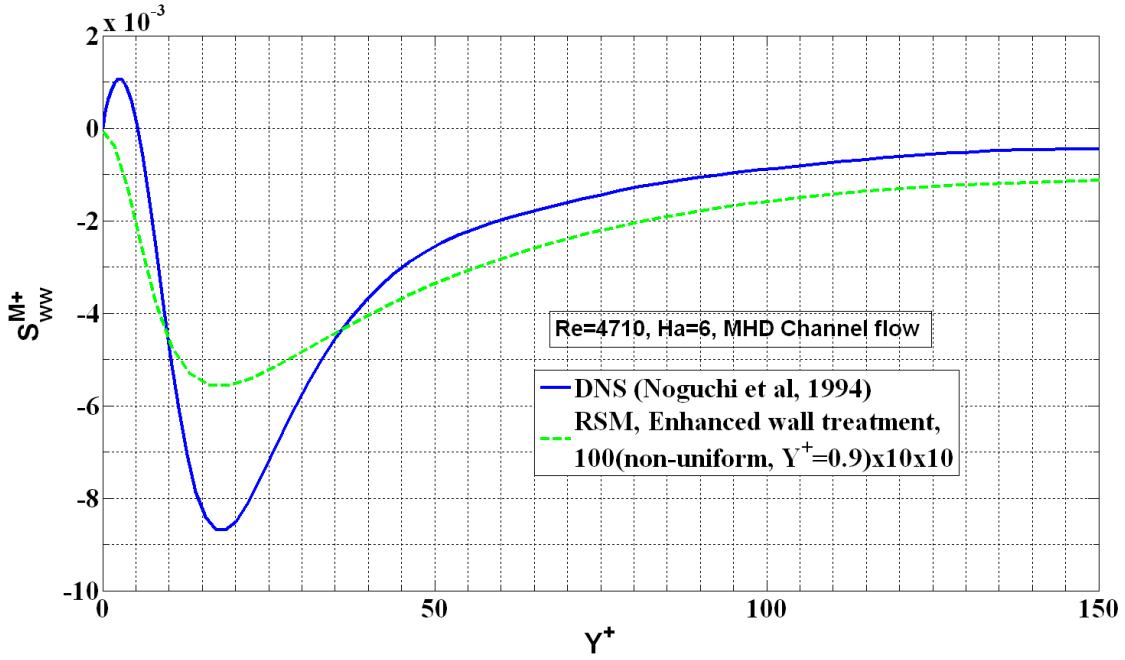

Figure 4.18 Comparison of the MHD source/sink in $\overline{w'w'}$-equation / budget (DNS) in low-Re MHD channel flow in RSM-LPS model with the DNS

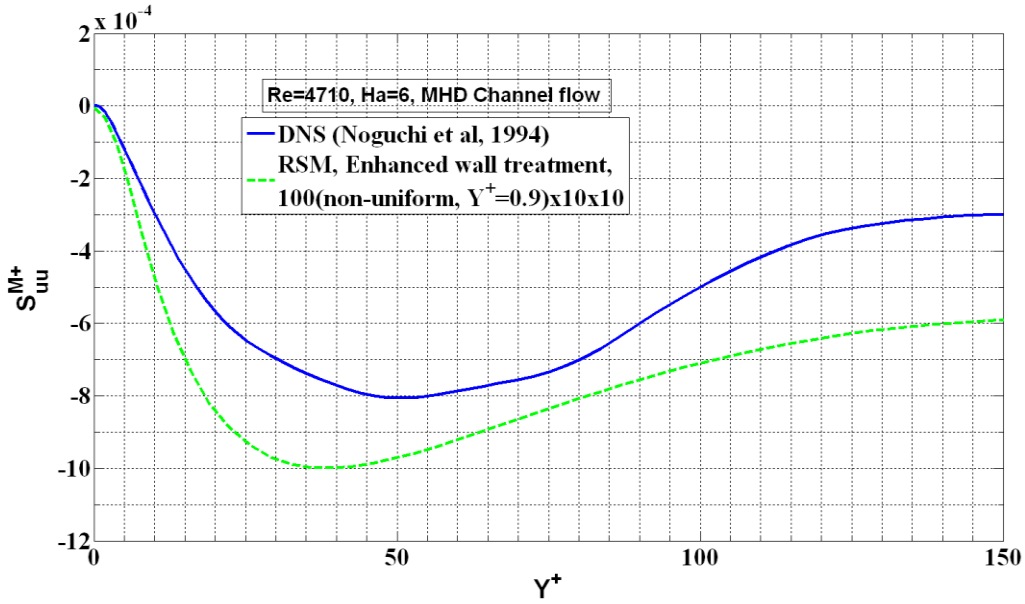

Figure 4.19 Comparison of MHD source/sink in $\overline{u'u'}$-equation / budget (DNS) in low-Re MHD channel flow in RSM-LPS model with DNS

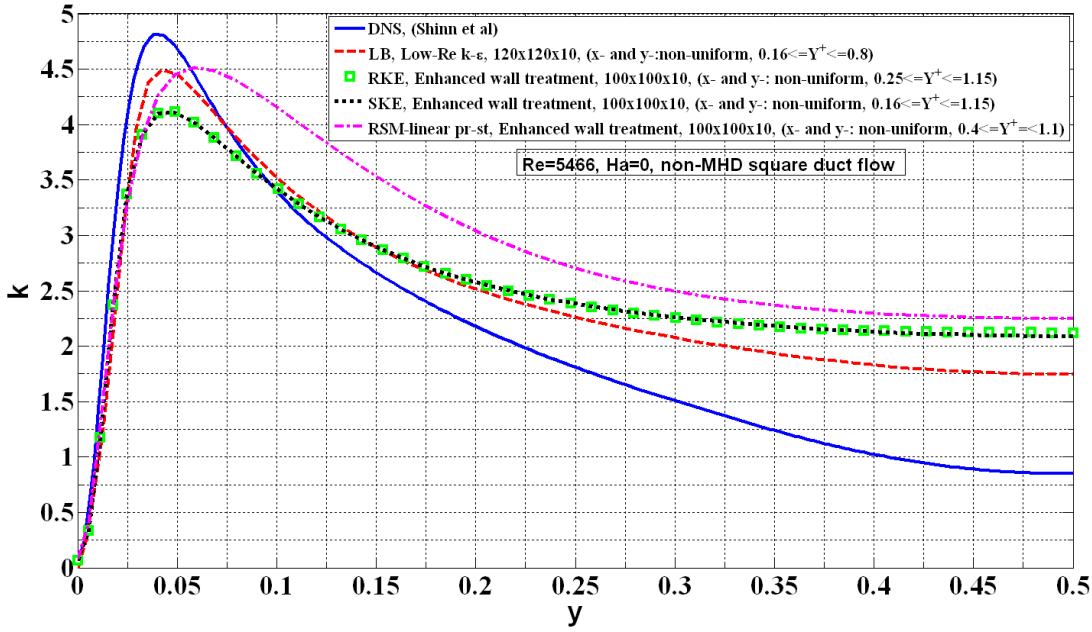

Figure 4.20 Comparison of TKE predicted by various models with DNS in non-MHD square duct along vertical bisector

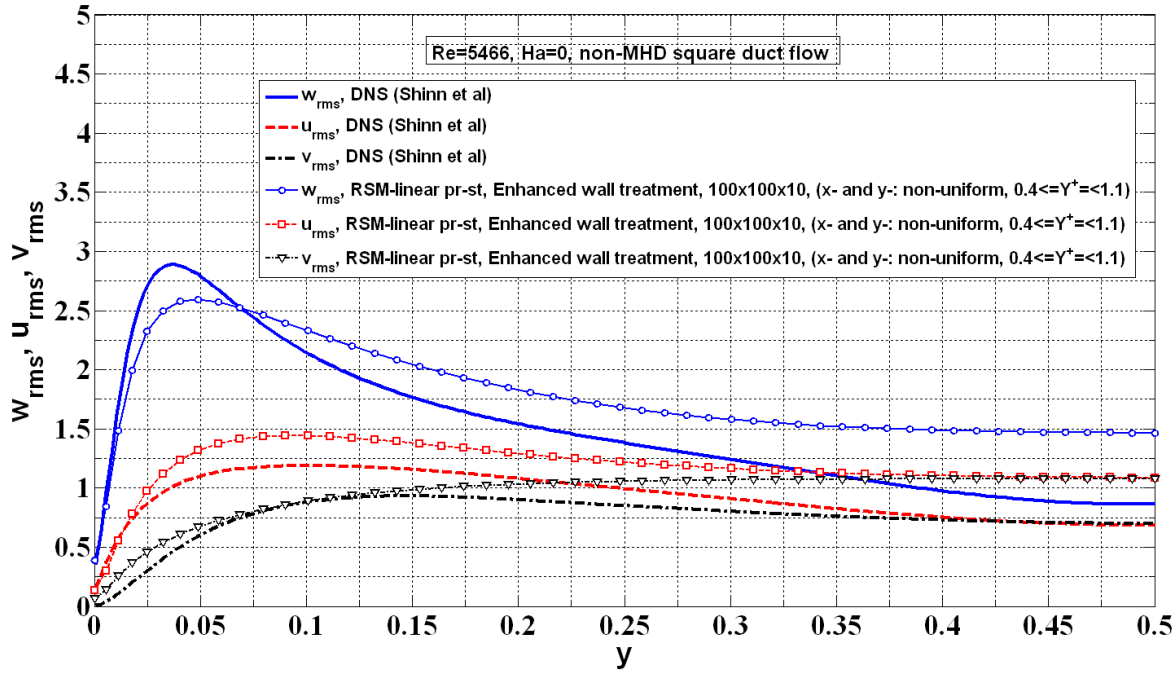

Figure 4.21 Comparison of RMS of velocity fluctuations predicted by RSM-LPS model with the DNS in non-MHD square duct along vertical bisector

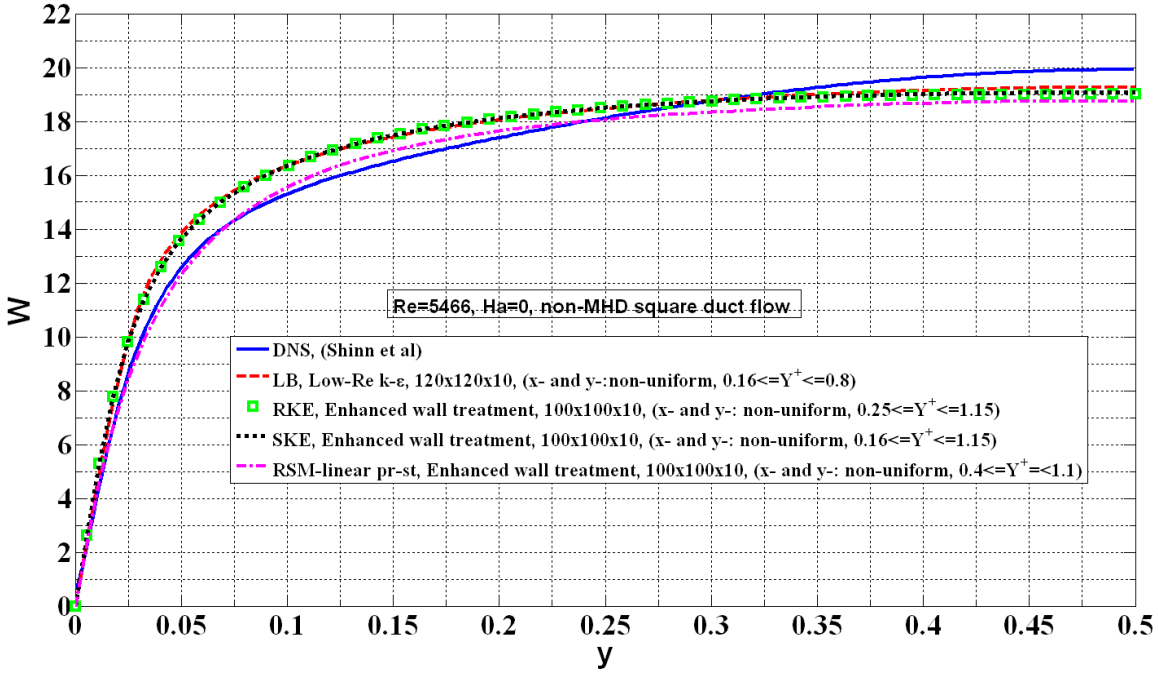

Figure 4.22 Comparison of mean axial velocity predicted by various models with the DNS in non-MHD square duct along vertical bisector

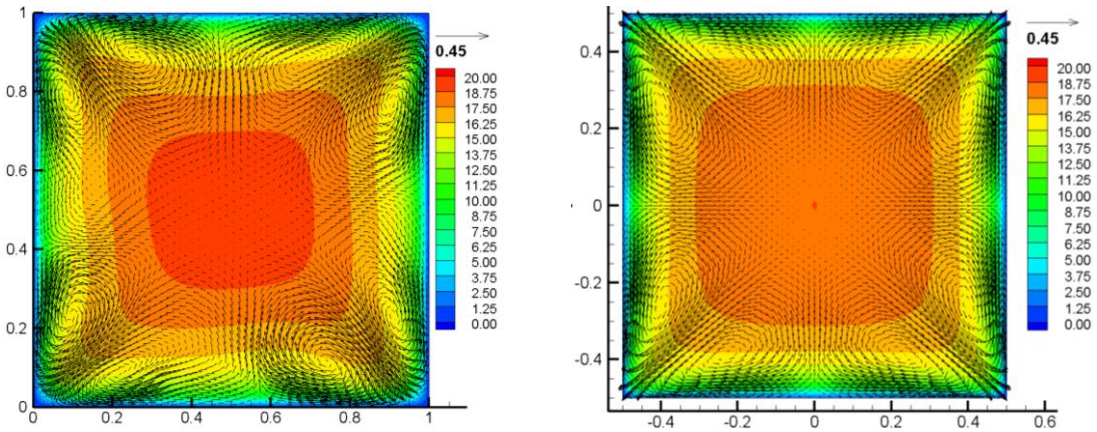

(a) DNS (Re=5466, Ha=0, Shinn et al [51]) (160x160x1024)

(b) RSM-linear-pr-strain, En wall treatment (Re=5466, Ha=0, 100x100x10)

Figure 4.23 Comparison of mean axial velocity contours and secondary velocity vectors in non-MHD square duct

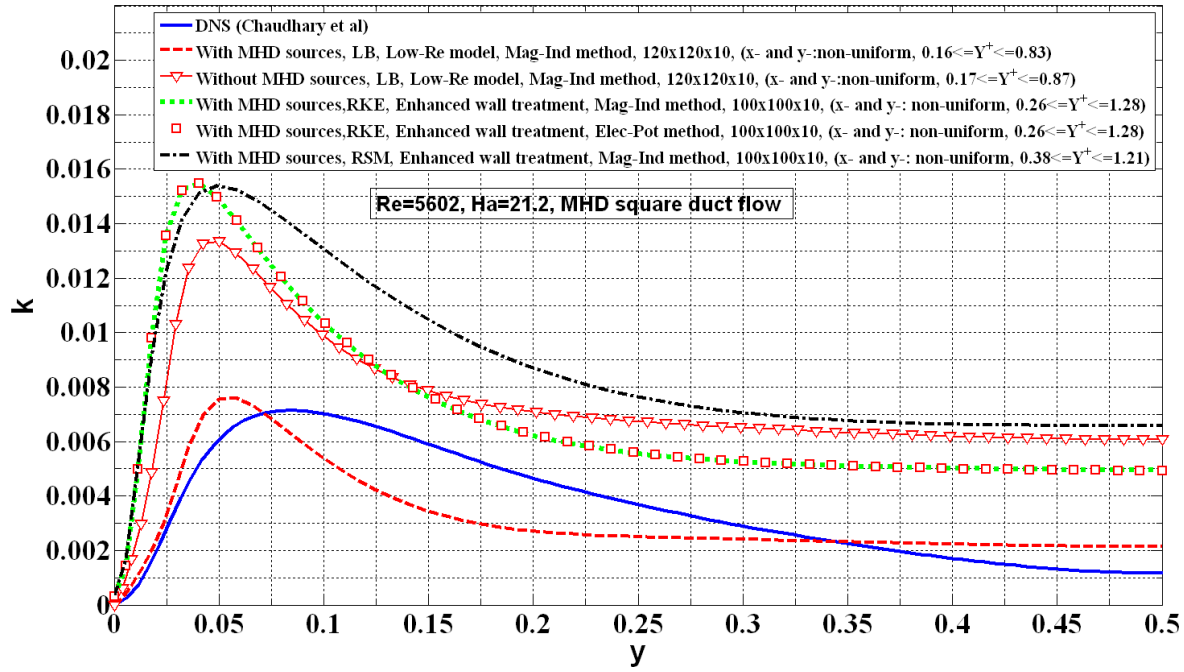

Figure 4.24 Comparison of TKE in various models with the DNS in MHD square duct along vertical bisector

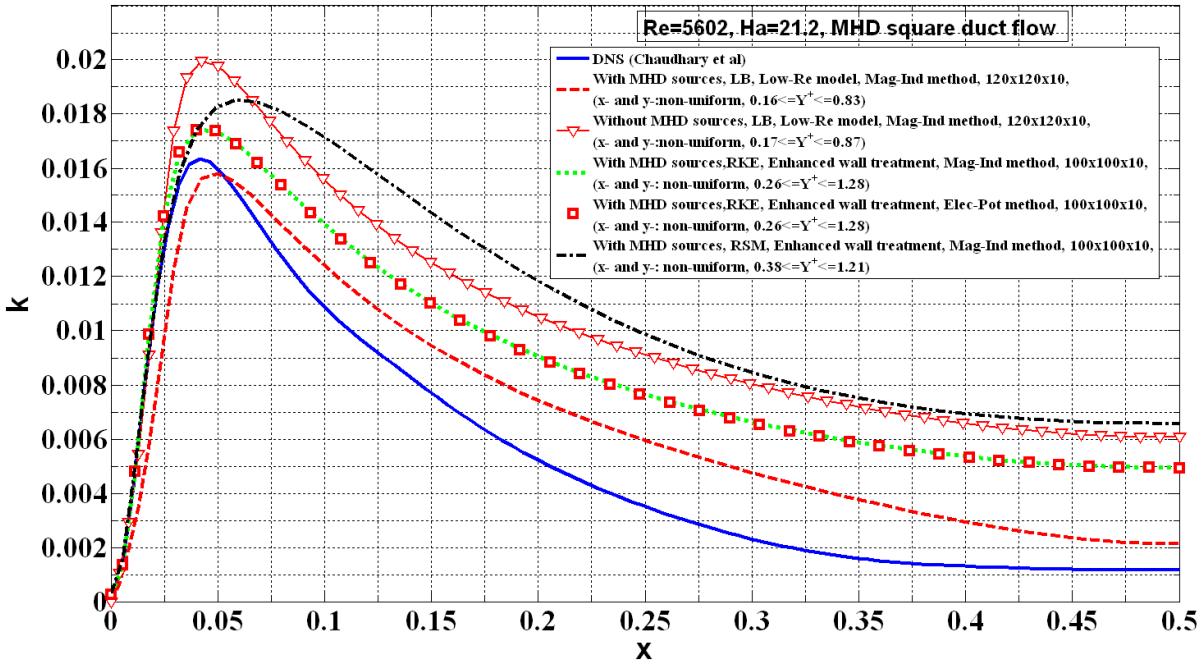

Figure 4.25 Comparison of TKE in various models with the DNS in MHD square duct along horizontal bisector

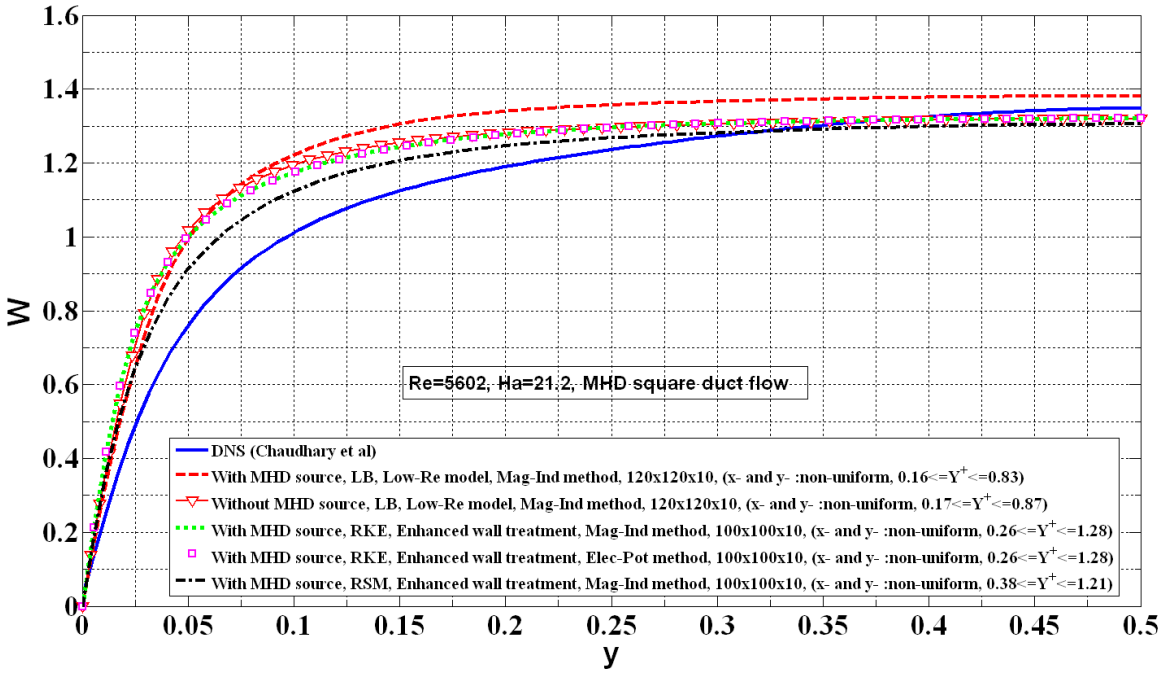

Figure 4.26 Comparison of the mean axial velocity predicted by various models with the DNS in MHD square duct along vertical bisector

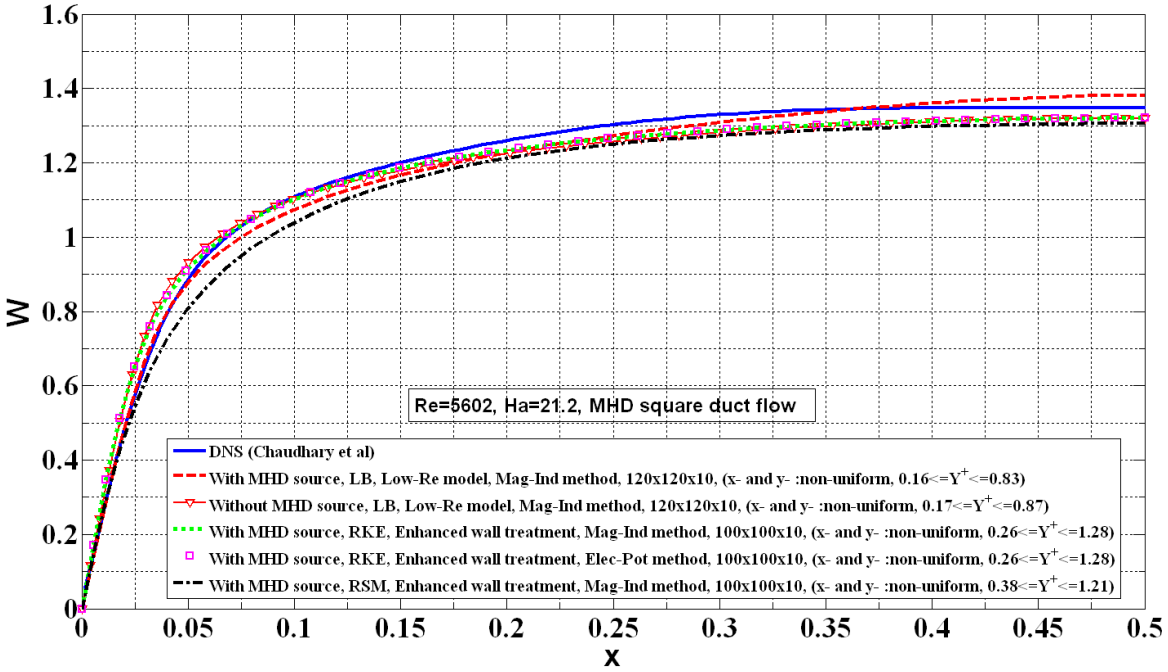

Figure 4.27 Comparison of mean axial velocity in various models with DNS in MHD square duct along horizontal bisector

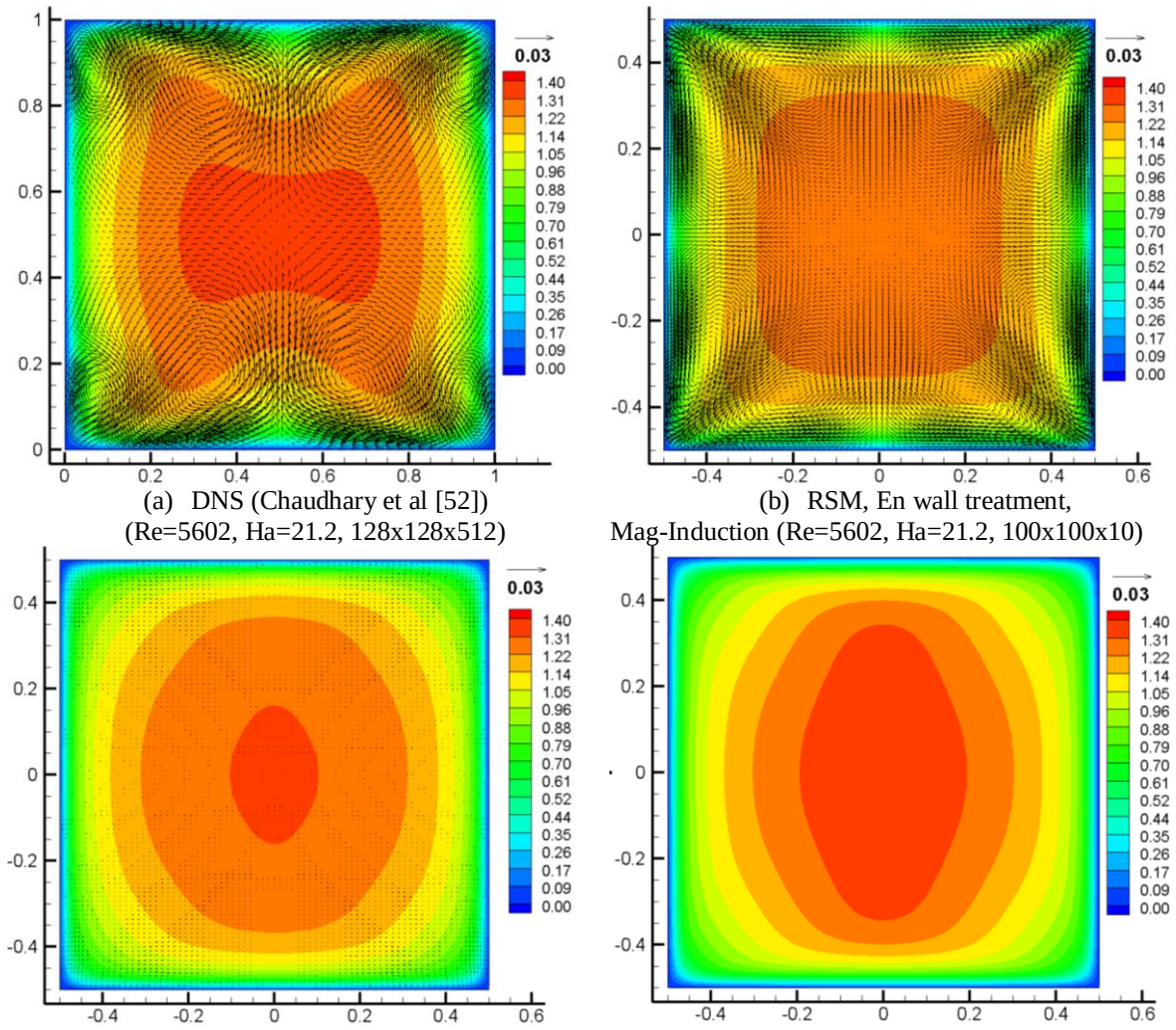

(a) DNS (Chaudhary et al [52]) (Re=5602, Ha=21.2, 128x128x512)

(b) RSM, En wall treatment, Mag-Induction (Re=5602, Ha=21.2, 100x100x10)

(c) Realizable k-ε, En wall treatment, Mag-Induction (Re=5602, Ha=21.2, 100x100x10)

(d) LB, Low-Re k-ε, Mag-Induction (Re=5602, Ha=21.2, 120x120x10)

Figure 4.28 Comparison of mean axial velocity contours and secondary velocity vectors in MHD duct

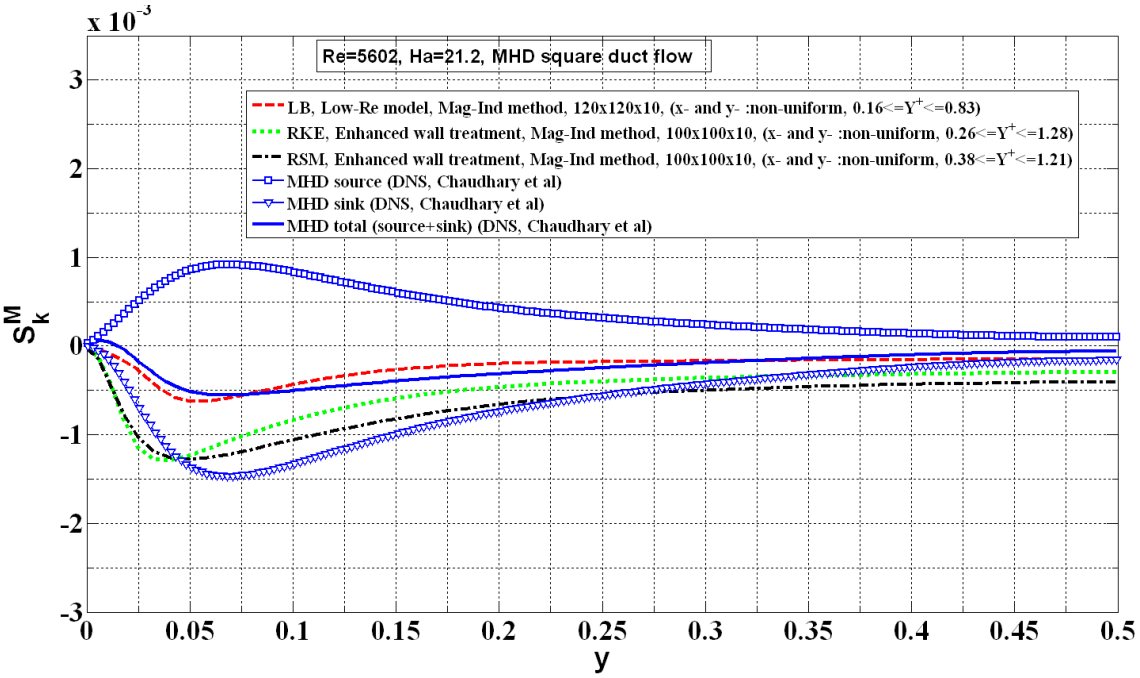

Figure 4.29 Comparison of MHD source/sink in k-equation / budget (DNS) predicted by various models with the DNS in MHD square duct along vertical bisector

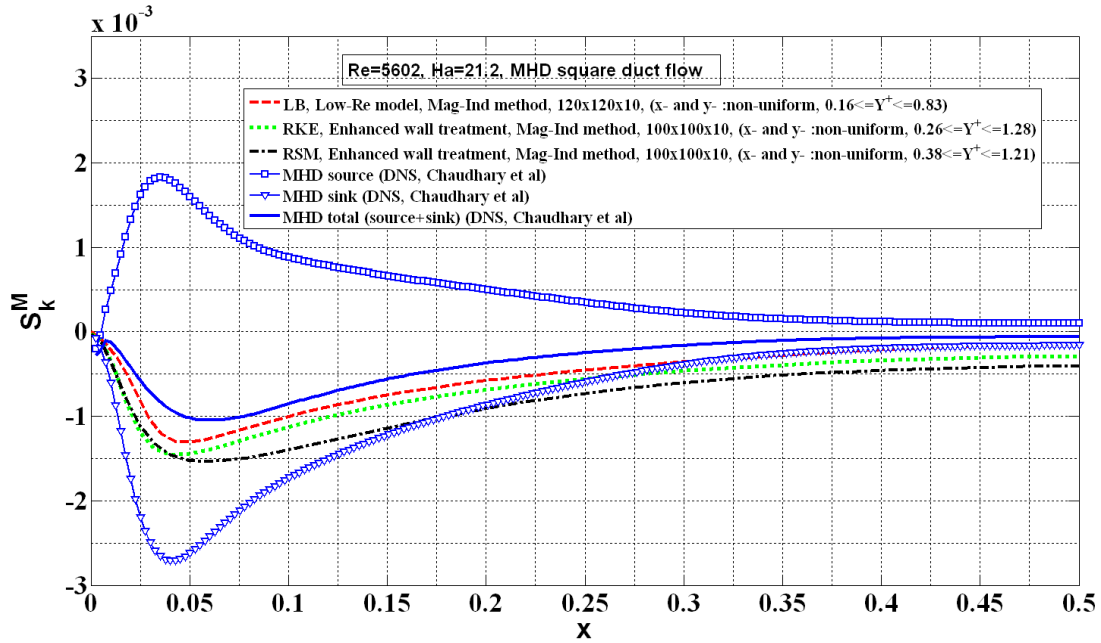

Figure 4.30 Comparison of MHD source/sink in k-equation / budget (DNS) in various models with the DNS in MHD square duct along horizontal bisector

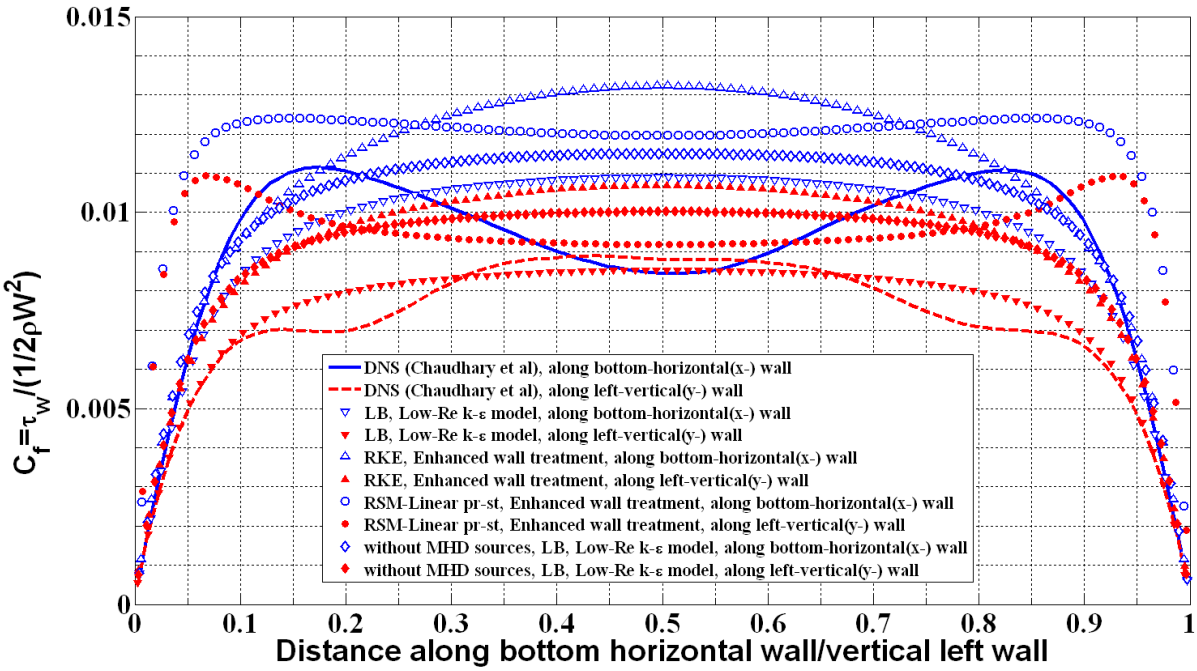

Figure 4.31 Comparison of the friction factor in MHD square duct along bottom-horizontal and left-vertical walls in various models with the DNS

4.8. References

1. C. G. Speziale, Analytical methods for the development of Reynolds-stress closures in turbulence, Annu. Rev. Fluid Mech., 1991, Vol. 23, pp. 107–57.
2. C. M. Hrenya, E. J. Bolio, D. Chakrabarti, and J. L. Sinclair, Comparison of low Reynolds number k-ε turbulence models in predicting fully developed pipe flow, Chemical Engineering Science, 1995, Vol. 50, No. 12, pp. 1923-1941.
3. R. Martinuzzi and A. Pollard, Comparative study of turbulence models in predicting turbulent pipe flow Part I: Algebraic stress and k-ε models, AIAA Journal, 1989, Vol. 27, No. 1, pp. 29-36.
4. A. Pollard, and R. Martinuzzi, Comparative study of turbulence models in predicting turbulent pipe flow Part II: Reynolds stress and k-ε models, AIAA Journal, 1989, Vol. 27, No. 12, pp. 1714-1721.
5. S. Thangam, and C. G. Speziale, Turbulent separated flow past a backward-facing step: A critical evaluation of two-equation turbulence models, NASA contractor Report 187532, 1991, ICASE Report No. 91023.
6. C. J. Steffen, Critical comparison of several low Reynolds number k-ε turbulence models for flow over backward facing step, AIAA, 1993, 93-1927, 29th AIAA, SAE, ASME and ASEE, Joint Propulsion Conference and Exhibit.
7. J.-Y. Kim, A. J. Ghajar, C. Tang, and G. L. Foutch, Comparison of near-wall treatment methods for high Reynolds number backward-facing step flow, Int. J. of Computational Fluid Dynamics, 2005, Vol. 19, No. 7, pp. 493-500.

8. S. H. Seyedein, M. Hasan, A. S. Majumdar, Modeling of a single confined slot jot impingement using various k-ε turbulence models, Appl. Math. Modeling, 1994, Vol. 18, pp. 526-537.

9. E. W. Miner, T. F. Swean Jr., R. A. Handler, and R. I. Leighton, Examination of wall damping for the k-ε turbulence model using direct simulation of turbulent channel flow, Int. J. for Numerical Methods in Fluids, 1991, Vol. 12, pp. 609-624.

10. T. Kobayashi, and S. Togashi, Comparison of turbulence models applied to backward-facing step flow, JSME International Journal, 1996, Series B, Vol. 39, No. 3, pp. 453-460.

11. X.-D. Yang, H.-Y. Ma, Y.-N. Huang, Prediction of homogeneous shear flow and a backward-facing step flow with some linear and non-linear k-ε turbulence models, Communications in Nonlinear Science and Numerical Simulation, 2005, Vol. 10, pp. 315-328.

12. S. Kenjereš, K. Hanjalić, On the implementation of effects of Lorentz force in turbulence closure models. Int. J. Heat Fluid Flow, 2000, Vol. 21, pp. 329-337.

13. S. Kenjereš, K. Hanjalić and D. Bal, A direct-numerical-simulation-based second-moment closure for turbulent magnetohydrodynamic flows, Phys. Fluids, 2004, Vol. 16, No. 5, pp. 1229-1241.

14. H-C Ji, R. A. Gardner, Numerical analysis of turbulent pipe flow in a transverse magnetic field. Int. J. Heat Mass Transf., 1997, Vol. 40, pp. 1839-1851.

15. S. Smolentsev, M. Abdou, N. Morley, A. Ying, T. Kunugi, Application of the "k-ε" model to open channel flows in a magnetic field, Int. J. Eng. Sci., 2002, Vol. 40, pp. 693-711

16. T. Kajishima, and Y. Miyake, A discussion on eddy viscosity models on the basis of the large eddy simulation of turbulent flow in a square duct, Computers & Fluids, 1991, Vol. 21, No. 2, pp. 151-161.

17. B. E. Launder and D. B. Spalding, Lectures in mathematical models of turbulence, Academic Press, 1972, London, England.

18. V. Yakhot and S. A. Orszag, Renormalization group analysis of turbulence: I. Basic theory, Journal of Scientific Computing, 1986, Vol. 1, No. 1, pp. 1-51.

19. T.-H. Shih, W. W. Liou, A. Shabbir, Z. Yang, and J. Zhu, A new k-ε eddy-viscosity model for high Reynolds number turbulent flows - Model development and validation, Computers & Fluids, 1995, Vol. 24, No. 3, pp. 227-238.

20. R. Abid, Evaluation of two-equation turbulence models for predicting transitional flows, Int. J. of Engineering Science, 1993, Vol. 31, No. 6, pp. 831-840.

21. C. K. G. Lam, and K. Bremhost, A modified form of the k-ε model for prediction of wall turbulence, Transactions of ASME, Journal of Fluids Engineering, 1981, Vol. 103, pp. 456-460.

22. B. E. Launder, and B. I. Sharma, Application of the energy-dissipation model of turbulence to the calculation of flow near a spinning disc, Lett. Heat Mass Transf., 1974, Vol. 1, pp. 131-138.

23. Z. Y. Yang and T.-H. Shih, A new time scale based k-ε model for near-wall turbulence, AIAA Journal, 1993, Vol. 31, No. 7, pp. 1191-1198.

24. K. Abe, T. Kondoh, and Y. Nagano, A new turbulence model for predicting fluid flow and heat transfer in separating and reattaching flows I: Flow field calculations, Int. J. Heat Mass Transfer, 1994, Vol. 37, No. 1, pp. 139-151.

25. K. C. Chang, W. D. Hsieh and C. S. Chen, A modified low-Reynolds-number turbulence model applicable to recirculating flow in pipe expansion, Transaction of the ASME, Journal of Fluids Engineering, 1995, Vol. 117, pp. 417-423.

26. W. D. Hsieh and K. C. Chang, Calculation of wall heat transfer in pipe-expansion turbulence flows, Int. J. Heat Mass Transfer, 1996, Vol. 39, No. 18, pp. 3813-3822.

27. M. M. Gibson and B. E. Launder. Ground effects on pressure fluctuations in the atmospheric boundary layer. J Fluid Mech., 1978, Vol. 86, pp. 491-511.

28. B. E. Launder, Second-moment closure: Present... and Future? Inter. J. Heat Fluid Flow, 1989, Vol. 10, No. 4, pp. 282-300.

29. B. E. Launder, G. J. Reece, and W. Rodi, Progress in the development of a Reynolds-stress turbulence closure, J. Fluid Mech., 1975, Vol. 68, No. 3, pp. 537-566.

30. FLUENT6.3-Manual (2007), ANSYS Inc., 10 Cavendish Court, Lebanon, NH, USA.

31. D. C. Wilcox, Turbulence modeling for CFD, 1998, second edition, DCW Industries, Inc., California.

32. B. E. Launder, and D. B. Spalding, The numerical computation of turbulent flows, Comput. Methods Appl. Mech. Eng., 1974, Vol. 3, pp. 269-289.

33. S.-E. Kim and D. Choudhary, A near-wall treatment using wall functions sensitized to pressure gradient, In ASME FED Vol. 217, Separated and Complex Flows, ASME, 1995.

34. B. Kader, Temperature and concentration profiles in fully turbulent boundary layers, Int. J. Heat Mass Transfer, 1981, Vol. 24, No. 9, pp. 1541-1544.

35. M. Wolfstein, The velocity and temperature distribution of one-dimensional flow with turbulence augmentation and pressure gradient, Int. J. Heat Mass transfer, 1969, Vol. 12, pp. 301-318.

36. S. B. Pope, Turbulent Flows, 2000, Cambridge University Press, Cambridge, United Kindom.

37. H. K. Versteeg, and W. Malalasekra, An Introduction to Computational Fluid Dynamics: The Finite Volume Method Approach. 1995, Essex, England: Longman Scientific Technical.

38. F. S. Lien and M. A. Leschziner, Assessment of turbulent transport models including non-linear RNG eddy-viscosity formulation and second-moment closure, Computers & Fluids, 1994, Vol. 23, No. 8, pp. 983-1004.

39. S. Fu, B. E. Launder, and M. A. Leschziner, Modeling strongly swirling recirculating jet flow with Reynolds-stress transport closures, 6^{th} Symposium on Turbulent Shear Flows, 1987, Toulouse, France.

40. B. E. Launder, Second-moment closure and its use in modeling turbulent industrial flows, Int. J. for Num. Meth. Fluids, 1989, Vol. 9, pp. 963-985.

41. B. E. Launder and N. Shima, Second-moment closure for near-wall sublayer: development and application, AIAA Journal, 1989, Vol. 27, No. 10, pp. 1319-1325.

42. V. C. Patel, W. Rodi, G. Scheuerer, Turbulence models for near-wall and low-Reynolds number flows: a review, AIAA, 1985, Vol. 23, No. 9, pp. 1308-1319.

43. F. White and G. Christoph, A simple new analysis of compressible turbulent skin friction under arbitrary conditions, Technical Report AFFDL-TR-70-133, Feb. 1971.

44. P. Huang, P. Bradshaw, and T. Coakley, Skin friction and velocity profile family for compressible turbulent boundary layers, AIAA Journal, 1993, Vol. 31, No. 9, pp. 1600-1604.

45. R. Moreau. Magnetohydrodynamics. Kluwer Academic Publishers, 1990.

46. B. Galperin, A second momentum closure model for MHD turbulence, J. Applied Mathematics and Physics, 1989, Vol. 40, pp. 740-757.

47. D. S. Kovner, and V. B. Levin, Turbulent electrically conducting pipe flow in a longitudinal magnetic field, Teplofiz, Vys. Temp., 1964, 2, 742.

48. S.-I. Satake, T. Kunugi, K. Takase, and Y. Ose, Direct numerical simulation of turbulent channel flow under a uniform magnetic field for large-scale structures at high Reynolds number, Phys. Fluids, 2006, Vol. 18, 125106.

49. K. Iwamoto, Y. Suzuki, and N. Kasagi, Reynolds number effects on wall turbulence: Toward effective feedback control, Int. J. Heat and Fluid flow, 2002, Vol. 23, pp. 678-689. http://www.thtlab.t.u-tokyo.ac.jp/

50. H. Noguchi, and N. Kasagi, Direct numerical simulation of liquid metal MHD turbulent channel flows, Preprint of JSME, 1994, No. 940-53, pp. 365-366. http://www.thtlab.t.u-tokyo.ac.jp/

51. A. F. Shinn, S. P. Vanka, and W. W. Hwu., Direct Numerical Simulation of Turbulent Flow in a Square Duct Using a Graphics Processing Unit (GPU), AIAA-2010-5029, 40th AIAA Fluid Dynamics Conference, June 2010.

52. R. Chaudhary, S. P. Vanka, and B. G. Thomas, Direct Numerical Simulation of Magnetic Field Effects on Turbulent Flow in a Square Duct, Phys. Fluids, 22, 075102, 2010.

53. T. J. Craft, B. E. Launder, and K. Suga, Development and Application of a Cubic Eddy-Viscosity Model of Turbulence, International Journal of Heat and Fluid Flow, Vol. 17, 2, 1996, pp. 108-115.

54. S. Nisizima, A numerical study of turbulent square-duct flow using an anisotropic k-ε model, Theoretical and Computational Fluid Dynamics, 1990, Vol. 2, No. 1, pp. 61-71.

55. H. K. Myong, and T. Kobayashi, Prediction of three-dimensional developing turbulent flow in a square duct with an anisotropic low-Reynolds-number k-ε model, Transactions of ASME, J. Fluids Engineering, 1991, Vol. 113, pp. 608-615.

56. C. G. Speziale, On nonlinear k-l and k-ε models of turbulence, J. Fluid mech., 1987, Vol. 178, pp. 459-475.

57. G. Mompean, S. Gavrilakis, L. Machiels, and M. O. Deville, On predicting the turbulence-induced secondary flows using non-linear k-ε models, Phys. Fluids, 1996, Vol. 8, No. 7, pp. 1856-1868.

58. D. Naot, A. Savit, and M. Wolfshtin, Numerical calculation of Reynolds stresses in a square duct with secondary flow, Heat and Mass Transfer, 1974, Vol. 7, No. 3, pp. 151-161.

59. A. O. Demuren and W. Rodi, Calculation of turbulence-driven secondary motion in non-circular ducts, J. Fluid Mech. 1984, Vol. 140, pp. 189-222.

60. W. Rodi, A new algebraic relation for calculating the Reynolds stresses, Z. Angew. Math. Mech. 1976, 56, 219.

CHAPTER 5. TRANSIENT MOLD FLUID FLOW WITH WELL- AND MOUNTAIN-BOTTOM NOZZLES IN CONTINUOUS CASTING OF STEEL

5.1. Introduction

Both the steady-state flow pattern and transient variations in the mold cavity are important to steel quality in continuous casting. Excessive meniscus velocities and surface turbulence lead to inclusion defects due to slag entrainment and level fluctuations in the mold [1, 2]. Insufficient surface flows lead to meniscus freezing and other surface defects [1, 2]. The mold flow pattern should be optimized to achieve a flat surface profile with stable meniscus velocities of the desired magnitude and minimum turbulence.

These important flow parameters are governed by the flow control system (stopper rod or slide gate), nozzle geometry, Submerged Entry Nozzle (SEN) depth, casting speed, strand cross-section dimensions, argon gas injection rate, slag behavior, and the application of electromagnetics [1]. The most influential and easily-changed of these parameters are the nozzle port geometry details (port angle, port area), and the nozzle bottom shape. In particular, the shape of nozzle bottom has an important influence on flow quality in the mold, including the surface velocity, surface level profile, and turbulent variations that vary the frequency and magnitude of their fluctuations and asymmetries. This paper applies computational model and water-model experiments to analyze and compare the effect of two popular nozzle bottom shapes on these flows.

5.2. Previous Work

Owing to the difficulty of plant experiments and the similar kinematic viscosity of water and steel, much previous insight into mold fluid flow has been gained using water models [1-6]

Although most studies have focused on steady-state flow patterns, a few studies have noted transient phenomena [3-11]. Honeyands and Herberton [8] observed surface level fluctuations in a thin-slab water model with a characteristic frequency that increased with casting speed, according to the time period for flow to circulate around the mold cavity. Gupta and Lahiri [5] observed flow asymmetries in the lower recirculation zones that alternated between sides like large-scale vortex shedding. Lawson and Davidson [9] used Laser Doppler Velocimetry (LDV) to measure oscillatory flow in a 0.33-scale thin-slab water model. Low frequency oscillation modes had the most oscillatory energy, especially below 5Hz in the jets, and below 0.2Hz in the mold overall. This is consistent with findings of Sivaramakrishnan et al [11] and Assar et al [3] from velocities measured in a 0.4-scale water model using Particle Image Velocimetry (PIV).

Many previous computational models have been applied to predict fluid flow exiting the nozzle [12-15]. Many researchers have shown that computational predictions of steady k-ε based Reynolds-Averaged Navier-Stokes (RANS) models [12-14, 16-18] can reasonably predict the steady flow pattern measured in water models. Such models have been applied to investigate the effect of port angle and port shape on flow pattern and jet characteristics exiting the nozzle port [12, 15]. Bai et al [13,14] extended such a model to include multiphase effects and asymmetries from the slide-gate orientation [12] to investigate the effect of gas injection, casting speed, gate opening, bubble size, port angle and port shape [13]. Nozzle bottom was not found to have much effect on the steady flow pattern. However, optimizing the steady-flow pattern is not as important as avoiding defects due to turbulent flow effects such as transient level fluctuations.

Several recent models have been developed to study transient flow phenomena in the mold. Huang and Thomas [17] showed that an unsteady RANS model could simulate flow

evolution in a caster and steel-slag interface level fluctuations induced by sudden changes of nozzle inlet conditions. Others have applied Large Eddy Simulation (LES) [11, 18-21] and showed it to match the time-average flow pattern measured in both water models [11, 18-21] and in the steel caster with electromagnetic sensors [21]. Complex time-varying flow structures have been observed in the LES simulation results, [19, 20] even during nominally steady casting conditions. The velocity variations due to turbulence were compared with measurement. In spite of its known importance, few parametric studies have considered transient flow variations. The effect of nozzle bottom shape remains unclear, so is the subject of this work.

5.3. Water Model Experiments

A $1/3^{rd}$ - scale water model was constructed to measure jet and surface velocities using both PIV and impeller velocity meters. Vertical movement of a centered (aligned) stopper rod controls the flow rate through an annular space of ~2 mm minimum thickness. Water flows down the nozzle and into the mold through bifurcated ports angled 25 degree downward. Figure 5.1 shows the geometry in front view (right) and side view (left). Water exits the bottom of the water-model mold through 11 outlets of 25 mm diameter. From there, water passes through a flow meter to the water storage bath. Water is then pumped back up to the tundish through a second flow meter, which is used by the stopper-rod control system to maintain constant flow rate. Table 5.1 provides details of the dimensions and casting conditions of the water model and the corresponding full-scale steel caster.

Figure 5.2 (a) shows the nozzle geometry with the well-shaped bottom. As typical, the ports are oversized with total port-to-bore ratio of 2.8. Figure 5.2 (b) and Figure 5.2(c) show close-ups of the well-bottom and mountain-bottom shapes. Both nozzles otherwise have the same geometry.

Velocity was measured using PIV just below the ports at the centerline plane of the mold for the well-bottom nozzle. A 2 mm thick plane was illuminated using laser light, and velocity vectors were computed by digital analysis of snapshots taken 0.6 ms apart. These velocities were measured every 0.14 s at each of the 125 x 56 grid of points in the 285-mm wide and 130-mm high measurement window and time-averaged over 360 seconds.

Velocities were also measured using impeller velocity probes. Time-varying data was collected at a frequency of 1 Hz. Figure 5.3 shows the location and orientation of each sensor probe. Each probe is a 35mm long open-ended tube (22mm inner and 28 mm outer diameter) containing a small propeller that rotates in proportion with water speed. Jet velocities were measured by touching the probe to the port bottom and aligning it with the port angle (25 degree down). Surface velocity was recorded 60 mm from each narrow face and 25 mm below the top free surface in the mold for both nozzles. The impeller velocity probes have a total response time of ~ 10s (i.e. 0.1 Hz), including electrical response time (~0.4s to reach 63% of end value) and mechanical response time (for the vanes to respond to increase or decrease in flow). The probes are accurate over the velocity range of 0.02-5 m/s. For each case, mean velocities were averaged over 2000s (except 1000s for mountain-surface) and corresponding isotropic turbulent kinetic energies were derived using standard root-mean square [22], assuming unmeasured components had the same variations. Finally, power spectra were calculated using the Mean Squared Amplitude (MSA) formulation [19] (formulation given in APPENDIX E1).

5.4. Computational Model

A computational model has been formulated to simulate time-averaged turbulent fluid flow in the nozzles and molds of well and mountain bottom nozzles. The steady-state, 3-dimensional, incompressible, Navier-Stokes equations for momentum conservation are solved

with the continuity equation, and the standard k and ε equations to model turbulence (Launder and Spalding [23]) are given by [24]. This approach needs a less-refined mesh, so is faster than the Direct Numerical Simulation (DNS) and LES methods, which are more accurate for transient flow.

The model domain contains only the liquid pool, so naturally has straight walls for the water model. When modeling the steel caster, the domain has curved walls to match the shape of the solidification front, which was calculated using CON1D [25]. In addition to standard no-slip wall laws used on all solid boundaries [22], downward velocity at the solidification front was fixed at the casting speed. To account for shell solidification, a source term of mass-sink per unit volume is added to the continuity equation as follows [26-27]:

$$\rho\left(\nabla \bullet \vec{v}\right) = S_{mass} = -\frac{\rho V_{casting} A}{V} \tag{5.1}$$

Where ρ is the density of the fluid (kg/m^3), $V_{casting}$ is the casting speed, A is the projection area in casting direction and V is the volume of the sink cells, which are 1-mm thick and extend over the domain walls boundaries that represent the solidification front. A corresponding sink term for the momentum extracted per unit volume into the shell is added to each of the three (x-, y- and z) momentum equations:

$$\vec{S}_{mom} = -\frac{\rho V_{casting} A}{V}\vec{v} \tag{5.2}$$

These terms were implemented with a User-Defined Function (UDF) C-language subroutine (given in APPENDIX A1.) in FLUENT [28]. More details on these sinks terms are given by Creech and Rietow [26-27].

Assuming symmetrical flow, 2-fold symmetry of the geometry enables a model of only quarter of the nozzle and strand, to minimize computation. The nozzle and strand are discretized using about 19,000 and 0.136 Million hexahedral cells respectively as shown in Figure 5.4. To better model flow entering the stopper region, a cylindrical portion of the tundish bottom (with 200 mm diameter and 150 mm height), is created around the top of the SEN. Figure 5.5 gives close-up views and meshes of the stopper and bottom regions of both nozzles. Average velocity with small values of k- and ε- (10^{-5} m^2/s^2, 10^{-5} m^2/s^3) were fixed at the circumference and top annular regions of the cylinder to match the flow rate for typical casting speed and dimensions (Table 5.1).

To improve efficiency, nozzle flow is simulated first, using pressure outlet boundary conditions. The velocities, turbulent kinetic energy and dissipation rate at the outlet plane from the nozzle ports are then used as boundary conditions for the inlet surface to the strand. Hershey et al [14] showed that this approach matches well with results of simulations that combine the nozzle and strand together. Convergence is easier because residuals in the important low-velocity regions of the strand are not overly influenced by small errors in the high velocities inside the nozzle. The meshes of the nozzle outlet and the strand inlet were identical with one-to-one mapping in order to ensure accurate flux balance between the two computational domains.

Free-slip boundaries with zero normal velocity were employed at the top free surface, and level fluctuations were calculated using pressure distribution along the free surface based upon potential energy conservation [17, 29]. The level variations (Δz) around flat surface in the computational model can be defined in terms of local and average surface pressure as,

$$\Delta z = \frac{p(x,y) - p_{\text{mean}}}{(\rho_l - \rho_{surface})g} \tag{5.3}$$

where, $p(x,y)$ and p_{mean} are surface local and average static pressures respectively, ρ_l and $\rho_{surface}$ are the densities of flowing fluid and surface layer fluid respectively and g is acceleration due to gravity.

Pressure outlet boundary conditions were also used at strand exit. In case of reverse flow entering the lower recirculation zone, small values of k- and ε- (10^{-5} m^2/s^2, $10^{-5} m^2/s^3$) were set at the strand domain exit, along with 0 Pa gauge pressure.

The equations for the three momentum components, k-, and ε- are discretized using the Finite Volume method in FLUENT [28] with 1st -order upwind schemes for convection terms, including Poisson's equation for pressure correction. These discretized equations are then solved for velocity and pressure using the Semi-Implicit Pressure Linked Equations (SIMPLE) algorithm, starting with initial conditions of zero velocity [29]. Standard wall laws were used as boundary conditions [30]. Finally, k- and ε- equations are solved. The turbulent viscosity field is obtained from k and ε and added to the molecular viscosity to obtain effective viscosity for the next step update. The segregated solver in FLUENT was used to solve all equations. In all simulations, convergence was defined when all scaled residuals were reduced below 10^{-4}. All computations were performed on a PC with a 2.66 GHz Intel® Xeon processor and 4.0 GB RAM. Each nozzle simulation converged in about 15 minutes and required around 1000 iterations. Strand simulations took around 3 hours with 7600 iterations for the mountain-bottom nozzle and about 2 hours with 4000 iterations for the well-bottom nozzle.

5.5. Model Validation

The computational model predictions are validated here by comparing with the time-averaged PIV, impeller velocity and turbulence measurements. Figure 5.5(a) shows the PIV measurement window, which extends down from the port bottom and Figure 5.5(b) shows the

average velocity magnitude contours. The bottom of the SEN extends into the top of the frame. The maximum velocity is 1.022 m/s on the upper left side. On the upper right side, shadow effects from the nozzle spoil the PIV measurements in the red-triangle region.

Figure 5.5(c) and Figure 5.5(d) gives velocity contours modeled using 2^{nd} order and 1^{st} order up-wind convection schemes respectively. With 2^{nd} order upwinding, Fig-2.5(c), the maximum velocity is 1.09 m/s and the jet is thinner, bending upward slightly. The jet shape matches most closely with the PIV measurements. With 1^{st}-order upwinding, Figure 5.5(d), numerical diffusion makes the jet thicker and more stable, and the maximum speed drops to 1.02 m/s. These results match closer to the measured jet velocity, and with the shape of the flow pattern deeper in the caster. Moreover, the 2^{nd} order scheme is less stable and did not converge for the mountain-bottom nozzle. Thus, the 1^{st} order scheme was used in further simulations.

A comparison of impeller measurements of velocity and turbulence with computational model predictions is summarized in Table 2.2. The velocity predictions agree with the time-average of the measurements about as well as the measurements on the right and left sides agree with each other. Moreover, the trends are consistent. The well-bottom nozzle velocity measurements show little variation between sides, and agree with the predictions within 1%. The mountain-bottom nozzle exhibits significant asymmetry between left and right, indicating that the time-averaging period was too short for this nozzle. The predictions agree within these variations. For example, surface velocity averaged over the last 500s is 0.180m/s, which matches exactly with the prediction.

Agreement with the turbulent kinetic energy measurements is not quite as good. The measured turbulence of the jet exiting the ports is one to two orders of magnitude smaller than at the surface. This is contrary to expectations that the jet should be more turbulent, as predicted

with the computational model. This is believed to be due to the known inability of the impeller probe to respond to the high-frequency fluctuations that dominate the jet turbulence, due to the inertia of the impeller. In addition, the fixed orientation of the probe is unable to measure non-axial fluctuations, which were observed to be significant in this region. Agreement is much better at the top surface, which has lower-frequency fluctuations. Measurements and predictions agree reasonably for the mountain-bottom nozzle, and are in the same range for the well-bottom nozzle. Moreover, the trends agree. Thus, the model predictions and measurements are used together to understand flow in the remainder of this work.

5.6. Computational Results

5.6.1. Nozzle Flow

Figure 5.6 gives the velocity contours and vectors near the stopper rod head and bottom region of both nozzles. The maximum velocity is 3.8 m/s and is found in the thinnest part of the annular region between the stopper rod and the tundish bottom. Figure 5.7 compares streamlines and Table 5.3 quantifies the jet characteristics [12] for both nozzles. The formulations of jet characteristics are given in Appendix-B. The jet in the well-bottom nozzle is more diffusive and thicker with a smaller back flow zone (27% vs. 30% in mountain bottom). In the mountain-bottom nozzle, flow goes straight along the side of the mountain with high velocity, producing a thinner and less diffusive jet with smaller horizontal spread- and vertical jet- angles.

Figure 5.8 compares velocity contours and vectors at port exit. Secondary flows from the mountain bottom nozzle are weaker, as flow is directed more towards the narrow face. Figure 5.9 gives velocity contours and vectors on lines angled 25 degrees from the port bottom in the mold region close to SEN. The maximum velocity is close to the port bottom in both ports with a steeper, thicker jet (also seen in Figure 5.6 and Table 5.3) from the well-bottom nozzle. Higher

outward, downward and horizontal weighted-average jet velocities exiting the mountain bottom nozzle are observed in both the experiments and computations. Turbulent kinetic energy is much higher in the well-bottom nozzle, with higher frequency fluctuations causing a more dissipative jet.

5.6.2. Mold Flow Pattern

Figure 5.10 presents the mold flow patterns at the mid-plane between wide faces for both nozzles. The higher dissipation rate leaving the port of the well-bottom nozzle causes the jet turbulent kinetic energy to decrease more as it moves through the mold. This thicker and more diffusive jet thus loses its momentum faster as it splits into upper and lower recirculation zones with weaker flow along the narrow face. Maximum velocity is found near the bottom of port exit, and is 1.23 m/s with the well-bottom nozzle. With the mountain-bottom nozzle, the jet is faster (1.31 m/s) which leads to higher surface velocity. The latter jet also bends upwards more as it crosses the mold, further contributing towards the higher surface velocity. Also, the lower recirculation zone is predicted to break up into more complex flow structures.

Figure 5.11 gives the vertical speed along the mid-plane vertical line at 10 mm from narrow face. The mountain-bottom nozzle has faster flow in the upper recirculation zone. The jet impinges the narrow face at 180 mm below the top free surface with both nozzles. The free surface level for both nozzles is given in Figure 5.12 at the mid-plane between wide faces. The surface is raised near the narrow face and SEN, as common with a double-roll flow pattern. The mountain-bottom nozzle gives around 2.5 times higher surface waves, owing to its ~1.5 times higher horizontal surface velocity, as shown in Figure 5.13 (a). This higher surface velocity agrees with the measurements, (Figure 5.15) and is due to the stronger flow up the narrow face,

The turbulent kinetic energies predicted for the two nozzles at the free surface are given in Figure 5.13 (b). The mountain-bottom nozzle gives ~5 times higher turbulent kinetic energy compared to the well-bottom. This is due to the low frequency and high magnitude fluctuations in the surface velocity for this nozzle.

5.7. Water Model Results

5.7.1. Jet Velocity

Figure 5.14 shows the jet velocities measured on the left and right sides with the impeller probe. Time-averaged jet velocities with the well-bottom nozzle are ~0.686 m/s and are quite symmetric, with the left and right sides matching within ~0.3% over 2000s. In the mountain bottom nozzle, the corresponding jet velocities average 0.950 m/s, which is significantly higher. They are also less symmetric with ~1.4% higher velocity on the left side, which indicates stronger, lower-frequency variations.

5.7.2. Surface Velocity

Figure 5.15 shows the measured histories of the horizontal velocities near the surface on the left and right side of the mold for both nozzles, along with the their time averaged values. For the well bottom nozzle, time-averaged horizontal surface velocities are ~0.109 m/s, with the right side 11.6% higher than the left. The mountain-bottom nozzle has more than 50% higher average surface velocities, 0.157 m/s, due to the higher jet velocity. Its asymmetry is also higher, with 12.1% higher velocity on the right side. Relative to the jet, these surface flow results show that asymmetry increases as the flow travels through the mold. Furthermore, the mountain-bottom nozzle is more susceptible to asymmetric flow.

5.7.3. Velocity Fluctuations

Power spectrums of the jet and surface velocity fluctuations of both nozzles can be seen in Figure 5.16 and Figure 5.17 respectively. Due to ~10s response time of the impeller probe, only energies for frequencies up to 0.1 Hz are plotted. In all cases, most of the energy is found in low frequencies. The general drop in energy observed with increasing frequency matches previous work [10, 15]. An exception is the small peak found at ~0.07 Hz (~14s). The same frequencies dominate in the jet and surface for both nozzles. Energy in the jet is higher in the well-bottom nozzle, especially at frequencies above 0.01 Hz. This is due to strong recirculation observed in the bottom of the nozzle (Figure 5.7). The mountain nozzle deflects the jet smoothly towards the ports (Figure 5.7), slicing through the flow like a knife-edge. This allows the jets to retain more of their momentum, but with less turbulence. This causes the trend in energy spectrum at the surface to reverse. The mountain-bottom nozzle experiences much greater surface velocity fluctuations. Figure 5.17 shows the increase to be more than an order of magnitude at frequencies ranging from 0.002 – 0.035 Hz, which corresponds with time periods of 33-500 s. This finding is also seen in Figure 5.15. The well bottom nozzle has energy distributed over a wider frequency range in both jet and surface velocities.

5.7.4. Mechanism

The increased velocity fluctuations and left-right asymmetry of the mountain-bottom nozzle are explained with Figure 5.18. Transient variations in nozzle flow may send higher velocity down one side of the nozzle. The mountain bottom slices the flow, sending this higher velocity flow directly out the adjacent port. The well bottom, on the other hand, mixes the flow so the jets exiting the ports are less sensitive to asymmetries.

5.8. Comparison of Water Model with Full-Scale Steel Caster

Simulations of a full-scale steel caster with well-bottom nozzle were performed to evaluate the water model findings. The laboratory water model has several differences from the real caster: **1.** Geometric scaling of all linear dimensions to 1/3rd, **2.** No solidifying shell and stationary walls, **3.** A domain bottom with water exiting through circular holes in a horizontal plate instead of a very long, gradually-tapering flow domain. **4.** Air above the free surface instead of powder, sintered and liquid slag layers. A steel caster was simulated with and without the solidifying shell for conditions in Table 5.1. Figure 5.19 gives the shell thickness profiles down the wide and narrow faces calculated using CON1D [25].

Figure 5.20 presents the velocity contours and streamlines at the mid-plane between wide faces in the steel caster with the solidifying shell. The casting speed for the full-scale caster matches the Froude number of 0.005 of the water model. The flow pattern is generally similar to the water model. Comparison of horizontal surface velocity between water model (after converting to full scale), and the steel caster is given in Figure 5.21. The horizontal axis is non-dimensionalized to compare both water model and caster. The vertical axis is simply the horizontal velocity for the steel caster. Horizontal velocity for the water model was multiplied by 1.732, (the square root of the length scale of 3) according to the Froude criterion. The horizontal velocity in the water model falls in between the caster velocities with and without the solidifying shell. Note that flow in the water model is in the transition regime (Re=2200 based on strand hydraulic diameter) while the steel caster is fully turbulent (Re=13500). The water model velocities would match the caster without the shell if it was fully turbulent.

The maximum surface velocity predicted in the real full-scale steel caster with the well-bottom nozzle is ~0.3 m/s, which is in the safe operating window of 0.2-0.4 m/s, [2]. Maximum

surface velocity with the mountain-bottom nozzle is predicted to be ~0.5 m/s, which is above the upper limit suggested by Kubota [2] to avoid flow problems such as slag entrainment. Thus, the well-bottom nozzle is preferred over the mountain-bottom nozzle for this steel caster and conditions. If casting conditions produced very small surface velocities, then the mountain-bottom nozzle might appear to be better. However, the results of this work suggest that changing the flow pattern in some other way and using the well-bottom nozzle is the best solution.

The free-surface level profile comparison between water model and steel caster is given in Figure 5.22. The free surface level without shell and air above matches most closely with water model, as expected, although the water model underpredicts by a factor of 2.3. Introducing the shell and adding slag both increase the profile variations. Thus, the water model underpredicts surface level variations in the caster using Froude scaling.

5.9. Summary

This work investigates well-bottom and mountain-bottom type nozzles both experimentally and numerically. The computational model agrees very well with measured velocities in all cases, but overpredicts turbulent kinetic energy in the jet and surface of the well bottom nozzle perhaps due to time resolution (~0.1 Hz) of the impeller probe and fluctuations being higher frequency. The measured surface turbulence in mountain bottom nozzle matches well with the simulations. Based upon experiments and the validated computational model, the following conclusions have been drawn, and are summarized in Table 2.4:

1. The jet from the well-bottom nozzle is thicker, steeper-downward and more diffusive, with higher turbulent kinetic energy and dissipation rate, relative to the mountain bottom nozzle jet.

2. The mountain-bottom nozzle produces a thinner jet with stronger, lower-frequency fluctuations, making it more asymmetrical in short-term time averages.
3. Velocity fluctuations decrease in frequency from the jet leaving the ports to the surface in both nozzles.
4. The mountain-bottom nozzle produces ~50% higher surface velocity in the mold.
5. The mountain-bottom nozzle causes surface velocity fluctuations with almost 96% of total measured energy at lower frequencies (33-500s time periods).
6. The higher velocity and turbulence at the surface causes higher variation in surface level profile, more level fluctuations, and easier slag entrainment with the mountain-bottom nozzle.
7. Full scale steel casters have proportionally higher speed, including higher surface velocities, and level fluctuations, which are reasonably characterized by Froude similarity. The above water-model findings are predicted to hold in the steel caster as well.
8. With less surface fluctuations, the well-bottom nozzle is recommended over the mountain-bottom shape for steel quality.

5.10. Tables and Figures

Table 5.1. Process parameters for experiments and computations

	Water model (1/3rd scale)	**Steel caster (full-scale)**
Stopper opening fraction	0.11	-
Nozzle port angle	25 deg down	25 deg down
Nozzle port area	23.3 mm (width) x 26.7mm (height)	69.9 mm (width) x 80.1 mm (height)
Nozzle bore diameter	25 mm	75 mm
Nozzle outer diameter	43 mm	129 mm
SEN Depth	60 mm	180 mm
Average port velocity	0.512 m/s	0.886 m/s
Fluid flow rate	38.2 LPM	595.4 LPM
Casting speed	1.02 m/min	1.76 m/min
Mold width	500 mm	1500 mm
Mold thickness	75 mm	225 mm
domain width	250 mm	750 mm
domain thickness	37.5 mm	112.5 mm (at the top)
domain length	1200 mm	3600 mm
Shell	no	Yes (see Figure-2.19)
Gas injection	no	No
ρ_{fluid}	998.2 kg/m^3 (water)	7020 kg/m^3 (steel)
μ_{fluid}	0.001003 kg/m-s (water)	0.006 kg/m-s (steel)
ρ_{slag}	----	3000 kg/m^3

Table 5.2(a) Comparison of predictions and impeller measurements in jet

	Jet Velocity (m/s)			Turbulent kinetic energy(m^2/s^2) (x 10^{-3})		
	Water model		Fluent	Water model		Fluent
	Left side	Right side		Left side	Right side	
Well bottom	**0.687**	**0.685**	**0.69**	**0.0611**	**0.0898**	**22.3**
Mountain bottom	**0.957**	**0.944**	**0.92**	**0.0216**	**0.0087**	**20.1**

Table 5.2(b) Comparison of predictions and impeller measurements near top surface

	Horizontal Surface Velocity (m/s)			Turbulent kinetic energy(m^2/s^2) (x 10^{-3})		
	Water model		Fluent	Water model		Fluent
	Left side	Right side		Left side	Right side	
Well bottom	**0.103**	**0.115**	**0.11**	**0.31**	**0.38**	**1.4**
Mountain bottom	**0.148**	**0.166**	**0.18**	**2.23**	**3.14**	**2.4**

Table 5.3 Computed jet characteristics in water model

Weighted Average Parameter	Well bottom nozzle	Mountain type nozzle
Port x-velocity (outward) (m/s)	0.75	0.92
Port y-velocity (downward) (m/s)	0.48	0.52
Port z-velocity (horizontal) (m/s)	0.065	0.076
Port turbulent kinetic energy (m^2/s^2)	0.040	0.018
Port turbulent dissipation rate (m^2/s^3)	2.11	0.64
Vertical jet downward angle (deg)	32.8	29.3
Horizontal jet angle (deg)	0	0
Horizontal spread (half) angle (deg)	5.0	4.7
Average jet speed (m/s)	0.89	1.06
Back-flow zone	27%	30%

Table 5.4 Evaluation of well-bottom and mountain-bottom nozzle flow characteristics

	Jet velocity		Surface velocity		Asymmetry (Due to flow transients)
	Average velocity	Fluctuations	Average velocity	Fluctuations	
Well bottom	Low (Thick jet)	High (High frequency)	Low	Low (High frequency)	Low
Mountain bottom	High (Thin jet)	Low (Low frequency)	High	High (Low frequency)	High

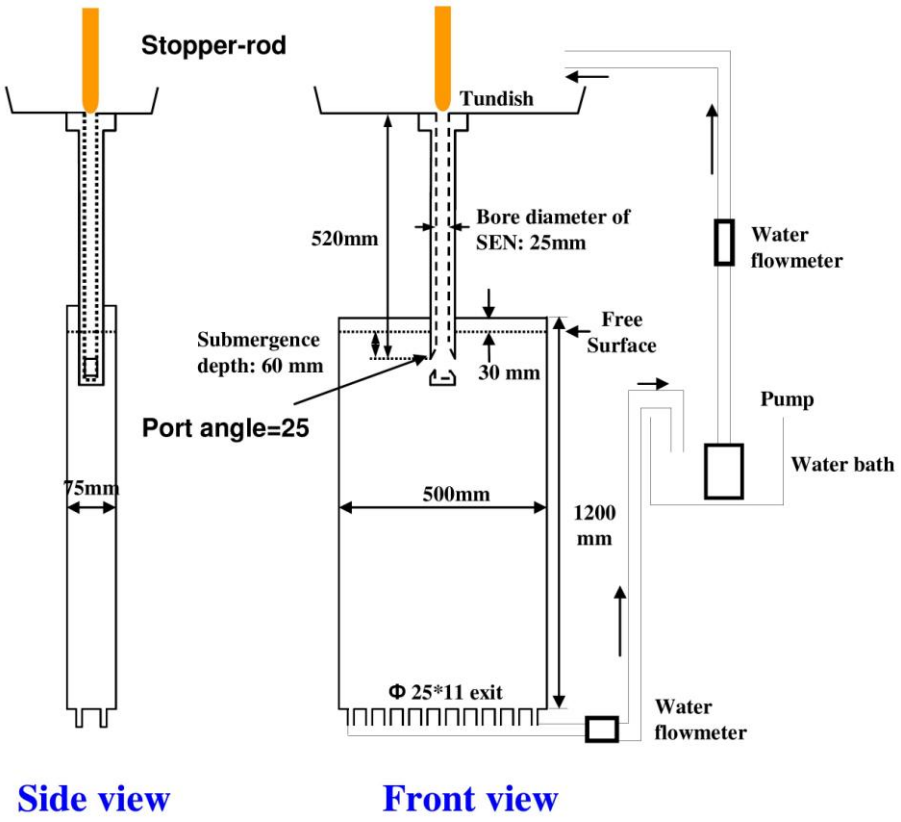

Figure 5.1. Dimensions of one-third scale water model with well-bottom nozzle

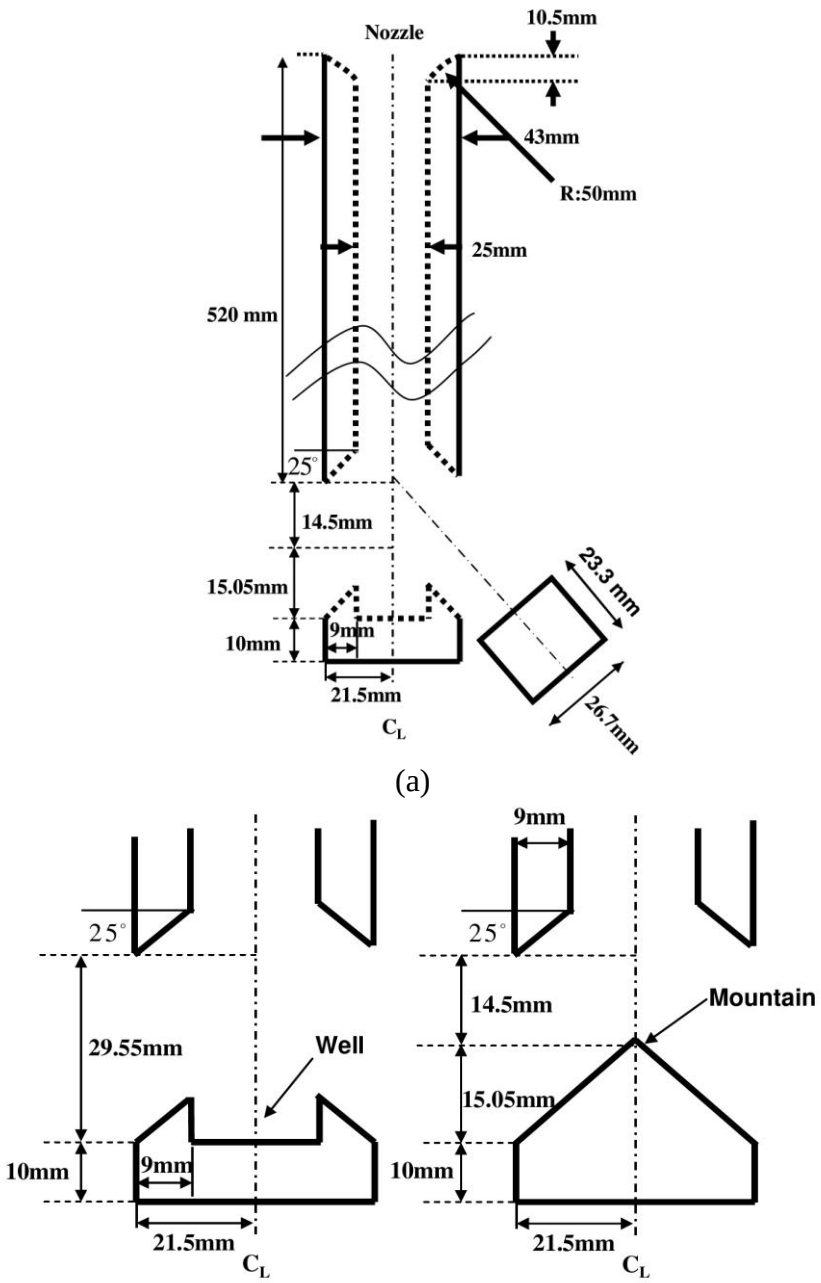

Figure 5.2. Geometry of (a) nozzle and close-up of: (b) well-bottom and (c) mountain-bottom shapes

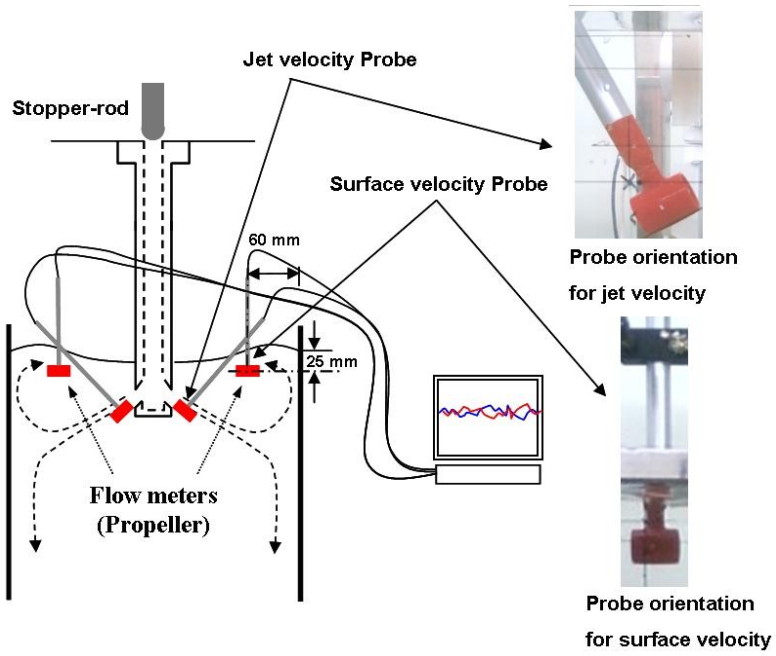

Figure 5.3. Schematic of the impeller-velocity probe locations and orientations

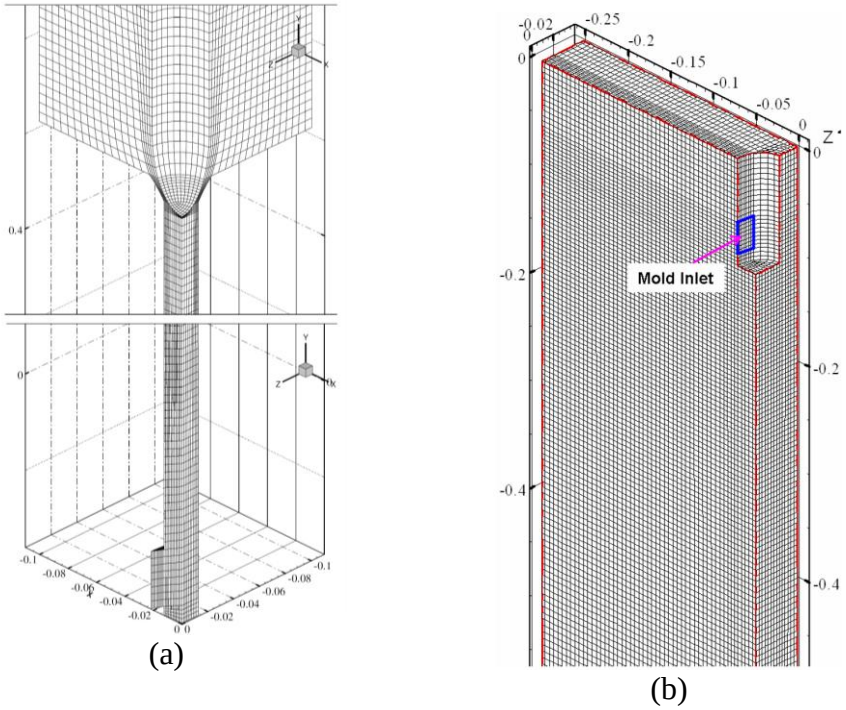

(a) (b)

Figure 5.4. Isometric view of (a) well bottom nozzle and (b) Strand quarter domains and meshes

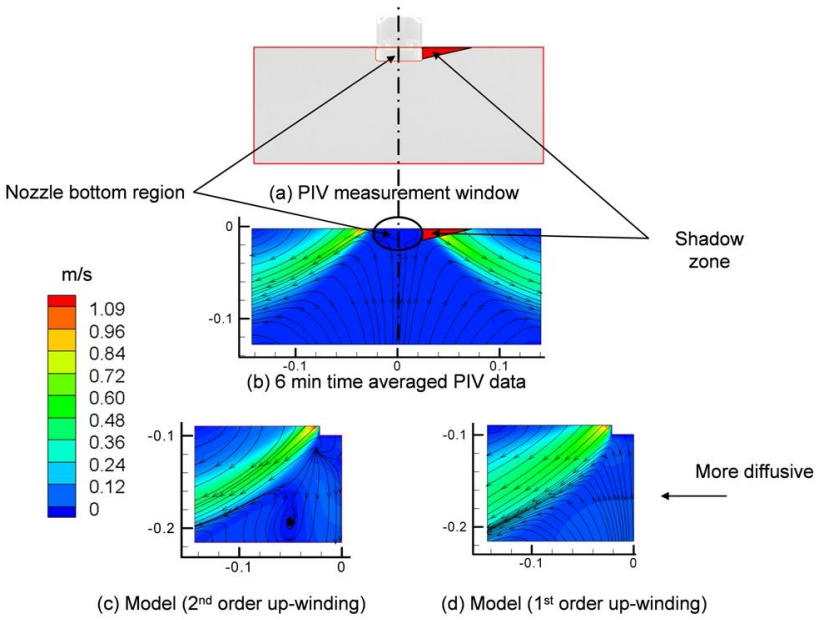

Figure 5.5. (a) PIV measurement window in water model with well-bottom nozzle with (b) PIV measured velocity (time-averaged over 6 min) (c) model velocity and streamlines (1st order up-wind) (d) model velocity and streamlines (2nd order up-winding)

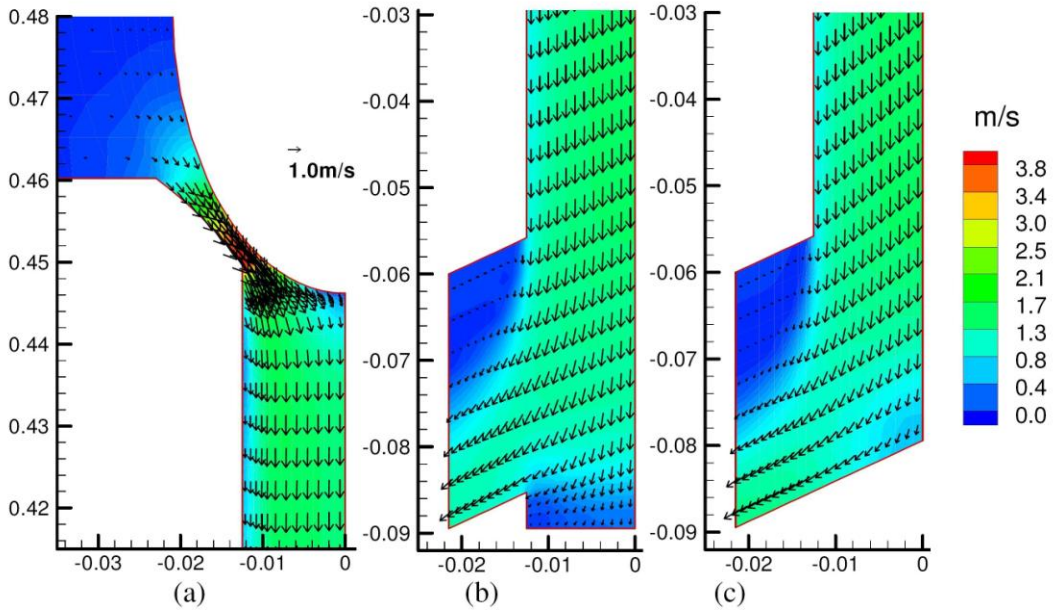

Figure 5.6. Comparison of velocity in (a) stopper-rod head region, (b) bottom region of well-bottom nozzle and (c) bottom region of mountain-bottom nozzle

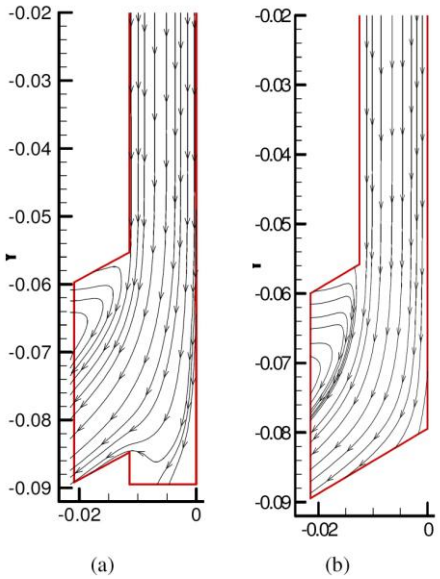

Figure 5.7. Comparison of streamlines in (a) well and (b) mountain bottom nozzles of water model

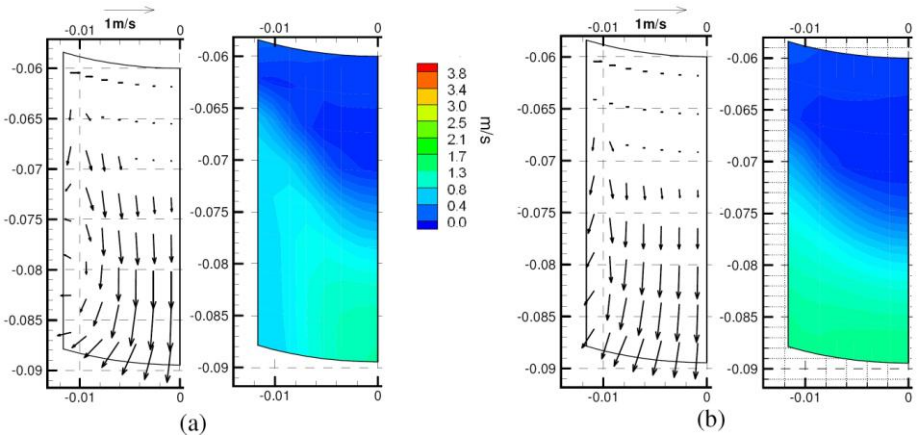

Figure 5.8. Comparison of the port velocities (a) well-bottom (b) mountain-bottom

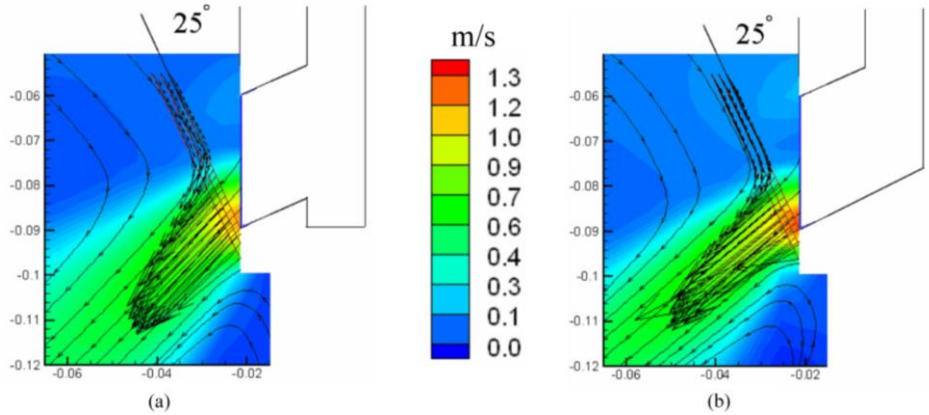

Figure 5.9. Calculated jet velocity vectors and speed contours near nozzle at mold centre plane in (a) well and (b) mountain bottom nozzles

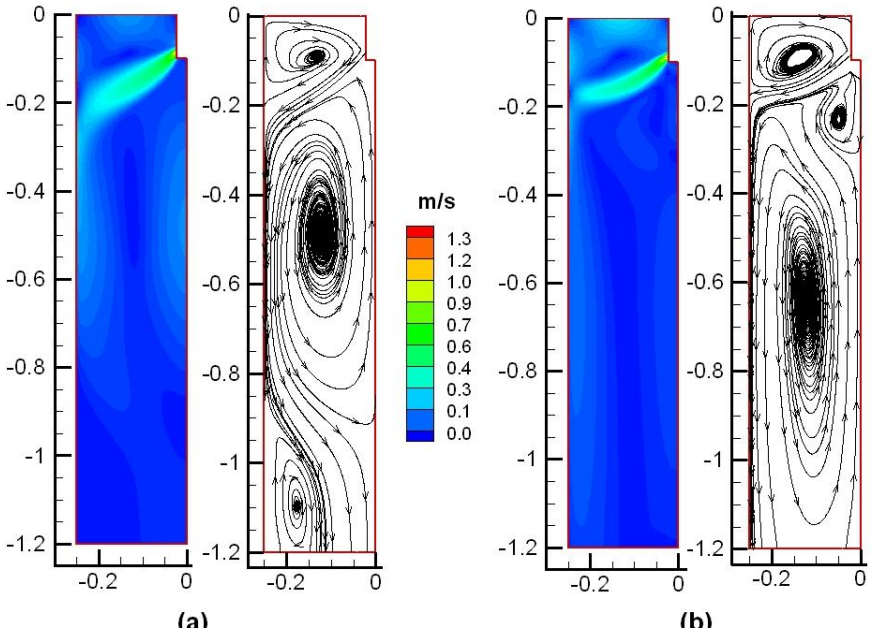

Figure 5.10. Velocity contours and streamlines at the mid-plane between wide faces with (a) well and (b) mountain bottom nozzles in water model mold mountain bottom nozzles

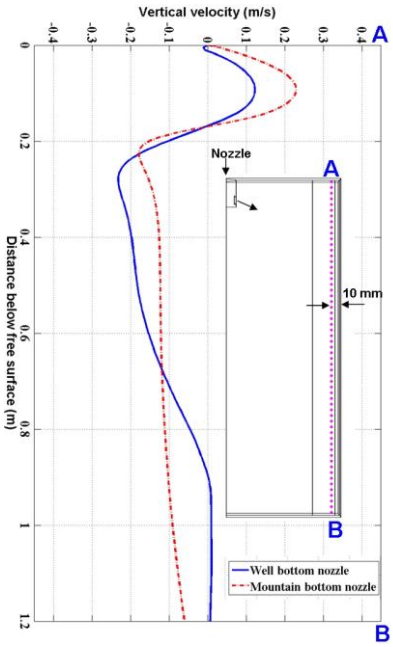

Figure 5.11. Vertical velocity at 10 mm from narrow face at the mid-plane between wide faces with well and mountain bottom nozzles in the water model mold

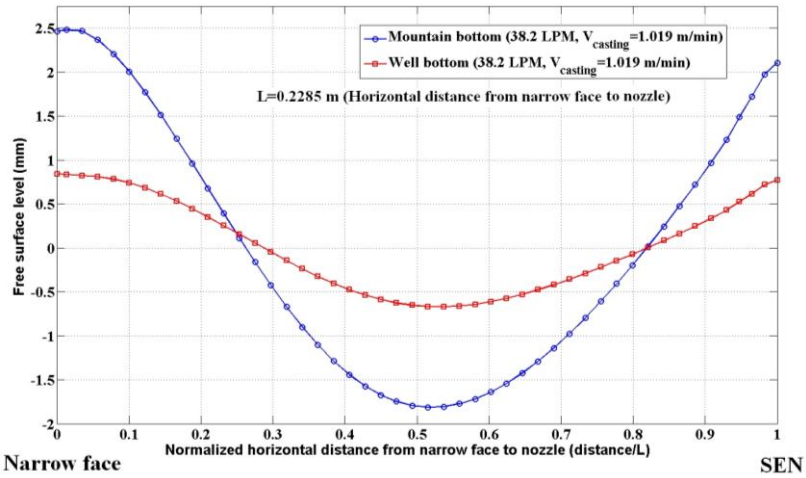

Figure 5.12. Free surface level comparison in well and mountain bottom nozzles of water model mold

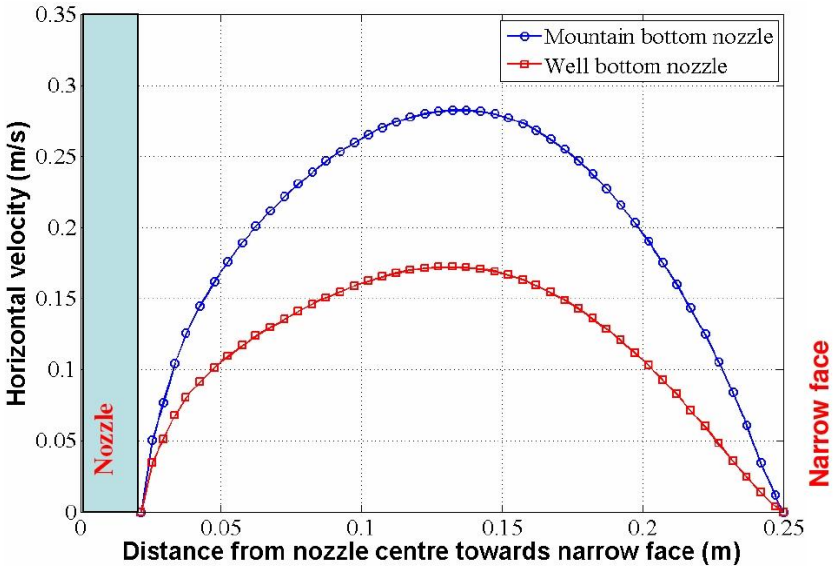

(a)

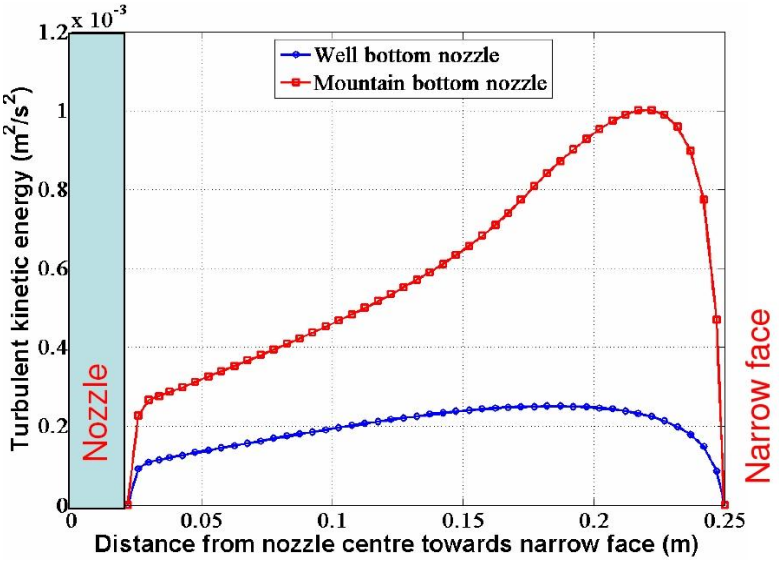

(b)

Figure 5.13. Comparison of (a) horizontal speed and (b) turbulent kinetic energy along the centerline at the free surface in two nozzles of water model mold

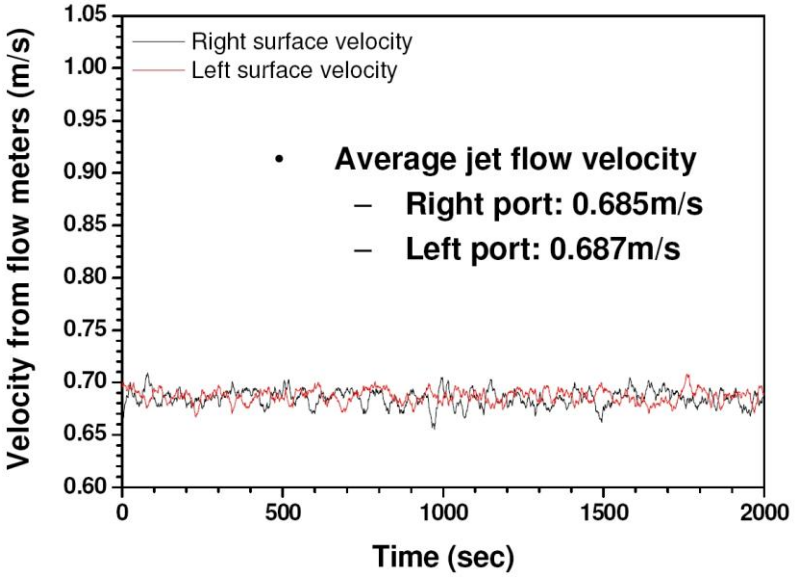

(a)

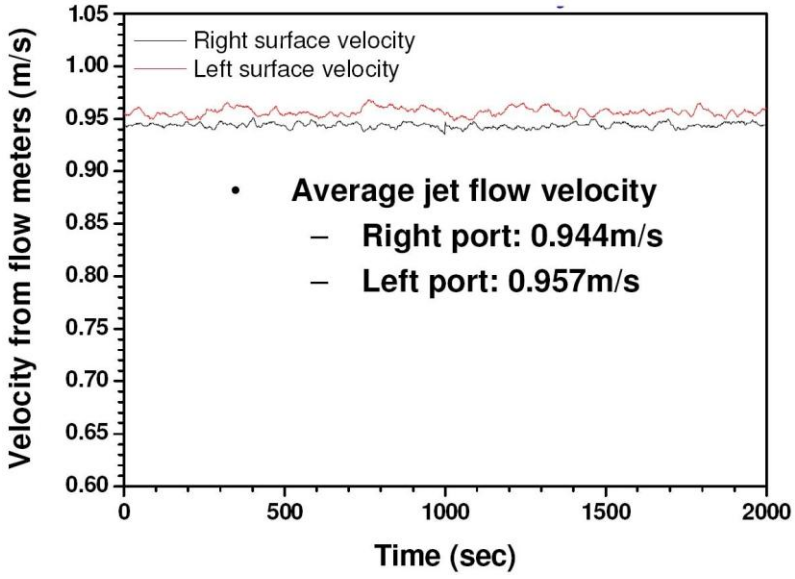

(b)

Figure 5.14. Instantaneous jet speed measured in the water model mold with (a) well and (b) mountain bottom nozzles

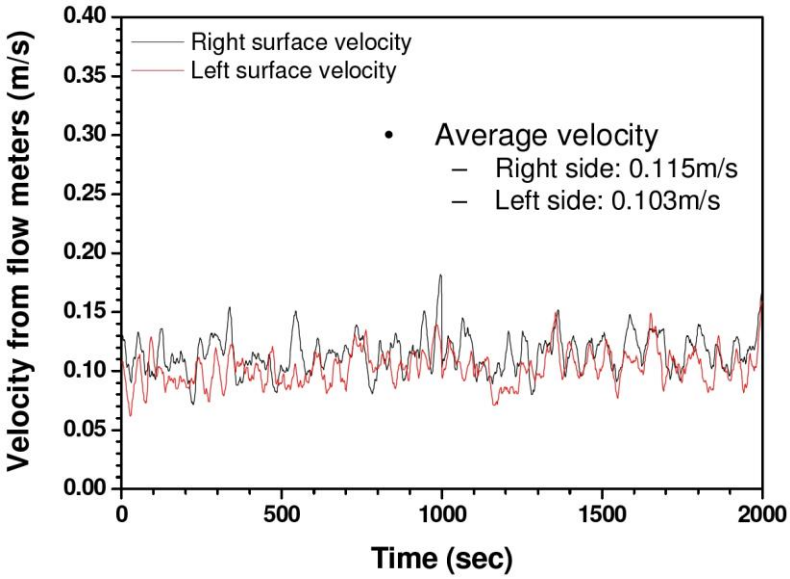

(a)

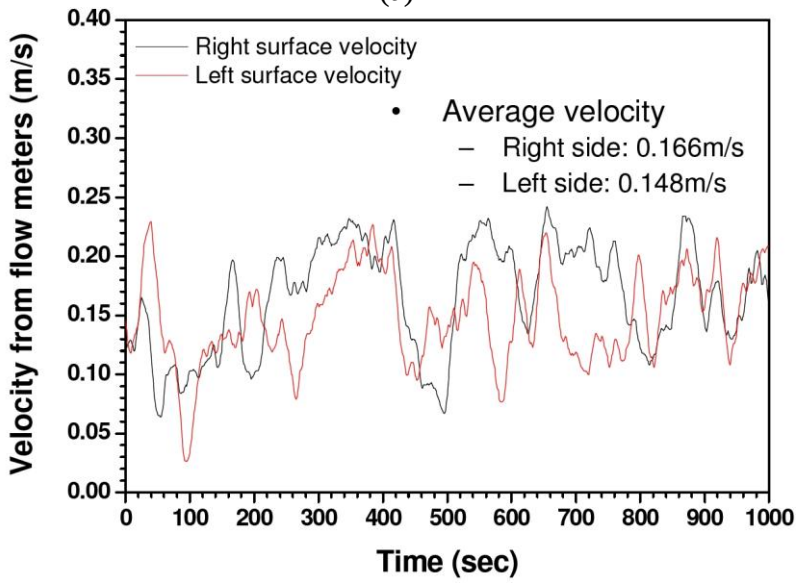

(b)

Figure 5.15. Instantaneous surface speed measured in water model mold with (a) well bottom nozzle and (b) mountain bottom nozzle

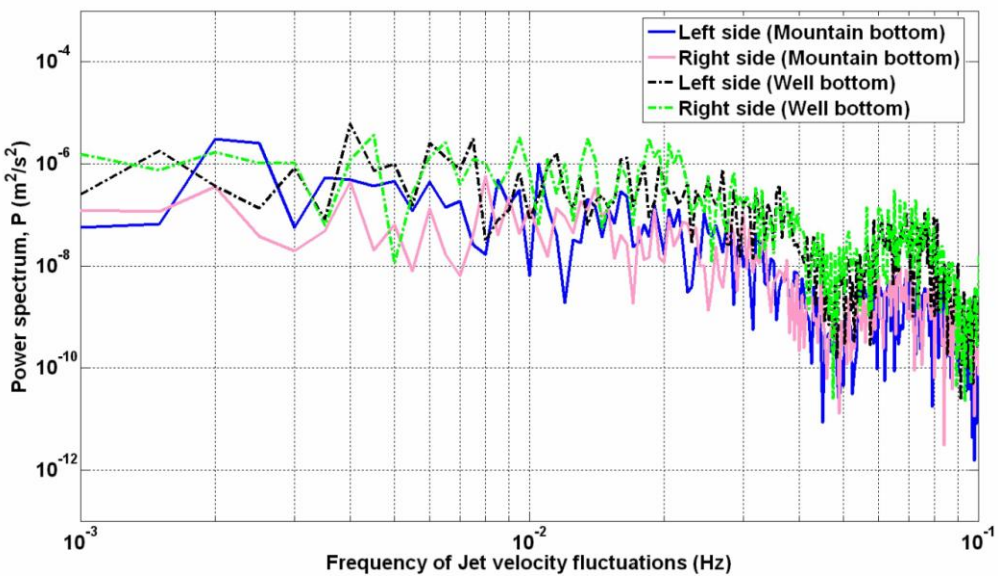

Figure 5.16. Power spectrum of jet velocity fluctuations measured in water model with well and mountain bottom nozzles

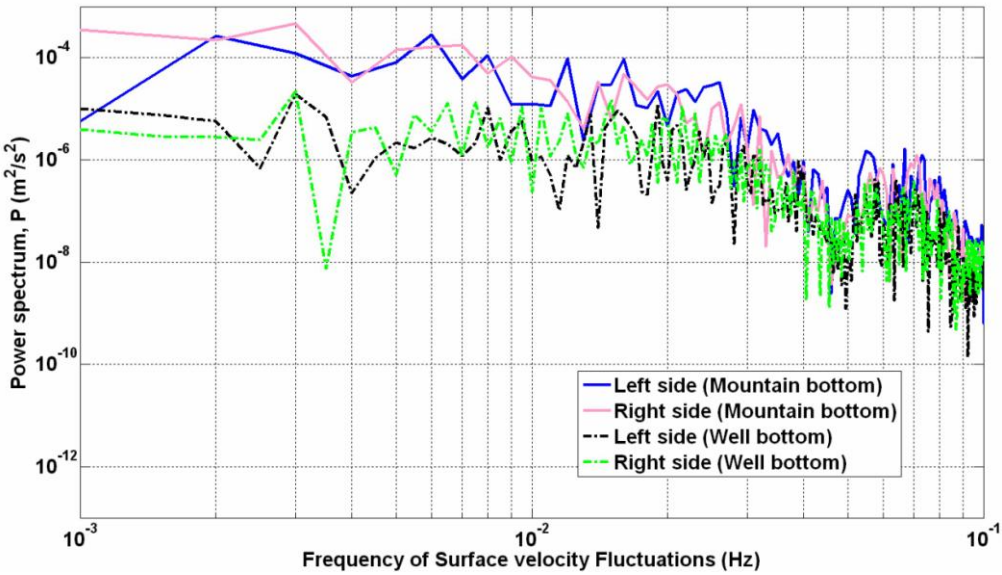

Figure 5.17. Power spectrum of surface velocity fluctuations measured in water model with well and mountain bottom nozzles

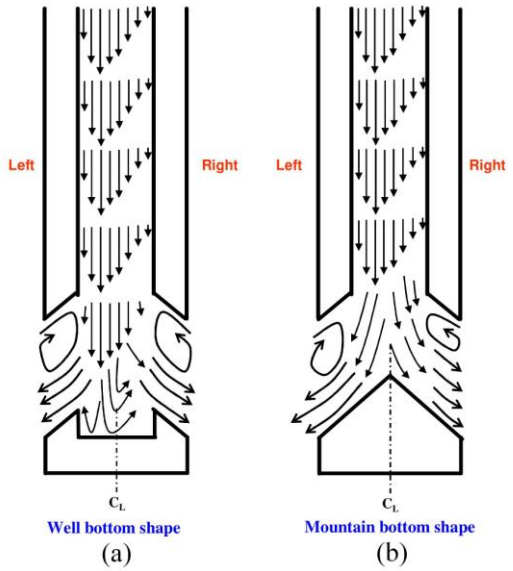

Figure 5.18. Schematic of effect of flow asymmetry (a) in well-bottom nozzle (b) mountain-bottom nozzle

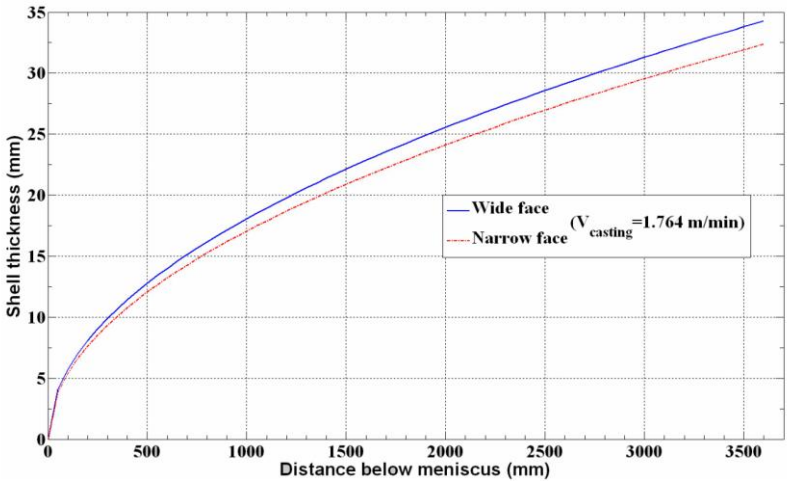

Figure 5.19. Shell thickness profile from CON1D.

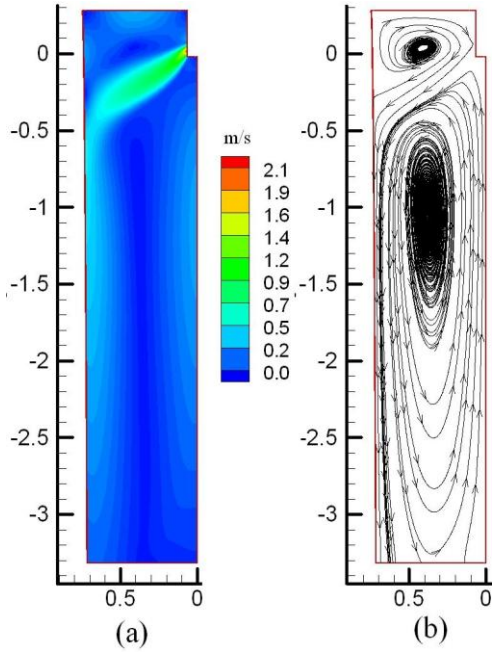

Figure 5.20 Velocity at mid-plane between wide faces (a) Contours and (b) Streamlines in full-scale steel caster with solidifying shell in the mold of well bottom nozzle

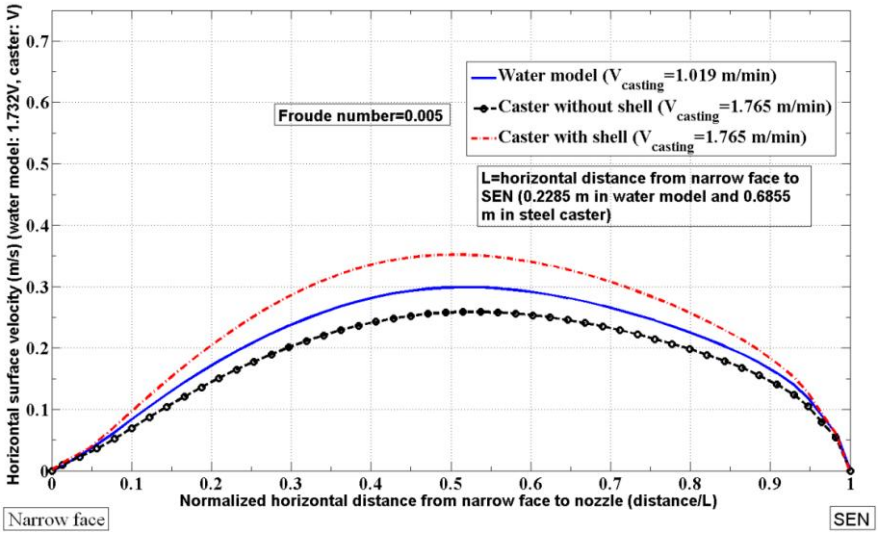

Figure 5.21. Comparison of surface velocities in mold of 1/3rd water model and steel caster using Froude number similarity (well bottom nozzle)

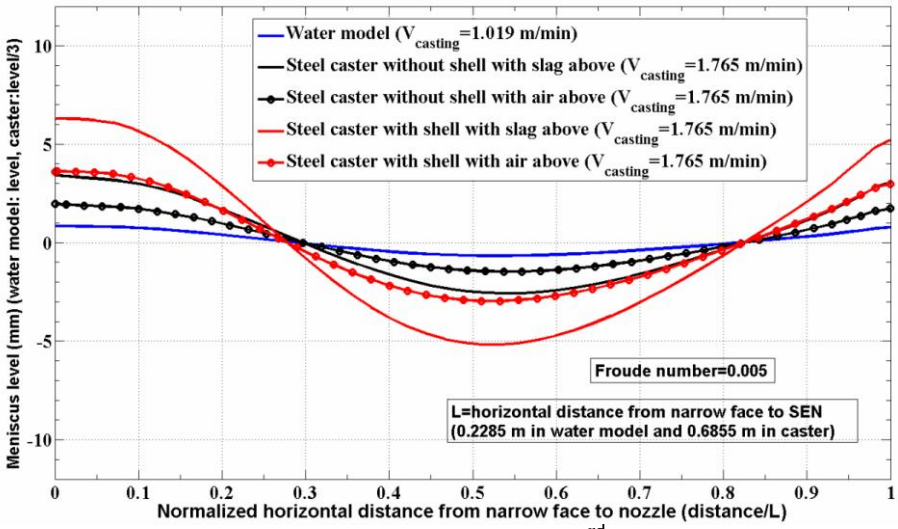

Figure 5.22. Comparison of liquid level in 1/3rd water model and steel caster with solidifying shell using Froude number similarity (well-bottom nozzle)

5.11. References

1. B. G. Thomas, *Chapter 14. Fluid Flow in the mold*, in *Making, Shaping and Treating of Steel*, A.W. Cramb, Editor. 2003, AISE Steel Foundation: Pittsburgh, PA.
2. J. Kubota, et al. *Meniscus Flow Control in the Mold by Travelling Magnetic Field for High Speed Slab Caster*. in *Steelmaking Conf. Proceedings*. 1991.
3. M. B. Assar, P. H. Dauby, and G.D. Lawson, *Opening the Black Box: PIV and MFC Measurements in a Continuous Caster Mold*, in *Steelmaking Conf. Proc.* 2000, ISS, Warrendale, PA: Pittsburgh, PA. p. 397-411.
4. D. Gupta and A. K. Lahiri, *A water model study of the flow asymmetry inside a continuous slab casting mold.* Metall. Mat. Trans. B-Process Metallurgy and Materials Processing Science, 1996. **27**(5): p. 757-764.
5. D. Gupta and A. K. Lahiri, *Water modeling study of the jet characteristics in a continuous casting mold.* Steel Research, 1992. **63**(5): p. 201-204.
6. B. G. Thomas, X. Huang, and R. C. Sussman, *Simulation of Argon Gas Flow Effects in a Continuous Slab Caster.* Metall. Trans. B, 1994. **25B**(4): p. 527-547.
6. B. G. Thomas, X. Huang, and R. C. Sussman, *Simulation of Argon Gas Flow Effects in a Continuous Slab Caster.* Metall. Trans. B, 1994. **25B**(4): p. 527-547.
7. B. G. Thomas and L. Zhang, *Mathematical modeling of fluid flow in continuous casting.* ISIJ International, 2001. **41**(10): p. 1181-1193.
8. T. Honeyands and J. Herbertson, *Flow Dynamics in Thin Slab Caster Moulds.* Steel Research, 1995. **66**(7): p. 287-293.

9. N. J. Lawson and M. R. Davidson, *Oscillatory flow in a physical model of a thin slab casting mould with a bifurcated submerged entry nozzle.* Journal of Fluids Engineering-Transactions of the Asme, 2002. **124**(2): p. 535-543.

10. Dong Xu, William K. Jones, and James W. Evans, *PIV Physical Modeling of Fluid Flow in the Mold of Continuous Casting of Steel*, in *Processing of Metals and Advanced Materials: Modeling, Deisgn and Properties*, B.Q. Li, Editor. 1998, TMS, Warrendale, PA: San Antonio, TX. p. 3-14.

11. S. Sivaramakrishnan, B. G. Thomas, and S. P. Vanka, *Large Eddy Simulation of Turbulent Flow in Continuous Casting of Steel*, in *Materials Processing in the Computer Age*, V. Voller and H. Henein, Editors. 2000, TMS, Warrendale, PA. p. 189-198.

12. H. Bai and B.G. Thomas, *Turbulent Flow of Liquid Steel and Argon Bubbles in Slide-Gate Tundish Nozzles: Part I. Model Development and Validation.* Metallurgical and Materials Transactions B, 2001. **32**(2): p. 253-267.

13. H. Bai and B.G. Thomas, *Turbulent Flow of Liquid Steel and Argon Bubbles in Slide-Gate Tundish Nozzles: Part II. Effect of Operation Conditions and Nozzle Design.* Metallurgical and Materials Transactions B, 2001. **32**(2): p. 269-284.

14. D. E. Hershey, B. G. Thomas, and F.M. Najjar, *Turbulent Flow through Bifurcated Nozzles.* Int. J. Num. Meth. in Fluids, 1993. **17**(1): p. 23-47.

15. F. M. Najjar, B. G. Thomas, and D. E. Hershey, *Numerical study of steady turbulent flow through bifurcated nozzles in continuous casting.* Metall. Mater. Trans. B, 1995. **26B**(4): p. 749-765.

16. B. G. Thomas, L. J. Mika, and F.M. Najjar, *Simulation of Fluid Flow Inside a Continuous Slab Casting Machine.* Metall. Trans. B, 1990. **21B**(2): p. 387-400.

17. X. Huang and B. G. Thomas, *Modeling of transient flow phenomena in continuous casting of steel.* Canadian Metallurgical Quarterly, 1998. **37**(3-4): p. 197-212.

18. K. Takatani, et al., *Mathematical model for transient fluid flow in a continuous casting mold.* ISIJ International, 2001. **41**(10): p. 1252-1261.

19. Q. Yuan, B.G. Thomas, and S.P. Vanka, *Study of Transient Flow and Particle Transport during Continuous Casting of Steel Slabs, Part 1. Fluid Flow.* Metal. & Material Trans. B., 2004. **35B**(4): p. 685-702.

20. Q. Yuan, et al., *Computational and Experimental Study of Turbulent Flow in a 0.4-Scale Water Model of a Continuous Steel Caster.* Metall. & Mater. Trans., 2004. **35B**(5): p. 967-982.

21. B. G. Thomas, et al., *Comparison of four methods to evaluate fluid velocities in a continuous slab casting mold.* ISIJ International, 2001. **41**(10): p. 1262-1271.

22. H. Versteeg and W. Malalasekra, *An Introduction to Computational Fluid Dynamics: The Finite Volume Method Approach*. 1995, Essex, England: Longman Scientific Technical.

23. B. E. Launder and D. B. Spalding, *Mathematical Models of Turbulence*. 1972: London Academic Press.

24. B. G. Thomas, *Chapter 5. Modeling of Continuous Casting*, in *Making, Shaping and Treating of Steel*, A.W. Cramb, Editor. 2003, AISE Steel Foundation: Pittsburgh, PA.

25. Y. A. Meng and B.G. Thomas, *Heat-transfer and solidification model of continuous slab casting: CON1D.* Metallurgical and Materials Transactions B, 2003. **34**(5): p. 685-705.

26. B. T. Rietow, *M.S. Thesis: Fluid Velocity Simulation and Measurement in Thin Slab Casting*, in *Mechanical and Industrial Engineering*. 2007, University of Illinois at Urbana-Champaign: Urbana.

27. D. Creech, *M.S. Thesis: Computational Modeling of Multiphase Turbulent Fluid Flow and Heat Transfer in the Continuous Slab Casting Mold*, in *Mechanical and Industrial Engineering*. 1999, University of Illinois at Urbana-Champaign: Urbana.

28. *FLUENT6.3-Manual* (2007), ANSYS Inc., 10 Cavendish Court, Lebanon, NH, USA.

29. G.A. Panaras, A. Theodorakakos, and G. Bergeles, *Numerical Investigation of the Free Surface in a continuous Steel Casting Mold Model.* Metall. Mater. Trans. B, 1998. **29B**(5): p. 1117-1126.

30. B. E. Launder and D. B. Spalding, *The numerical computation of turbulent flows.* Computer Methods in Applied Mechanics and Engineering, 1974. **3**(2): p. 269-289.

CHAPTER 6. EFFECT OF STOPPER-ROD MISALIGNMENT ON FLUID FLOW IN CONTINUOUS CASTING OF STEEL

6.1. Introduction

Continuous casting solidifies most steel worldwide [1]. Final product quality depends greatly on the flow pattern of molten steel in the mold, especially near the top surface. To avoid surface defects, and internal inclusions from slag entrainment, the surface velocity and turbulence levels need to be maintained within an optimum range [2-3]. Turbulent flow in the mold of a continuous caster is governed by the geometries of the nozzle, mold, and flow control surfaces (slide-gate or stopper-rod), casting speed, argon gas injection, and electromagnetic forces [2].

Asymmetric flow causes transient fluctuations and is a main cause of product defects [4-6]. Asymmetric flow causes high surface velocity on one side and low on the other. This causes transient cross-flow between the narrow gap between the submerged entry nozzle (SEN) and mold, leading to surface defects, vortex formation, slag entrapment, and other defects [5-6]. In addition to aggravating turbulent fluctuations and the associated intermittent problems, asymmetric flow can create a constant flow bias on the top surface of mold. This increases the chance for velocity on one side to exceed the critical range, leading to slag entrainment [4-5] and accompanying sliver defects [4-5, 7]. At the same time, it may cause insufficient velocity on the other side, leading to meniscus freezing, and associated surface defects [2].

Previous researchers have studied the effects on nozzle and mold flows of various asymmetries, including turbulence [8], slide-gates [9-11], nozzle clogging [12] and misaligned nozzles [13-17]. Yuan et al [8] performed large eddy simulation (LES) to study the natural transients and asymmetries associated with turbulent flow in otherwise symmetric “quasi-steady”

flow conditions. Flow in the mold cavity was found to switch between double-roll and complex flow patterns with many vortices. Bai et al [9-10] studied the effect of slide gate orientation on asymmetric flow. A 90-degree (front-back) gate orientation caused swirl in the jet leaving the nozzle, while a 0-degree (right-left) orientation caused severe right-left flow asymmetry, with over 2/3 of the mass flow leaving the right port for a 50% open gate. Lee et al [11] found that front-back asymmetry caused by a 90-degree slide-gate was responsible for particle entrapment on the inner radius. Mahmood [12] computed the asymmetric flow caused by nozzle clogging based on clog samples collected at the steel plant. A two-fold difference in surface velocity between opposite sides of the SEN leading to vortex formation was found. Asymmetric effects were enhanced by increasing casting speed and reducing SEN depth [5-6, 12]. Modeling by Zhang et al [13] found a similar great effect of SEN clogging on asymmetric flow, causing increased slag entrainment, inclusion entrapment and possible breakouts due to excessive local superheat impingement. Yokoya et al [14] used water model experiments and computational predictions to study the effect of off-centered SEN in billet casting. Similar to slab casting, surface flow was predicted through the gap between the nozzle and mold, due to this asymmetry. Water model studies by Gupta et al [15] found that off-centering the nozzle along the wide faces by more than 4% of the mold width caused noticeable asymmetries in time-averaged flow in the mold. The flow asymmetry was observed to persist deep into the liquid pool, many meters below the meniscus [16]. Li et al [17-18] concluded that the size and intensity of vortexing depends on the off-centerness of the SEN, and the casting speed.

Another potential cause of detrimental asymmetric flow is stopper-rod misalignment. Stopper misalignment may be caused by accidental faulty placement, buoyancy forces due to the density difference between the light-weight ceramic stopper-rod and the molten steel, thermal

distortion of the support beams due to radiation heat from the steel pool below, and drag force due to cross flow in the tundish. These effects on mold flow and vortex formation are unknown. Flow with stopper-rod control is generally considered to be much more symmetrical than with slide gates. Considering the variations of turbulent fluctuations, however, it is not easy to indentify if there is an extra asymmetry caused by the stopper or not. Yuan et al [19] and Mahmood [12] reported significant asymmetric flow just below the stopper, especially if there is cross-flow across the bottom of the tundish, but the consequence to mold flow was not studied. The current work focuses on quantifying the effect of stopper-rod misalignment on nozzle flow, mold flow and vortex formation, in a 1/3rd water model of a continuous casting process, both numerically and experimentally.

6.2. Investigation Methods

6.2.1. Water Model Experiments

The effect of stopper-rod misalignment was investigated experimentally using a 1/3rd-scale water model of the steel caster at Gwangyang Works, POSCO, South Korea. Figure 6.1 shows a schematic of the 1/3rd scale water model. During operations, water is pumped from a water storage bath below the mold tank into the tundish through a flow meter. From the tundish, water falls via gravity through stopper head region, SEN bore, and exit ports into the mold cavity. Water exits the bottom of the mold through 11 outlets of 25 mm diameter and passes through a flow meter before entering the water bath again. The two flow meters (before tundish and after mold) along with the stopper-rod and variable-speed pump together control the flow rate in the mold to maintain the desired surface level.

To perform water model measurements, the stopper-rod was either aligned or moved 2 mm towards the front or towards the left to investigate misalignment, as shown in the top view in

Figure 6.2. Impeller velocity probes were positioned 15 mm below top free surface on both sides of the SEN at either 150 or 60 mm from narrow faces (NF) to measure horizontal surface velocities as shown in Figure 6.3(a). Instantaneous surface velocity data was collected at a sampling frequency of 1 Hz. Each probe is a 35 mm long open-ended tube (22 mm inner and 28 mm outer diameter) containing a small propeller that rotates in proportion with the water flow speed as shown in the close-up in Figure 6.3(b). The probe has a total response time of ~ 10 seconds (i.e. 0.1 Hz), including electrical response time (~0.4 seconds to reach 63 % of end value) and mechanical response time (for the vanes to respond to increase or decrease in flow). The probes are accurate over the velocity range of 0.02 ~ 5 m/s. For each case, mean velocities were averaged up to 2000 seconds and corresponding isotropic turbulent kinetic energies were derived using the standard root mean square relation [20], assuming unmeasured components had the same variations. Table 6.1 gives operational details on the water model measurements and further data is given elsewhere [21].

To visualize vortex formation, sesame seeds were added to the top surface as tracer particles and vortexing phenomena were recorded with a high speed video camera. The number and location of all vortices lasting at least 2s were measured from the high speed video. The total number of vortices observed at each location was then divided by total recording time (10 minutes) to calculate vortex formation frequency.

6.2.2. Computational Model

To augment the experimental investigation, a three-dimensional (3-D) finite-volume computational model has been formulated to investigate the time-averaged turbulent flow in the nozzle and the mold with aligned and two misaligned (front and left) positions of the stopper-rod as shown in the top view in Figure 6.2. The steady-state, incompressible, Navier-Stokes

equations with standard k- and ε- turbulence model (Launder and Spalding [22]) have been solved in FLUENT [23] to simulate the time-averaged turbulent flow.

To minimize computational effort, symmetry was exploited. One-quarter nozzle and mold domains were used to simulate flow with the aligned stopper-rod. Figure 6.4(a) shows the quarter nozzle with mesh with the aligned stopper-rod case. For front and left-misalignments, right- and back-half domains were used respectively. A similar mesh to the aligned case was used for the misaligned cases with 54000 hexahedral cells in back half for left misalignment and 33000 hexahedral cells in right half for front misalignment. Figure 6.4(b) shows the stopper head region of the upper tundish nozzle (UTN) and dimensions for these misaligned cases. To model the flow entering the stopper-head region, a cylindrical portion of the tundish bottom (with 200 mm diameter and 150 mm height) is created above the SEN. Figure 6.5 shows the typical back-half mold domain with mesh used in left misalignment of stopper-rod.

To improve efficiency and convergence, nozzle flow is simulated first, assuming a pressure outlet boundary condition at the port exit planes. The velocities, turbulent kinetic energy and dissipation rate at the outlet from the nozzle ports are then applied as boundary conditions for the inlet to the mold. Hershey et al [24] showed that this approach matches well with the results of simulations that combine the nozzle and strand together. Convergence is easier because residuals in the important low-velocity regions of the strand are not overly influenced by small errors in the high velocities inside the nozzle. The meshes of the nozzle outlet and the strand inlet were identical with one-to-one mapping in order to ensure accurate flux balance between the two computational domains.

Average velocity, kinetic energy, k, (10^{-5} m^2/s^2), and its dissipation rate, ε, (10^{-5} m^2/s^3), were fixed at the circumference and top annular region of the cylinder (representing part of the

tundish) to match the flow rate required for the casting speed of 0.917 m/min. The top free surface was assumed flat with a free-slip boundary condition. Free surface level profile was calculated from the pressure distribution along this free surface based on potential energy conservation [25-26]. The equation 5.3 given previously in CHAPTER 5 was used for the same. Like the steel caster, the strand outlet was modeled with no bottom and a constant-pressure outlet boundary condition. The water model bottom deflects the flow somewhat, but this difference is expected to be small, due to long domain and is limited to the lower region. In order to handle reverse flow from the strand exit in the lower recirculation zone, small values of k and ε (10^{-5} m^2/s^2 and 10^{-5} m^2/s^3) were set at the strand domain exit, along with 0 Pa gauge pressure. The vertical wide and narrow face walls were considered stationary. Standard wall laws were used as boundary conditions for all the walls [27]. Table 6.1 gives various process parameters, physical properties of water and dimensional details about the 1/3rd water model.

The equations for the three momentum components, k-, ε-, and Pressure Poisson Equation (PPE) are discretized using the Finite Volume Method (FVM) in FLUENT [20] with 1st -order upwind scheme for convection terms. These discretized equations are then solved for velocity and pressure using the Semi-Implicit Pressure Linked Equations (SIMPLE) algorithm, starting with initial conditions of zero velocity in the whole domain. The segregated solver in FLUENT was used to solve all equations. In all simulations, convergence was defined when all scaled residuals were reduced below 10^{-4}. All computations were performed on a PC with a 2.66 GHz Intel® Xeon processor (Intel Corp., Santa Clara, US) and 4.0 GB RAM. Further details about the computational model are given elsewhere [24, 28-29].

6.3. Model Validation

The computational model was first validated by comparison with the near-surface velocities measured by the velocity probe on both sides of the SEN. Mean velocities ($\bar{u}$), turbulent kinetic energies (k), and standard deviations (σ), were calculated from 1000 or 2000 sec of instantaneous measured velocity data in different cases using the following equations:

$$\mathrm{k} = (3/2)\sigma^2 = (3/2)(1/N)\sum_{n=1}^{N}(u_i - \bar{u})^2 \tag{6.1}$$

where N is total number of measured data points, and u_i is the instantaneous horizontal surface velocity. This equation to estimate the measured k assumes isotropic turbulence.

Table 6.2 compares time-averaged surface velocities of the computational model and measurements. The measured standard deviations were ~0.02m/s (or ~20% of the mean). The mean velocity predictions fall within the range of +/- one standard deviation of the mean of the measurements in all cases. Errors are generally less than 9% at 60mm from the narrow faces, and less than 25% at 150mm. The only exception is for the left-misalignment case on the left side, where the maximum error is 13% at 60mm and 40% at 150mm. The larger error at this location is due to the complex vortex flow pattern found at this location not being as accurately resolved by the current Reynolds-Averaged Navier Stokes (RANS) k-ε turbulence model. The computational model predicts higher surface velocity at 150 mm from NF relative to 60 mm, because this location is closer to mid-way between SEN and narrow faces. Surprisingly, the experiments give similar velocities at 150 and 60 mm from the narrow faces.

The experiments and simulations exhibit the same trends. Measurements for the aligned and front-misaligned cases show the expected right-left symmetry within ~5%, which is less than the standard deviation of the measurements of ~20%. This symmetry is imposed in the

computational model. Left-misalignment causes significant right-left asymmetry with the right side having higher surface velocity.

Table 6.3 compares the computed turbulent kinetic energy with values extracted from the measurements using Eq.(6.1). Turbulent kinetic energy matches well (same order) with measurements in all cases. The largest differences are seen on the left side of left-misalignment, due to complex vortex formation. The vortices increase the measured turbulence, but are not captured perfectly by the computational model. Overall, the observed differences are reasonable considering the anisotropy of real turbulence, total measurement time, sampling frequency, probe response time and numerical errors (truncation and round-off).

For consistency, all simulations were performed with the standard k-ε model with standard wall laws. This simple, readily-available model has reasonable accuracy in a wide range of flows and excellent computational efficiency. It is not the best for asymmetric flow with vortex formation. However, other RANS models were found to produce similar or worse behavior for the current problem. Time-varying models (such as DNS, LES) may perform better but are very computationally intensive. An extensive investigation of the advantages and disadvantages of various flow models is reported elsewhere [29].

6.4. Nozzle Flow Results

6.4.1. Effects Near Stopper Head

The effect of stopper misalignment on flow near the stopper head and tundish bottom is presented in Figure 6.6. As expected, high velocity flow is predicted through the restricted flow area between the stopper-head and the curved tundish bottom or UTN. There is much less flow through the most restricted side, due to higher pressure loss. In left/front misalignment, only ~15% (~0.08 kg/s) of the flow rate is from the restricted left/front quarter of the nozzle near

stopper head with the remaining ~35% (~0.20 kg/s) pouring through the larger quarter opening on the right/back side. The symmetric flow through the aligned one-quarter nozzle model is 25% (~0.14 kg/s).

Stagnation regions exist under the stopper-head and along the SEN bore wall below the curved tundish bottom. For the misaligned cases, Figure 6.6(b) shows the increased velocity (18% higher than average) through the larger high-flow area, which is the right side in left-misalignment and the back side in front-misalignment. This creates higher momentum steel falling from this side towards the opposite side of the SEN bore wall. Velocity is lower on the restricted, low flow-rate side. Figure 6.6(c) shows the cross-section perpendicular to section shown in Figure 6.6(b) for the front/left misalignment cases. Here, the stagnation region below the stopper-head is lessened due to the high-momentum flow crossing sides in the other plane.

6.4.2. Effects Near SEN Ports

Velocity magnitude contours and streamlines near the bottom well of the SEN are presented in Figure 6.7 for the same three alignment cases. The aligned stopper rod shows a 14% shorter jet at port exit (centerplane) compared to the front misaligned and left side of left-misalignment cases. The jet on the right side in left misalignment has the maximum height (~28% more than on the left side). The higher momentum of flow down the left side of the nozzle bore with left misalignment can also be seen in Figure 6.7(c). Figure 6.8 and Table 6.4 respectively show the flow patterns and jet characteristics [30] at the ports for the aligned, front- and left-misaligned stopper-rod cases. The equations for jet characteristics are presented in Appendix-C. The jets from the aligned stopper-rod case are naturally front-back symmetric, with 19% reverse-flow area on the top of the port. The vertical jet angle, horizontal spread angle, weighted turbulent kinetic energy and dissipation rate in the aligned stopper case, are higher than

in any of the misaligned cases. In the front-misaligned stopper rod case, the jet is bent towards the back causing front-back asymmetry but still has same reverse flow fraction (19%) as in the aligned stopper-rod. The left side jet in the left-misaligned case has higher reverse flow port area (28%) than the right side (12%) and any other jet. The jet with left-misalignment naturally is front-back symmetric but has right-left asymmetry. Although the flow exiting the left-side port with the left-misaligned stopper rod is smaller than the right, average jet speed on the left side is higher.

Usually, the effect of inlet velocity asymmetries in turbulent pipe flow should disappear if [31],

$$\frac{L}{D} > 4.4\,\mathrm{Re}^{1/6} \tag{6.2}$$

where Re=DUρ/μ, L: pipe length, D: pipe diameter, U: mean axial velocity, ρ: density, μ: molecular viscosity. For the current water model, Eq. (6.2) predicts a critical L/D of ~24. Since current water model has a smaller L/D (SEN bore length (from tundish bottom to ports)/bore diameter) of ~21, the effects of stopper misalignment are expected to persist past the SEN ports. This is consistent with the findings of this work. Extending Eq. (6.2) to the real caster, where the casting speed of 1.6 m/min is root(3) times faster than speed in the Froude-scaled 1/3-scale water model [32], the critical (L/D) further increases to ~32. Thus, asymmetry effects are expected to be at least as strong in the real steel caster, as found in this work.

6.5. Mold Flow Results

6.5.1. Flow Pattern

Mold flow patterns for the aligned, front- and left-misaligned stopper-rods are presented in Figure 6.9. Overall, the flow is a classic “double-roll” in all cases, as the jets impinge first upon the narrow faces, then flow up and back across the surface towards the SEN.

With the aligned stopper-rod case, the jet flows mostly toward NF. With front-misalignment, more flow exits the front side of the ports but the jet bends towards the back mold face (outer radius), as can be seen in port velocity vectors in Figure 6.8(b). This flow impinges close to the corners between wide and narrow faces. As it flows up the narrow faces, the flow deflects towards the front side, leading to lower velocities in the mid-plane, as seen in Figure 6.9(b) and Figure 6.10. Smaller horizontal spread angle and lower vertical jet angles gives this case higher surface velocity than the other cases, especially towards the front side.

In the left-misaligned stopper-rod case, the right port has higher mass flow rate but lower velocity compared to left side (biased flow). The flow pattern created by this imbalance is shown at the mold mid-plane in Figure 6.9(c).

Vertical velocity down a path 10 mm from the narrow faces on each side of the SEN is shown in Figure 6.11 for all three cases. The jet hits almost at the same location (180 mm) on the left side of the three cases. On the right side of the left misalignment case, the jet impinges slightly higher (140 mm) than the other two cases. Left misalignment shows stronger flow down the left side and weak reverse flow on the right side, owing to the asymmetric flow pattern.

6.5.2. Surface Velocity

Due to its importance on final product quality, the surface velocities predicted for the 3 cases are compared on both sides of the SEN in Figure 6.12. In the aligned stopper-rod case, even though the port velocity is highest, the steeper downward vertical jet angle and higher horizontal spread angle leads to less upward flow and weaker surface velocity. The surface velocity is highest with front misalignment and lowest on the left side with left misalignment. With left-misalignment, the shallower jet with lower velocity but higher flow rate on the right side gives higher surface velocity on the right side.

The measured histories of horizontal surface velocity on both sides of the SEN are presented in Figure 6.13 for all 3 cases. The velocities measured by the impeller 15 mm below the surface are given at 60 mm (left) and 150 mm (right) from the narrow faces. The mean velocity on left and right sides agree at both locations (i.e. 60 mm and 150 mm), within one standard deviation (Table 6.2). Thus, the flow has right-left symmetry as expected with an aligned stopper. Asymmetry is worse at 150 mm location (5% difference) than the 60mm location (1% difference) due to transient nature of jet.

The front-misaligned case also exhibits the expected right-left symmetry (within one standard deviation). Again, asymmetry is worst at 150mm (9% different) than at 60mm (2% different). In the left-misaligned case, velocity is almost symmetric at 60 mm, (9% different). Asymmetry is clearly visible at 150 mm in this case, as the right side is 32% faster than the left, due to the shallower jet on the right. This experimental finding of prominent asymmetry at 150 mm with a left-misaligned stopper rod and higher velocity on the right side is consistent with the simulation results (Figure 6.12).

6.5.3. Surface Level Profile

A comparison of free-surface level at the mid-plane on both sides of the SEN in all cases is given in Figure 6.14. The double-roll flow causes a higher surface near the narrow faces and SEN in all cases. Higher surface velocities cause higher level profile variations. Front-misaligned case shows highest level near the narrow faces. The left side of the left-misalignment cases has the flattest surface, owing to the slower upward velocity along the left narrow face, and lower surface pressure from vortex formation on the left side of the SEN.

6.5.4. Vortex Formation

Transient mold flow, caused by wobbling jets, may cause intermittent chaotic vortex formation on both sides of the SEN in the mold cavity. In addition, right-left biased flows form more vortices on the left side, as explained earlier due to flow through the gap from the right. Figure 6.15 (a) shows an example of vortex formation with the left misaligned stopper rod using sesame seeds to visualize surface entrainment. The vortex, forming preferentially on the left side as shown, carries sesame seeds down to the jet. In real casters, liquid mold slag entrapped in this way causes sliver defects on lower product quality.

Figure 6.15(b) presents the measured frequency of the vortex formation on both sides of the SEN for all 3 cases. All of the vortices are found in four regions close to the SEN. As expected, the formation frequency on the right and left sides is about the same (within 10%) in the aligned and front-misaligned cases. The front-misaligned case forms 26% more vortices than the aligned. The most vortices form on the left side of the left-misaligned case, i.e. more than double the frequency produced on the right side. The right side of this case also has the fewest vortices (~30% less than the aligned case). These findings about vortices are consistent with model predicted and measured surface velocities.

Although, steady RANS k-ε turbulence model cannot predict vortex formation frequency, it can predict the location of mean vortex through surface velocity vectors. Figure 6.15(c) shows the modeled surface velocity vectors in the left-misaligned stopper-rod case, clearly showing two vortices on the left side near the SEN, which reinforces the experimental findings. The standard k-ε model with standard wall laws performs best on a hexahedral coarse mesh, with symmetrical, well-shaped elements of similar size. Such a mesh was not possible for the complex asymmetric

geometry of the misaligned nozzle, which explains why the predicted vortex shape is too elongated. More accurate predictions would require a transient computational model.

6.6. Conclusions

In this paper, the effect of stopper-rod misalignment on the fluid flow through a water model of continuous casting of steel has been investigated both experimentally and numerically. The computational model matches well with measured surface velocities and turbulent kinetic energies. The model predictions and measurements are consistent and together reveal new insights into the effects of stopper-rod misalignment.

With an aligned stopper-rod, flow and vortex formation show both right-left and back-front symmetry within the standard deviation of the measurements of ~20%. In front misalignment, flow from the UTN region with higher momentum hits the bottom of the nozzle towards the front side and exits the front of the ports but is directed towards the back side of the mold (wide face). This causes front-back asymmetry in surface velocity. The surface velocity is right-left symmetric within the standard deviation of the measurements. With left misalignment, the higher momentum flow hits the left side of the SEN bottom, causing a thin, steep, high-velocity jet exiting the left port. The right port has a slower, shallower jet but with higher mass flow rate (54%), so produces higher surface velocity on the right side of this case. This right-left asymmetry on the surface velocity in this case is stronger close to SEN (at 150 mm), where vortices form. These findings are consistent in both the simulations and measurements.

Intermittent vortices form in all cases with similar frequencies on the right and left in the aligned and front-misaligned cases. The main cause of these vortices is the transient wobbling of the jet causing stronger surface flow from right to left at some times and from left to right at other times. The right-left asymmetry in the measured surface velocities is higher close to SEN

in all cases. With left-misalignment, the significant right-left asymmetry in velocity causes significantly more vortices to form on the left, relative to the right. In summary, this study shows the importance of the alignment of stopper-rod in continuous casting and how a misaligned stopper causes significant asymmetric flow and increased formation of detrimental vortices.

6.7. Tables and Figures

Table 6.1 Process parameters for experimental setup and numerical simulations in 1/3rd water model

	1/3rd Water model
Casting speed	0.917 m/min
Water flow rate	34.4 LPM
Mold width	500 mm
Mold thickness	75 mm
Computational domain width	250 mm
Computational domain thickness	37.5 mm
Computational domain length	1200 mm
SEN depth	60 mm
ρ_{fluid}	998.2 kg/m^3 (water)
μ_{fluid}	0.001 kg/m-s (water)
Stopper-rod	Centered (i.e. aligned), front-, and left-misaligned (2mm)
Nozzle port angle	35 degree
Nozzle port area	23.3 mm(width) x 26.7mm(height)
Nozzle bore diameter (inner/outer)	25 mm/43 mm
Distance between tundish bottom and nozzle bottom	560 mm
Shell	no
Gas injection	no

Table 6.2 Comparison of mean near-surface velocities between computational predictions and experiments at four locations

	Unit: m/s	60mm from left NF	150mm from left NF		150mm from right NF	60mm from right NF
Aligned	Measurements	0.093	0.098		0.103	0.094
	Standard deviation	0.018	0.018		0.019	0.022
	Model Predictions	0.102	0.120		0.120	0.102
Front misaligned	Measurements	0.094	0.105	**Nozzle**	0.096	0.096
	Standard deviation	0.018	0.019		0.018	0.021
	Model predictions	0.097	0.122		0.122	0.097
Left misaligned	Measurements	0.096	0.084		0.111	0.105
	Standard deviation	0.023	0.016		0.018	0.017
	Model predictions	0.084	0.060		0.104	0.095

Table 6.3 Comparison of turbulent kinetic energy between computational predictions and experiments at 150 mm and 60 mm from NFs on both sides of SEN

	Unit: mm^2/s^2	60mm from left NF	150mm from left NF		150mm from right NF	60mm from right NF
Aligned	Measurements	486	472		530	691
	Model Predictions	690	375		375	690
Front misaligned	Measurements	479	552	**Nozzle**	507	637
	Model predictions	724	533		533	724
Left misaligned	Measurements	822	404		488	425
	Model predictions	357	140		300	502

Table 6.4 Jet characteristics of aligned, front-misaligned and left-misaligned stopper-rod nozzle ports' jets

	Centered		Front-misaligned stopper-rod		Left-misaligned stopper-rod	
	Left	Right	Left	Right	Left	Right
Weighted average nozzle port velocity in x-direction(outward)(m/s)	0.66	0.66	0.68	0.68	0.73	0.69
Weighted average nozzle port velocity in y-direction(downward)(m/s)	0.53	0.53	0.51	0.51	0.53	0.35
Weighted average nozzle port velocity in z-direction(horizontal)(m/s)	0.058 (towards outward in half port)	0.058 (towards outward in half port)	0.022 (towards outer radius in full port)	0.022 (towards outer radius in full port)	0.055 (towards outward in half port)	0.021 (towards outward in half port)
Weighted average nozzle port turbulent kinetic energy (m^2/s^2)	0.060	0.060	0.026	0.026	0.020	0.028
Weighted average nozzle port turbulent kinetic energy dissipation rate (m^2/s^3)	3.24	3.24	1.15	1.15	0.83	1.29
Vertical jet angle (degree)	39.17	39.17	36.88	36.88	36.24	27.25
Horizontal jet angle (degree)	0	0	1.9	1.9	0	0
Horizontal spread (half) angle (degree)	5.08	5.08	-	-	4.33	1.76
Average jet speed (m/s)	0.85	0.85	0.85	0.85	0.91	0.78
Back-flow zone (%)	19	19	19	19	28	12
Flow rate (%)	50	50	50	50	45.62	54.38
Maximum velocity magnitude (m/s)	1.23	1.23	1.16	1.16	1.09	1.06

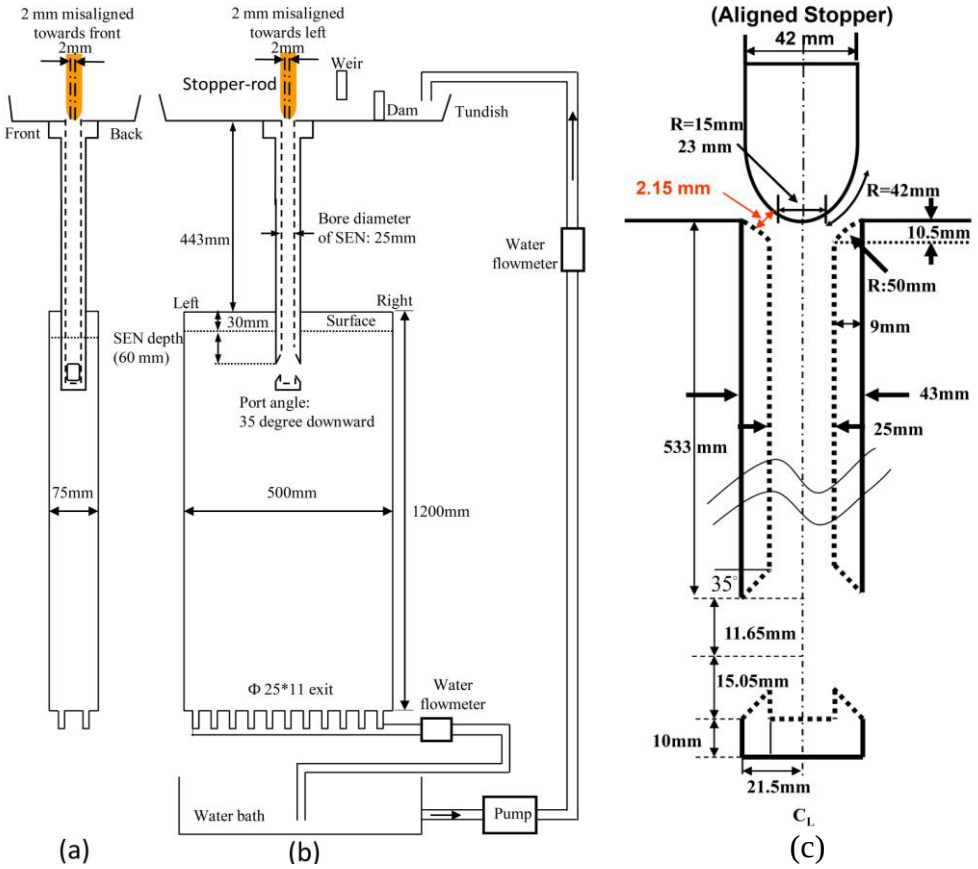

Figure 6.1. Schematic of 1/3rd water model showing 2 mm stopper-rod misalignment (a) right side view, (b) front view, and (c) close look at aligned stopper-rod nozzle

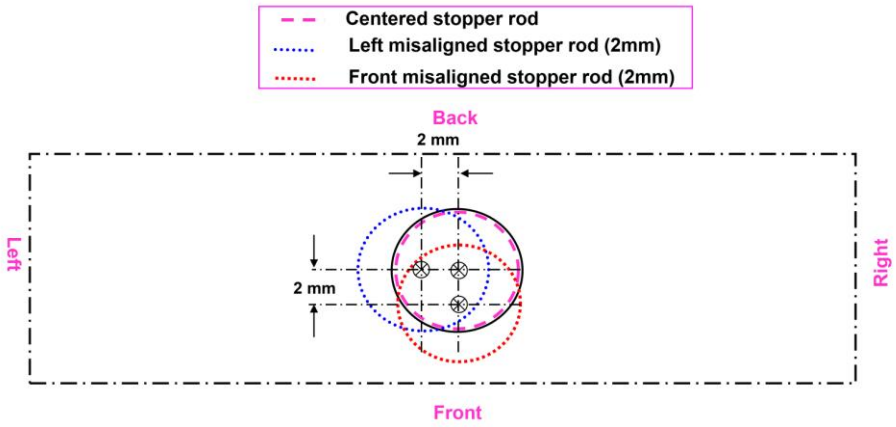

Figure 6.2. Top view of three stopper-rod positions studied

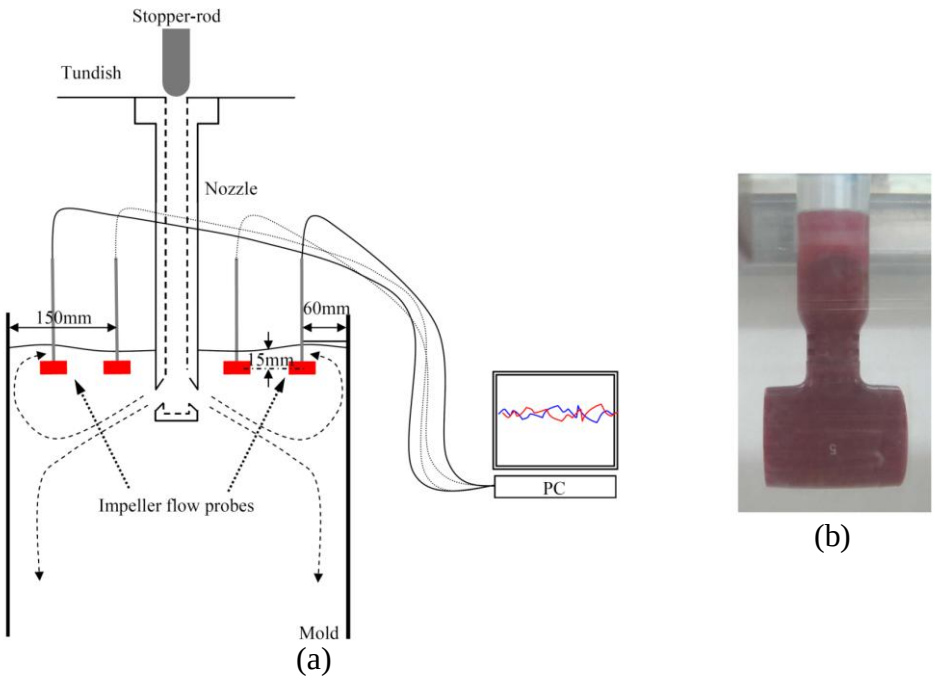

Figure 6.3. (a) Schematic of the impeller probe with locations and (b) Close-up of the probe

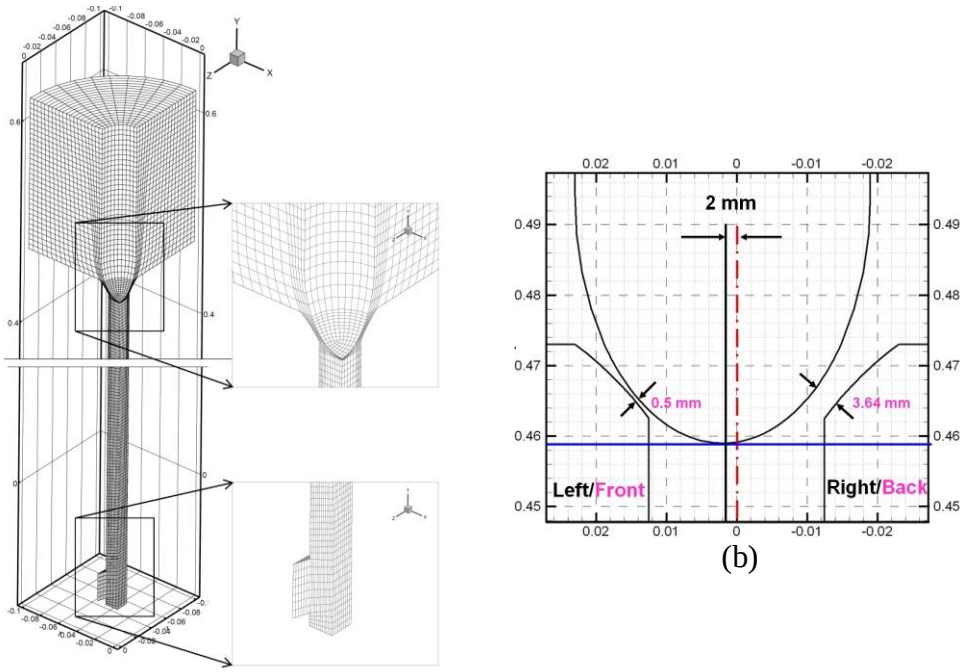

Figure 6.4. (a) Centered stopper rod with nozzle (Quarter nozzle: 22400 Hexahedral cells) and (b) Dimensional details after misalignment

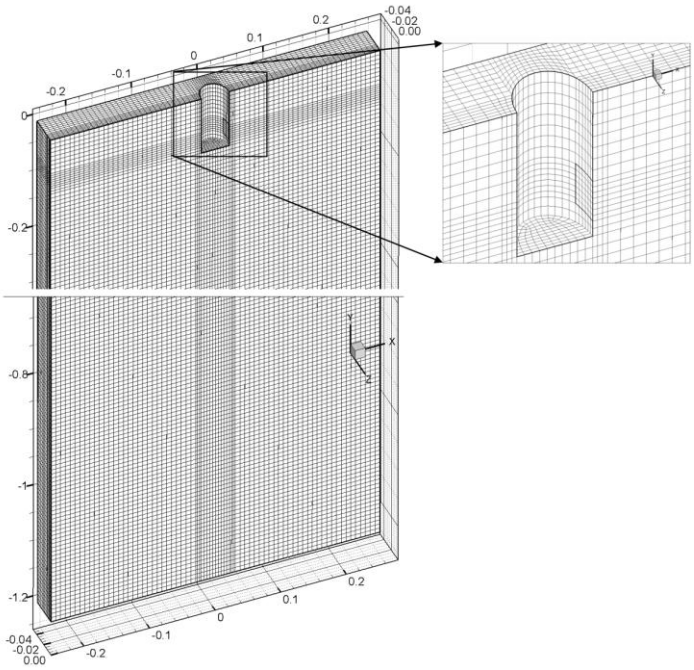

Figure 6.5. Back-half mold mesh (90,000 hexahedral cells in quarter mold, i.e. 360,000 hexahedral cells in full mold)

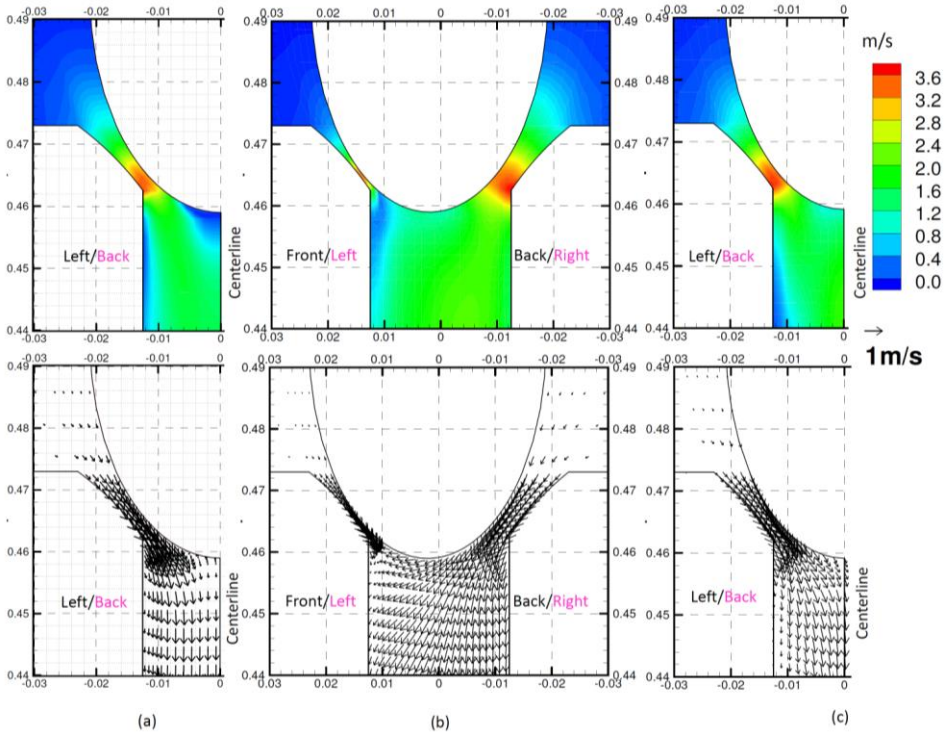

Figure 6.6. Velocity contours and vectors near stopper-rod head region at the center plane with (a) Aligned, (b) 2 mm front(side-view) / left(front-view) misaligned, and (c) 2 mm front(front-view) / left(side-view) misaligned stopper-rod

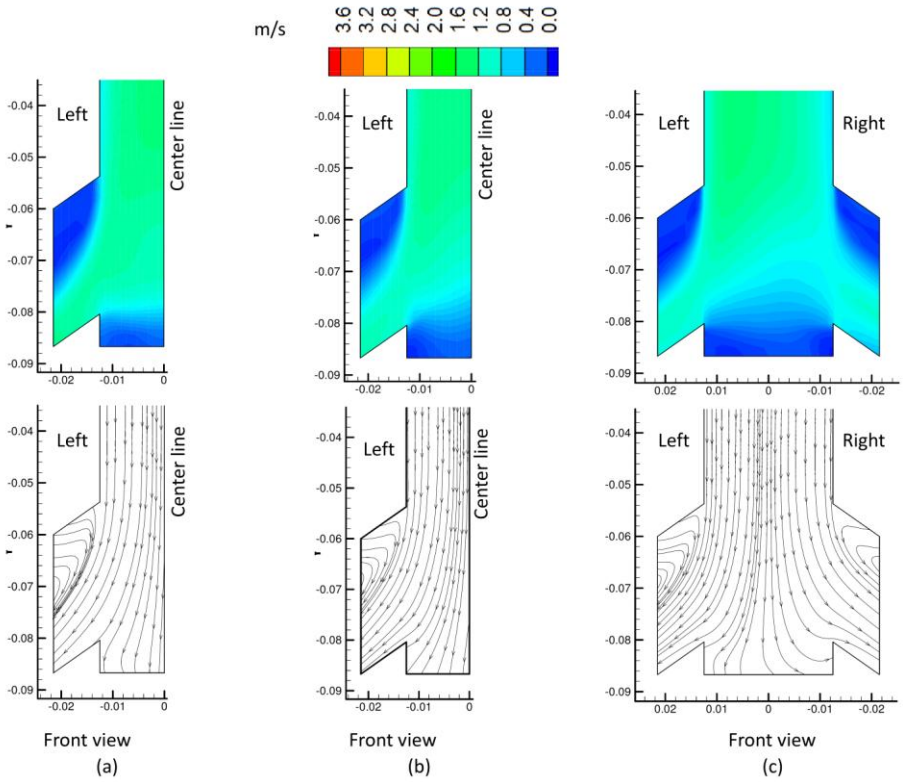

Figure 6.7. Velocity contours and streamlines in the bottom portion of the nozzle with (a) aligned, (b) 2 mm front-misaligned, and (c) 2 mm left-misaligned stopper-rod

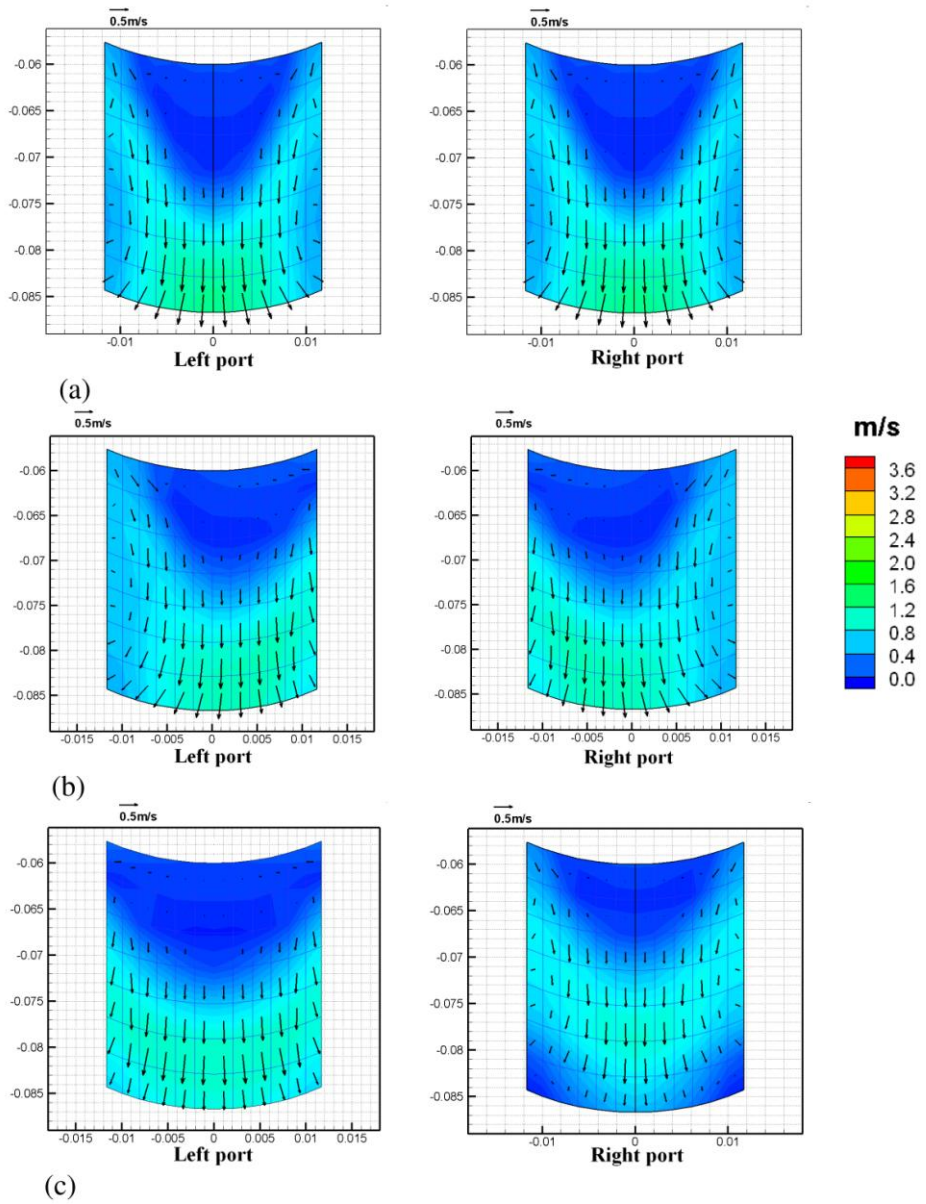

Figure 6.8. Port velocities with (a) aligned, (b) 2 mm front misaligned, and (c) 2 mm left misaligned stopper-rod cases

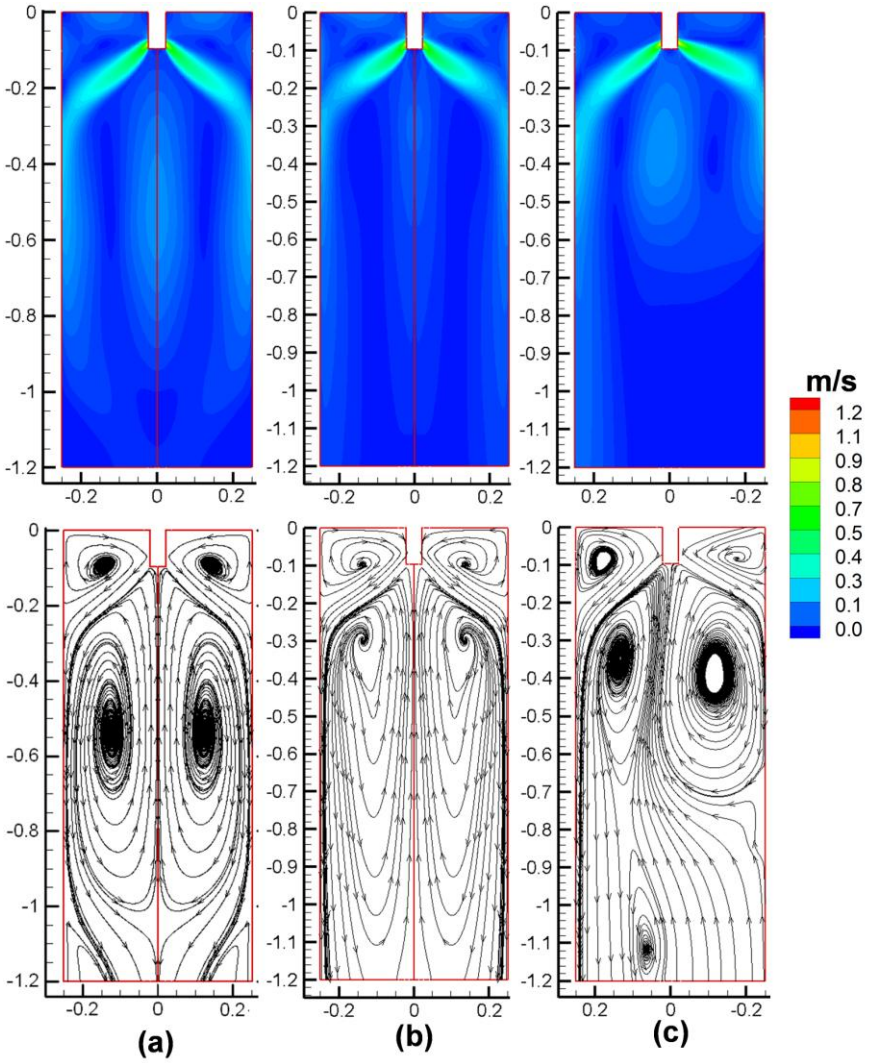

Figure 6.9. Velocity contours and streamlines on the center plane between wide faces with (a) aligned, (b) 2 mm front-misaligned, and (c) 2 mm left-misaligned stopper-rod cases

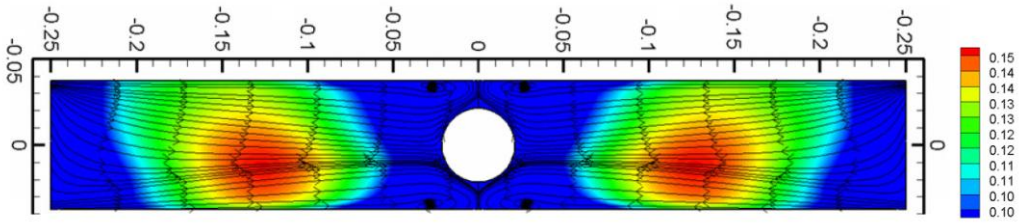

Figure 6.10. Surface velocity contours with streamlines in front-misaligned stopper-rod case

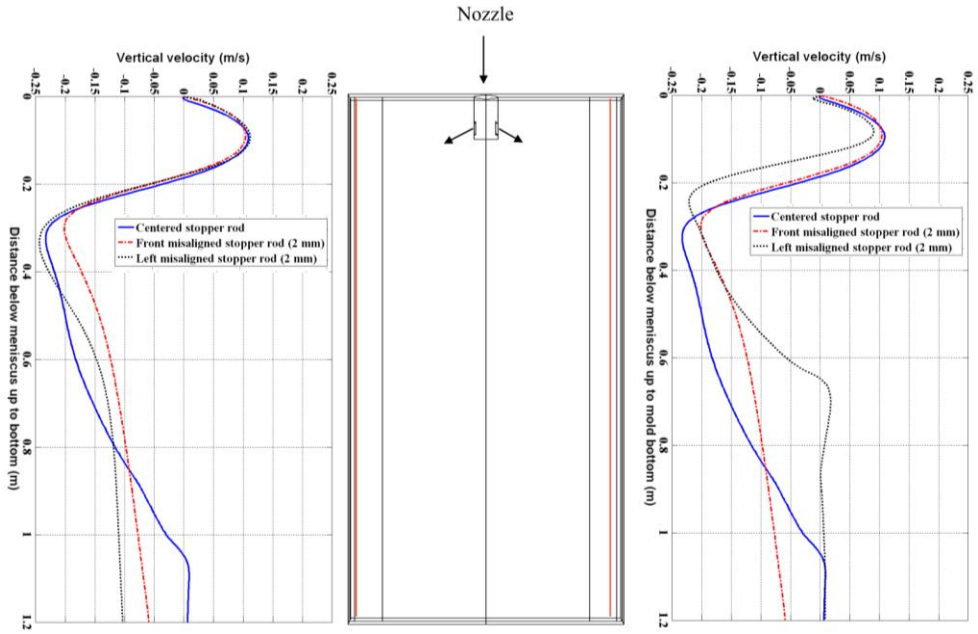

Figure 6.11. Comparison of vertical velocities (at 10 mm from narrow faces along the mold length) on both sides of SEN comparing aligned, front-misaligned and left-misaligned stopper-rod cases

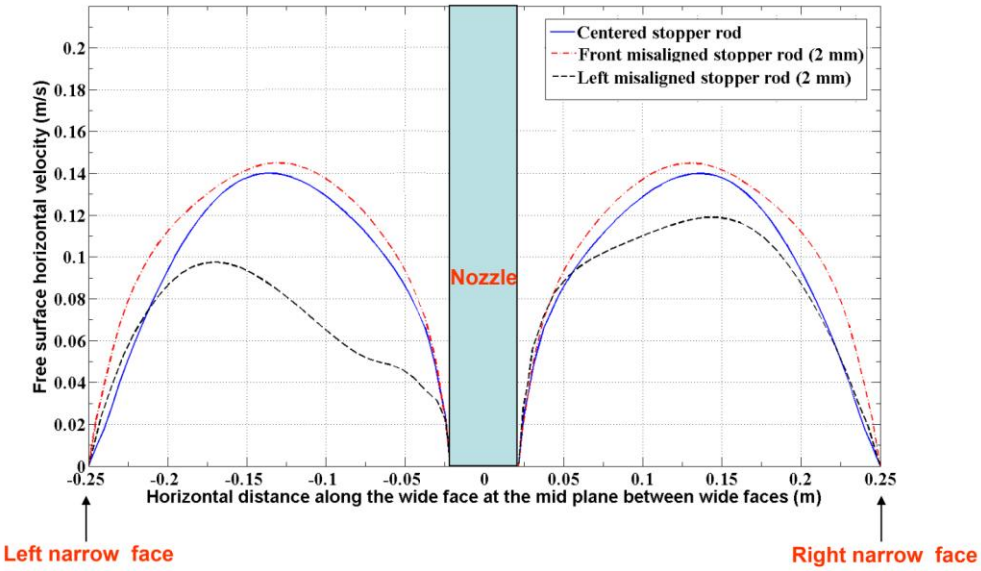

Figure 6.12. Comparison of horizontal surface velocity magnitudes in aligned, front-misaligned and left-misaligned stopper-rod cases

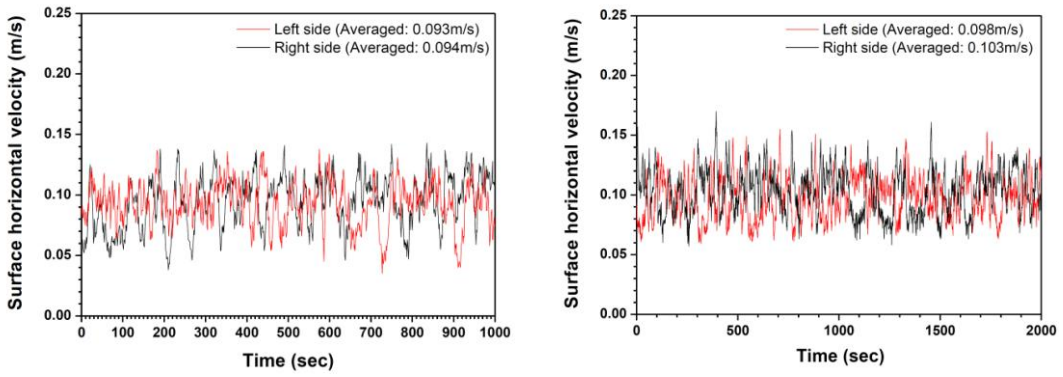

(i) (ii)

(a)

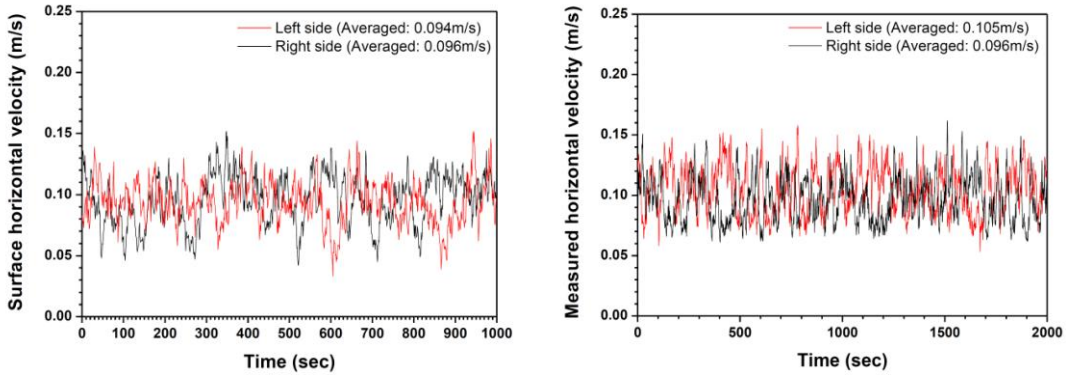

(i) (ii)

(b)

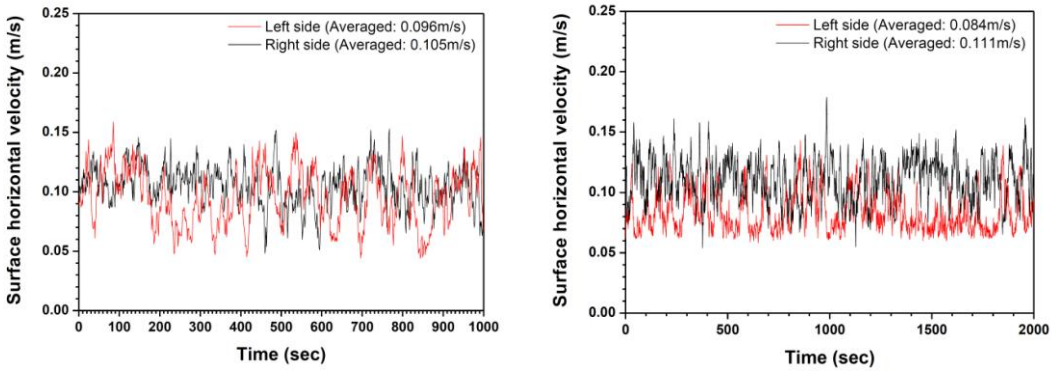

(i) (ii)

(c)

Figure 6.13. Measured surface velocities with (a) aligned, (b) 2 mm front misaligned, and (c) 2 mm left misaligned stopper-rod ((i) Left figures: 60 mm from narrow faces, (ii) Right figures: 150 mm from narrow faces)

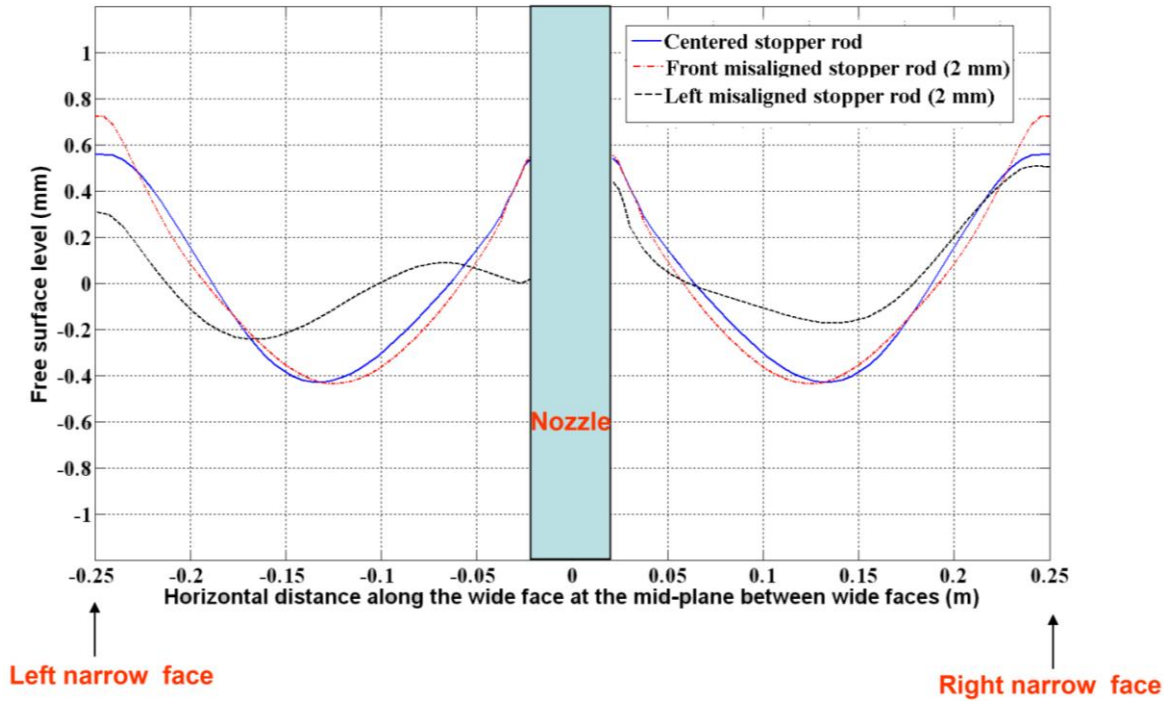

Figure 6.14. Comparison of free surface levels in between aligned, front-misaligned and left-misaligned stopper-rod cases

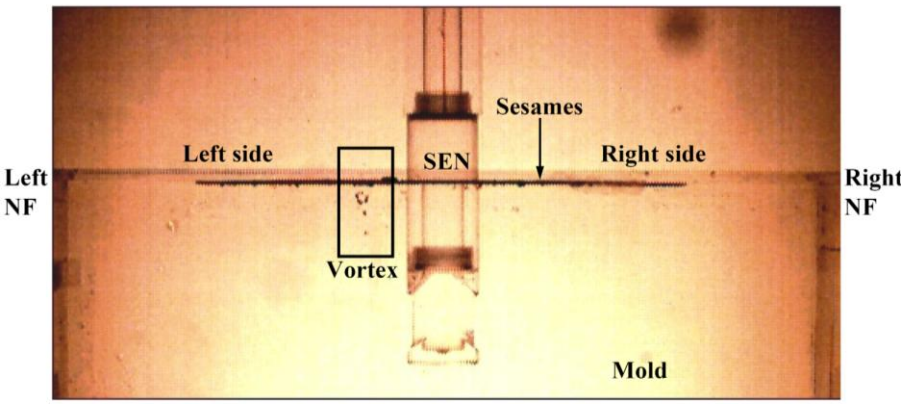

(a)

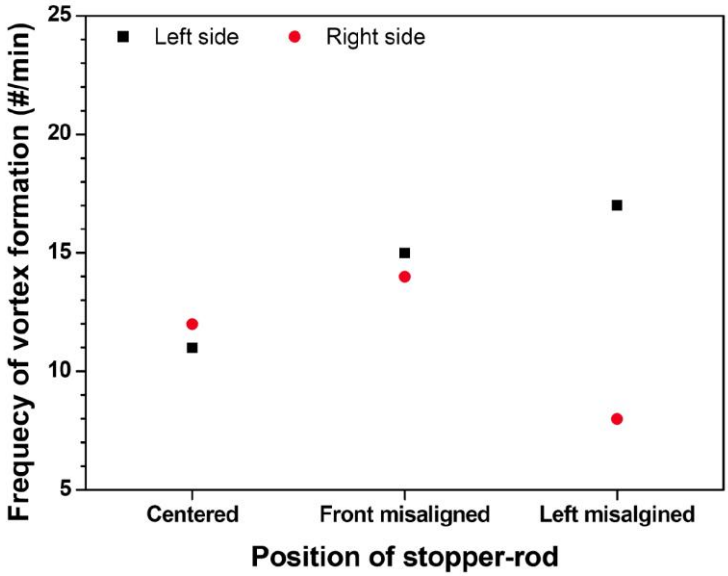

(b)

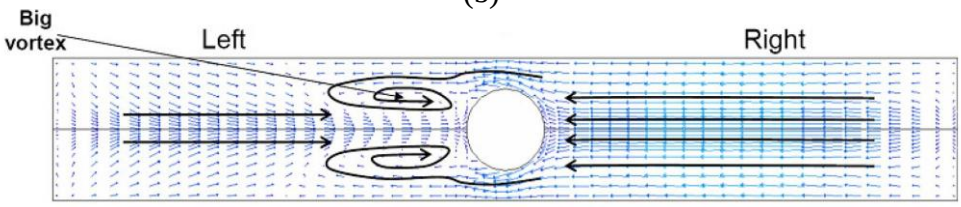

(c)

Figure 6.15. (a) Experimental observation of vortex formation, (b) frequency of vortex formation around SEN in mold (60 mm), and (c) its RANS simulation with left misalignment

6.8. References

1. *World Steel in Figures*. 2007, International Iron and Steel Institute: Brussels, Belgium, www.worldsteel.org.
2. B. G. Thomas, *Chapter 14. Fluid Flow in the mold*, in *Making, Shaping and Treating of Steel*, A.W. Cramb, Editor. 2003, AISE Steel Foundation: Pittsburgh, PA.
3. J. Kubota, et al. *Meniscus Flow Control in the Mold by Travelling Magnetic Field for High Speed Slab Caster*. in *Steelmaking Conf. Proceedings*. 1991.
4. S. Feldbauer, and A. Cramb, *Insight into Slag Entrainment in the mold of a continuous Caster,* in PTD Conf. Proceedings, 13 (Warrendale, PA: Iron and Steel Society, 1995), pp. 327-340.
5. J. Hebertson, et al, *Modeling of Metal Delivery to Continuous Casting Moulds*, in Steelmaking Conf. Proc. 1991, ISSS, Warrendale, PA: Washington, D.C. Pp. 171-185.
6. T. Honeyands, and J. Herbertson, *Flow Dynamics in Thin Slab Caster Moulds*, Steel Research, 1995, 66(7), pp. 287-293
7. W. H. Emling, et al. *Subsurface Mold Slag Entrainment in Ultra Low Carbon Steels*, in 77th Steelmaking Conference Proceedings. 1994: ISS, Warrendale, PA.
8. Q. Yuan, B. G. Thomas, and S. P. Vanka, *Study of Transient Flow and Particle Transport during Continuous Casting of Steel Slabs, Part I. Fluid Flow*, Metall. Mat. B., 2004, 35B(4), pp. 685-702.
9. H. Bai, and B. G. Thomas, *Turbulent Flow of Liquid Steel and Argon Bubbles in Slide-Gate Tundish Nozzles, Part I, Model Development and Validation*, Metall. Mat. Trans. B, 2001, 32B(2), pp. 253-267.

10. H. Bai, and B. G. Thomas, *Turbulent Flow of Liquid Steel and Argon Bubbles in Slide-Gate Tundish Nozzles, Part II, Effect of Operation Conditions and Nozzle Design*, Metall. Mat. Trans. B, 2001, 32B(2), pp. 269-284.

11. Go-Gi Lee, et al., *Asymmetric Multi-phase Fluid Flow and Particle Entrapment in a Continuous Casting Mold*. in *AISTech 2008*. 2008. Pittsburgh, PA.

12. S. Mahmood, *Modeling of flow asymmetries and particle entrapment in nozzle and mold during continuous casting of steel slabs*, MS Thesis, 2006, *Mechanical Science & Engineering*, University of Illinois at Urbana-Champaign, IL.

13. L. Zhang, Y. Wang, and X. Zuo, *Flow Transport and Inclusion Motion in Steel Continuous-Casting Mold under Submerged Entry Nozzle Clogging Condition*, Metall Mat Trans B, Vol. 39, 2008, pp. 534-550.

14. S. Yokoya, et al, *Swirling Flow Effect in Off-center Immersion Nozzle on Bulk Flow in Billet Continuous Casting Mold*, ISIJ International, 2001, 41(10), pp. 1215-1220.

15. D. Gupta, S. Chakraborty, and A. K. Lahiri, *Asymmetry and oscillation of the fluid flow pattern in a continuous casting mould: A water model study*. ISIJ International, 1997, 37(7), pp. 654-658.

16. D. Gupta, and A. K. Lahiri, *A water model study of the flow asymmetry inside a continuous slab casting mold*. Metallurgical and Materials Transactions B-Process Metallurgy and Materials Processing Science, 1996. 27(5): p. 757-764.

17. B. K. Li, T. Okane, and T. Umeda, *Modeling of biased flow phenomena associated with the effects of static magnetic-field application and argon gas injection in slab continuous casting of steel*. Metall. Mat. Trans. B-Process Metallurgy and Materials Processing Science, 2001. 32(6): p. 1053-1066.

18. B. Li, and F. Tsukihashi, *Vortexing flow patterns in a water model of slab continuous casting mold.* ISIJ International, 2005. 45(1): p. 30-36.

19. Q. Yuan, B. Zhao, S. P. Vanka, and B. G. Thomas, *Study of Computational Issues in Simulation of Transient Flow in Continuous Casting*, Steel Research, Special Issue: Simulation of Fluid Flow in Metallurgy, Jan 2005, Vol. 76, No. 1, pp. 33-43.

20. H. K. Versteeg, and W. Malalasekra, *An Introduction to Computational Fluid Dynamics: The Finite Volume Method Approach*. 1995, Essex, England: Longman Scientific Technical.

21. S.-M. Cho, G.-G. Lee, S.-H. Kim, R. Chaudhary, O.-D. Kwon, B. G. Thomas, *Effect of Stopper-rod Misalignment on Asymmetric Flow and Vortex Formation in Steel Slab Casting*, 2010 TMS Annual Meeting & Exhibition, Feb. 14-18, 2010, Seattle, WA.

22. B. E. Launder, and D. B. Spalding, *Mathematical Models of Turbulence.* 1972: London Academic Press.

23. *FLUENT6.3-Manual* (2007), ANSYS Inc., 10 Cavendish Court, Lebanon, NH, USA.

24. D. E. Hershey, B. G. Thomas, and F. M. Najjar, *Turbulent Flow through Bifurcated Nozzles.* Int. J. Num. Meth. in Fluids, 1993. 17(1): p. 23-47.

25. X. Huang, and B. G. Thomas, *Modeling of transient flow phenomena in continuous casting of steel.* Canadian Metallurgical Quarterly, 1998. 37(3-4): p. 197-212.

26. G. A. Panaras, A. Theodorakakos, and G. Bergeles, *Numerical Investigation of the Free Surface in a continuous Steel Casting Mold Model.* Metall. Mat. Trans. B, 1998. 29B(5): p. 1117-1126.

27. B. E. Launder, and D. B. Spalding, *The numerical computation of turbulent flows.* Computer Methods in Applied Mechanics and Engineering, 1974. 3(2): p. 269-289.

28. R. Chaudhary, G.-G. Lee, B. G. Thomas, and S.-H. Kim, *Transient Mold Fluid Flow with Well- and Mountain-Bottom Nozzles in Continuous Casting of Steel*, Metall. Mat. Trans B, Vol. 39, No-6, Dec 2008.

29. R. Chaudhary, B. G. Thomas, and S. P. Vanka, *Evaluation of turbulence models in MHD channel and square duct flows*, CCC Report, 201011, Department of Mechanical Science and Engineering, University of Illinois at Urbana-Champaign, IL, US.

30. H. Bai, and B. G. Thomas, *Turbulent Flow of Liquid Steel and Argon Bubbles in Slide-gate Tundish Nozzles: Part I. Model Development and Validation*, Metall. Mat. Trans. B, 2001, 32(2), pp. 253-267.

31. F. M. White, Fluid Mechanics, Fourth Edition, Mc-Graw Hill, 1999.

32. R. Chaudhary, B. T. Rietow, and B.G. Thomas, *Differences between Physical Water Models and Steel Continuous Casters: A Theoretical Evaluation*, Materials Science and Technology Conference, AIST/TMS, Pittsburgh, PA, Oct. 25-29, 2009.

CHAPTER 7. TRANSIENT TURBULENT FLOW IN A LIQUID-METAL MODEL OF CONTINUOUS CASTING, INCLUDING COMPARISON OF SIX DIFFERENT METHODS

7.1. Introduction

Optimization of fluid flow in the continuous casting process is important to minimize defects in steel products. Turbulent fluid flow in the submerged entry nozzle (SEN) and the mold are the main causes of entrainment of slag inclusions and the formation of surface defects [1]. Computational models combined with physical models are useful tools to study the complex turbulent flow in these systems [2].

Reynolds-averaged Navier-Stokes (RANS) models and water models are among the most popular techniques to analyze these systems [3-7]. Relatively few studies have exploited accurate fine-grid large eddy simulations (LES) to quantify transient flow in the nozzle and mold of continuous casting of steel [8-13] and even fewer have applied filtered unsteady RANS (URANS) models [14]. Yuan et al. [8] combined LES and particle image velocimetry (PIV) measurements in a 0.4 scale water model. The LES predictions matched well with the measurements. Transient oscillations were observed between two different flow patterns in the upper region: a wobbling stair-step downward jet, and a jet which bends midway between the narrow face and SEN. Long term flow asymmetries were observed in the lower region of the mold. Interaction of the flow from the two sides of the mold caused large velocity fluctuations near the top surface. Ramos-Banderas et al. [9] also found that LES model predictions agreed well with instantaneous velocity field measurements using digital PIV in a water model of a slab caster. Flow changed significantly due to vertical oscillations of the jet. Turbulence induced natural biasing without the influence of any other factors such as slide-gate, gas injection or SEN

clogging. Instantaneous velocity showed periodic behavior and frequencies of this behavior were reported increasing with flow rate.

In another work, Yuan et al. [10] performed LES and inclusion transport studies in a water model and a thin slab caster. Complex time varying structures were found even in nominally steady conditions. The flow in the mold switched between double-roll flow and complex flow with many rolls. Zhao et al. [11] performed LES with superheat transport and matched model predictions with plant and full scale water model measurements. The jet exiting the nozzle showed chaotic variations with temperature fluctuations in the upper liquid pool varying $\pm 4\,^{o}C$ and heat flux $\pm 350\,kw/m^2$. Addition of the static-k SGS model had only minor effects.

Qian et al [12] employed LES with a DC magnetic field effects in a slab continuous casting process. A new "vortex brake" was proposed and its effect on vortex suppression was studied. The effect of the location of the magnetic field on vortex formation was also studied. The magnetic when applied at free surface, suppressed turbulence and biased vortices significantly. Liu et al. [13] applied LES in a continuous casting mold to study the transient flow patterns in the upper region. The turbulent asymmetry in the upper region was reported all the times. The upper transient roll was found to break into number of small scale vortices.

Very few previous studies have been undertaken to evaluate the accuracy of turbulent flow simulations with measurements. One of the few [15] found that flow simulations using both LES with the classical Smagorinsky sub-grid scale model, and RANS with the standard k-ε model, showed good quantitative agreement with time-average velocity measurements in a 0.4 scale water model using PIV, and in an operating slab casting machine using an electromagnetic

probe. Another [16] showed that very fine meshes were required, and that imposing symmetry could drastically change the LES flow pattern.

This work investigates transient turbulent flow in the nozzle and mold of a typical continuous casting process by comparing computations with previous horizontal velocity measurements [17-19] using ultrasonic Doppler velocimetry (UDV) in a GaInSn model of the process. In addition, it evaluates the accuracy and performance of five different computational models, including two LES models, a filtered URANS model, and two steady RANS models for such flows. In addition, Reynolds stresses, turbulent kinetic energy (TKE), and power spectra are presented and analyzed. The LES instantaneous velocities were further processed to perform proper orthogonal decomposition (POD) to identify significant modes in the turbulent velocity fluctuations.

7.2. Velocity Measurements using Ultrasonic Doppler Velocimetry

Velocity measurements were performed in a GaInSn model of the continuous casting process at Forschungszentrum Dresden-Rossendorf (FZD), Dresden, Germany [17-19]. Figure 7.1(a), 7.1(b) and 7.1(c) respectively show the front, side and bottom views of the model. The GaInSn eutectic metal alloy is liquid at room temperature (melting point ~10^{o}C). Liquid GaInSn from the tundish flows down a 10-mm diameter 300-mm long SEN, exiting through two horizontal (zero degree angle) nozzle ports into a Plexiglas mold with 140mm (width) x 35mm (thickness) and vertical length of ~300mm. The bifurcated nozzle ports were rectangular 18mm high X 8mm wide, with 4-mm radius chamfered corners. The liquid metal free surface level was maintained around 5 mm below mold top. The liquid metal flows out of the mold bottom from two 20-mm diameter side outlet pipes.

Ultrasonic Doppler Velocimetry (UDV) was used to measure horizontal velocity in the mold midplane between wide faces by placing 10 ultrasonic transducers along the narrow face spaced 10 mm apart vertically and facing towards SEN. Each transducer measured instantaneous horizontal velocity along a horizontal line comprising the axis of the ultrasound beam. The velocity histories were collected along the 10 lines for around 25 sec to create 125 frames. These measurements were performed using a DOP2000 model 2125 velocimeter (Signal Processing SA, Lausanne) with ten 4-MHz transducers (TR0405LS, active acoustic diameter 5 mm). More details on these measurements can be found in [17-19].

7.3. Computational Models

7.3.1. Standard k-ε Model (SKE)

In steady-state Reynolds-averaged Navier-Stokes (RANS) methods, the ensemble-averaged mass (continuity) and momentum balance equations are given as [20-21]:

$$\frac{\partial \overline{u}_i}{\partial x_i} = 0 \tag{7.1}$$

$$\frac{\partial \overline{u}_i}{\partial t} + \frac{\partial \overline{u}_i \overline{u}_j}{\partial x_j} = -\frac{1}{\rho}\frac{\partial \overline{p}^*}{\partial x_i} + \frac{\partial}{\partial x_j}\left(\left(\nu + \nu_t\right)\left(\frac{\partial \overline{u}_i}{\partial x_j} + \frac{\partial \overline{u}_j}{\partial x_i} \right) \right) \tag{7.2}$$

Where, the modified pressure is $\overline{p}^* = \overline{p} + \frac{2}{3}\rho k$. The above equations are solved after dropping the first term and using turbulent (eddy) viscosity,

$$\nu_t = C_\mu k^2 / \varepsilon \tag{7.3}$$

where the model constant $C_\mu = 0.09$. This approach requires solving two additional scalar transport equations for the k and ε fields. The standard $k-\varepsilon$ model is widely used in previous

work, and further details can be found in [22], [23] and [24]. The enhanced wall treatment (EWT) [23, 25-26] is used for wall boundaries and the equations are solved using FLUENT [24].

7.3.2. Realizable k-ε Model (RKE)

The Realizable $k-\varepsilon$ model [27] is another steady RANS model similar to the standard k-ε model. This model ensures that Reynolds normal stresses are positive and satisfies the Schwarz inequality ($\overline{u'_i u'_j}^2 \le \overline{u'^2_i u'^2_j}$), which may be important in highly strained flows. These "realizable" conditions are achieved by making C_μ a special function of the velocity gradients and k and ε. In addition to C_μ, the RKE model also has some different terms in the dissipation rate (ε) transport equation, which is derived from the exact transport equation of mean-square vorticity fluctuations, $\varepsilon = \nu \overline{\omega_i \omega_i}$, where vorticity, $\omega_i = \frac{\partial u'_k}{\partial x_j} - \frac{\partial u'_j}{\partial x_k}$. More details on the formulations of RKE are given in [27, 23-24].

7.3.3. "Filtered" Unsteady RANS Model (URANS)

Unsteady RANS (URANS) models solve the transient Navier Stokes Eqs. 7.1-7.2. Results with standard k-ε URANS always exhibit excessive diffusion, and in some flows, almost match steady-RANS, showing almost no time variations [28]. In the "filtered" URANS approach, the eddy viscosity is decreased to lessen this problem of excessive diffusion, while capturing the large-scale transient features of turbulent flows. Johansen et al [28] improved on the standard k-ε model by redefining the turbulent viscosity as:

$$\nu_t = C_\mu \min\left(1.0, f\right) k^2 / \varepsilon \tag{7.4}$$

where, $f = \Delta\ \varepsilon / k^{3/2}$, and Δ is the constant filter size defined as the cube root of the maximum cell volume in the domain or 2.16mm here. For fine grids, f is smaller than 1, so V decreases,

and there is less "filtering" of the velocities relative to the standard SKE URANS. This turbulent viscosity model was implemented in the current work into the standard k-ε model in FLUENT via a user defined function (UDF) (given in APPENDIX A2.) and solved with EWT at wall boundaries.

7.3.4. Large Eddy Simulations with CU-FLOW [29-31]

The 3-D time dependent filtered Navier-Stokes (N-S) equations and continuity equation for large eddy simulations can be written as [20-21],

$$\frac{\partial u_i}{\partial x_i} = 0 \tag{7.5}$$

$$\frac{\partial u_i}{\partial t} + \frac{\partial u_i u_j}{\partial x_j} = -\frac{1}{\rho}\frac{\partial p^*}{\partial x_i} + \frac{\partial}{\partial x_j}\left(\left(\nu + \nu_s\right)\left(\frac{\partial u_i}{\partial x_j} + \frac{\partial u_j}{\partial x_i}\right)\right) \tag{7.6}$$

Where, the modified pressure is $p^* = p + \frac{2}{3}\rho k_r$, k_r is residual kinetic energy.

The "sub-grid scale" (SGS) viscosity, ν_s, [21] needed to "close" this system can be found using any of several different models, including the classical Smagorinsky model [32], dynamic Smagorinsky-Lilly model [33-35], dynamic kinetic energy sub-grid scale model [36] and the wall-adapting local eddy-viscosity (WALE) model [37]. Among these popular models, the WALE model is mathematically more reasonable and accurate in flows involving complicated geometries [37]. This model captures the expected variation of eddy viscosity with the cube of distance close to the wall without any expensive or complicated dynamic procedure or need of Van-driest damping as a function of y+, which is difficult in a complex geometry [37]. The WALE SGS model is used in the current work and is defined as [37],

$$\nu_s = L_s^2 \frac{\left(S_{ij}^d S_{ij}^d\right)^{3/2}}{\left(S_{ij}S_{ij}\right)^{5/2} + \left(S_{ij}^d S_{ij}^d\right)^{5/4}} \tag{7.7}$$

where, $S_{ij} = \frac{1}{2}\left(\frac{\partial u_i}{\partial x_j} + \frac{\partial u_j}{\partial x_i}\right)$,

$S_{ij}^d = \frac{1}{2}\left(g_{ij}^2 + g_{ji}^2\right) - \frac{1}{3}\delta_{ij} g_{kk}^2$, $g_{ij}^2 = g_{ik}g_{kj}$, $g_{ij} = \frac{\partial u_i}{\partial x_j}$, $\delta_{ij} = 1$, if i=j, else $\delta_{ij} = 0$

and $\Delta = \left(\Delta x \Delta y \Delta z\right)^{1/3}$, Δx, Δy, and Δz are the grid spacing in x, y and z directions.

For the CU-FLOW LES model, the length scale is defined as $L_s = C_w \Delta$, $C_w^2 = 10.6 C_s^2$ [37] and C_s is Smagorinsky constant taken to be 0.18 [37]. The advantage of this method is that the SGS model viscosity converges towards the fluid kinematic viscosity ν as the grid becomes finer and Δ becomes small.

Near-Wall Treatment

A wall-function approach given by Werner-Wengle [38] is used for the LES models, to compensate for the relatively coarse mesh necessarily used in the nozzle and the highly turbulent flow (Re~41,000, based upon nozzle bore diameter and bulk axial velocity). This wall treatment assumes a linear profile ($U^+ = Y^+$ for $Y^+ = y u_\tau / \nu \le 11.8$) combined with a power law profile ($U^+ = A\left(Y^+\right)^B$ for $Y^+ > 11.8$) for the instantaneous tangential velocity in each cell next to a wall boundary, assuming $A = 8.3$, $B = 1/7$. These velocity profiles are analytically integrated in the direction normal to the wall to find the cell-filtered tangential velocity component u_p in the cell next to the wall, which is then related to instantaneous filtered wall shear stress [38] (derivation given in APPENDIX D).

When $|u_p| \le \mu / (2\rho\Delta z) A^{2/(1-B)}$, i.e. the cell next to the wall is in viscous sublayer, the wall stress in the tangential momentum equations is imposed according to a standard no slip wall boundary condition,

$$|\tau_w| = 2\mu |u_p| / \Delta z \tag{7.8}$$

where Δz is the thickness of the near-wall cell in the wall normal direction.

Otherwise, when $|u_p| > \mu / (2\rho\Delta z) A^{2/(1-B)}$, the wall stress in Eq. (7.8) is replaced by the following wall stress defined by Werner-Wengle [38]:

$$|\tau_w| = \rho \left[(1-B)/2A^{\frac{1+B}{1-B}} \left(\mu / (\rho\Delta z)\right)^{1+B} + \frac{1+B}{A} \left(\mu / (\rho\Delta z)\right)^{B} |u_p| \right]^{\frac{2}{1+B}} \tag{7.9}$$

In both situations, the wall is impenetrable and wall normal velocity is zero.

7.3.5. LES FLUENT

The commercial code, FLUENT [24], was also used to solve the same equations given in Section 7.3.4, with the exception that L_s and C_s were instead defined as:

$$L_s = \min(\kappa d, C_w \Delta),\ C_w^2 = 10.6 C_s^2,\ \kappa = 0.418 \text{ and } C_s = 0.10 \tag{7.10}$$

where, d is distance from cell center to the closest wall. The lower value of $C_s = 0.10$ has been claimed to sustain turbulence better on relatively coarse meshes [37, 39, 24].

7.4. Modeling Details

The five different computational models were applied to simulate fluid flow in the GaInSn model described in Section 7.3. The computational domains are faithful reproductions of the nozzle and mold geometries shown in Figure 7.1, except near the outlet. Realizing the only small importance of the bottom region and the difficulty in creating hexahedral meshes, the

circular bottom outlets are approximated with equal-area rectangular outlets. This approximation also changes the shape of the mold bottom, as shown in Figure 7.1(c) and (d). Further details on the dimensions, process parameters (Casting speed, flow rate etc.) and fluid properties (density and viscosity) [17-19] are presented in Table 7.1.

7.4.1. Domain and Meshes

To minimize computational cost, the two-fold symmetry of the domain was exploited for the RANS (RKE and SKE) simulations. Specifically, one quarter of the combined nozzle and mesh domain was meshed using a mostly-structured mesh of ~0.61 million hexahedral cells. Figure 7.2(a) and 7.2(b) respectively show an isometric view of the mesh of the mold and port region used in the steady RANS calculations.

In the "filtered" URANS and LES calculations, time dependent calculations of turbulent flow required simulation of the full 3-D domain. The combined nozzle and mold meshes used in the URANS and LES-FLUENT simulations had similar cells as the steady RANS models, but with a total of ~0.95 million and ~1.33 million hexahedral cells respectively. The LES-CU-FLOW simulation used a much finer mesh (~5 times bigger than LES-FLUENT) with ~7 million (384x192x96) brick cells. Figure 7.2(c) and 7.2(d) respectively show the brick mesh used in LES-CU-FLOW near the nozzle port and mold mid-plane.

7.4.2. Boundary Conditions

In the steady RANS and "filtered" URANS models, a constant velocity condition was used at the nozzle inlet ($U_m = 1.4$ m/s , equivalent to 110ml/sec flow rate) with k and ε values of $0.01964 \text{m}^2/\text{s}^2$ and $0.55 \text{m}^2/\text{s}^3$ respectively calculated using relations ($k = 0.01 U_m^2$, and $\varepsilon = k^{1.5} / 0.05D$, where D is hydraulic diameter) given by [40]. The LES-FLUENT model

used the same nozzle length and constant velocity profile, fixed at the mean velocity without any perturbation. Flow in this straight pipe extending down from the tundish bottom was able to develop accurate fully-developed turbulence, owing to the long L/D=30.

In LES-CU-FLOW, the nozzle bore was truncated at the level of the liquid surface in the mold to lessen the computational burden. This gives L/D of ~7.2 which is not sufficient for flow to develop in the nozzle. Due to this shorter bore length, an inlet mapping condition proposed in [41] was implemented to make the flow develop within the short distance. In this condition, all three velocity components at the inlet were copied from a downstream section at L/D=4 with the axial velocity component multiplied by a factor of $Q_{\text{required}} / Q_{\text{at L/D=4}}$ in order to maintain the desired flow rate (Q_{required}) against frictional losses.

In both LES and RANS, the top surface of the mold was taken to be a free-slip boundary. All solid domain walls were given no-slip conditions using EWT in RANS (RKE and SKE) models, and the Werner-Wengle formulation in LES. In LES-FLUENT, the outlets at the mold bottom were given a constant pressure "outlet" boundary condition (0 Pa gauge). In LES-CU-FLOW, the domain outlets were truncated even with the narrow face walls and the following convective outlet boundary condition was implemented in implicit form for all three velocity components [42],

$$\partial \vec{V} / \partial t + U_{\text{convective}} \partial \vec{V} / \partial n = 0, \text{ where } \vec{V} = u, v, w \tag{7.11}$$

Where $U_{\text{convective}}$ is set to the average normal velocity at the outlet plane. To maintain the required flow rate, the outlet normal velocity from Eq. (7.11) is corrected between iterations as follows:

$$u_{\text{normal}}^{new} = \left(Q_{\text{required}} - Q_{\text{current}} \right) / Area_{outlet} + u_{\text{normal}} \tag{7.12}$$

7.4.3. Numerical Methods

During steady RANS calculations, the ensemble-averaged equations for the three momentum components, turbulent kinetic energy (k-), dissipation rate (ε-), and Pressure Poisson Equation (PPE) are discretized using the Finite Volume Method (FVM) in FLUENT [24] with either 1^{st} or 2^{nd}-order upwind schemes for convection terms. Both upwind schemes were investigated to assess their accuracy. These discretized equations are then solved using the segregated solver for velocity and pressure using the semi-implicit pressure linked equations (SIMPLE) algorithm, starting with initial conditions of zero velocity in the whole domain. Convergence was defined when the unscaled absolute residuals in all equations reduced below $1x10^{-04}$.

In "filtered" URANS calculations, the same ensemble averaged equations as in steady SKE RANS with EWT were solved at each time step using the segregated solver in FLUENT after implementing the filtered eddy viscosity using a UDF. Convection terms were discretized using 2^{nd} order upwind scheme. The implicit fractional step method was used for pressure-velocity coupling with the 2^{nd} order implicit scheme for time integration. For convergence, the scaled residuals were reduced by 3 orders of magnitude every timestep ($\Delta t = 0.004$ sec). Starting from initial conditions of zero velocity in the whole domain, turbulent flow was allowed to develop by integrating the equations for 20.14 sec before collecting statistics. After reaching stationary turbulent flow in this manner, velocities and turbulence statistics were then collected for ~31 sec. URANS solves two additional transport equations for turbulence k and ε, so is slower than LES for the same mesh per timestep. Adopting a coarser mesh, which allows a larger timestep, makes this method much more economical than LES overall. More on this will be discussed in the following computational cost section.

In LES-CU-FLOW, the filtered LES equations Eqs. (7.5-7.7) were discretized using the FVM on a structured Cartesian staggered grid. Pressure-velocity coupling is resolved through a fractional step method with explicit formulation of the diffusion and convection terms in the momentum equations with the Pressure Poisson Equation (PPE). Convection and diffusion terms were discretized using the second order central differencing scheme in space. Time integration used the explicit second order Adams-Bashforth scheme. Neumann boundary conditions are used at the walls for the pressure fluctuations (p'). The PPE equation was solved with a geometric multigrid solver. The detailed steps of this method are outlined in Chaudhary et al. [29]. Every time step, residuals of PPE are reduced by 3 orders of magnitude. Starting with a zero velocity field, the flow-field was allowed to develop for ~21 sec and then mean velocities were collected for ~ 3 sec (50,000 timesteps, $\Delta t = 0.0006\,\text{sec}$). Finally, mean velocities, Reynolds stresses and instantaneous velocities were collected for a further 25.14 sec.

In LES-FLUENT, the filtered equations were discretized and solved in FLUENT using the same methods as the "filtered" URANS, except for using a much smaller timestep ($\Delta t = 0.0002\,\text{sec}$), and basing convergence on the unscaled residuals. Flow was allowed to develop for 23.56 sec before collecting results for a further 21.48 sec.

7.4.4. Computational Cost

The computations with FLUENT (RANS, URANS and LES) were performed on an 8-core PC with a 2.66 GHz Intel® Xeon processor (Intel Corp., Santa Clara, US) and 8.0 GB RAM, using 6 cores for steady RANS and LES and 3 cores for "filtered" URANS. The quarter-domain steady RANS models (RKE and SKE) took ~8 hrs CPU time total. The full-domain "filtered" URANS model took ~28 sec per timestep, or ~100hrs total CPU time for the 51 sec simulation.

Thus, the steady RANS models are over one order of magnitude faster than URANS to compute the time-average flow pattern.

The full-domain LES-FLUENT model took ~26 sec per timestep or ~1626 hours (67days) total CPU time for the total 225,200 timesteps of the total 45 sec simulation (23.5s flow developing + 21.5 (averaging time)). Considering the similar mesh sizes, the "filtered" URANS model (0.95 million cells) is more than one order of magnitude faster than the LES model (1.33 million cells) using FLUENT. The steady RANS models are over 200 times faster than this LES model, because they can exploit a coarser mesh and finish in one step.

LES calculations using CU-FLOW were performed on the same computer but using the installed graphic processing unit (GPU). CU-FLOW took around 13 days to simulate ~48 sec. Thus, LES-CU-FLOW is about five times faster than LES-FLUENT. Considering its five-times better-refined mesh, (~7 million cells) and the 6 processing cores used by FLUENT, CU-FLOW is really more than two orders of magnitude faster than LES-FLUENT. This shows the great advantage of using better algorithms, which also can exploit the GPU.

7.5. Comparison of Computations and Measurements

The predictions of the five different computational models first validated with pipe flow measurements, and then are compared with the UDV measurements in the mold apparatus. Further comparisons between models and measurements in this apparatus are given throughout the rest of this paper, including comparisons of time-averaged velocities in the nozzle and mold, averaged turbulence quantities, and instantaneous velocity traces at individual points.

Nozzle Bore

Flow through the nozzle controls flow in the mold, so the time/ensemble average axial velocity in the SEN bore is presented in Figure 7.3 comparing the model predictions, with

measurements by Zagarola et al [43] of fully-developed pipe flow at a similar Reynolds number (Re_D=DU/ν ~ 42,000). All models match the measurements [43] closely, except for minor differences in the core and close to the wall. The RANS methods match well here because this is a wall-attached flow at high Reynolds number, and these models were developed for such flows. The results from URANS are quite similar to steady SKE RANS so are not presented. Velocity from LES-CU-FLOW also matches very closely at both distances down the nozzle (L/D=3 and 6.5 below the inlet), which validates the mapping method described in Section 7.4.2 to achieve fully-developed, transient turbulent flow within a short distance. The minor differences are due to the coarse mesh for this high Reynolds number preventing LES from completely resolving the smallest scales close to the wall. Overall, the reasonable agreement in the nozzle bore of all models with this measurement demonstrates an accurate inlet condition for the mold predictions.

Mold

All five models are next compared with the UDV measurements in the liquid-metal-filled mold. Figure 7.4 compares the time/ensemble average horizontal velocity at the mold midplane as contour plots. Figure 7.5 compares these horizontal velocity predictions along three horizontal lines (95 mm, 105mm 115 mm from mold top) at the mold mid-plane between wide faces. The time-averaging range for the three transient models were 31.19s (SKE URANS), 21.48s (LES-FLUENT), and 25.14s (LES-CU-FLOW) which can be compared with 24.87s of time averaging of the measured flow velocities.

LES is seen to match best with the measurements. Due to the small number of data frames in the measurements (~125 over 24.87 sec), the time averages show some wiggles. Close to the SEN and narrow-face walls, the measurements give inaccurate zero values, perhaps due to distance from the sensor and/or interference from the walls of the nozzle and narrow face. Its

match with measurements along the 3 lines in Figure 7.5 is almost perfect. Furthermore, it matched well with the low values measured along seven other lines (not presented). Based on this agreement and its physically reasonable predictions near walls, the LES predictions are concluded to be more accurate than the measurements, at least for the evaluation of the other models.

Minor differences between CU-FLOW and FLUENT LES predictions are seen. The CU-FLOW velocities show a wider spread of the jet with a stronger "nose" at port outlet, compared to FLUENT. This effect is more realistic and physically expected due to the transient stair-stepping behavior of the swirling jet exiting the nozzle port. It shows that the flow pattern is more accurately resolved by CU-FLOW, owing to its much finer mesh (~5.3 times).

The other models show less accurate predictions than LES in both jet shape (Figure 7.4) and horizontal velocity profiles (Figure 7.5). The jet from steady SKE is thinner and directed straighter towards the narrow face, due to the inability of this steady model to capture the real transient jet wobbling. More jet spreading is predicted with 1^{st}-order upwinding than with the second-order scheme of the steady SKE model. This is caused by the extra numerical diffusion of the 1^{st} order scheme, which makes it match closer with both the measurements and the LES flow pattern. When considering its better numerical stability and simplicity, the 1^{st}-order scheme is better than the higher order scheme for this problem. Among the steady RANS models (SKE and RKE), SKE matched more closely, so was selected for URANS modeling and further steady-RANS evaluations. The "filtered" URANS model resolves turbulence scales bigger than the filter size and smaller scales are modeled with the two-equation k-ε model. This model captures some jet wobbling and thus gives predictions somewhat in between LES and steady RANS. Overall, all methods agreed reasonably well, with the RANS models being least accurate,

URANS next, followed by measurements, LES-FLUENT, and LES-CU-FLOW being most accurate.

7.6. Time-Averaged Results

7.6.1. Nozzle Flow

In addition to the line-plot comparison of axial velocity in the nozzle bore with measurements (Figure 7.3), model predictions of axial velocity contours and secondary velocity vectors are compared in Figure 7.6. The SKE, "filtered" URANS and LES-FLUENT models exhibit almost no secondary flows (Figure 7.6(a)). Interestingly, the stair-step mesh in CU-FLOW generates minor mean secondary flows which have a maximum magnitude of around ~2% of the mean axial velocity through the cross-section (Figure 7.6(b)). These secondary flows move towards the walls from the core in four symmetrical regions. This causes slight bulging of the axial velocity which is similar to secondary flow in a square duct at the corners bisectors [29]. These very small secondary flows have negligible effects on flow in the nozzle bottom and mold.

The jets leaving the nozzle ports directly control flow in the mold, so a more detailed evaluation of velocity in the nozzle bottom region was preformed. The predicted velocity magnitude contours at the nozzle bottom mid-plane are compared in Figure 7.7(a)-(d). Qualitatively, the flow patterns match reasonably well in all models, except for minor differences in the steady SKE model. This reasonable match by steady SKE, comparable with other transient methods, is expected due to the high Reynolds number flow (Re~42,000) in the entire nozzle, for which steady SKE model is most suitable. Flow patterns with LES-CU-FLOW and LES-FLUENT are very similar.

The jet characteristics [44] (given in APPENDIX B.) exiting the nozzle port predicted by different models are summarized in Table 7.2. Significant differences are seen between the different models. The steady SKE gives a bigger back flow region (34%), and URANS a smaller one (17.6%), compared to LES-FLUENT (25.1%). Although the weighted downward velocity is quite similar (within ~8%) in all models, the weighted outward and horizontal velocities are quite different. Thus, the jet angles differ significantly, which greatly affects mold flow. The steady SKE model predicts the shallowest downward jet angle, and the "filtered" URANS model the steepest. The URANS model also predicts the largest horizontal spread angle (9.2 degree).

A comparison of velocity magnitude along the mid-port- and 2-mm-forward-offset vertical lines is presented in Figure 7.8. In the upper back flow region, all models agree, but significant differences are seen in the lower outward flow region. In the outward flow region, a high velocity convex profile is predicted along the midport, while a lower-velocity with a humped profile is seen along the offset line. This hump is due to swirling flow inside the nozzle. Although LES-CU-FLOW and LES-FLUENT velocities generally match closely, larger differences are seen at the port. This difference is responsible for the slight differences in jet shape in the mold (Figure 7.4) discussed previously, and is due to the more diffusive nature of the coarser mesh used for LES-FLUENT.

7.6.2. Mold Flow

To show the mold flow pattern and further compare the different models, time-averaged velocity magnitude contours and streamlines are presented at the mold midplane in Figure 7.9. All models predict a classic symmetrical "double-roll" flow pattern, with two upper counter-rotating recirculation regions, and two lower recirculation regions. Along the top surface, velocity from the narrow face to the SEN is very slow, owing to the deep nozzle submergence.

This might cause meniscus freezing surface defects in a real caster, but the flow system is useful for model evaluation.

The velocity contours are similar between the transient models, but significant differences are seen with steady SKE RANS, which underpredicts the jet spread. The thinner and more focused jet gives higher velocity in both the upper and lower recirculation regions. In addition, the jet angle is too shallow, causing even more excessive surface flow. The upper eye is too centered in overly-rounded upper rolls, relative to the LES flow, where the eye is closer to the narrow face. The lower eye is too high, relative to the elongated low eye of LES. These inaccuracies of SKE RANS are likely due to the assumption of isotropic turbulence and underprediction of swirl in the nozzle bottom, compounded by the recirculating nature of the flow, and the lower Reynolds number in the mold, which are known to cause problems [23].

In the transient models, the jet region is dominated by small turbulence scales, so attains right-left symmetry after only ~1-2 sec of time averaging. This contrasts with the lower rolls, which are still asymmetrical even after ~21-31 secs time averaging, which suggests the dominance of large scale structures in these regions. The upper rolls structures are intermediate. This asymmetry reduces with more time averaging. The "filtered" URANS is similar to the LES models, but, exhibits even more asymmetries in the upper and lower rolls.

The surface velocity predicted by different models at the mold-mid plane between wide faces is compared in Figure 7.10(a). The 3 transient methods all predict similar trends, although values are different. The LES-CU-FLOW profile is slowest. The steady SKE model gives a different profile close to SEN where it predicts reverse flow towards the narrow face. Across the rest of the surface, the steady SKE model matches the other models. All of the surface velocities

are very slow, (5-7 times smaller than a typical caster (~0.3) [1] which is a major cause of the differences between models.

The vertical velocity across the mold predicted by different models 35 mm below surface at mold midplane is compared in Figure 7.10(b). The transient models all matched closely. Due to the jet being thinner with a shallower angle, the steady SKE predicts much stronger recirculation in the upper zone, with velocity ~5 times faster up the narrow face and ~2 times faster down near the SEN than LES.

The vertical velocity along a vertical line 2mm from the narrow face wall at mold midplane is presented in Figure 7.11. The profile shape from all models is classic for a double-roll flow pattern [5-6]. This velocity profile also indicates the behavior of vertical wall stress along the narrow face. The positive and negative peaks match the beginning of the upper and lower recirculation zones respectively. The crossing from positive to negative velocity denotes the stagnation/impingement point (~110 mm below the top free surface in all models). The transient models agree closely, except for minor differences in URANS in the lower recirculation. Steady SKE predicts significantly higher extremes, giving higher positive values in the upper region and lower negative values in the lower region. This mismatch of steady SKE is consistent with the other velocity results, and indicates that care must be taken when using this model.

7.6.3. Turbulence Quantities

The turbulent kinetic energy (TKE), Reynolds normal stress components which comprise TKE, and Reynolds shear stress components are evaluated in the nozzle and mold, comparing the different models. Figure 7.12 compares TKE profiles along the nozzle port center- and 2-mm-offset- vertical lines for four different models. As expected, TKE is much higher in the outward

flowing region than in the reverse flow region. TKE along the 2mm-offset line is higher than along the center-line.

The Steady SKE and URANS models greatly underpredict TKE along both lines. URANS does not perform any better than steady SKE in resolving turbulence in nozzle. The LES-FLUENT and LES-CU-FLOW models give similar trends but higher TKE is produced with LES-CU-FLOW owing to its better resolution. This produces the strongly-fluctuating nose in the mold that better matches the measurements. The TKE of LES-CUFLOW is presented at the mold-mid planes in Figure 7.13. Turbulence originates in the nozzle bottom, where a V-shaped pattern is seen, and decreases in magnitude as the jets move further into the mold.

The TKE of the RANS models (k) has a high error, underpredicting turbulence by ~100% in Figure 7.12, which is much higher than the 3-15% mismatch with the velocity predictions exiting the nozzle (Figure 7.8). The "filtered" URANS model performs slightly better, but still underpredicts TKE by ~40%. Similar problems of RANS models in predicting turbulence have been found in previous work in channels [23], square ducts [23] and in continuous casting molds [15]. This is due in large part to the RANS model assumption that turbulence is isotropic, ignoring its variations in different directions. The TKE in LES is based on its true definition as the sum of three resolved components:

$$\text{TKE} = 0.5\left(\overline{u'u'} + \overline{v'v'} + \overline{w'w'}\right) \tag{7.13}$$

where $\overline{u'u'}$, $\overline{v'v'}$ and $\overline{w'w'}$ are the Reynolds normal stresses. The LES models predict all six independent components of the Reynolds stresses including the 3 normal and also 3 shear components, which indicate interactions between in-plane velocity fluctuations.

The four most significant Reynolds stress components from the CU-FLOW LES model in the two mold midplanes are shown in Figure 7.14. The most significant turbulent fluctuations are

in the y-z plane (side view) near the bottom of the nozzle. These $\overline{w'w'}$ and $\overline{v'v'}$ normal Reynolds stress components signify the alternating rotation direction of the swirling flow in the well of the nozzle. The $\overline{v'v'}$ out-of-plane fluctuation is the largest component in the front view. The $\overline{w'w'}$ vertical component is the largest and most obvious component near the front and back of the nozzle bottom walls in the side view. Their importance is explored in more detail in Section 7.7.4. The x-z plane components ($\overline{w'w'}$, $\overline{u'u'}$, and $\overline{u'w'}$) in the front view follow the up-down wobbling of jet at the port exit, which causes the stair-stepping phenomenon [8]. These horizontal ($\overline{u'u'}$) and vertical ($\overline{w'w'}$) show how this wobbling extends into the mold region, accompanied by the swirl, as evidenced by the $\overline{v'v'}$ variations. Further insight into the turbulent velocity fluctuations quantified by these Reynolds stresses is revealed from the POD analysis in Section 7.7.4.

7.7. Transient Results

Having shown the superior accuracy of LES methodology, the predictions from CU-FLOW and LES-FLUENT were applied to further investigate the transient flow phenomena. Specifically, the model predictions of transient flow behavior are evaluated together with measurements at individual locations, followed by spectral analysis to reveal the main turbulent frequencies, and a proper orthogonal decomposition (POD) analysis to reveal the fundamental flow structures.

7.7.1. Transient Flow Patterns

Instantaneous flow patterns from three different transient models at mold mid-plane are shown in Figure 7.15(a)-(c). These instantaneous snapshots of velocity magnitude were taken near the end of each simulation. Since the developed turbulent flow fields continuously evolve with time and fluctuate during this “pseudo-steady-state” period, there is no correspondence in

time among the simulations. Each snapshot shows typical features of the flow patterns captured by each model. Due to the fine mesh, LES-CU-FLOW captures much smaller scales than LES-FLUENT. The flow field in URANS is a lot smoother due to a coarse mesh with a much larger spatial and temporal filter sizes. The instantaneous flow patterns are consistent with the mean flow field discussed previously. The maximum instantaneous velocity at the mold-mid plane is ~10% higher than the maximum mean velocity.

7.7.2. Transient Velocity Comparison

Model predictions with LES-FLUENT and measurements of time histories of horizontal velocity are compared at five different locations in the mold, (points 1-5 in Figure 7.16), in Figure 7.17. The measurements were extracted using an ultrasonic Doppler shift velocity profiler with ultrasonic beam pulses sent from behind the narrow face wall into the GaInSn liquid along the transducer axis. Due to divergence of the beam, the measurement represents an average over a cylindrical volume, with ~0.7 mm thickness in the beam direction, and diameter that increases with distance from the narrow face. Figure 7.16 shows the three beams (emitted from blue cylinders), their slightly diverging cylinders (red lines), and the averaging volumes (rectangles) for the points investigated here. The overall temporal resolution was ~0.2 sec, for the data acquisition rate used to obtain the data presented here. To make fair, realistic comparisons with the high-resolution LES model predictions, spatial averaging over the same volumes and moving centered temporal averaging of 0.2 sec was also performed on the model velocity results.

Close to the SEN at point 1, Figure 7.17(a), the horizontal history predicted by LES greatly exceeds the inaccurate measured signal. The predicted velocity (~1.2 m/s) is consistent with the actual mass flow rate through the port. With spatial and temporal averaging included, the predicted time variations are very similar to the measured signal. This figure also includes

part of the actual LES velocity history predicted at this point, with the model resolution of ~0.0002s time step and 0.2-2mm grid spacing. This high-resolution prediction reveals the high-amplitude, high-frequency fluctuations expected close to the SEN, for the large Reynolds number (Re=42,000) in this region.

The individual effects of temporal and spatial averaging are investigated further at point 2, Figure 7.17(b). This point is near the narrow face above the mean jet impingement region, so has much smaller velocity fluctuations and significantly lower frequencies. Both temporal/spatial-averaging together, and temporal averaging alone bring the predictions closer to the measured history. Spatial averaging alone has only a minor effect.

Including temporal averaging smooths the predictions so that they match well with the measured velocity histories at other points (point 3, 4 and 5) as well. Points 3 and 4 have stronger turbulence and thus higher frequencies and fluctuations than at point 2, but are smaller than at point 1. Figure 7.17(e) shows that the signals obtained with a moving average to match the measurement introduce a time delay. Offsetting the moving average backwards in time by 0.1s (half of the averaging interval) produces a signal that matches a central average of the real signal. Overall, the predictions agree well with the measurements, so long as proper temporal averaging is applied according to the 0.2s temporal filtering of the measurement method. The higher resolution of the LES model enables it to better capture the real high frequency fluctuations of the turbulent flow in this system.

7.7.3. Spectral Analysis

To further clarify the real frequencies in velocity fluctuations, Figure 7.18 presents a mean-squared amplitude (MSA) power spectrum, according to the formulation in [10] (formulation given in APPENDIX E1). This gives the distribution of energy with frequency, for

velocity magnitude fluctuations at points 6 and 7 (See Figure 7.16). The general trend of increasing turbulent energy at lower frequencies is consistent with previous work [5, 10]. As expected, point 6 which is close to the SEN shows much higher energy, mainly distributed from 3-100 Hz, relative to point 7, which is near the narrow face. This behavior of increasing velocity fluctuations at higher frequency is consistent with the higher Reynolds number. According to the power spectrum, frequencies above 5 Hz (0.2s period) are important. These higher frequencies represent small scale, medium to low energy turbulent eddies which cannot be captured by the measurements.

7.7.4. Proper Orthogonal Decomposition and Flow Variations in the Nozzle Bottom-Well

Proper orthogonal decomposition (POD) has been applied to gain deeper insight into the fundamental transient flow structures that govern the fluctuations of the velocity field, according to the formulation in [45-46]. This technique separates the complicated spatial and temporal-dependent fluctuations of the real 3-D transient velocity field, $u_z^{'}(\mathbf{x},t)$, into a weighted sum of spatially-varying characteristic modal functions, by performing a single-value decomposition (SVD) [45-46],

$$u_z^{'}(\mathbf{x},t) = \sum_{k=1}^{M} a_k(t)\phi_k(\mathbf{x}) \tag{7.14}$$

where $\phi_k(\mathbf{x})$ are orthonormal basis functions which define a particular velocity variation field and $a_k(t)$ are the temporal coefficients. The first few terms provide a low-dimensional visually-insightful description of the real high-dimensional transient behavior. The representation naturally becomes more accurate by including more terms (larger M).

Writing the discrete data set, $u_z^{'}(\mathbf{x},t)$ in the form of a matrix $[U_z^{'}]$, with t in rows and $\mathbf{x}$ in columns, the SVD of $[U_z^{'}]$ is

$$[U_z^{'}]=[U][S][V]^T \tag{7.15}$$

where $[U]$ and $[V]$ are orthogonal matrices and $[S]$ is a diagonal matrix. Further defining $[W]$ as $[U][S]$ gives $[U_z^{'}]=[W][V]^T$, where the k$^{\text{th}}$ column of $[W]$ is $a_k(t)$ and the k$^{\text{th}}$ row of $[V]^T$ is $\phi_k(x)$. The matrix $[S]$ has diagonal elements in decreasing order as $s_1 \geq s_2 \geq s_3 \geq s_4 .....s_q \geq 0$, where $q=\min(M,N)$; $s_i{}'s$ are called singular values and the square of each s value represents the velocity fluctuation energy in the corresponding orthogonal mode (k$^{\text{th}}$ row of V^T). The k$^{\text{th}}$ rank approximation of $[U_z^{'}]$ is defined as Eq. (7.15) with $s_{k+1}=s_{k+2}.....=s_q=0$.

To perform SVD, the velocity fluctuation data was arranged in the following matrix form,

$$[U_z^{'}]=\left[\left\{u_x^{'}\right\}_1 \quad \left\{u_x^{'}\right\}_2 .....\left\{u_x^{'}\right\}_N,\ \left\{u_y^{'}\right\}_1 \quad \left\{u_y^{'}\right\}_2 .....\left\{u_y^{'}\right\}_N,\ \left\{u_z^{'}\right\}_1 \quad \left\{u_z^{'}\right\}_2 .....\left\{u_z^{'}\right\}_N\right] \tag{7.16}$$

where $\left\{u_x^{'}\right\}_N$, $\left\{u_y^{'}\right\}_N$ and $\left\{u_z^{'}\right\}_N$ are column vectors representing a time series of three components of velocity at a particular point. Matrix $[U_z^{'}]$ has size MxN, where N is the number of spatial velocity-data points and M is the number of time instances.

In the current work, SVD was performed on the instantaneous velocity fluctuations predicted by LES-CU-FLOW at the mid-plane between the mold wide faces near the nozzle bottom and jet. This region was selected for POD analysis due to its strong transient behavior and large scale fluctuations of the wobbling jets exiting the two ports. Orthogonal modes were calculated by solving Eqs. 7.15-7.16 with a code in MATLAB (given in APPENDIX C). Matrix $[U_z^{'}]$ was formulated for POD analysis based on 193 (x-) x 100(z-) spatial values for each

velocity component selected for 6 sec with a time interval of 0.006s (total N= $19300\text{x}3 = 57900,\ M = 1000$).

Figure 7.19 presents contours of the most significant velocity variation components in the first four orthogonal modes, which contain ~30% of the fluctuation energy. In the first two modes (containing ~22.% of the energy), the only significant component, v', shows the alternating swirling flow in the well of the nozzle. In modes 3 and 4, the only significant components are the horizontal and vertical velocity variations (u' and w'), which are associated with up-down jet wobbling.

Figure 7.20 presents the temporal coefficients of these modes, and shows a positive/negative oscillatory behavior that indicates periodic switching of the direction of these modes. The singular values, which are a measure of the energy in each mode, are presented together with the cumulative energy fraction in Figure 7.21. The singular values reduce exponentially in their significance with increasing mode number. The first 400 modes contain ~88% of the total fluctuation energy.

The importance of different modes can be visualized by reconstructing instantaneous velocity profiles from their singular values. Four such reduced rank approximations of the fields are given in Figure 7.22. Figure 7.22(a) presents the time average of 6 sec data and 7.22(b) shows the original instantaneous velocity profile at t=0 sec. The rank-400 approximation, with 88% of the energy, approximates the original snapshot reasonably well. The rank-15 approximation, with 40% of energy, captures much of the nozzle velocity fluctuations, but misses most of the turbulent scales contained in the jet. This indicates that the turbulent flow in this mold is very complex, and contains important contributions from many different modes. This is likely a good thing for stabilizing the flow and avoiding quality problems.

The nozzle well swirl effects associated with the most-important 1st and 2nd modes can be understood better with the help of instantaneous velocities in the well of nozzle. Figure 7.23 presents instantaneous and time-average velocity vectors and contours at the mid-plane slice between narrow faces, looking into a nozzle port. As seen in Figure 7.23(c), the behavior of v in the 1st mode is due to swirl in the SEN bottom well, and has 15.66% of the total energy. The swirl direction of rotation periodically switches, which causes corresponding alternation of the v contours in Figure 7.19(a) and 7.23(c). This is also seen in the $\overline{v'v'}$ peaks in Figure 7.14(c). The alternating swirl also causes the strongest vertical flow to alternate between the front and back walls of the nozzle, as observed in the $\overline{w'w'}$ peaks in Figure 7.14(a) and in w in Figure 7.23(b). The temporal coefficient of the first mode in Figure 7.20 suggests that the switching frequency is ~3Hz. It is interesting to note that these continuously alternating rolls are not apparent in the symmetrical time average of this flow field, shown in Figure 7.23(d). A spectral analysis on v' in Figure 7.24 of a node in the nozzle bottom region further revealed the dominance of ~3-4Hz frequencies, which is consistent with the frequencies of the temporal coefficients of the 1st mode. This revelation of swirl with periodic switching illustrates the power of the POD analysis, which matches and quantifies previous observations of the transient flow structures in the nozzle bottom well [3].

Another interesting mode is the up and down oscillation of the jet exiting the nozzle, which is manifested in u' and w' of mode 3, which is shown in Figure 7.19(c)-(d). The temporal coefficient of mode 3 in Figure 7.20 quantifies the period of this wobbling to be again ~3-5Hz, which means it is likely related to the alternating swirl directions, as previously proposed [3]. This transient flow behavior has also been observed in previous work, where it was labeled

"stair-step wobbling" [8]. To control mold turbulence, it seems important to control the 1st swirling mode, which sends turbulence to the mold in the form of u' and w'.

To identify further modes in other planes requires extension of the POD analysis to complete three dimensional instantaneous flow fields, which is beyond the scope of the current work. Even in two dimensions, however, this work shows the capability of POD analysis to illustrate and quantify transient structures in a new way, making it another powerful tool for the analysis of LES velocity results.

7.8. Summary and Conclusions

In this work, computational models are combined with measurements in a GaInSn model to investigate turbulent flow in the nozzle and mold of a typical continuous casting process. This work also evaluates the performance of five different computational models, including two steady RANS models, "filtered" URANS, LES with FLUENT, and LES with an in-house GPU based CFD code (CU-FLOW).

LES predictions of time-averaged horizontal velocity match very well with the measurements, except where limitations in the measurements give unreasonably lower values close to the SEN and narrow face walls. Time and spatial averaging of the LES predictions to match the experimental resolution of <5Hz produces transient velocity histories that match closely with the measurements. Spectral analysis of the LES predictions confirms a large range of velocity fluctuation frequencies near the SEN (up to ~300Hz, for 2 orders of magnitude drop in energy) and close to narrow face (up to ~30Hz, for 2 orders of magnitude drop in energy). The fluctuation energy generally drops with distance from the nozzle, especially at the higher frequencies.

LES-CU-FLOW was the best model, with better accuracy than LES-FLUENT, owing to its higher resolution with a ~5 times finer mesh, and tremendously better computational efficiency, owing to its better numerics and use of a GPU methodology. The "filtered" URANS model performed in between LES and steady RANS, missing the high-frequency fluctuations, but capturing the long-time variations associated with large structures. .The RANS models matched time-averaged velocity closely in the nozzle, but greatly underpredicted turbulence exiting the ports. This caused mismatches in the mold, especially with turbulence, so caution is needed when using steady RANS models. Among steady RANS models, SKE performed better than RKE.

The flow pattern is a stable, classic double-roll flow pattern, controlled by the strong turbulent nature of the flow structures in the bottom of the nozzle. The resolved Reynolds stresses and TKE show strong fluctuations in vertical velocity ($\overline{w'w'}$) and velocity normal to wide faces ($\overline{v'v'}$) associated with alternating directions of swirl in the bottom of the nozzle, and with wobbling of the jet in the mold. A POD analysis further reveals that the strongest transient flow structures are associated with nozzle bottom swirl and jet wobbling. The modes associated with this swirl contained 22% of the fluctuation energy. To control turbulence in the mold, it is important to control these modes.

7.9. Tables and Figures

Table 7.1 Process parameters

Volume flow rate	110 *ml/s*
Nozzle inlet bulk velocity	1.4 *m/s*
Casting speed	1.35 *m/min*
Mold width	140 *mm*
Mold thickness	35 *mm*
Mold length	330 *mm*
Total nozzle height	300 *mm*
Nozzle port dimension	8*mm*(width)×18*mm*(height)
Nozzle bore diameter(inner/outer)	10*mm*/15*mm*
Nozzle port angle	0 degree
SEN submergence depth	72*mm*
Density(ρ)	6360 kg/m^3
Dynamic viscosity(μ)	0.00216 *kg/m s*

Table 7.2 Comparison of the jet characteristics in steady SKE, "filtered" URANS and LES

Properties	Steady SKE model	"Filtered" URANS (SKE)	LES model (FLUENT)
	Left port	Left port	Left port
Weighted average nozzle port velocity in x-direction(outward)(m/s)	0.816	0.577	0.71
Weighted average nozzle port velocity in y-direction(horizontal)(m/s)	0.073	0.0932	0.108
Weighted average nozzle port velocity in z-direction(downward)(m/s)	0.52	0.543	0.565
Weighted average nozzle port turbulent kinetic energy (m^2/s^2)	0.084	0.0847	0.142
Weighted average nozzle port turbulent kinetic energy dissipation rate (m^2/s^3)	15.5	15.8	---
Vertical jet angle (degree)	32.5	43.3	38.5
Horizontal jet angle (degree)	0.0	0.0	0.0
Horizontal spread (half) angle (degree)	5.1	9.2	8.6
Average jet speed (m/s)	0.97	0.8	0.91
Back-flow zone (%)	34.0	17.6	25.1

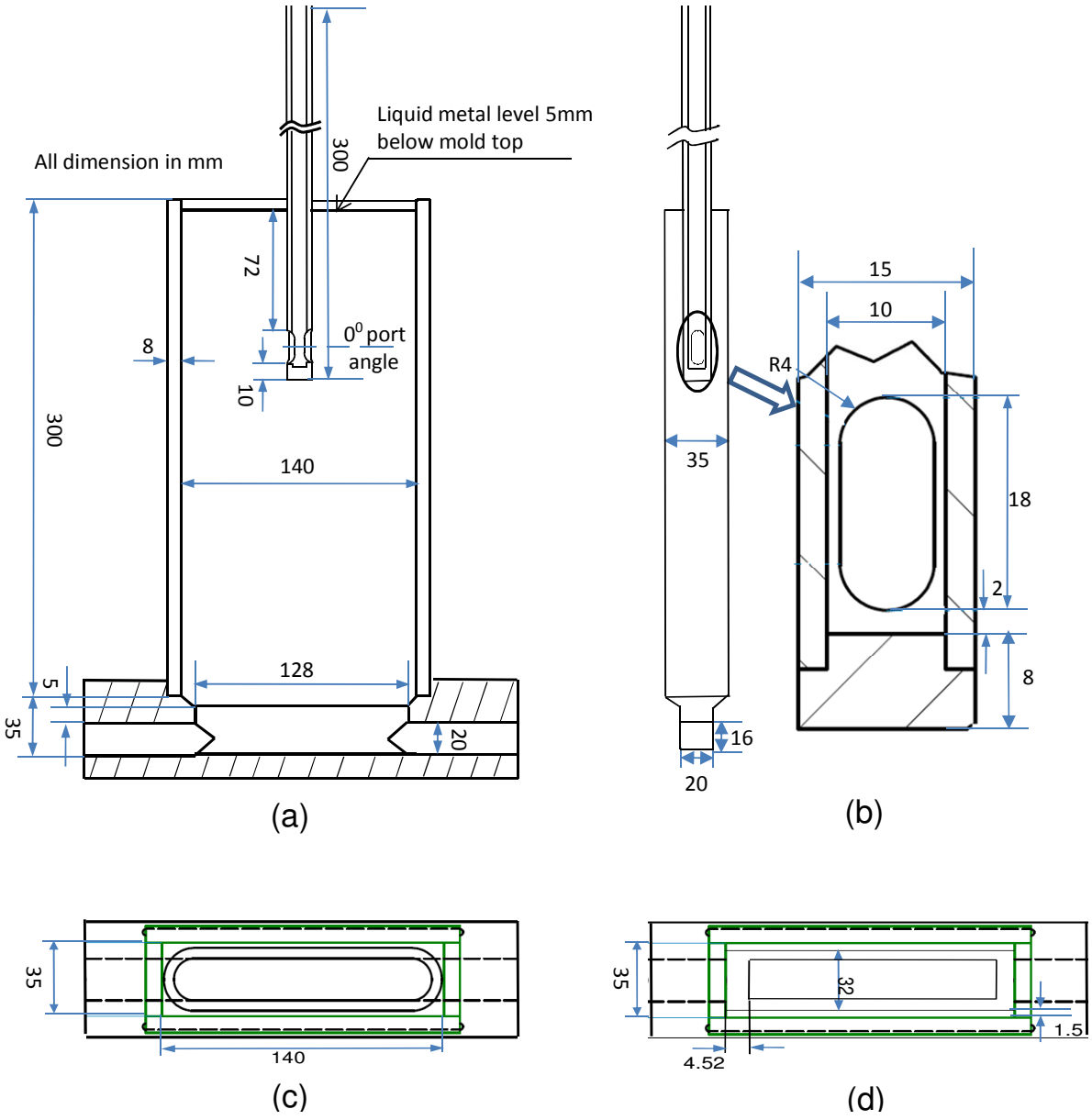

Figure 7.1 Geometry of GaInSn model of continuous casting [17-19] in mm (a) front view of the nozzle and mold apparatus (b) side view of the model domain with approximated bottom (c) bottom view of the apparatus (d) bottom view showing approximation of circular outlets with equal-area rectangles

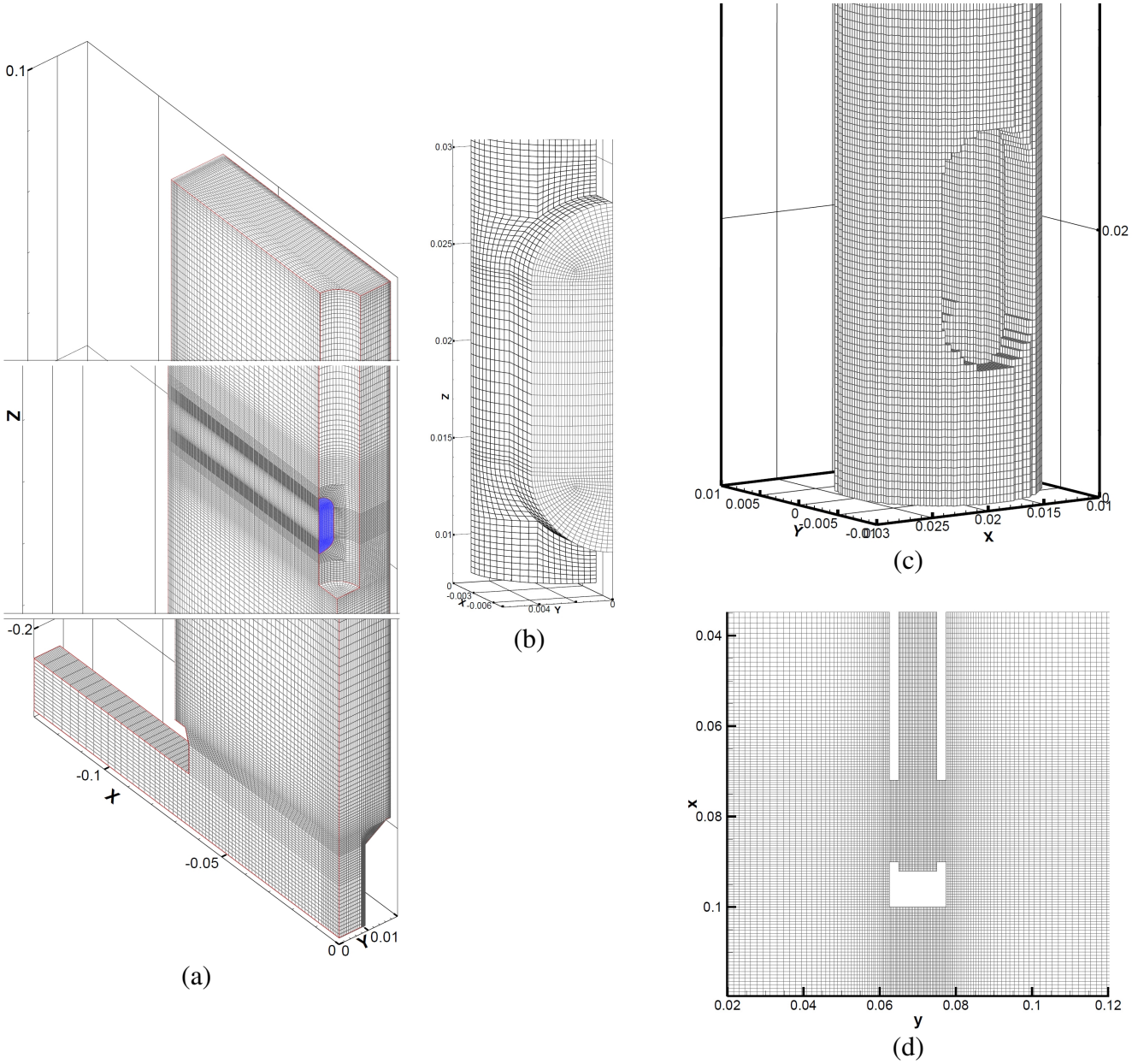

Figure 7.2 Computational meshes (a) Mold of steady RANS quarter-domain (~0.6 million cells) (b) Nozzle-port of steady RANS mesh (c) Nozzle mesh surfaces of LES-CU-FLOW (~7 million cells) (d) Mold mid-plane mesh of LES-CU-FLOW

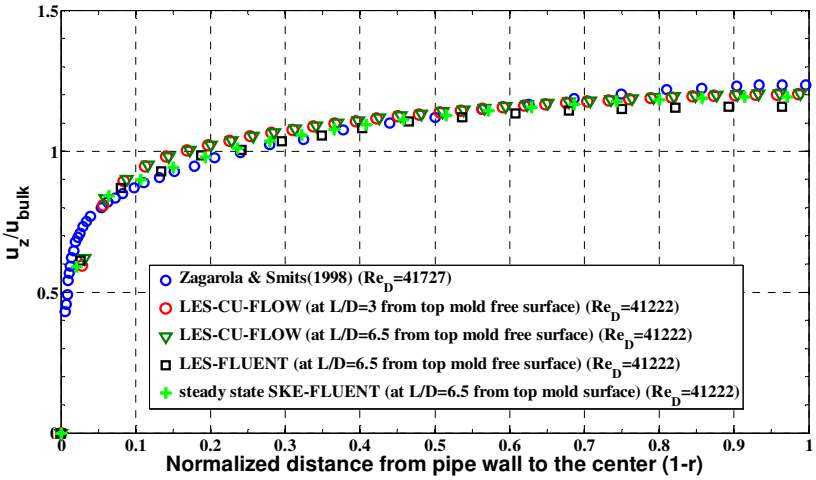

Figure 7.3 Axial velocity along nozzle radius (horizontal bisector) predicted by different models compared with measurements of Zagarola et al. [43].

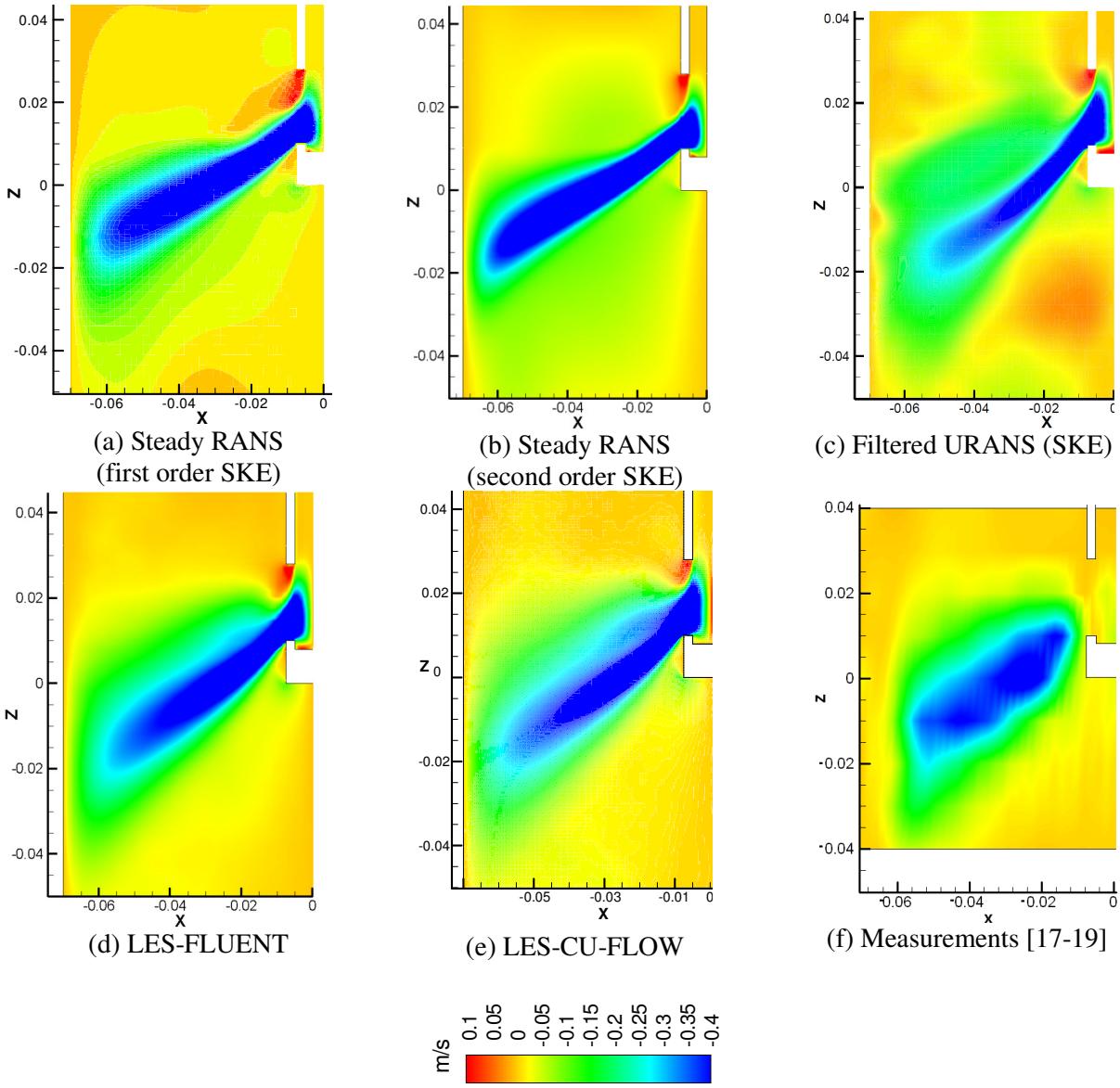

(a) Steady RANS (first order SKE)

(b) Steady RANS (second order SKE)

(c) Filtered URANS (SKE)

(d) LES-FLUENT

(e) LES-CU-FLOW

(f) Measurements [17-19]

Figure 7.4 Average horizontal velocity contours in the mold mid-plane compared between different models and measurements.

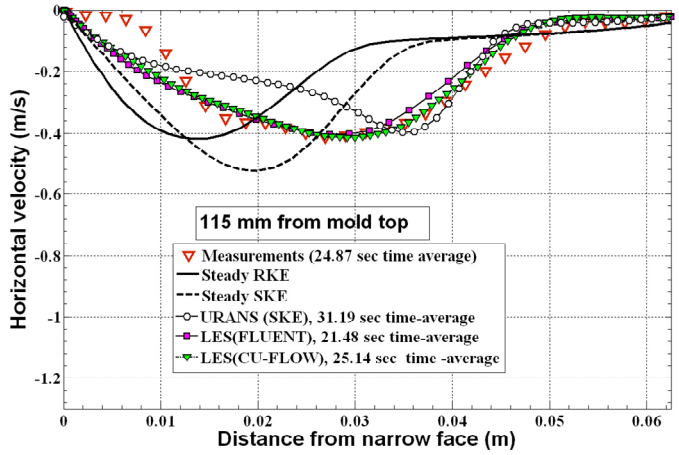

(a) at 115 mm from mold top

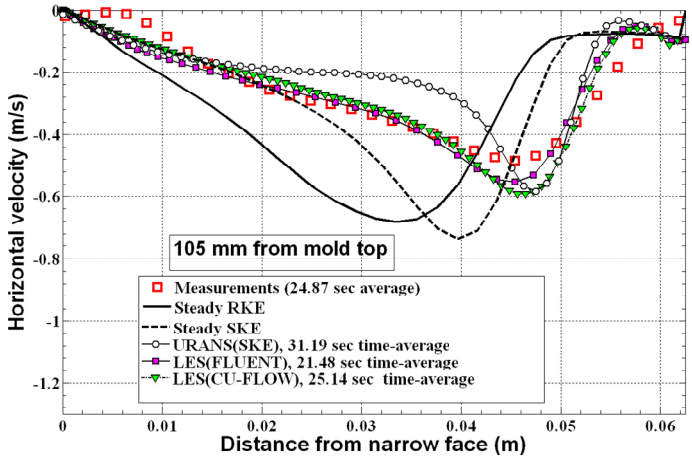

(b) at 105 mm from mold top

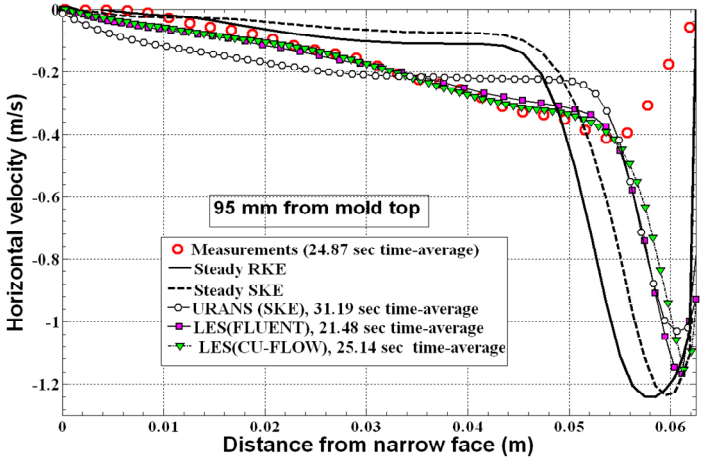

(c) at 95 mm from mold top

Figure 7.5 Average horizontal velocity along three horizontal lines predicted by different models compared with measurements

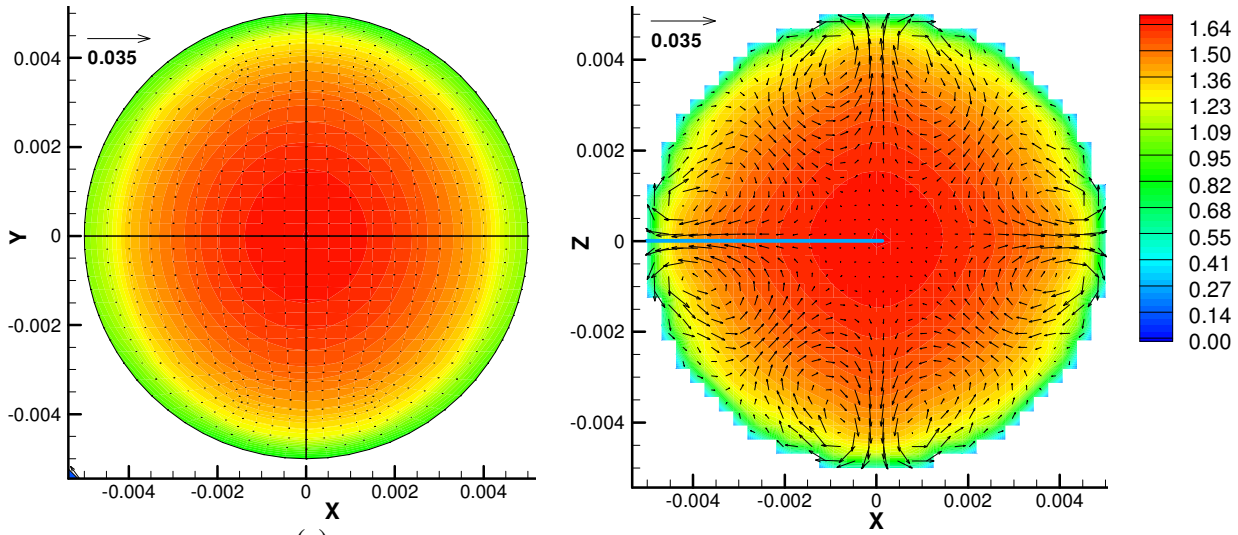

Figure 7.6 Axial velocity (m/s) with secondary velocity vectors at nozzle bore cross-section (a) steady SKE: ensemble-average (b) LES-CU-FLOW: time average

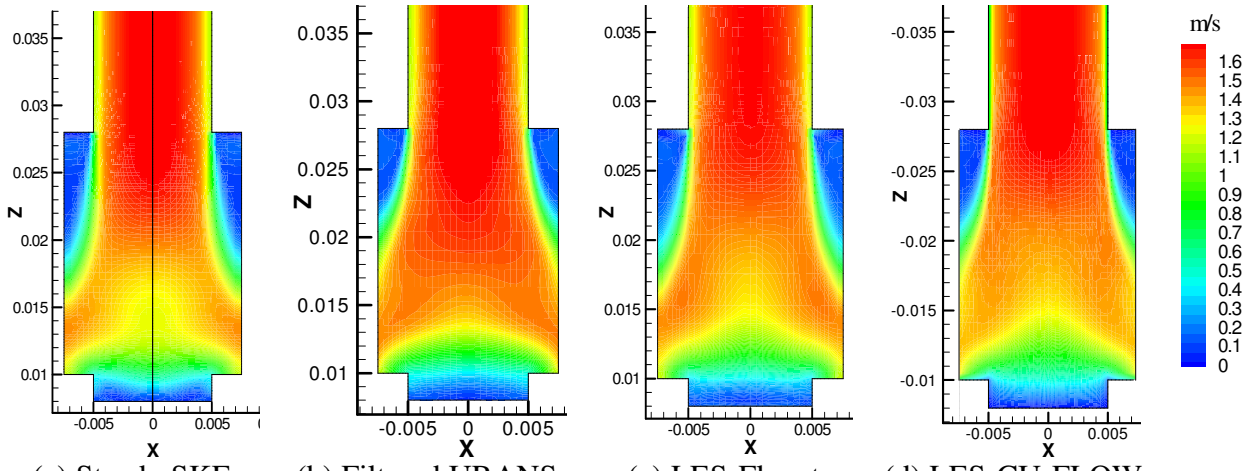

Figure 7.7 Average velocity magnitude contours in nozzle mid-plane near bottom comparing (a) Steady SKE (b) Filtered URANS (c) LES-FLUENT (d) LES-CU-FLOW

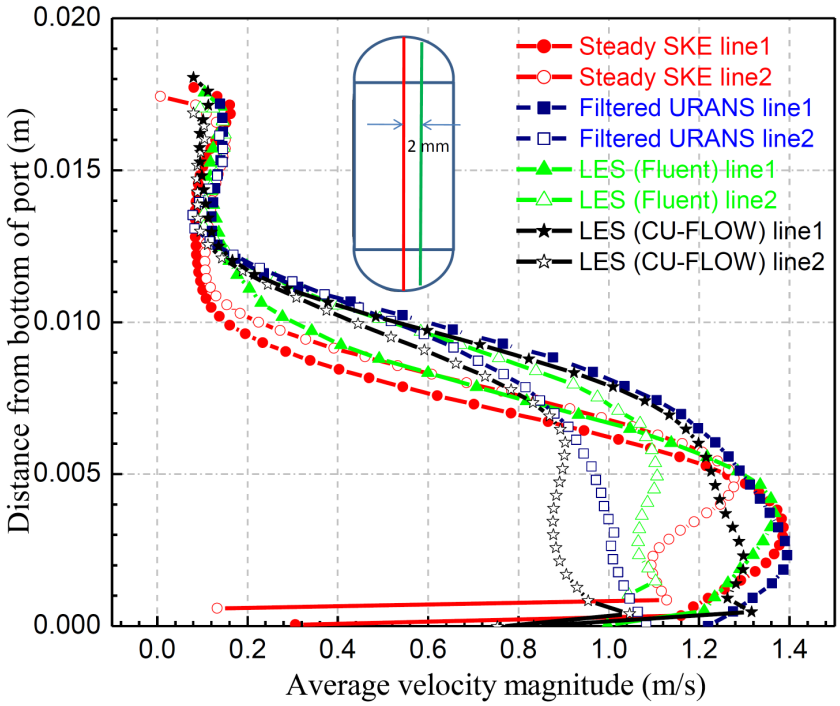

Figure 7.8 Comparison of port velocity magnitude along two vertical lines in outlet plane

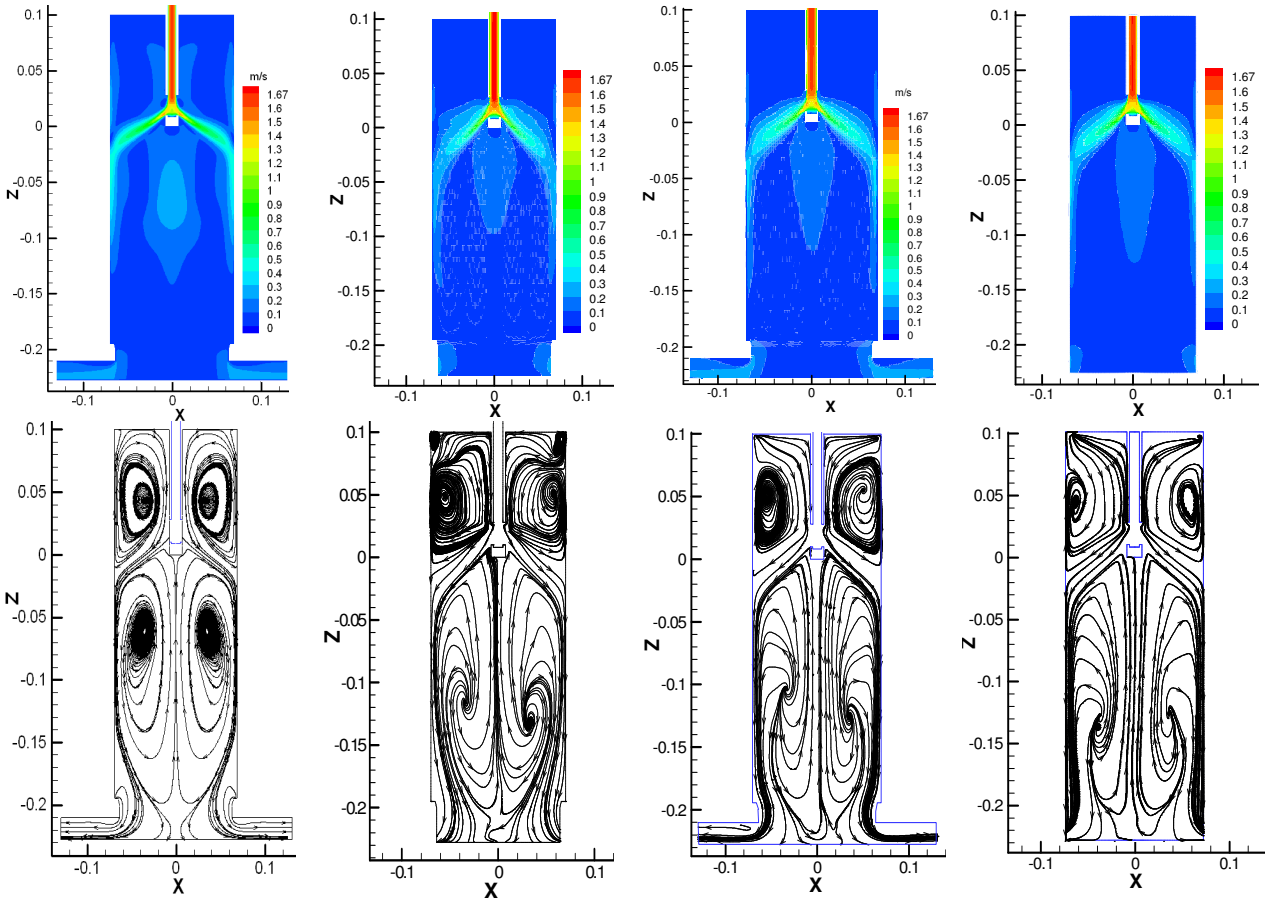

(a) steady RANS (SKE) (b) Filtered URANS (c) LES-FLUENT (d) LES-CU-FLOW

Figure 7.9 Comparison of time/ensemble average velocity magnitude (above) and streamline (below) at the mold mid-plane between wide faces

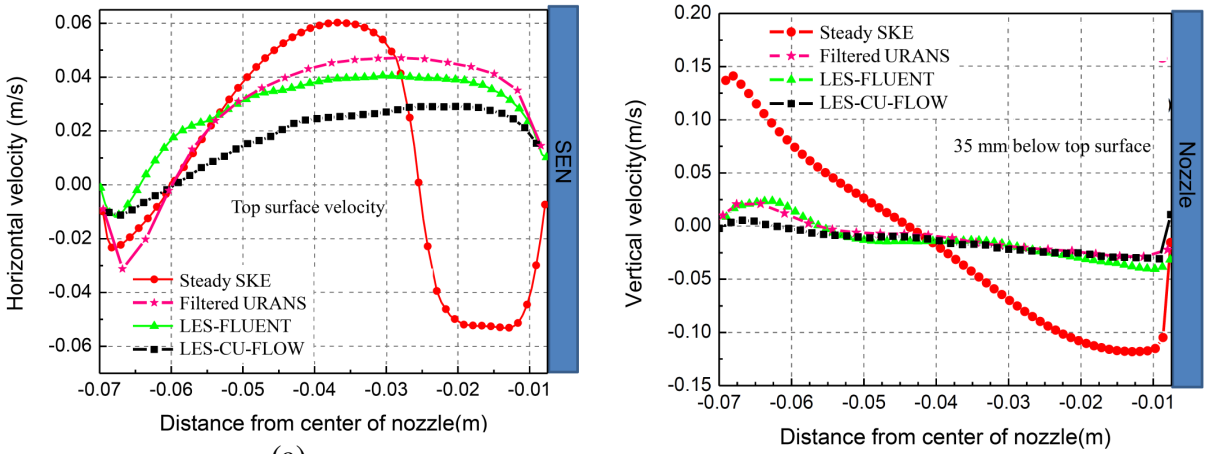

Figure 7.10 Average velocity profile at mold mid-plane comparing different models (a) horizontal velocity at top surface (b) vertical velocity at 35mm below top surface

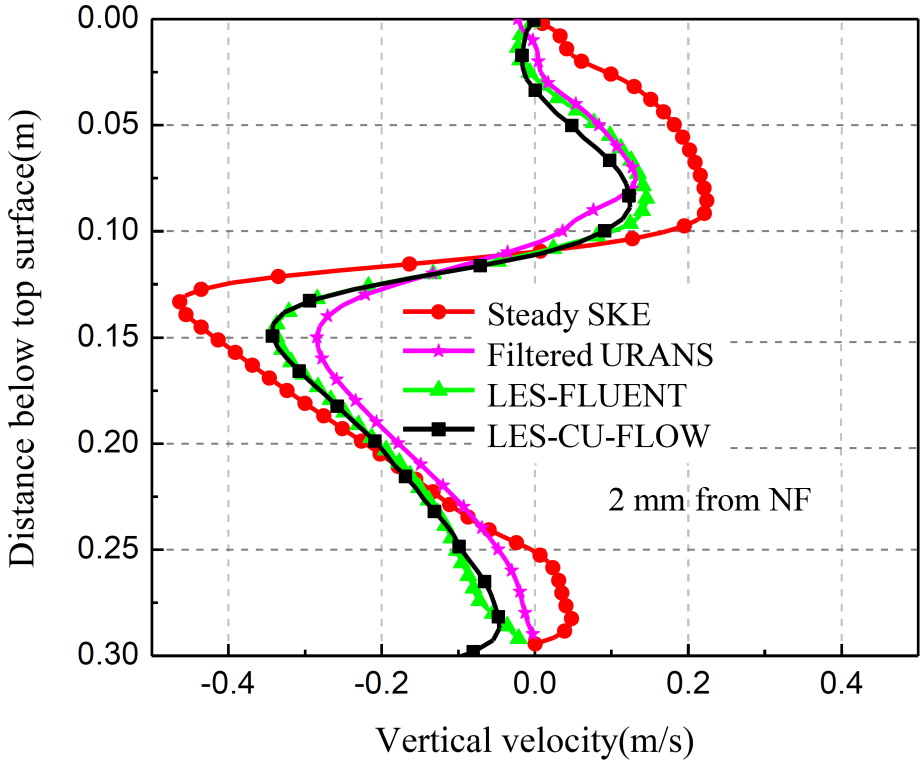

Figure 7.11 Comparison of time/ensemble average vertical velocity in different models at 2 mm from NF along mold length

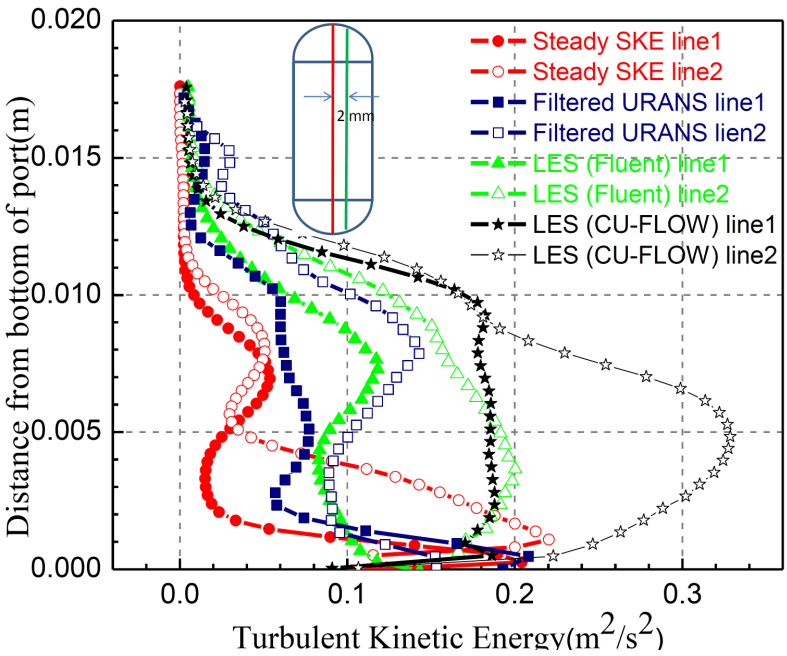

Figure 7.12 Comparison of TKE predicted by different models along two vertical lines at the port

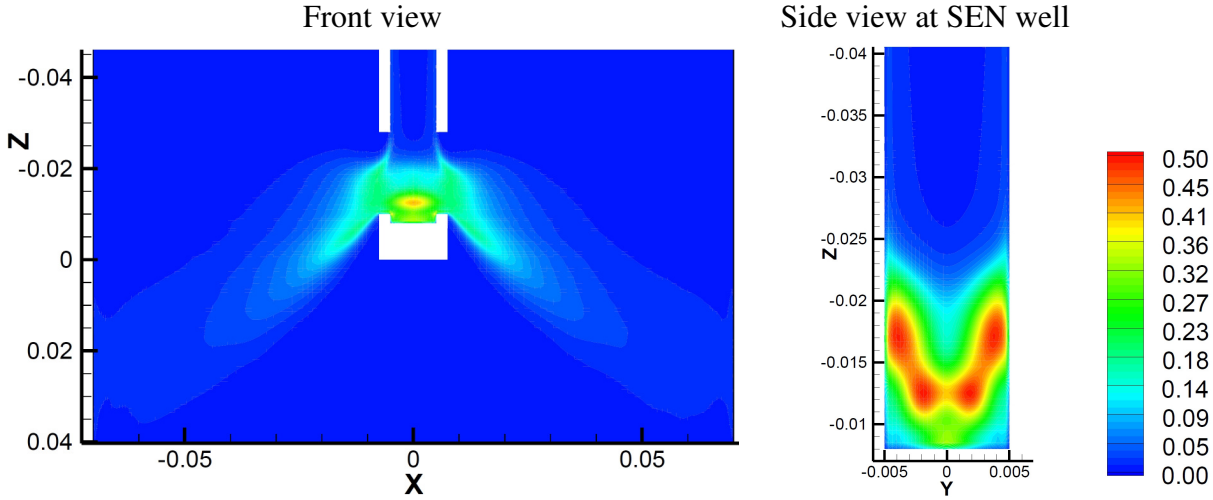

Figure 7.13 Resolved turbulent kinetic energy at mold mid-planes between wide and narrow faces

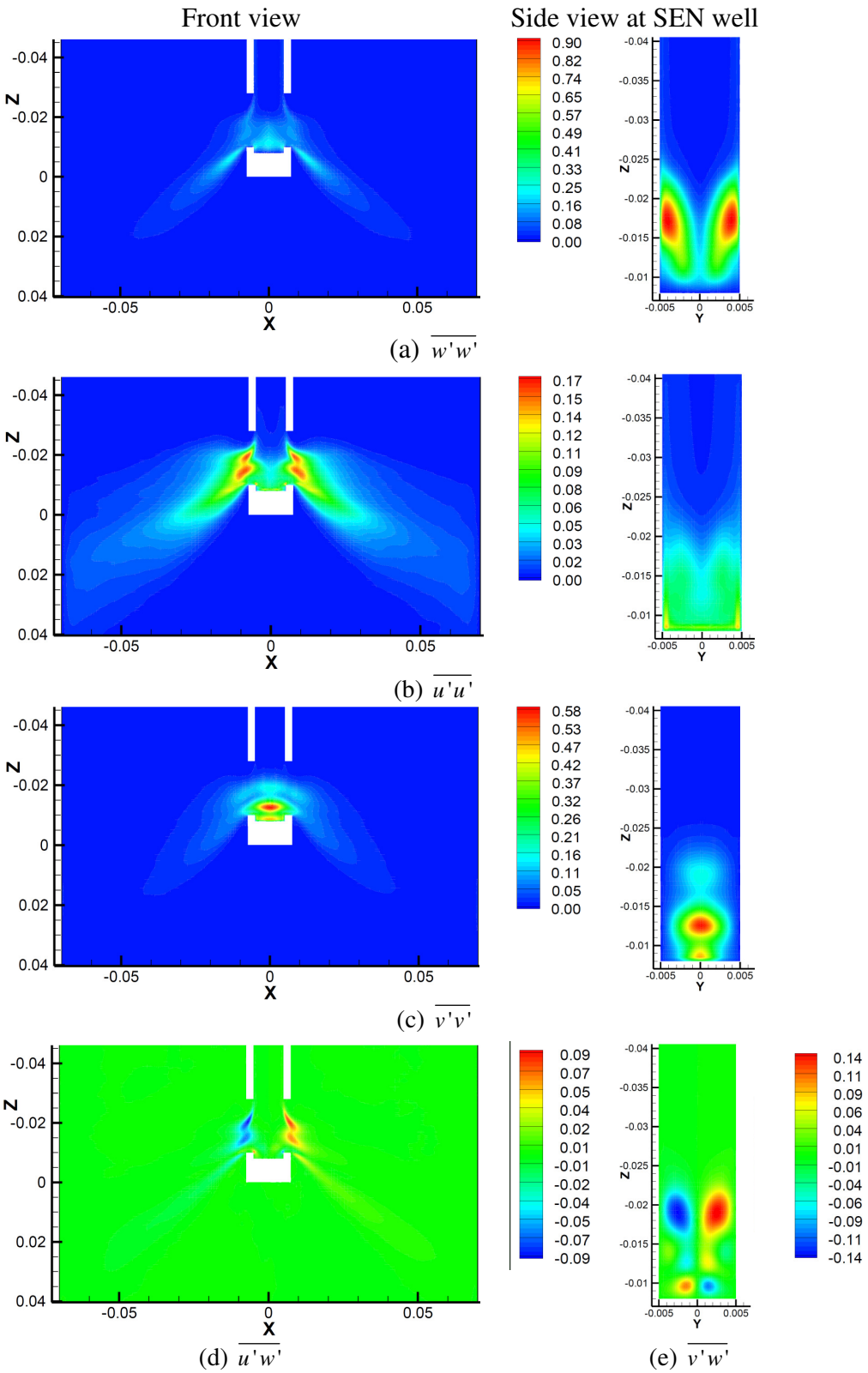

Figure 7.14 Resolved Reynolds normal and in-plane shear stresses at mold mid-planes between wide and narrow faces

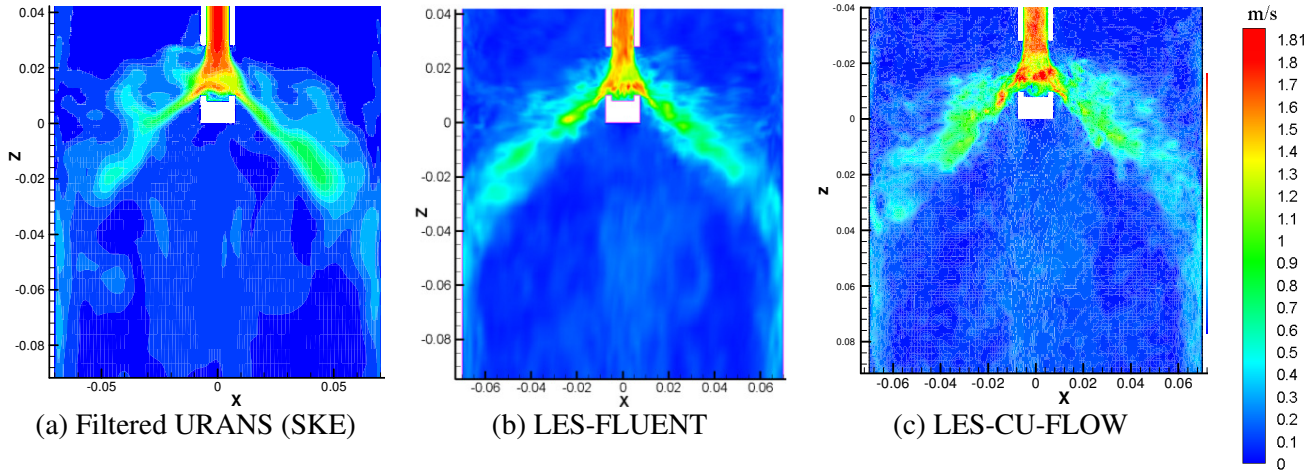

(a) Filtered URANS (SKE) (b) LES-FLUENT (c) LES-CU-FLOW

Figure 7.15 Instantaneous velocity magnitude contours comparing different transient models

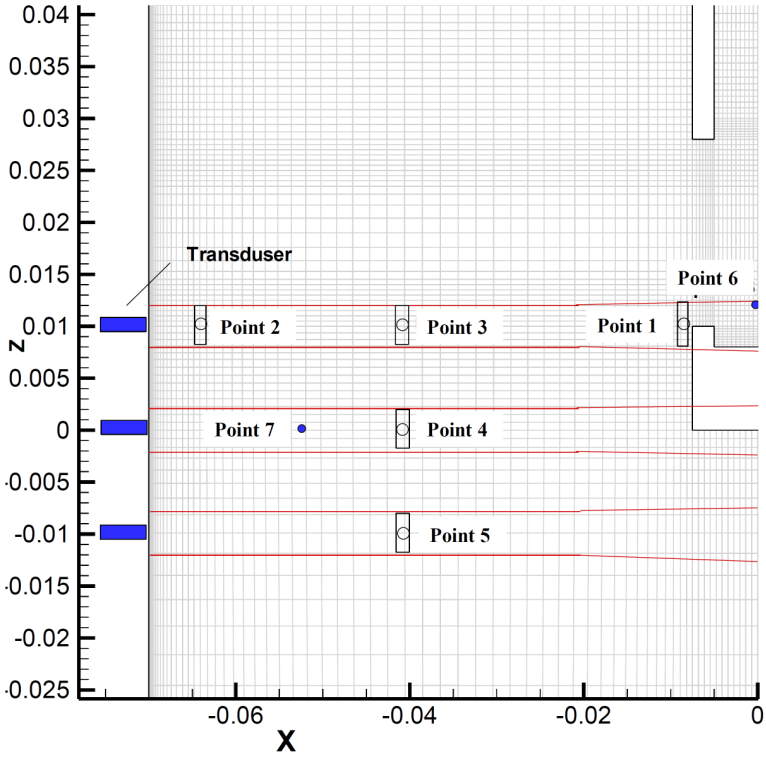

Figure 7.16 Spatial-averaging regions where instantaneous horizontal velocity points are evaluated in the midplane between widefaces. (Lines are boundaries of the cylindrical UDV measurement regions; coordinates in m)

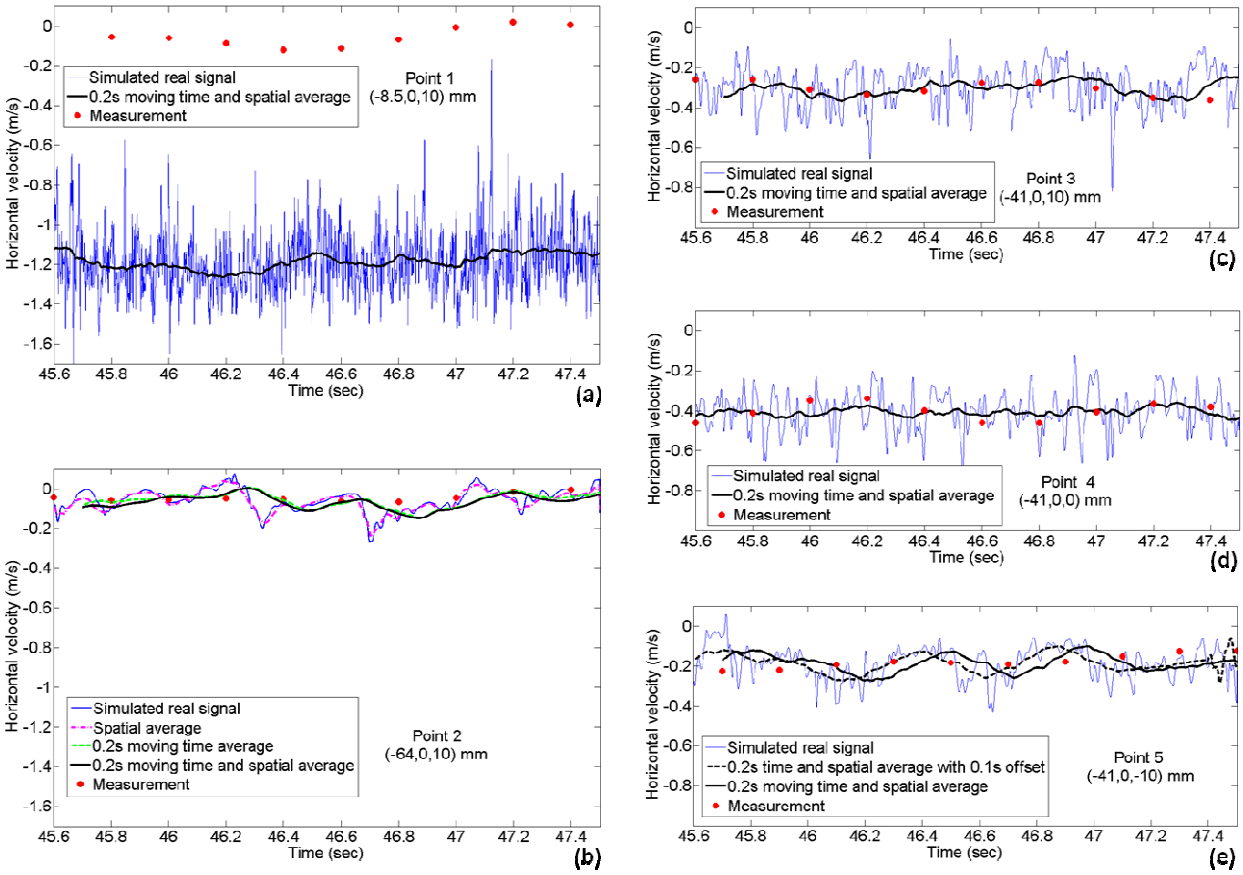

Figure 7.17 Instantaneous horizontal velocity histories comparing LES-FLUENT and measurements at various points (see Fig-7.16) in the nozzle and mold mid-plane (point coordinates in mm)

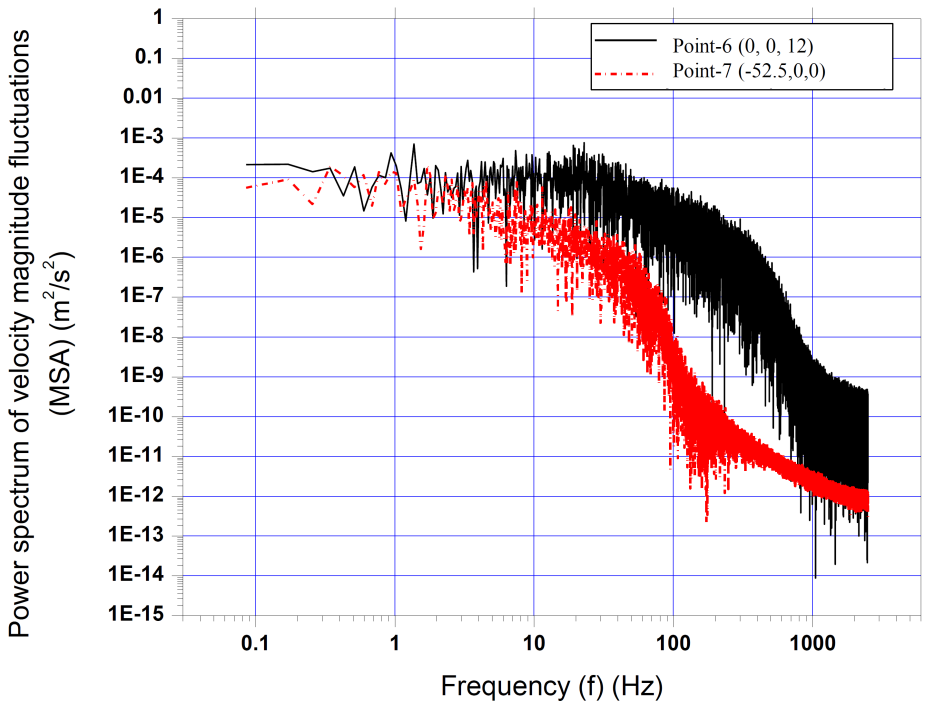

Figure 7.18 Power spectrum (Mean-Squared Amplitude) of instantaneous velocity magnitude fluctuations at two points (see Fig-7.16) in the nozzle and mold

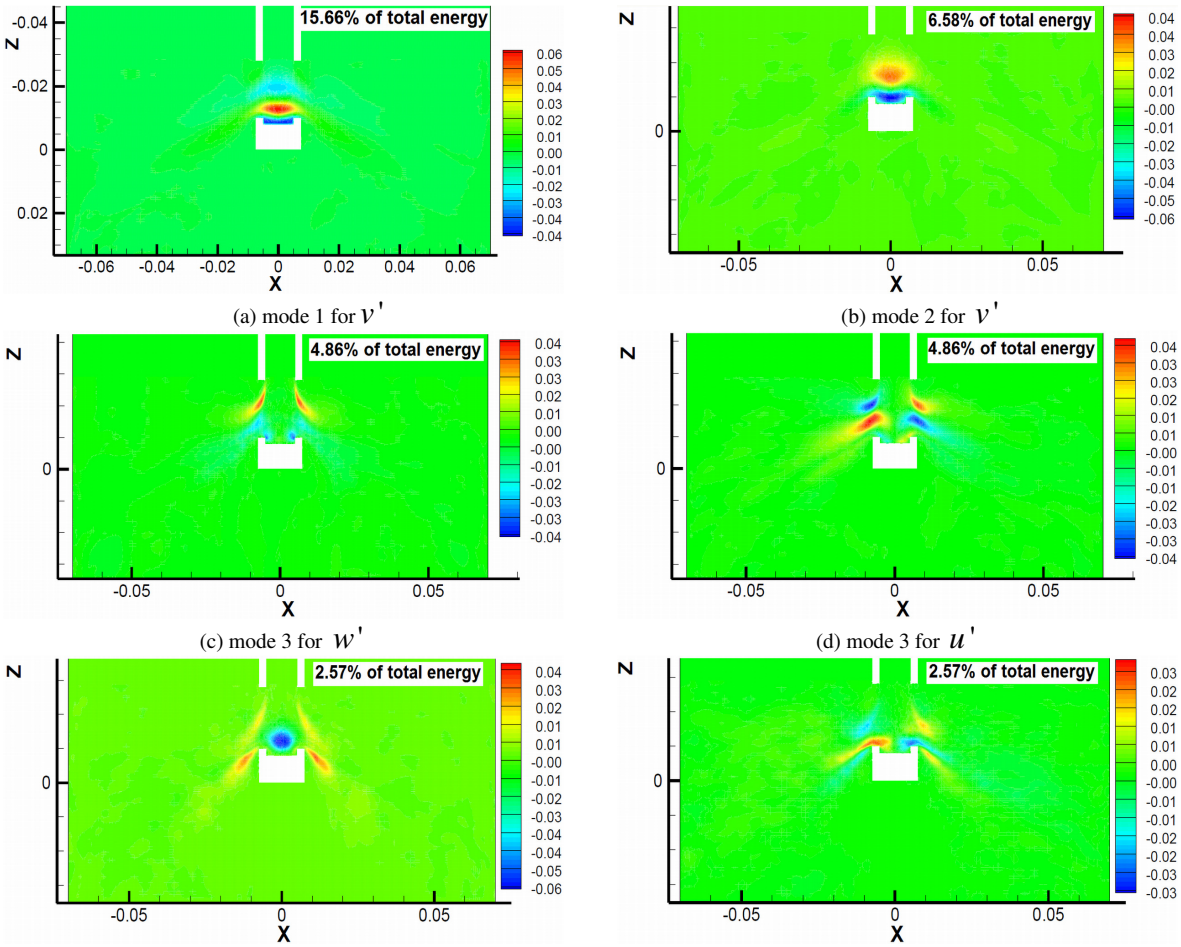

(a) mode 1 for v'

(b) mode 2 for v'

(c) mode 3 for w'

(d) mode 3 for u'

(e) mode 4 for w'

(f) mode 4 for u'

Figure 7.19 First four proper orthogonal decomposition (POD) modes (containing ~30% of total energy) showing different velocity component fluctuations (u', v', or w')

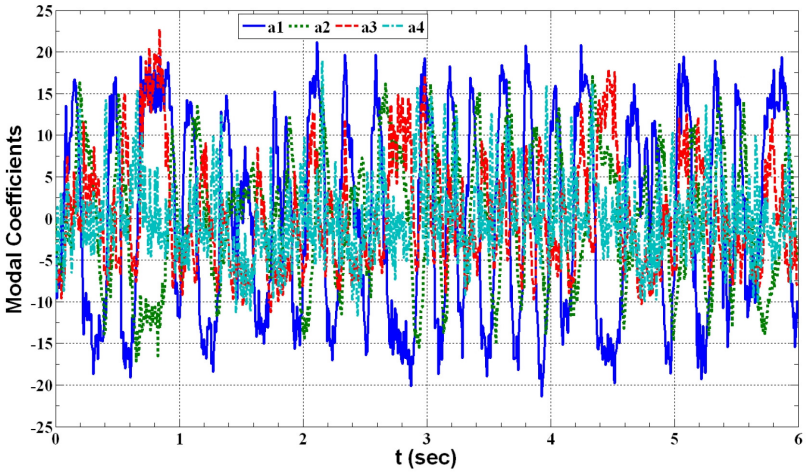

Figure 7.20 POD Modal coefficients (or Modal contributions)

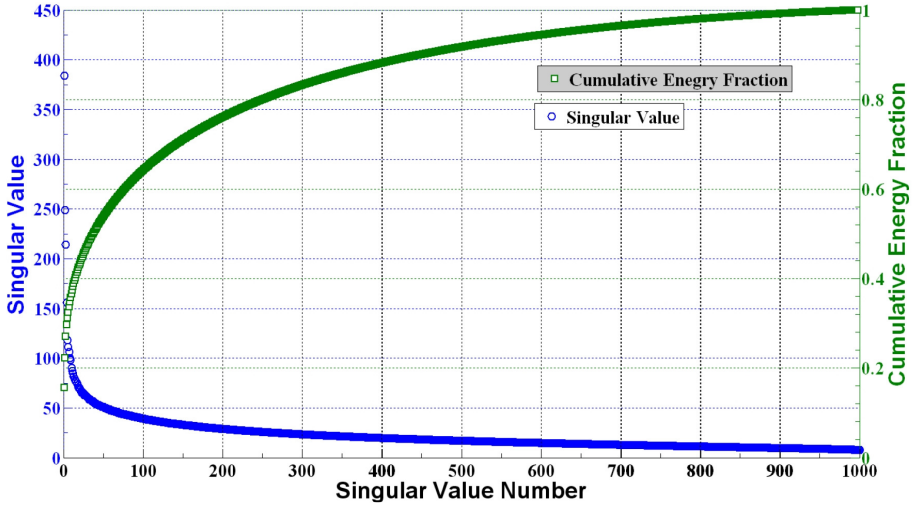

Figure 7.21 Singular values and cumulative energy in different POD modes of velocity fluctuations ($\vec{u}'$)

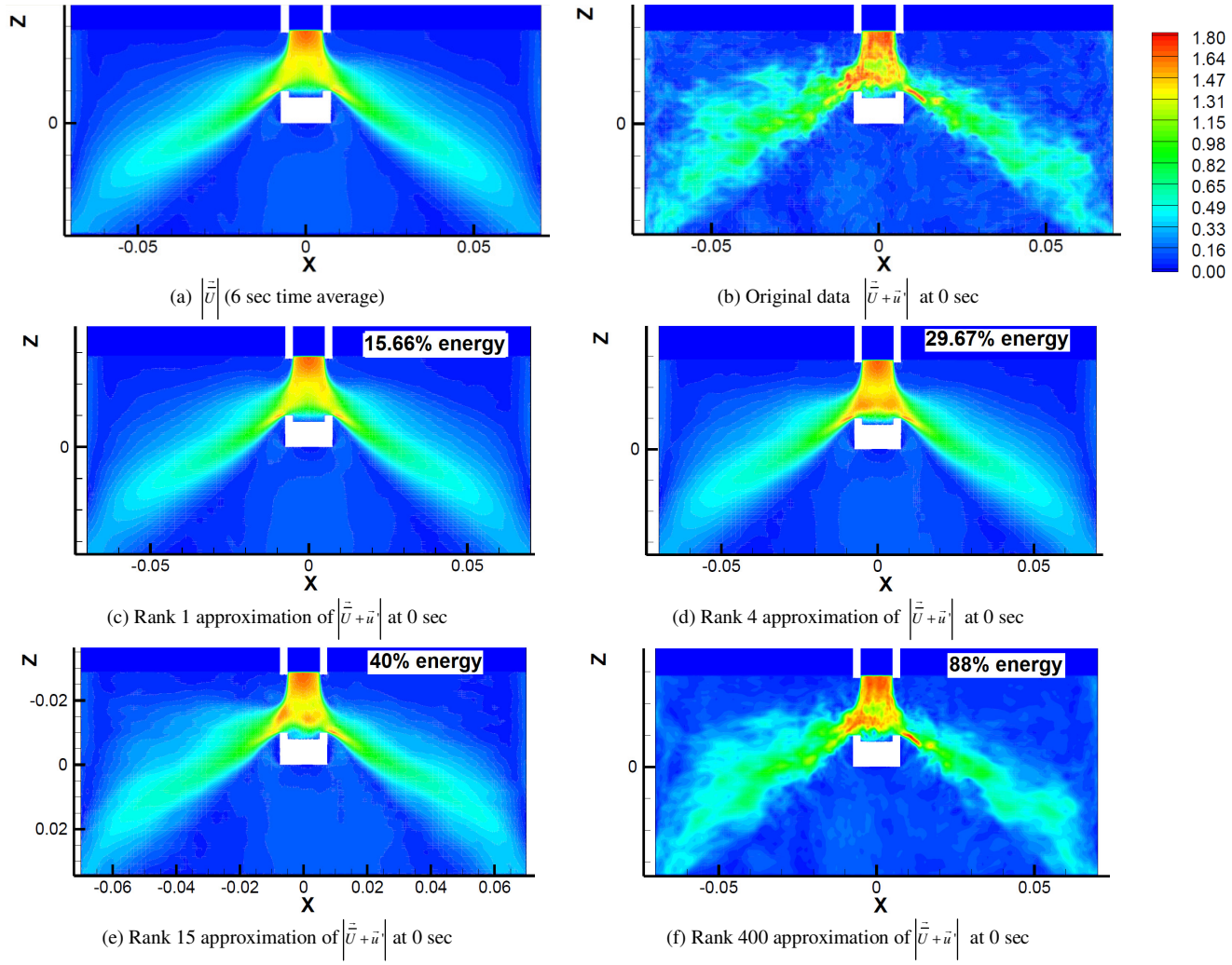

(a) $\left|\bar{\vec{U}}\right|$ (6 sec time average)

(b) Original data $\left|\bar{\vec{U}}+\vec{u}'\right|$ at 0 sec

(c) Rank 1 approximation of $\left|\bar{\vec{U}}+\vec{u}'\right|$ at 0 sec

(d) Rank 4 approximation of $\left|\bar{\vec{U}}+\vec{u}'\right|$ at 0 sec

(e) Rank 15 approximation of $\left|\bar{\vec{U}}+\vec{u}'\right|$ at 0 sec

(f) Rank 400 approximation of $\left|\bar{\vec{U}}+\vec{u}'\right|$ at 0 sec

Figure 7.22 POD reconstructions of velocity magnitude in mold centerline showing contours of (a)Time-average and (b) an instantaneous snapshot calculated by LES CU-FLOW at 0s compared with (c-f) four approximations of the same snapshot using different ranks

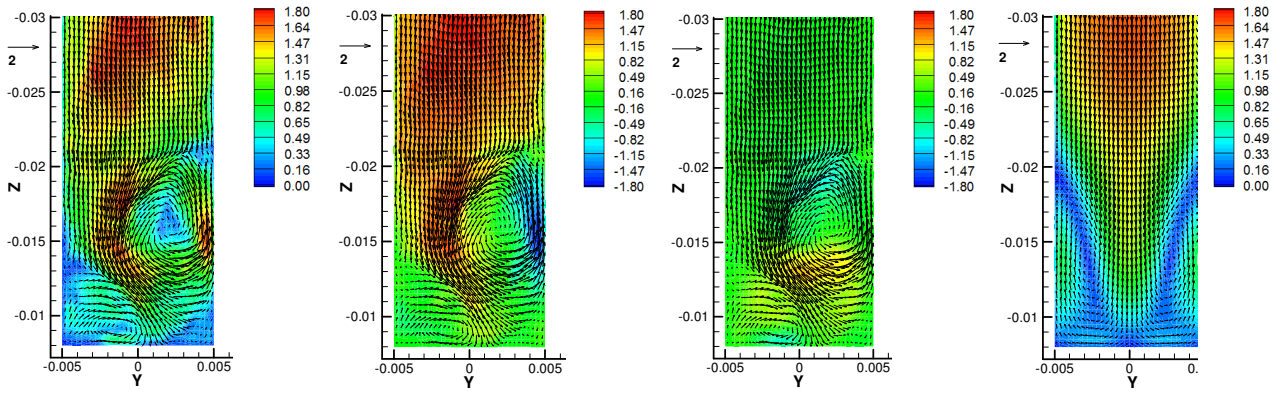

(a) $\vec{V}$ and $|\vec{V}|$ (b) $\vec{V}$ and w (c) $\vec{V}$ and v (d) $\bar{\vec{V}}$ and $|\bar{\vec{V}}|$

Figure 7.23 Flow pattern in the SEN bottom well midplane, showing an instantaneous velocity vector snapshot colored with contours of (a) velocity magnitude (b) vertical velocity and (c) horizontal velocity (d) Time-average velocity vectors and velocity magnitude contours

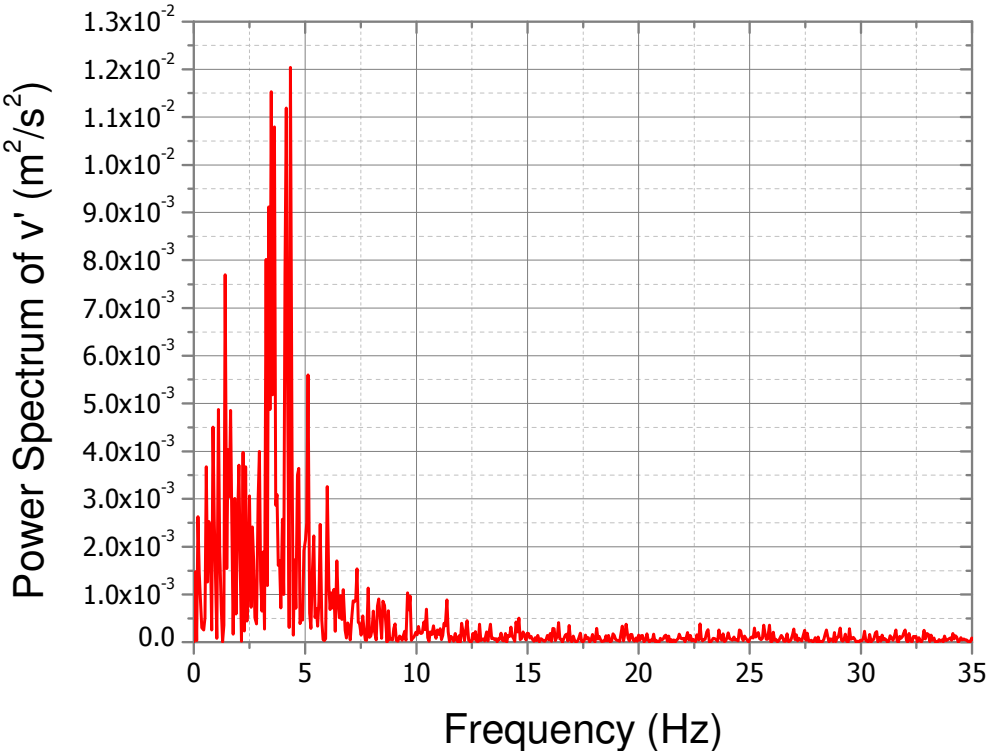

Figure 7.24 Power spectrum (MSA) of wide face normal velocity fluctuations at SEN nozzle bottom center at 95 mm below mold top

7.10. References

1. B. G. Thomas, Fluid flow in the mold, Chapter 14 in Making, Shaping and Treating of Steel, 11th Edition, vol. 5, Casting Volume, Editor: A. Cramb, AISE Steel Foundation, Oct. 2003, Pittsburgh, PA, pp. 14.1-14.41.
2. B. G. Thomas, Modeling of continuous casting, Chapter 5 in Making, Shaping and Treating of Steel, 11th Edition, vol. 5, Casting Volume, Editor: A. Cramb, AISE Steel Foundation, Oct. 2003, Pittsburgh, PA, pp. 5.1-5.24.
3. D. E. Hershey, B. G. Thomas, and F. M. Najjar, Turbulent flow through bifurcated nozzles, Int. J. Num. Meth. in Fluids, 1993, 17(1), pp. 23-47.
4. B. G. Thomas, L. J. Mika and F. M. Najjar, Simulation of fluid flow inside a continuous slab-casting machine, Metall. Trans. B, 1990, vol. 21B, pp. 387-400.
5. R. Chaudhary, G.-G. Lee, B. G. Thomas, and S.-H. Kim, Transient Mold Fluid Flow with Well- and Mountain-Bottom Nozzles in Continuous Casting of Steel, Metall. Mat. Trans B, 2008, vol. 39B, no. 6, pp. 870-884.
6. R. Chaudhary, G.-G. Lee, B.G. Thomas, S.-M. Cho, S.-H. Kim, and O.-D. Kwon, Effect of Stopper-Rod Misalignment on Fluid Flow in Continuous Casting of Steel, Metall. Mat. Trans. B, 2011, vol. 42, 2, pp. 300-315.
7. X. Huang and B. G. Thomas, Modeling of transient flow phenomena in continuous casting of steel, Canadian Metallurgical Quarterly, 1998, vol. 37, no. 3-4, pp. 197-212.
8. Q. Yuan, S. Sivaramakrishnan, S.P. Vanka and B. G. Thomas, Computational and experimental study of turbulent flow in a 0.4 scale water model of a continuous steel caster, Metall. Mat. Trans. B, 2004, vol. 35B, pp. 967-982.

9. A. Ramos-Banderas, R. Sanchez-Perez, R. D. Morales, J. Palafox-Ramos, L. Demedices-Garcia, and M. Diaz-Cruz, Mathematical simulation and physical modeling of unsteady fluid flow in a water model of a slab mold, Metall. Mat. Trans. B, 2004, vol. 35B, pp. 449-460.

10. Q. Yuan, B. G. Thomas and S. P. Vanka, Study of transient flow and particle transport in continuous steel caster molds: Part I. Fluid flow, Metall Mat. Trans. B, 2004, vol. 35B, pp. 685-702.

11. B. Zhao, B. G. Thomas, S. P. Vanka and R. J. O'Malley, Transient fluid flow and superheat transport in continuous casting of steel slabs, Metall. Mat. Trans. B., 2005, vol. 36B, pp. 801-823.

12. Z.-D. Qian and Y.-L. Wu, Large eddy simulation of turbulent flow with the effects of DC magnetic field and vortex brake application in continuous casting, ISIJ International, 2004, vol. 44, no. 1, pp. 100-107.

13. R. Liu, W. Ji, J. Li, H. Shen, and B. Liu, Numerical simulation of transient flow patterns of upper rolls in continuous slab casting moulds, Steel Research Int., 2008, 79, no. 8, pp. 50-55.

14. K. Pericleous, G. Djambazov, J. F. Domgin and P. Gardin, Turbulence Model Performance in Continuous Casting Simulations, Proc. of the Sixth International Conf. on Engineering Computational Technology, Civil-Comp Press, Stirlingshire, UK, 2008.

15. B. G. Thomas, Q. Yuan, S. Sivaramakrishnan, T. Shi, S. P. Vanka and M. B. Assar, Comparison of four methods to evaluate fluid velocities in a continuous slab casting mold, ISIJ Int., 2001, vol. 41, no. 10, pp. 1262-1271.

16. Yuan, Q., B. Zhao, S.P. Vanka, and B.G. Thomas; “Study of Computational Issues in Simulation of Transient Flow in Continuous Casting”, Steel Research International, Special Issue: Simulation of Fluid Flow in Metallurgy, Jan. 2005, Vol. 76, No. 1, pp. 33-43.

17. K. Timmel, S. Eckert, G. Gerbeth, F. Stefani, and T. Wondrak, Experimental modeling of the continuous casting process of steel using low melting point alloys – the LIMMCAST program, ISIJ International, 2010, 50, No. 8, pp. 1134-1141.

18. K. Timmel, S. Eckert, and G. Gerbeth, Experimental investigation of the flow in a continuous-casting mold under the influence of a transverse, direct current magnetic field, Metall. Mat. Trans. B, 2011, vol. 42, 1, pp. 68-80.

19. K. Timmel, X. Miao, S. Eckert, D. Lucas, and G. Gerbeth, Experimental and numerical modeling of the steel flow in a continuous casting mould under the influence of a transverse DC magnetic field, Magnetohydrodynamics, 2010, vol. 46, 4, pp. 337-448.

20. S. B. Pope, Turbulent Flows, 2000, Cambridge University Press, Cambridge, United Kindom.

21. J. O. Hinze, Turbulence, McGraw-Hill Publishing Company,1975, NewYork.

22. B. E. Launder, and D. B. Spalding, Mathematical Models of Turbulence. 1972: London Academic Press.

23. R. Chaudhary, B.G. Thomas and S.P. Vanka, Evaluation of turbulence models in MHD channel and square duct flows, CCC 201011, Continuous Casting Consortium Report, Dept. of Mechanical Sc & Eng., University of Illinois at Urbana-Champaign, IL.

24. FLUENT6.3-Manual (2007), ANSYS Inc., 10 Cavendish Court, Lebanon, NH, USA.

25. B. Kader, Temperature and concentration profiles in fully turbulent boundary layers, Int. J. Heat Mass Transfer, 1981, 24(9), pp. 1541-1544.

26. M. Wolfstein, The velocity and temperature distribution of one-dimensional flow with turbulence augmentation and pressure gradient, Int. J. Heat Mass transfer, 1969, 12, pp. 301-318.

27. T.-H. Shih, W. W. Liou, A. Shabbir, Z. Yang, and J. Zhu, A New k-ε Eddy-Viscosity Model for High Reynolds Number Turbulent Flows - Model Development and Validation, Computers & Fluids, 1995, vol. 24(3), pp. 227-238.

28. S. T. Johansen, J. Wu, W. Shyy, Filter-based unsteady RANS computations, Int. J. Heat and Fluid Flow, 25, 2004, pp. 10-21.

29. R. Chaudhary, S.P. Vanka and B.G. Thomas, Direct numerical simulations of magnetic field effects on turbulent flow in a square duct, Phys. of Fluids, 22, 075102, 2010.

30. R. Chaudhary, A.F. Shinn, S. P. Vanka and B. G. Thomas, Direct Numerical Simulations of Transverse and Spanwise Magnetic Field Effects on Turbulent Flow in a 2:1 Aspect Ratio Rectangular Duct, Computers & Fluids, Submitted, Nov. 2010.

31. A. F. Shinn, S. P. Vanka, and W. W. Hwu, Direct numerical simulation of turbulent flow in a square duct using a graphics processing unit (GPU), AIAA-2010-5029, 40th AIAA Fluid Dynamics Conference, June 2010.

32. J. Smagorinsky, General circulation experiments with the primitive equations I. The basic experiment, Month. Wea. Rev., 1963, 92, pp. 99-164.

33. M. Germano, U. piomelli, P. Moin, W. H. Cabot, Dynamic subgrid-scale eddy viscosity model, In summer Workshop, Center for Turbulence Research, 1996, Stanford, CA.

34. D. K. Lilly, A proposed modification of the Germano subgrid-scale closure model, Phys. Fluids, 1992, vol. 4, pp. 633-635.

35. S.-E. Kim, Large eddy simulation using unstructured meshes and dynamic subgrid-scale turbulence models, Technical Report AIAA-2004-2548, 34th Fluid Dynamic Conference and Exhibit, June 2004, AIAA.

36. W.-W. Kim and S. Menon, Application of the localized dynamic subgrid-scale model to turbulent wall-bounded flows, Technical Report AIAA-97-0210, 35th Aerospace Science Meeting, Jan. 1997, AIAA.

37. F. Nicoud and F. Ducros, Subgrid-scale stress modeling based on the square of the velocity gradient tensor, Flow, Turbulence and Combustion, 1999, vol. 63(3), pp. 183-200.

38. H. Werner and H. Wengle, Large-eddy simulation of turbulence flow over and around a cube in a plate channel, in 8th symposium on turbulent shear flows, 1991, Munich, Germany.

39. P. Moin and J. Kim, Numerical investigation of turbulent channel flow, J. Fluid Mech., 118, 1982, pp. 341-377.

40. K. Y. M. Lai, M. Salcudean, S. Tanaka and R. I. L. Guthrie, Mathematical modeling of flows in large tundish systems in steelmaking, Metall. Mat. Trans. B, 17B, 1986, pp. 449-459.

41. M. H. Baba-Ahmadi and G. Tabor, Inlet conditions for LES using mapping and feedback control, Computers & Fluids, 38, 6, 2009, pp. 1299-1311.

42. A. Sohankar, C. Norberg, and L. Davidson, Low-Reynolds-number flow around a square cylinder at incidence: Study of blockage, onset of vortex shedding and outlet boundary condition, Int. J. for Num. Meth. in Fluids, 26, 1998, pp. 39-56.

43. M. Zagarola, and A. Smits, Mean-flow scaling of turbulent pipe flow, J. Fluid Mech., 373, 1998, pp. 33-79.

44. H. Bai, and B.G. Thomas, Turbulent Flow of Liquid Steel and Argon Bubbles in Slide-gate Tundish Nozzles: Part I. Model Development and Validation, Metall. Mat. Trans. B, 2001, 32(2), pp. 253-267.

45. P. Holmes, J. L. Lumley, and G. Berkooz, Turbulence, Coherent Structures, Dynamical Systems and Symmetry, Cambridge University Press, UK, 1996.

46. A. Chatterjee, An introduction to proper orthogonal decomposition, Current Science, 78, 7, 10, April 2000, pp. 808-817.

CHAPTER 8. EFFECT OF ELECTROMAGNETIC RULER BRAKING (EMBr) ON TRANSIENT TURBULENT FLOW IN CONTINUOUS SLAB CASTING USING LARGE EDDY SIMULATIONS

8.1. Introduction

Electromagnetic braking is an efficient and non-intrusive way to control the turbulent flow pattern and its stability in the nozzle and the mold region of the continuous casting process for steel slabs. Turbulent flow in this process is the main cause of expensive defects, including surface quality, internal quality, and inclusion-related defects. As explained in more detail elsewhere [1-2], surface defects due to meniscus freezing arise if the surface flow near the slab-metal interface is too slow to provide convective mixing. Slag entrainment defects will occur if the flow is too fast, or the liquid profile is not flat enough. Finally, and most importantly, intermittent defects of both kinds may occur due to sudden fluctuations in the liquid level.

Extensive work exits on steady Reynolds-averaged Navier-Stokes (RANS) and physical water models without electromagnetic brakes (EMBrs) in continuous casting systems [3]. Use of steady RANS models in EMBr cases is also in plenty [3]. Very few studies considered transient models such as large eddy simulation (LES) [4-8] and unsteady RANS (URANS) [8] to analyze the turbulent flows in these systems. The use of LES and measurements together for the study of EMBr is relatively rare [9-11].

Qian et al. [9] employed LES with a DC magnetic field effects in a slab continuous casting process. The effect of SEN depth and port angle on vortex formation was analyzed and the mechanism of vortex formation was outlined. A new “vortex brake” was proposed and its effect on vortex suppression was studied. The effect of the location of the magnetic field on vortex formation was also studied. The magnetic, when applied at free surface, suppressed

turbulent and biased vortices significantly. Kageyama et al. [10] developed a coupled LES-electromagnetic field-free surface model to be used to simulate turbulent flow in the continuous casting machines. This model was tested in a couple of problem but was never extended to simulate turbulent flows in continuous casting systems. Miki et al. [11] applied a LES model to investigate the cause of internal defects in a continuous casting slab mold. The unbalanced flow was found to be responsible for the internal defects in the form of bubble and inclusions. FC mold was reported reduces turbulent variations in the mold and thus thereby reducing the internal defects caused by bubbles and inclusions.

All above works considered primitive LES models and the real effects of EMBr on the turbulence and flow structures were not studied and the works were only limited to the vortex formation and inclusions transport in unbalanced flow. To develop more advanced LES model and perform a rigorous validation before using it for a thorough investigation of turbulent flows in continuous casting machines, the current work is considered. We combined LES with the measurements [12-14] using ultrasonic Doppler velocimetry (UDV) in a small scale GaInSn liquid metal model of continuous casting process with electromagnetic braking. In our previous work [8], we presented an extensive investigation of turbulent flows and also assessed various state of art transient and steady models, including model considered in current work, in non-EMBr liquid metal GaInSn model. Current work is an extension of our previous work with electromagnetic braking effects.

This work presents a thorough investigation of the effects of single/double ruler types EMBrs and their locations on the turbulent flows in the continuous casting nozzle and molds. The instantaneous flow, time-average flow, power spectrums, proper orthogonal decomposition (POD) analysis, Reynolds stresses, turbulent kinetic energy (TKE), TKE budgets are investigated

to understand the effect of electromagnetic braking on turbulent flow. The recommendations are presented for the favorable locations of the ruler brakes from the point of view of stable and least defect prone turbulent flow in the mold of a continuous casting process.

8.2. Model Caster Geometry and Velocity Measurements

The current work uses a liquid metal GaInSn physical model used previously in non-EMBr work [12-14]. The velocity measurements in this model are performed at Forschungszentrum Dresden-Rossendorf (FZD), Dresden, Germany [12-14]. Further details on the physical GaInSn model and measurements can be found in Chaudhary et al. [8] and Timmel et al. [12-14]. Ultrasonic velocity profiler is used to measure instantaneous horizontal velocity at various vertical positions at mold midplane along different horizontal lines. The GaInSn model has a mold of 140 mm (width) x 35 (mm) (thickness). The facility uses a zero degree angle bifurcated nozzle having inner bore diameter of 10 mm. Figures 8.1(a), 8.1(b) and 8.1(c) show the schematic of this facility with front-, side- and bottom-views respectively. The "orange" rectangular region in the front-view, Figure 8.1(a), shows the location of the 92mm (location of pole center) single-ruler brake.

8.3. Computational Model

8.3.1. Fluid Flow

The large eddy simulation model developed for this work solves the following 3-D filtered continuity and time dependent Navier-Stokes (N-S) equations [15-16]:

$$\frac{\partial u_i}{\partial x_i} = 0 \tag{8.1}$$

$$\frac{\partial u_i}{\partial t} + \frac{\partial u_i u_j}{\partial x_j} = -\frac{1}{\rho}\frac{\partial p^*}{\partial x_i} + \frac{\partial}{\partial x_j}\left(\left(\nu + \nu_s\right)\left(\frac{\partial u_i}{\partial x_j} + \frac{\partial u_j}{\partial x_i}\right)\right) + \frac{1}{\rho}\vec{F}_L \tag{8.2}$$

Where, $\vec{F}_L$ is the filtered Lorentz force due to magnetic field, described in section 8.3.2. The modified pressure, p^*, is $p+\frac{2}{3}\rho k_r$, k_r is residual kinetic energy. To account for the unresolved velocity scales, the following sub-grid scale (SGS) viscosity (ν_s) with wall-adapting local eddy viscosity model (WALE) model [17] was applied,

$$\nu_s = L_s^2 \frac{\left(S_{ij}^d S_{ij}^d\right)^{3/2}}{\left(S_{ij}S_{ij}\right)^{5/2}+\left(S_{ij}^d S_{ij}^d\right)^{5/4}} \tag{8.3}$$

Where, $S_{ij}=\frac{1}{2}\left(\frac{\partial u_i}{\partial x_j}+\frac{\partial u_j}{\partial x_i}\right)$, $S_{ij}^d=\frac{1}{2}\left(g_{ij}^2+g_{ji}^2\right)-\frac{1}{3}\delta_{ij}g_{kk}^2$, $g_{ij}=\frac{\partial u_i}{\partial x_j}$

$\delta_{ij}=1$, if i=j, else $\delta_{ij}=0$. As the grid is refined, accuracy improves to approach that of a direct numerical simulation, because ν_s approaches zero, owing to the dependency of coefficient, L_s on grid size,

$$L_s = C_w\left(\Delta x\Delta y\Delta z\right)^{1/3} \tag{8.4}$$

Where $C_w^2=10.6C_s^2$, $C_s=0.18$. Δx, Δy, and Δz are the grid spacing in x, y and z directions.

8.3.2. Magnetohydrodynamic (MHD) Equations

In liquid metal MHD flows, the induced magnetic field is negligible compared to externally applied magnetic field. In such a case, the Ohm's law can be combined with conservation of current to derive a Poisson equation for electric potential which can then be used along with instantaneous velocity field and external magnetic field to calculate Lorentz force [18-19]. This Lorentz force is added as a source term in momentum equations [18-19]. The following are the filtered MHD equations for incompressible-MHD flow:

$$\vec{F}_L = \vec{J} \times \vec{B}_0 \tag{8.5}$$

$$\vec{J} = \sigma\left(-\nabla\phi + \vec{v} \times \vec{B}_0\right) \tag{8.6}$$

$$\nabla^2\phi = \nabla \cdot \left(\vec{v} \times \vec{B}_0\right) \tag{8.7}$$

The external magnetic field is given as: $\vec{B}_0 = \left(B_{0x} = 0.0, B_{0y}(\vec{x}), B_{0z} = 0.0\right)$. Here B_{0y} is the magnetic field normal to wide faces which has been measured as well as calculated for GaInSn model [13-14].

The above governing equations of LES for incompressible-MHD flows have been solved in our in-house graphic processing unit (GPU) based code (LES-CU-FLOW [18-19]). The details about the numerical methodology, boundary conditions and meshes were presented previously in our non-EMBr work in [8] but will be reviewed again in the following sections.

8.3.3. Computational Domain, Mesh and Boundary Conditions

The computational domain used in LES calculations is the faithful reproduction of the geometry given in Figure 8.1. To avoid complications in creating brick mesh, the bottom region of the mold is approximated with equal area rectangular as previously presented in our non-EMBr work in CHAPTER 7 in Figure 7.1(d). More details on various dimensions, process parameters and fluid properties specific to current work can be found in Table 8.1.

The mesh in LES model consists of ~ 7 million (384x192x96) brick cells in the whole domain as presented in CHAPTER 7 in Figure 7.2(c) and 7.2(d). To minimize computational burden and avoid wastage of mesh, the nozzle bore was trimmed at the top free surface of the liquid metal and a mapping condition [20, 8] was used to get fully developed turbulent flow in short nozzle pipe length of L/D~7.2. The same inlet mapping condition when used in our previous non-EMBr work is found performing very well [8].

The top free surface in the mold is taken free-slip boundary with zero normal velocity and shear stresses. All walls of the domain are considered no-slip and insulated for current density [18-19] and Werner-Wengle wall treatment was used [21]. The mold outlet was trimmed in the forward flow region at the narrow faces and a convective outlet boundary condition was used [22]. The formulations and implementation details on the inlet mapping condition, Werner-Wengle wall treatment, and convective boundary condition are given in our non-EMBr work [8].

8.3.4. Numerical Method and Computational Cost

The coupled filtered N-S-MHD equations have been discretized using the Finite Volume Method (FVM) on a structured Cartesian staggered grid. Detailed steps of the method are outlined in Chaudhary et al. [18]. A geometric multigrid solver is used to solve the pressure Poisson (PPE) and electric potential Poisson (EPPE) equations. Neumann boundary condition is used for electric potential which ensures insulated boundary condition for current density. The Lorentz force is added as an explicit source into the momentum equations. The calculations are initiated with a fully developed no-EMBr flow and the flow field is allowed to develop for ~5 secs before starting collecting means. The mean velocities were collected alone for ~ 3 sec (50,000 timesteps, $\Delta t = 0.00006\,\text{sec}$). Once mean velocities stabilizes then the collection of Reynolds stresses and TKE budgets is initiated as well. Thereafter, the mean velocities, Reynolds stresses and TKE budget terms are collected together for ~25 secs.

The computations are performed on a personal computer with a 2.66 GHz Intel® Xeon processor (Intel Corp., Santa Clara, US) and 8.0 GB RAM with a graphic processing unit (GPU, NVIDIA C1060 with 4 GB memory) installed on it. CU-FLOW took ~26 days to integrate total of ~48 sec. The time requirement in flow with EMBr is around double of non-EMBr as it requires the solution of additional Poisson equation, EPPE, and current density equations.

8.4. Electromagnetic Brake Configurations

The current work evaluates static electro-magnetic fields, EMBr, with three different "ruler" brakes. Two of the brakes are single-ruler configurations at different locations below the top surface (92mm, and 121mm), and have measurement data for horizontal velocities provided by Timmel et al. [13-14]. The third brake is a double-ruler type, typical of that in commercial application, where it is known as Flow-Control or "FC-mold" EMBr (ABB), and has only model predictions.

The magnetic field in single-ruler brakes is unidirectional (+ve) however in double-ruler brake upper (-ve) and lower (+ve) regions of the mold have fields in the opposite directions. Figure 8.2(a) presents the strength of magnetic field in three directions in a 0.310T single-ruler brake [13-14]. Here, 0.310T is the strength of magnetic field at pole center. The origin in this figure on horizontal axis signifies the location of the pole center of the brake. The magnetic field is almost constant across the width but changes significantly in vertical and thickness directions. The field is stronger at the pole in vertical direction but weaker at pole while looking in thickness direction. The magnetic field shown in Figure 8.2(a) when placed with pole center at 92 mm location gives 92-mm ruler brake, and while at 121 mm gives 121-mm ruler brake. To generate double-ruler brake, the field strength shown in Figure 8.2(a) is halved and placed at 40mm from the top surface in opposite direction while the lower brake with strength shown in Figure 8.2(a) is placed at 121mm from free surface. Since, the fields in double-ruler brake are in opposite directions therefore they have canceling effects and field strength is weaker in the nozzle port region. The strength of the magnetic field in different single/double ruler EMBr cases along mid-vertical line is shown in Figure 8.2(b) and at midplane is shown in contours in Figure 8.2(c)-(e).

8.5. Comparison of Model Predictions with Measurements

Figure 8.3 compares the time-average predictions of horizontal velocity from LES-CU-FLOW with UDV measurements along 95, 105 and 115 mm lines from the mold top in different cases. The non-EMBr case is presented in Figure 8.3(a), and the EMBr cases with single-ruler brakes located at 92 mm and 121 mm below the liquid level are in Figure 8.3(b) and 8.3(c) respectively. As mentioned in our previous non-EMBr work [8] and also stated by Timmel et al. [12-14], the measurements close to SEN along 95 mm line and close to narrow face are inaccurate perhaps due to wall effects and measurement inabilities. The LES predictions matches well in non-EMBr as well as in EMBr cases along the three lines. The predictions in 121 mm ruler brake are slightly off from measurements. The reason for the mismatch in this case is not very clear, when model performed very well in other non-EMBr and 92-mm EMBr cases.

To assess the model predictions with measurements further, the comparison of the time-averaged horizontal velocity contours with measurements at the mold-mid plane close to jet region in two EMBr cases is presented in Figure 8.4(a) and 8.4(b). The comparison of LES-CU-FLOW predictions with measurements in non-EMBr case was previously presented [8] and therefore is not given here. The inability of measurements close to SEN and NF can be seen where values are inaccurately underpredicted. The measurements show wiggles in time-average data due to lack of number of frames (total ~125 frames for a ~25 sec time). Besides, the measurements show weird behavior by measuring lower values at the center of the jet which is physically unrealistic. As the model predictions and measurements together suggest, the time-average jet in 92-mm ruler brake bent upward. The jet from 121-mm ruler brake is more forward and hits the narrow face more straight on the lower side. The values and the behavior of jet match well between measurements and predictions for both ruler brakes.

The assessment of model predictions with measurements for transient velocities is presented in Figure 8.5 for three points for 4 sec velocity data. The point 1 is close to narrow face (NF) (10mm) and at 95mm from mold top at midplane. The point 2 and 3 are respectively at 95 and 105 mm from mold top at the mold center (~40 mm from NF) at midplane between wide faces. As can be seen, point 2 is in high speed jet region and therefore shows combined effects of high and low frequencies. Points 1 and 3 are away from jet region and only have low frequencies. These velocities are in 92-mm EMBr case and show very low frequencies. More on this low frequency behavior will be discussed later when we present other results for this case. As previously shown in our non-EMBr work [8], the measurements have huge temporal filtering and therefore are unable to capture higher frequencies. Same limitations on measurements can be seen here. The predictions with spatial averaging on measuring volumes and 0.2 sec moving time-average matches best with the measurements. Overall, the LES predictions are found matching measurements well for time-average as well as instantaneous velocities.

8.6. Results and Discussion

The LES predictions and measurements for two locations (92 mm and 121mm) of single-ruler EMBr (pole strength 0.310T) have been combined to analyze the effect of the location of electromagnetic braking. Further, the LES model is extended to study the influence of a proposed double-ruler brake designed based on two opposite directional single-rulers on the flow. The interesting effects of the ruler location and single- vs. double-ruler brakes are witnessed on instantaneous and time-average flow structures.

8.6.1. Transient Flow Patterns

Figures 8.6(a), (b), (c) and (d) present the instantaneous flow patterns with no-EMBr, two-single and one-double ruler brakes. The instantaneous flow fields are significantly altered

with the presence of magnetic field. Magnetic field suppresses turbulence and encourages the formation of large scale vortical structures in the mold whose axis are aligned with the magnetic field. These large vortical structures move into the upper- and lower-recirculation regions like laminar unsteady flows. This is the tendency towards quasi 2-d turbulence in presence of a strong magnetic field and insulated walls normal to the magnetic field. This behavior is mostly dominant in the upper and lower recirculation regions. Similar behavior is reported by Timmel et al. based on their ultrasonic Doppler velocimetry measurements [13-14]. Others have also reported the tendency of turbulent flow growing with large scale vortical structures aligned with magnetic field [23]. In this condition, the viscous and magnetic dissipation of turbulence reduces and flow becomes dominated with large scale variations [23].

Location of magnetic field also significantly changes the flow patterns. With 92 mm ruler brake, the magnetic field is strongest right at the port region and flow becomes laminarized in the nozzle bottom which leads to the dominance of large scales in the mold when jet comes out. This jet has shown the tendency of very large frequency where flow on one side forms a circular roll within smaller region right next to port and on the other side flow hits narrow face and partly goes up on the surface and partly downward. This behavior keeps on flipping on right and left sides with very large frequencies. When the ruler brake is lowered by 29mm (pole location 121mm), the magnetic field is now weaker at the nozzle well and flow sustain more turbulence at the nozzle bottom than previous case. The more mixing at the nozzle bottom due to turbulence keeps the jet more stabilized besides the jet mid-way upward bending is reduced. The jet in lower field hits narrow face and partly goes up on the surface and partly downward. Because of the jet hitting at narrow faces, the surface velocity in 29 mm lower brake is much faster than previous case. This case seems to have smaller vortical structures than 92mm ruler brake. In case

of double ruler brake, the magnetic field is weakest at the nozzle bottom and turbulence is weakly suppresses. The jet coming out of port has lot of mixing due to turbulence and it bends in the lower regions very close to the bottom of the SEN in the mold. This jet bending keeps on flipping on both sides with time. Due to this lower bending, this case seems to have vortical structures smaller than 92mm ruler brake but bigger than 121mm. The analysis of instantaneous velocities and flow patterns from animations suggests that stronger magnetic field should be avoided at the nozzle-bottom well. Further insight on these behaviors will be gained with time-average flows fields, velocity histories, POD analysis, Reynolds stresses, TKE and TKE budgets in the following sections.

8.6.2. Time-Averaged Flow Field

The predicted time-averaged velocity magnitude for non-EMBr and EMBr cases is presented in Figure 8.7. The time averaging of velocity field is performed from ~25 sec in different cases. As can be seen, the time average flow in non-EMBr case is quite symmetric on both right and left sides of SEN. This symmetry in jet region is achieved within ~1-2 sec of time averaging. This behavior suggests the dominance of high frequencies. In case of 92 mm ruler brake, jet shows right-left asymmetry in the time-average flow field. The strong magnetic field at nozzle bottom suppresses turbulence strongly. The jet in this case forms a roll on one side and hits straight narrow face on other before sending flow to surface and downward. This asymmetry in ~25s time-average flow in 92 mm EMBr was initially thought of the purely the effect of slightly asymmetric magnetic field. But later on, we investigated the flow with perfectly symmetric magnetic field ruler at 92 mm and we integrated flow up to ~48 sec and we still found asymmetric flow. A coarse mesh (~0.8 million brick cells) was then used and flow was time averaged for much longer times, ~200 sec, the right left asymmetry reduced significantly and

time-average flow became very much symmetric. The time-averaged flow field showed circular rolls on both sides as shown on the left side in the current case. This behavior suggests the strong magnetic field at nozzle bottom created large scales and long time variations.

In case of 121mm ruler brake, the magnetic field is slightly weaker in the nozzle bottom and flow is relatively more turbulent at the nozzle bottom. The flow when averaged on a perfectly right-left symmetric magnetic field showed right-left symmetry in velocity magnitude within ~5 sec of time averaging. In double ruler brake, the field is weakest at the nozzle bottom and flow sustains much more turbulence (very similar turbulence at nozzle bottom as in non-EMBr case). To confirm the asymmetry in time-average flow in double-ruler brake, we analyzed flow field with a perfectly symmetric double ruler brake. The flow achieved perfect right-left and front-back symmetry within 26 s. This behavior suggests that this case has turbulence with much smaller scales than 92mm EMBr however bigger than 121mm EMBr.

The behavior of the instantaneous and time-average flow in different brakes suggested that very strong magnetic field at nozzle bottom encourages very large scale variations in the flow and slightly asymmetric magnetic field can further exaggerate this behavior leading to a fully biased flow.

8.6.3. Anisotropic Suppression of Turbulence at SEN Bottom-Well and in the Mold

To understand the influence of magnetic field on turbulence suppression at nozzle bottom and other parts of the mold, Figure 8.8(a) present the three components of velocity fluctuations as a function of time in different cases at nozzle bottom center (95 mm from mold top). As can be seen, the positive-negative flipping of v' signifies the alternation of swirl in the nozzle bottom. The frequency of this alternation is ~3-4Hz which has already been quantified in our previous non-EMBr work [8]. Other components of velocity fluctuations at this location have

higher frequency variations than v'. Magnetic field suppresses all three components of velocity fluctuations. The suppression is stronger with stronger magnetic field. It is very fascinating to see that among the three velocity fluctuations, the velocity fluctuation parallel (v') to the magnetic field is most strongly suppressed. This anisotropic suppression of turbulence by magnetic field significantly reduces the nozzle bottom swirl and its front-back alternation. This reduction in alternation reduces mixing in the nozzle bottom leading to a smoother jet coming out of ports with large scales.

To further look into the effects of this anisotropic suppression on the mold flow. We present the three velocity fluctuations at the mold midplane close to the left port exit (95 mm from mold top and 58mm from left NF) and around the mold center (115 mm from mold top and 29.45mm from left NF) in Figure 8.8(b) and Figure 8.8(c) respectively. The velocity fluctuations suggest more isotropic behavior at the port exit but flow further in the mold becomes more and more anisotropic. At the port exit, v' shows similar positive-negative variations with similar ~3-4 Hz frequencies as found in nozzle bottom swirl in Figure 8.8(b). This behavior suggests the influence of swirl and its alternation on the flow at port exit. This effect is not seen further away around the center of the mold. At mold center, the flow starts showing large scales behavior in the plane. The velocity variations in the direction of magnetic field direction show smaller scales.

8.6.4. Proper Orthogonal Decomposition Analysis

The proper orthogonal decomposition (POD) formulations were previous presented in CHAPTER 7 with reference to our no-EMbr work [8]. The POD analysis splits velocity fluctuations into orthonormal spatial modes and corresponding temporal coefficients. The data matrix $[U_z^{'}]$ for POD analysis has been formulated based on 193 (x-) x 100(z-) spatial values for

each velocity component selected for 12 sec with a time interval of 0.006s (total N= $19300\text{x}3 = 57900,\ M = 2000$).

Figure 8.9 presents the variations in three velocity components in first two modes for three EMBr cases. Interesting facts about velocity variations in different cases in first two modes can be seen. In 92 mm EMBr case, the 1st mode has significant variations in horizontal velocity (u') at mold center and 2nd mode has variations in vertical velocity (w') close to left NF. These two variations are in-plane and responsible for the large scale in plane variations of the jet. This behavior is consistent with instantaneous velocity patterns in this case where on the left flow forms a roll and on the right hits NF while wobbling. The velocity variations in wide face normal velocity (v') are almost negligible in the first two dominating modes. This suggests that swirl and its alternation in nozzle bottom have been suppressed and is not dominating in 92 mm EMBr case.

In 121mm EMBr case, the magnetic field is lowered by 29 mm and turbulence is sustained more in nozzle bottom well than in 92 mm EMBr case. As can be seen, the 1st mode has variations in v' signifying swirl and its alternation combined with jet wobbling at the ports in terms of w' and u' variations. The 2nd mode has most of the variations in horizontal velocity (u').

In double ruler case, the magnetic field is weakest at the nozzle bottom region and turbulence is sustained. The flow in this case shows similar behavior as in non-EMBr case presented previously in CHAPTER 7. The nozzle bottom swirl and its alternation (in terms of v' in 1st mode) is most significant followed by variations in vertical (w') and horizontal (u') velocities in 2nd mode suggesting right-left alternation of flow rolls below SEN.

The different EMBr cases have different level of energies in different modes. Figure 8.10 presents the cumulative energy in different modes in different cases. The first two modes in 92 mm EMBr has 31% of energy followed by 23.5% in double ruler and then 14.7% in 121mm ruler case. The largest energy containing scales are dominating in 92 mm EMBr followed by in double ruler and then in 121mm ruler case. The flow in 92 mm ruler and double-ruler cases forms bigger continuously circulating rolls in upper- and lower-recirculation zones respectively and is the main cause of these large scale behaviors in these cases. The flow in 121mm EMBr case does not form any continuous recirculation and therefore gives energy spread across more scales, same can be seen in Figure 8.10.

To understand the transient behavior of these modes, Figure 8.11 presents the variations of temporal coefficients of first four modes as a function of time for a total of 6 sec. The variations show positive-negative alternating behavior. The variations contain low frequencies mixed with local high frequency variations in these coefficients. The temporal coefficients in no-EMBr case show highest frequency variations. Although double ruler brake shows similar variations as no-EMBr case but there are sudden jumps after around 3.5 sec. These variations are associated with the alternating roll below the SEN in this case. The temporal coefficients in 121mm EMBr case showed weakest magnitude of variations. The variations in 92-mm EMBr case have only low frequencies and miss the superimposition of high frequency fluctuations, as seen in other cases.

8.6.5. Reynolds Stresses and TKE

The turbulent kinetic energy and Reynolds stresses at midplane between wide and narrow faces in different cases are presented in Figures 8.12(a)-(d) and Figures 8.13(a)-(d) respectively. The case which has weakest magnetic field at the nozzle bottom, i.e. double ruler case, sustains

maximum turbulence (next to no-EMBr case) at nozzle bottom and shows the dominance of nozzle bottom swirl and its alternation in terms of v' and w'. The nozzle bottom swirl and its alternation has been suppressed strongly in 92mm and 121 mm EMBr cases, more strongly in 92mm case. It is interesting to note that although all velocity fluctuations at the nozzle bottom well in 92 and 12mm cases are suppressed strongly, the velocity fluctuations in horizontal velocity (u') in the mold are strong in the case which has strong suppression at nozzle well. This behavior is due to reduced mixing at the nozzle bottom giving large scale variations causing horizontal velocity (u') to vary a lot in the mold. These variations in the horizontal velocity could be detrimental to the quality of the steel product. Reynolds shear stresses ($\overline{u'w'}$ and $\overline{v'w'}$) showed similar behavior with the intensity of the magnetic field and therefore are not presented here.

8.6.6. MHD Source and Sink to TKE

The magnetic field interacts with the instantaneous velocities and causes source as well as sink to the turbulent kinetic energy transport equation [18]. The source and sink terms to TKE transport equation caused by wide face normal magnetic field are presented below [18-19]:

$$\text{MHD Source} = \frac{\sigma B_{0y}}{\rho}\left(\overline{u'\frac{\partial \phi'}{\partial z}} - \overline{w'\frac{\partial \phi'}{\partial x}}\right) \tag{8.8}$$

$$\text{MHD Sink} = -\frac{\sigma B_{0y}^2}{\rho}\left(\overline{w'^2} + \overline{u'^2}\right) \tag{8.9}$$

Figure 8.14 presents these two terms and their sum for different cases at the mold midplane between wide faces. As previously found in square and rectangular ducts [18-19], the profiles of these source and sink terms are quite similar with sink being stronger than source thus causing net suppression of turbulence. The strongest net effect MHD source and sink terms on turbulence is in 92mm EMBr case where magnetic field is very strong at the well bottom and jet

region. These strong effects of magnetic field through the net effect of MHD source and sink terms are responsible for large scale variations in horizontal velocity fluctuations as seen in Figure 8.6. In 121mm EMBr and double ruler brake cases, the MHD source and sink terms are weaker than in 92mm EMBr case. These terms are important as they are helpful in modeling the magnetic field effects on turbulence in RANS models.

8.7. Summary and Conclusions

The current work studies the effects of electromagnetic braking (EMBr) on turbulent flow in the nozzle and mold during continuous casting of steel slabs using 4 transient large eddy simulations. The LES model reasonably matches both time-average and filtered transient histories of ultrasonic Doppler velocimetry measurements in a small scale GaInSn model of the studied geometry, including two single-ruler EMBr cases, and a non-EMBr case studied previously [8]. In addition, the model is able to capture high-frequency velocity fluctuations, and velocities near the SEN and NF, which are missed by the measurements. The model captures interesting effects of the braking on transient and time-average flow fields.

Applying a strong magnetic field across the entire mold width, including the nozzle bottom region, suppressed turbulence and swirl in the nozzle bottom, and ports, leading to large scale vortical structures whose axis are aligned with the magnetic field. These vortices show tendency towards 2-D turbulence. Similar behavior was reported by Timmel et al. in their measurements [13-14]. The suppression of turbulence in the nozzle leads to the suppression of nozzle bottom swirl and its alternation. Due to this reason, the mixing effect in the mold reduces and jet comes out of the ports as straight laminarized and causing large scale variations in the mold in terms of horizontal velocities. Stronger the magnetic field at the nozzle-bottom well, the larger and long terms transients are generated in the mold. The alignment of magnetic field is

important in such cases where a stronger magnetic field is applied at the port and jet regions. The slightly asymmetric magnetic field on right and left when combined with large scale variations in such cases may cause fully biased flow in the mold. As the intensity of magnetic field goes down at nozzle bottom, the flow sustains turbulence and related mixing leading to a more stabilized jet. The jet shows more energy distribution in larger scales in 92 mm EMBr case followed by double ruler and then in 121mm EMBr cases. The more energy in larger scales in these two cases is due to formation of long time continuously rotating flow in upper- and lower-recirculating zones respectively. The flow in 121mm EMBr location although show smaller variations but due to jet hitting the narrow faces, this case has higher surface velocity. The flow is found to be most stable either with non-EMBr case or with double ruler brake where magnetic field is weakest at nozzle bottom and thereby the turbulence suppression is weakest at the nozzle bottom and alternation of swirl sustains mixing leading to a stable jet. The only problem with double ruler brake is that due to relatively stronger field in lower recirculation region it bends jet and forms alternating rolls on right-left sides below SEN. It is not sure if this long time variation below SEN is detrimental to the quality of the steel as it happens at the center of the mold.

Overall, this work suggests the importance of the location and of the strength of electromagnetic braking in continuous casting nozzle and mold. Stronger magnetic field should be avoided at the nozzle bottom and jet regions to avoid large scale variations and higher surface velocities.

8.8. Tables and Figures

Table 8.1 Process parameters

Volume flow rate/ Nozzle bulk inlet velocity	110 *ml/s* / 1.4 *m/s*
Casting speed	1.35 *m/min*
Mold width	140 *mm*
Mold thickness	35 *mm*
Mold length	330 *mm*
Total nozzle height	300 *mm*
Nozzle port dimension	8*mm*(width)×18*mm*(height)
Nozzle bore diameter(inner/outer)	10*mm*/15*mm*
SEN depth	72*mm*
Density(ρ)	6360 kg/m^3
Viscosity(μ)	0.00216 *kg/m s*
Nozzle port angle	0 degree
Shell	No
Gas injection	No
Electrical Conductivity (σ)	$3.2x10^{06}$ (1/(ohm m))
EMBr (Single/Double ruler)	Yes

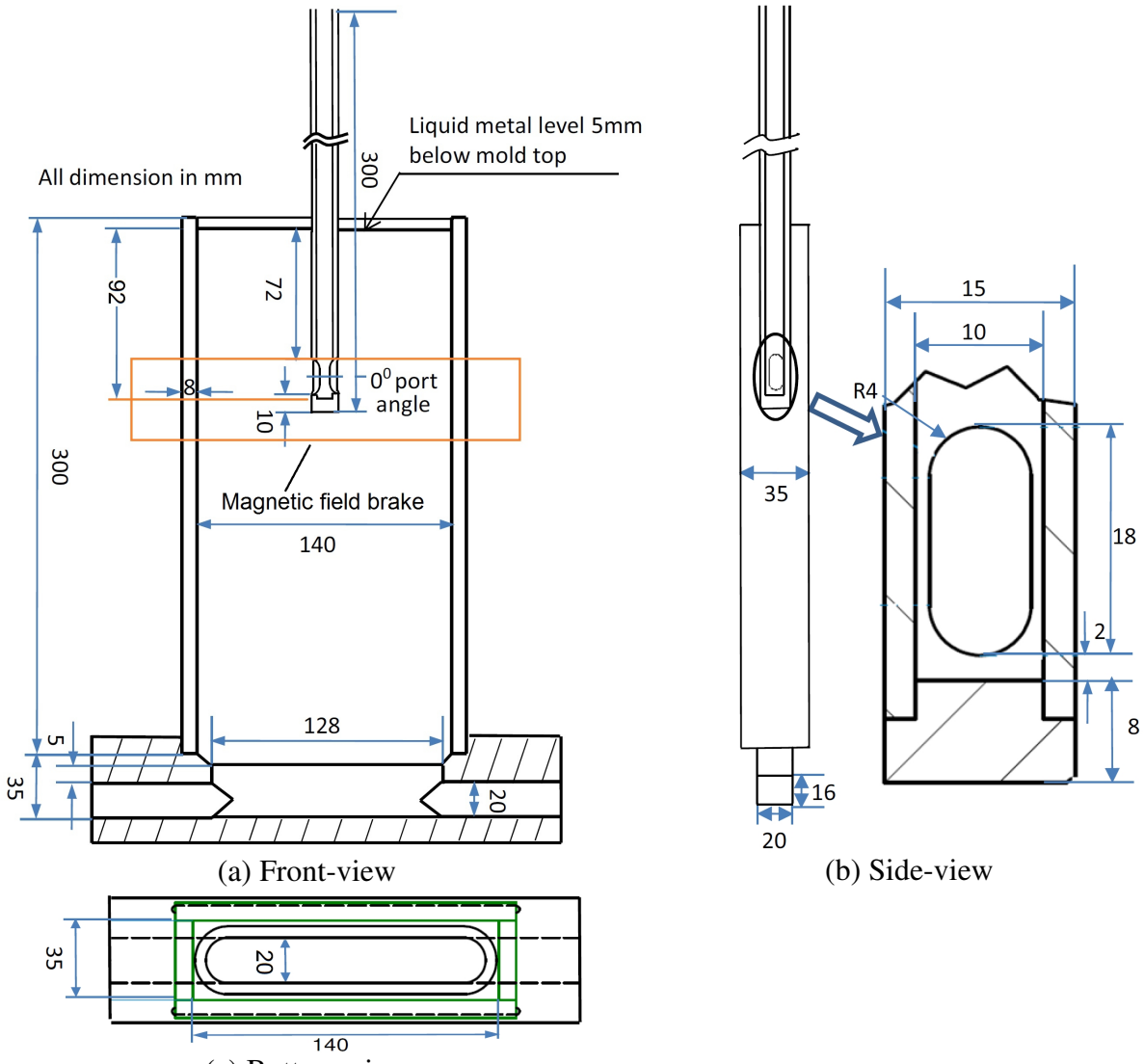

Figure 8.1 Geometry of GaInSn model [12-14] of continuous casting with single ruler EMBr shown by "orange" rectangle with pole center at 92 mm from free surface

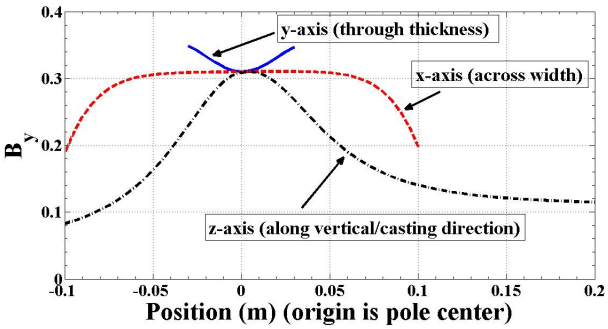

(a) Magnetic field strength in x-, y- and z-directions with a 0.310T brake [13-14]

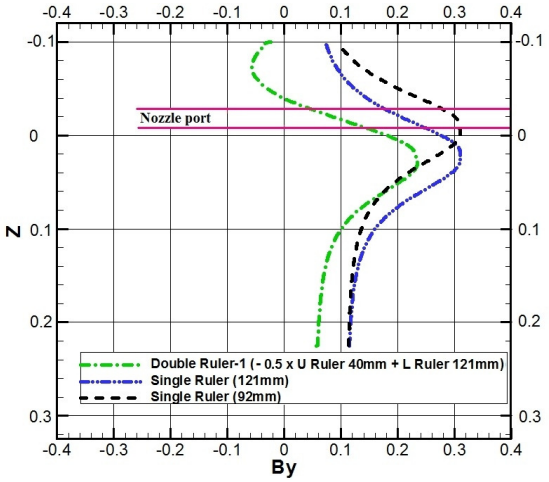

(b) Magnetic field along mid-vertical line with different brakes

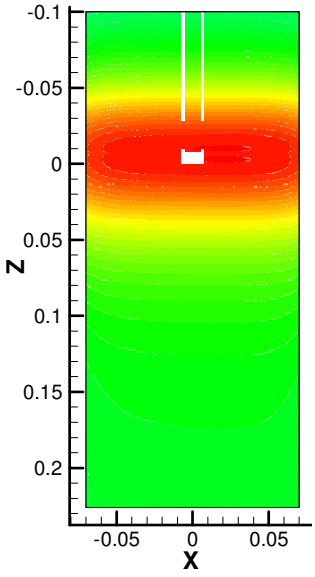

(c) 92-mm ruler brake

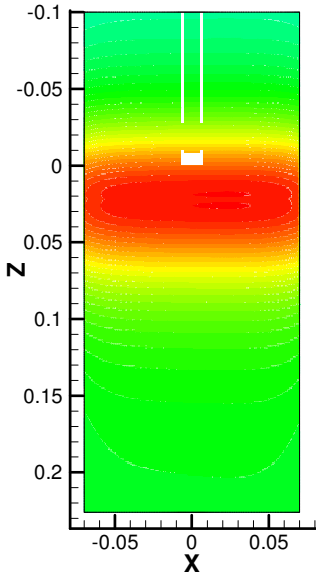

(d) 121-mm ruler brake

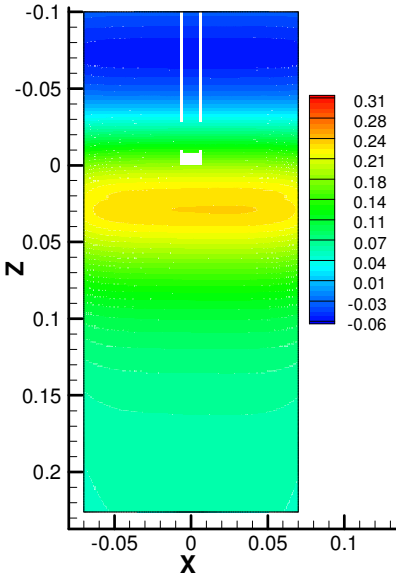

(e) Double ruler brake

Figure 8.2 (a) Magnetic field strength variation in x-, y- and z- directions with a single-ruler brake and (b) field strength with different ruler brakes along mid-vertical line (magenta lines showing location of ports) (c)-(e) mid-plane contours with different ruler brakes

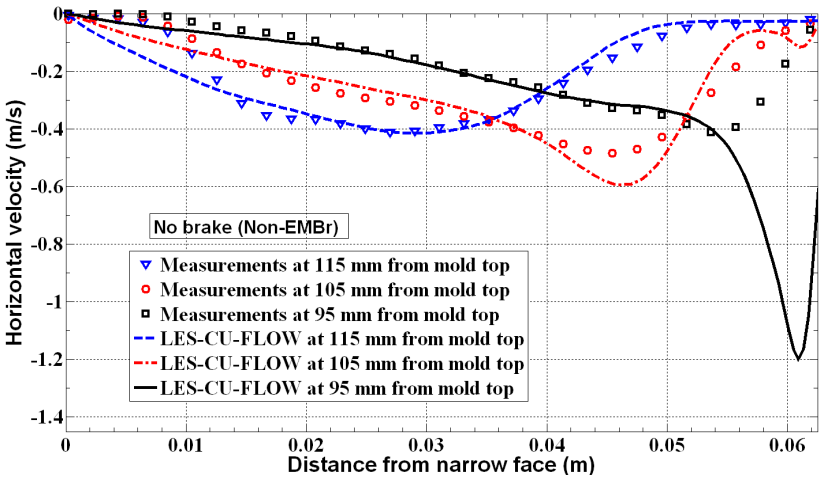

(a) Non-EMBr

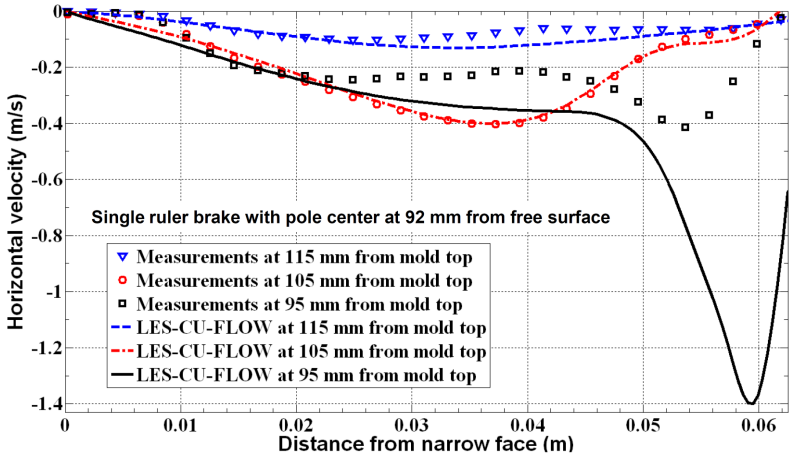

(b) Single ruler EMBr at 92 mm

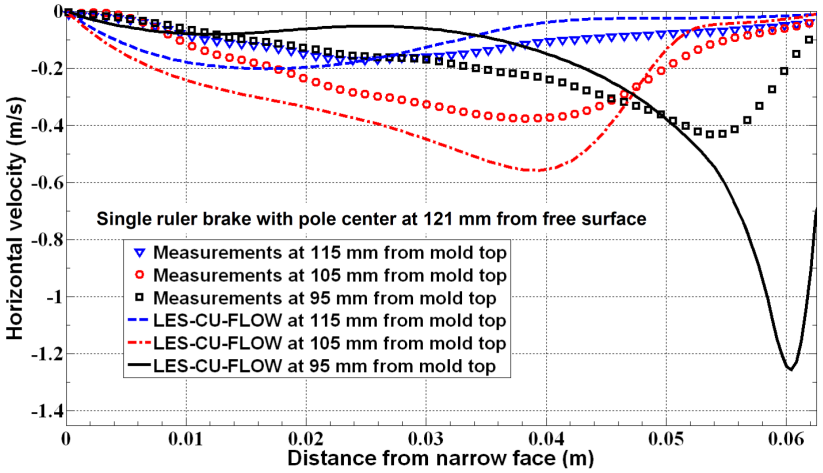

(c) Single ruler EMBr at 121 mm

Figure 8.3 Time-average horizontal velocity profiles comparing LES-CU-FLOW and ultrasonic Doppler velocimetry measurements [12-14] in 3 different cases, showing effect of EMBr.

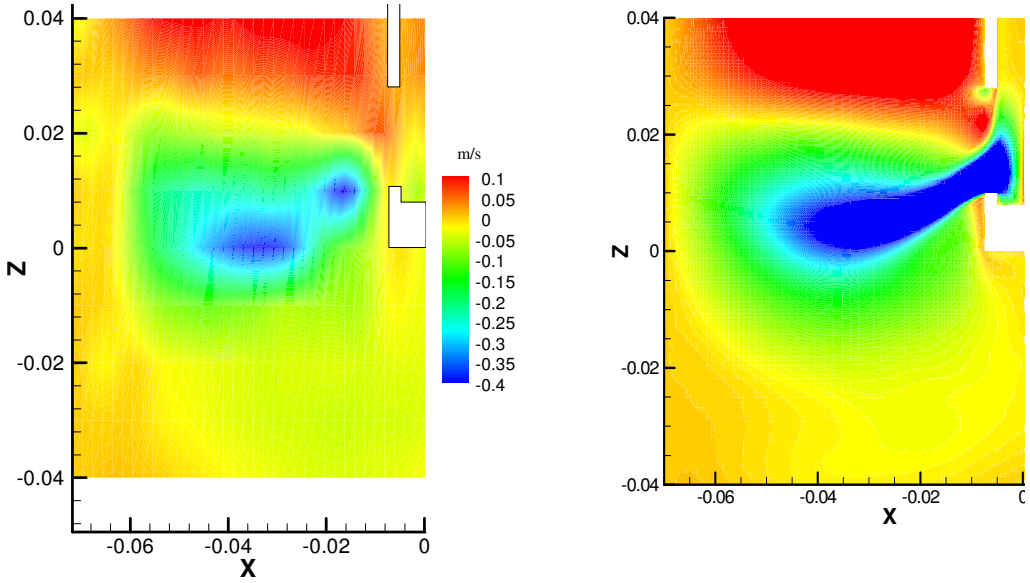

(i) Measurements [13]

(ii) LES-CU-FLOW

(a)

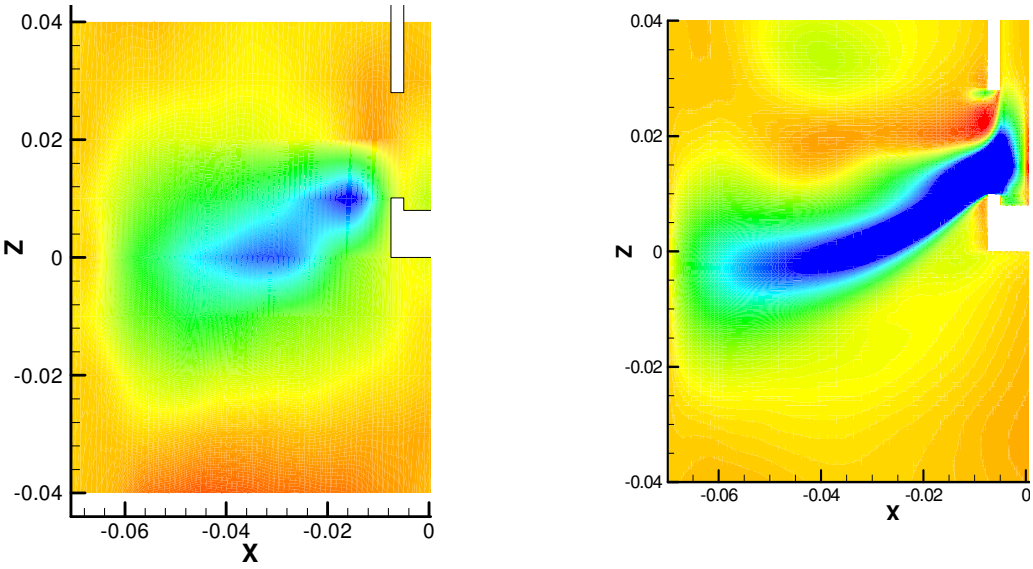

(i) Measurements [14]

(ii) LES-CU-FLOW

(b)

Figure 8.4 Time-average horizontal velocity contours comparing LES-CU-FLOW predictions and UDV measurements [13-14] with different magnetic field locations (a) Single ruler brake across nozzle (EMBr) centered 92 mm below free surface (b) Single ruler brake below nozzle (EMBr) centered 121 mm below free surface

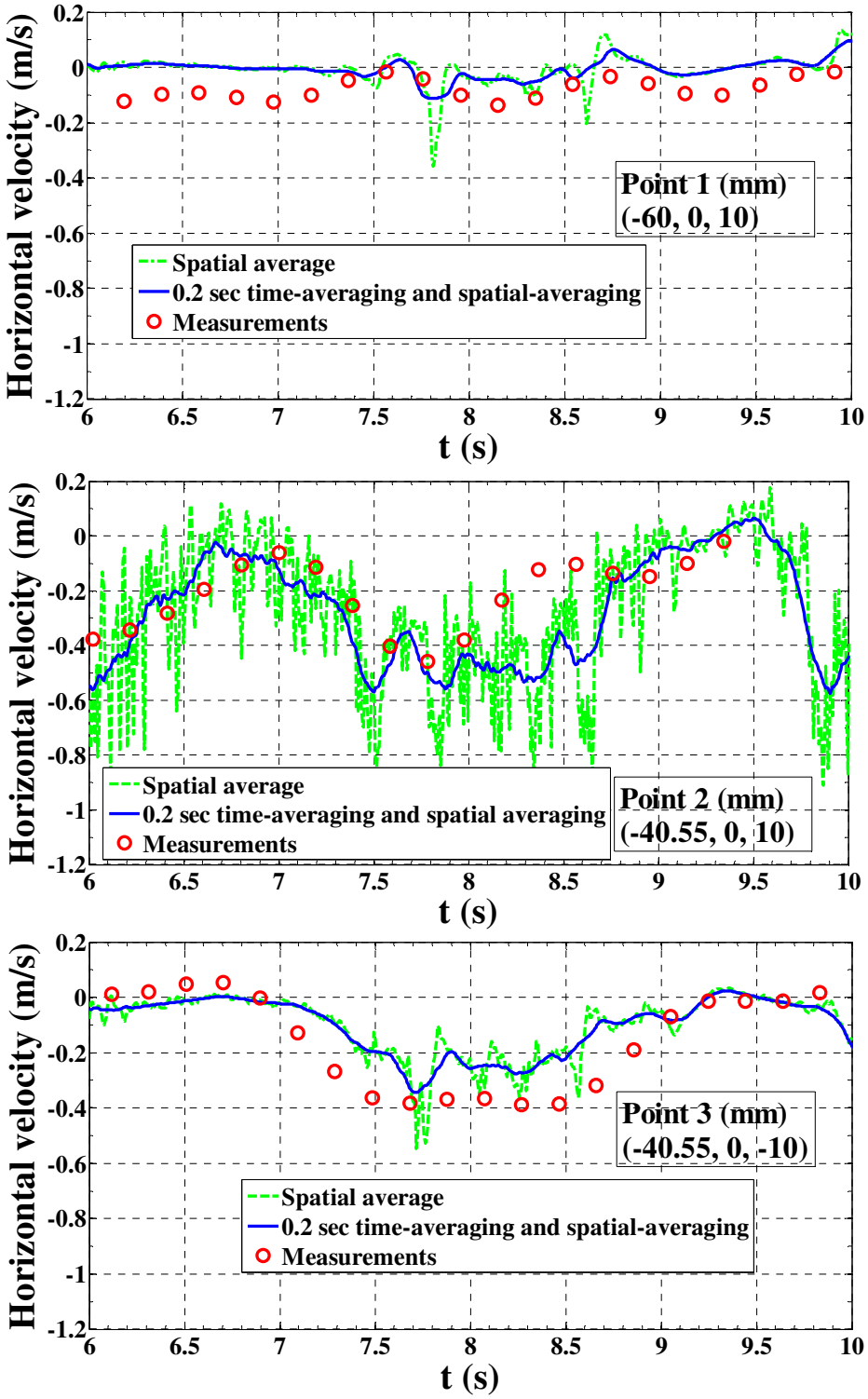

Figure 8.5 Transient horizontal velocity comparing LES-CU-FLOW predictions and measurements [13] with 92-mm EMBr at different points at mold midplane

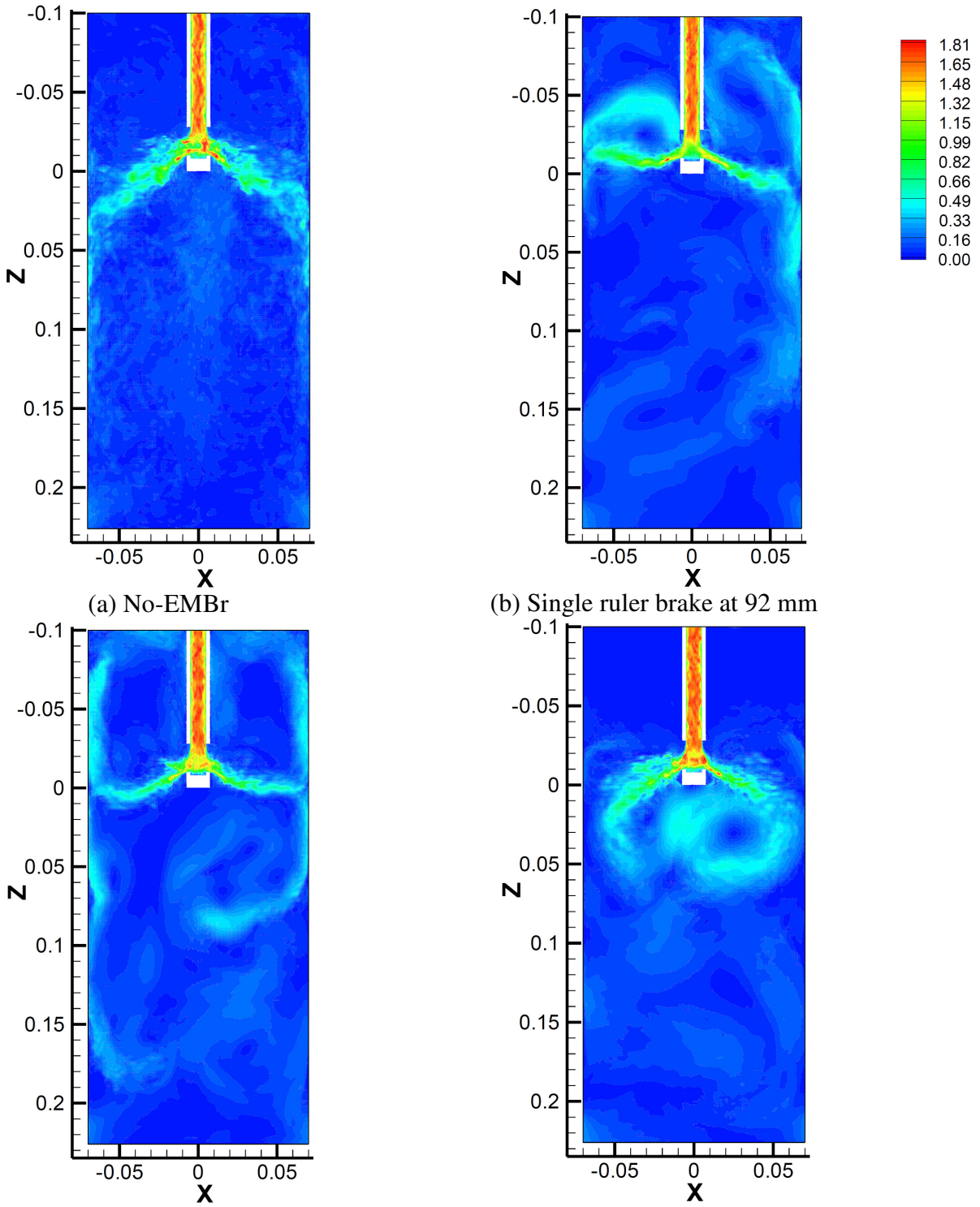

(a) No-EMBr

(b) Single ruler brake at 92 mm

(c) Single ruler brake at 121 mm
(i.e. 29 mm below 92 mm ruler in (d))

(d) Double ruler brake

Figure 8.6 Instantaneous velocity magnitude at mold mid-plane in different EMBr and non-EMBr cases

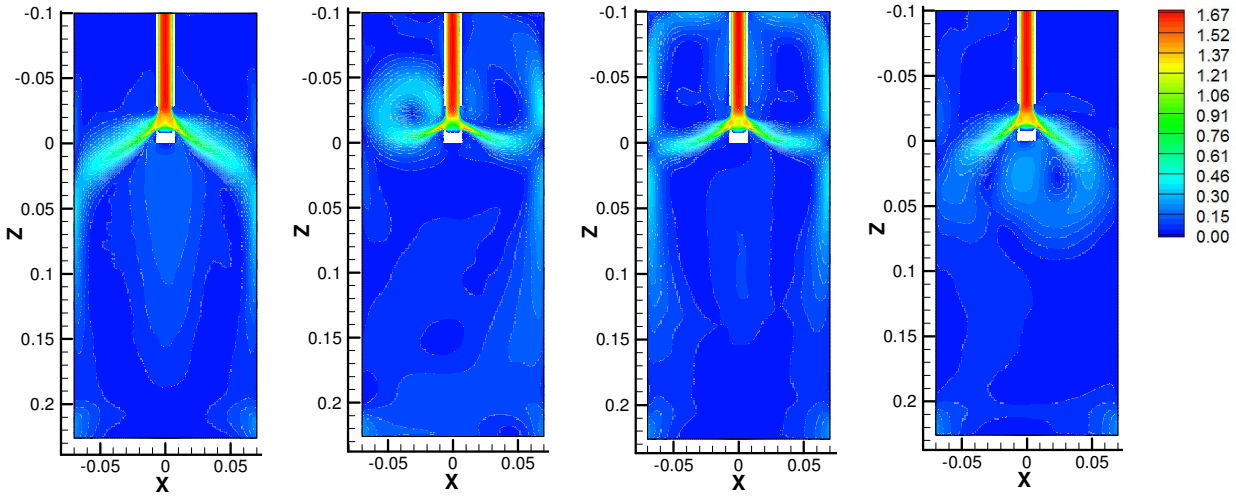

(a) No EMBr (b) 92-mm EMBr (c) 121-mm EMBr (d) Double ruler

Figure 8.7 Effect of magnetic field location and strength on time-averaged (~25 sec) velocity magnitude

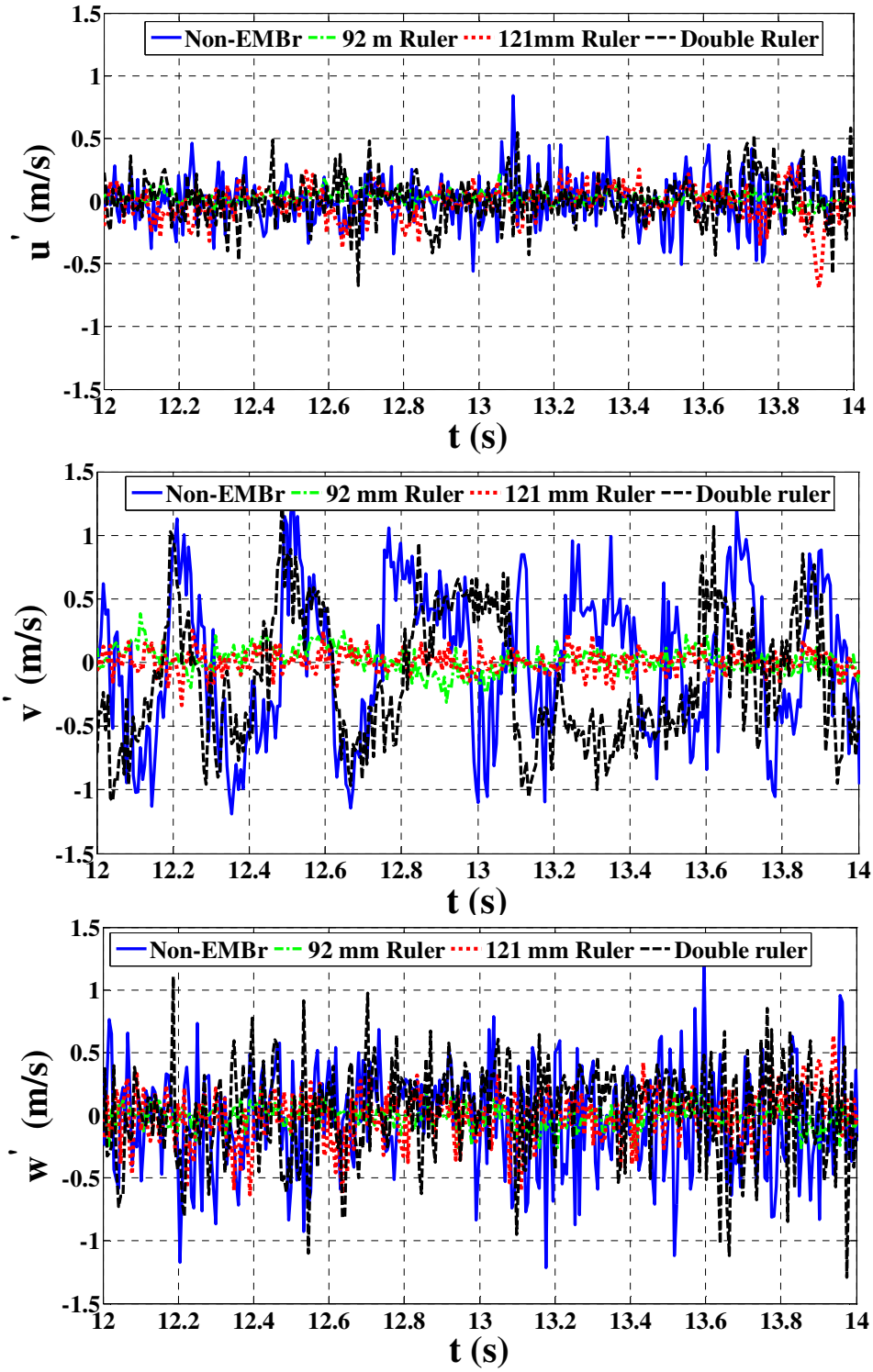

Figure 8.8(a) Three components of velocity fluctuations at the SEN bottom center (95 mm from mold top) in different cases.

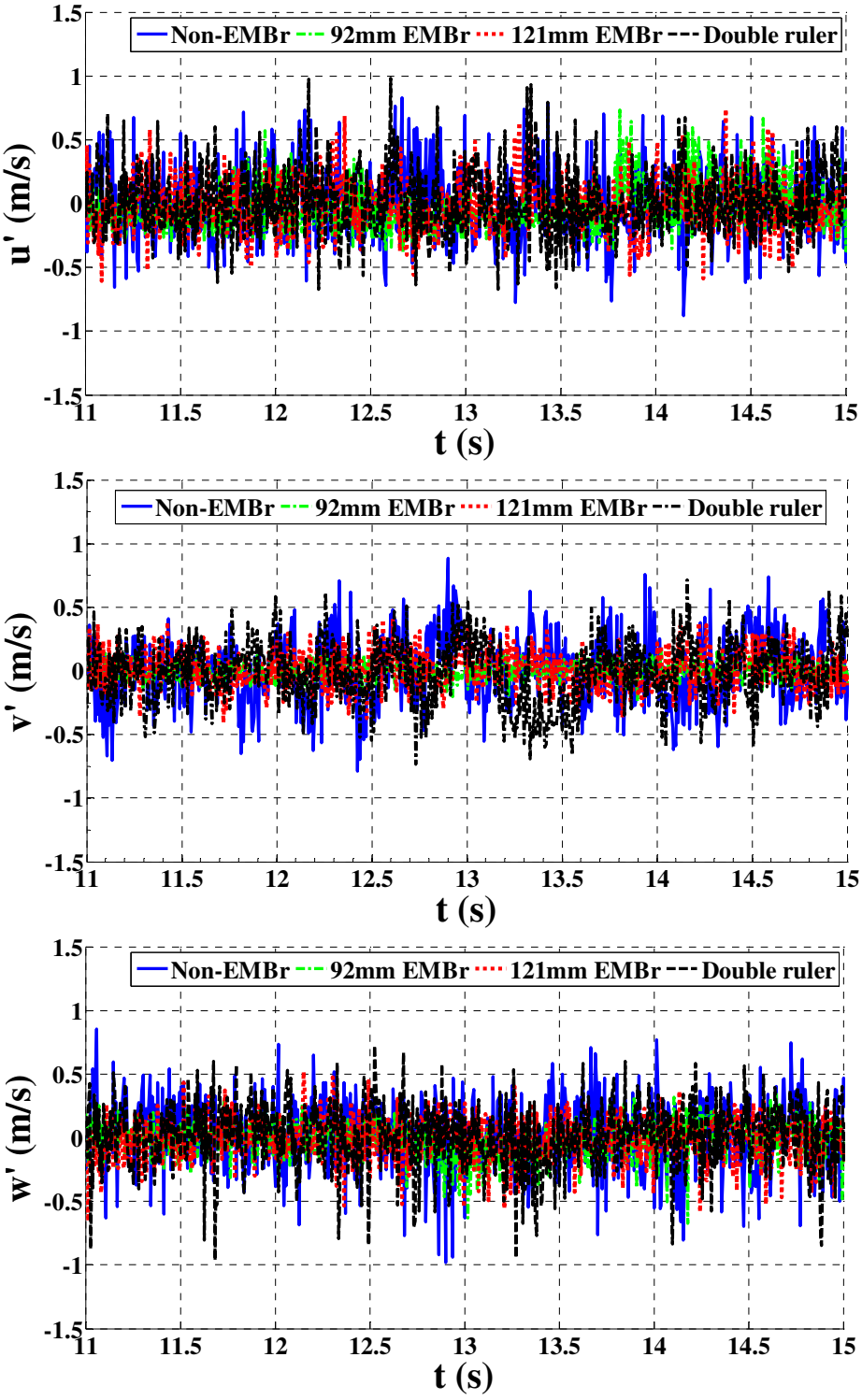

Figure 8.8(b) Three components of instantaneous velocity fluctuations in the mold midplane (95 mm from mold top and 58 mm from left NF)

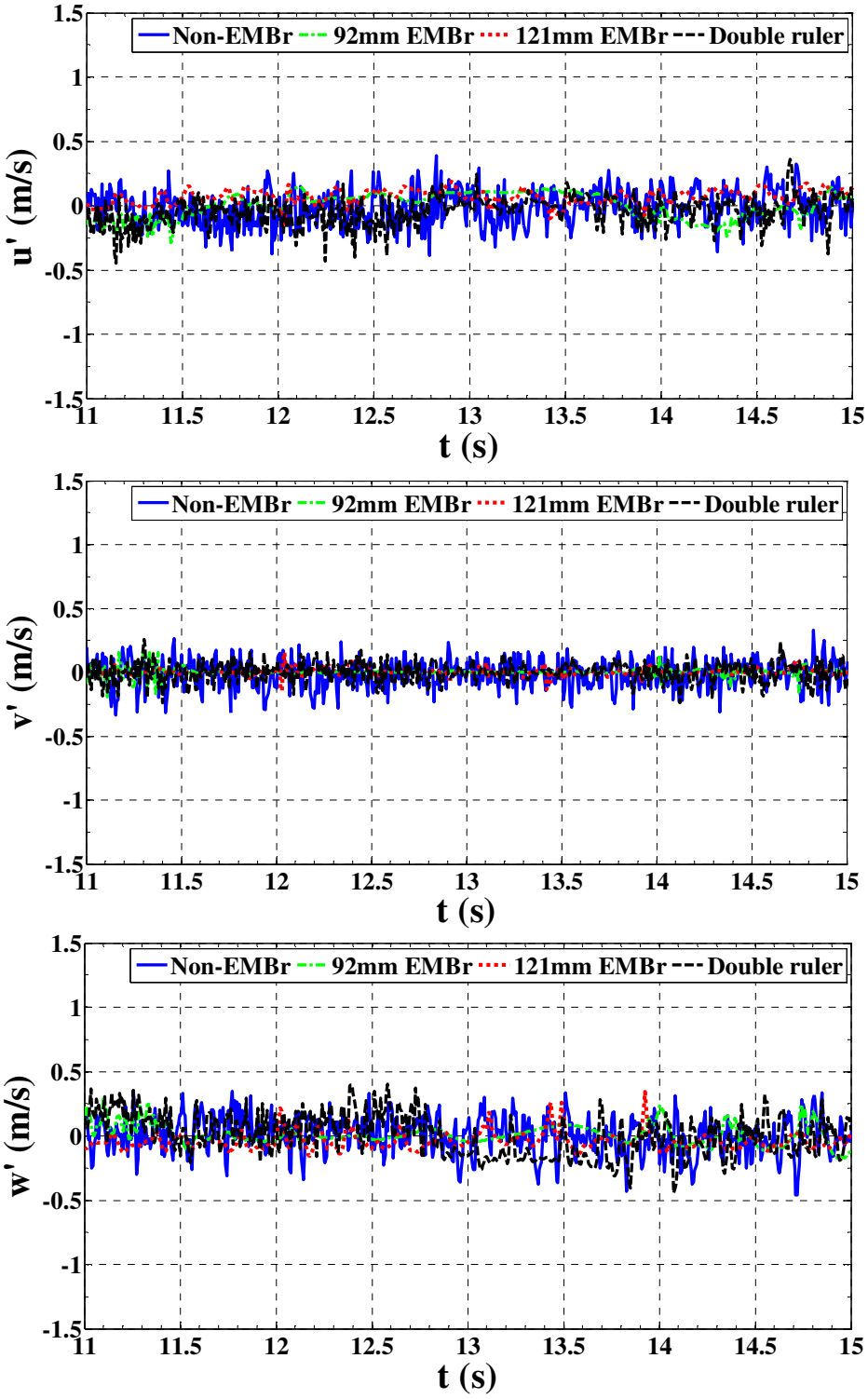

Figure 8.8(c) Three components of instantaneous velocity fluctuations in the mold midplane (115 mm from mold top and 29.45 mm from left NF)

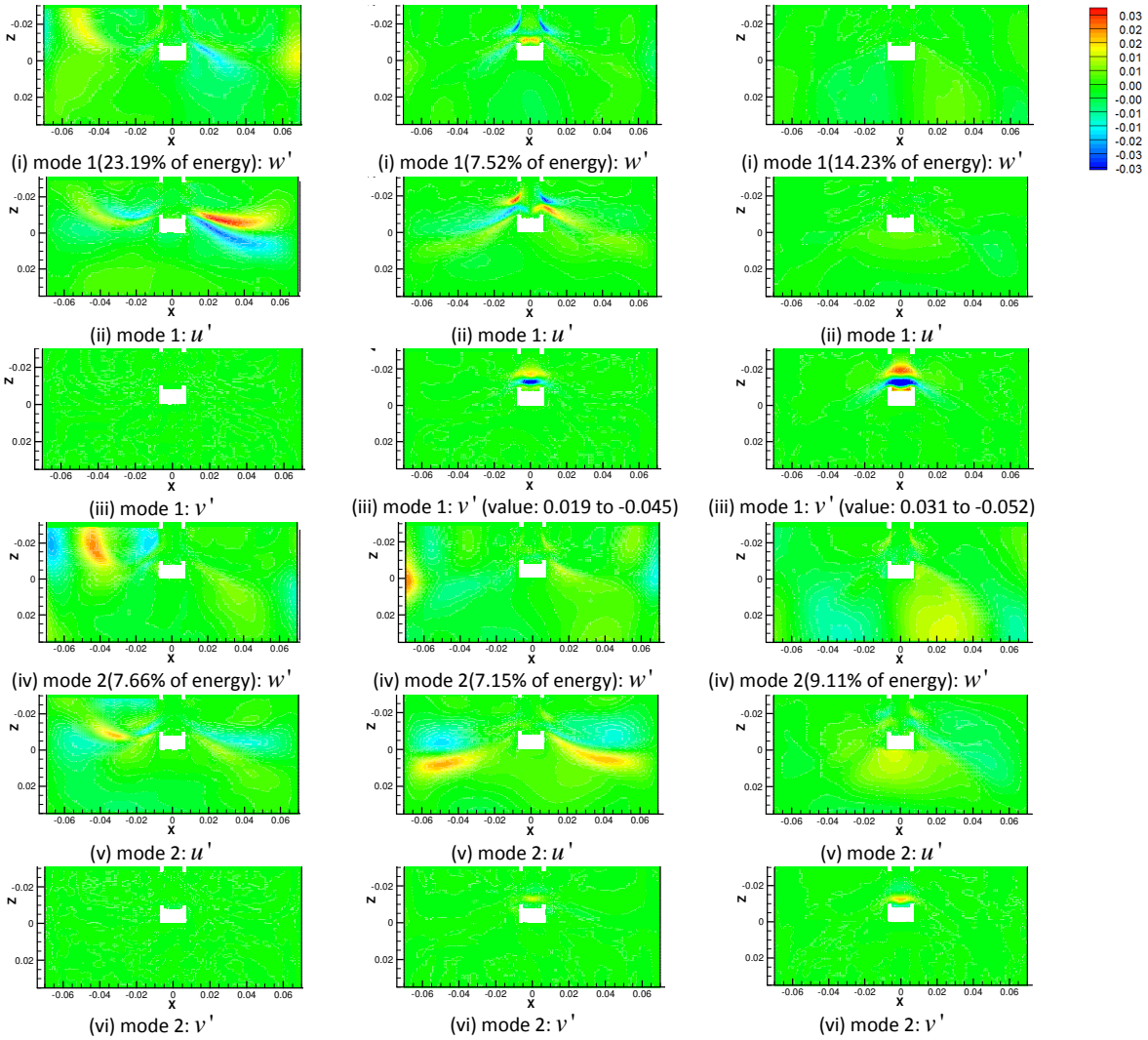

(a) 92mm EMBr (b) 121 mm EMBr (c) Double ruler

Figure 8.9 First two modes with corresponding velocity fluctuations

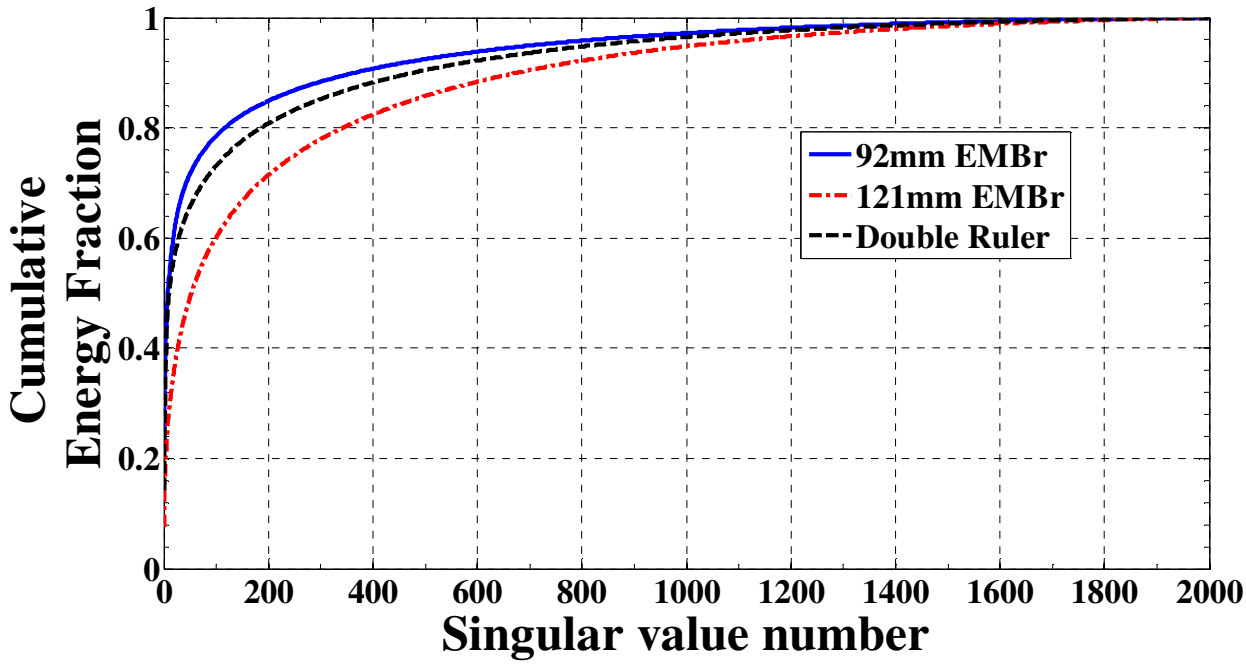

Figure 8.10 Cumulative energy fraction as a function of singular values

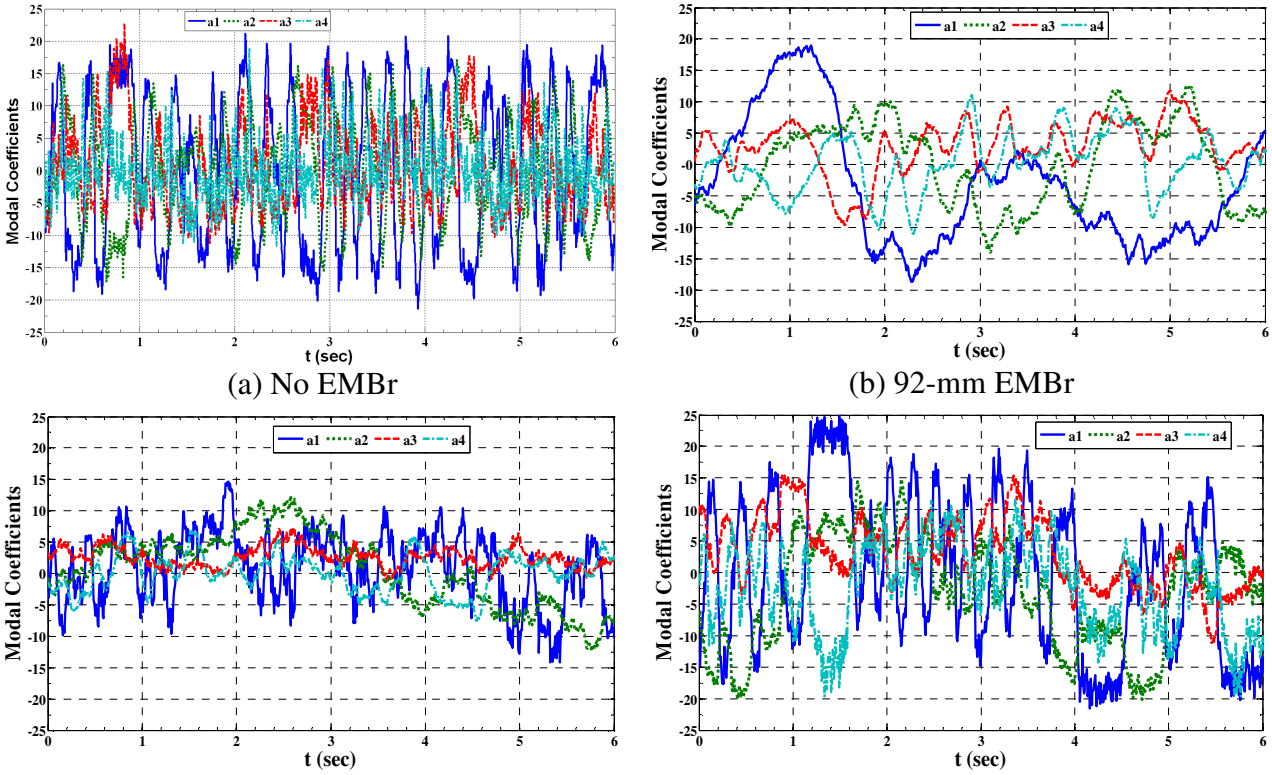

(a) No EMBr (b) 92-mm EMBr

(c) 121-mm EMBr (d) Double ruler

Figure 8.11 Temporal coefficients of first four modes in different cases

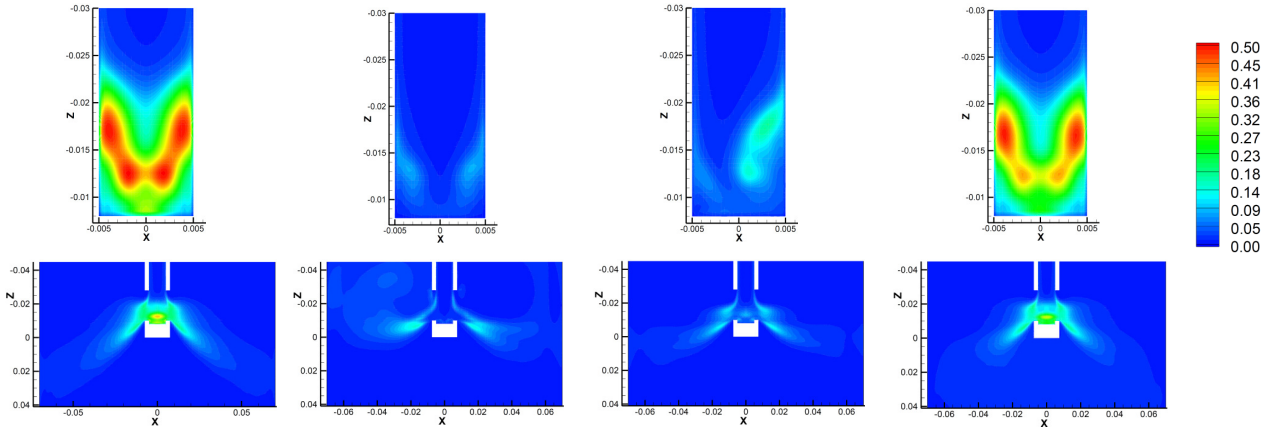

(a) No EMBr (b) 92-mm EMBr (c) 121-mm EMBr (d) Double ruler

Figure 8.12 Turbulent kinetic energy at mold mid-planes between wide faces (below) and between narrows faces inside nozzle (above) for 4 different cases

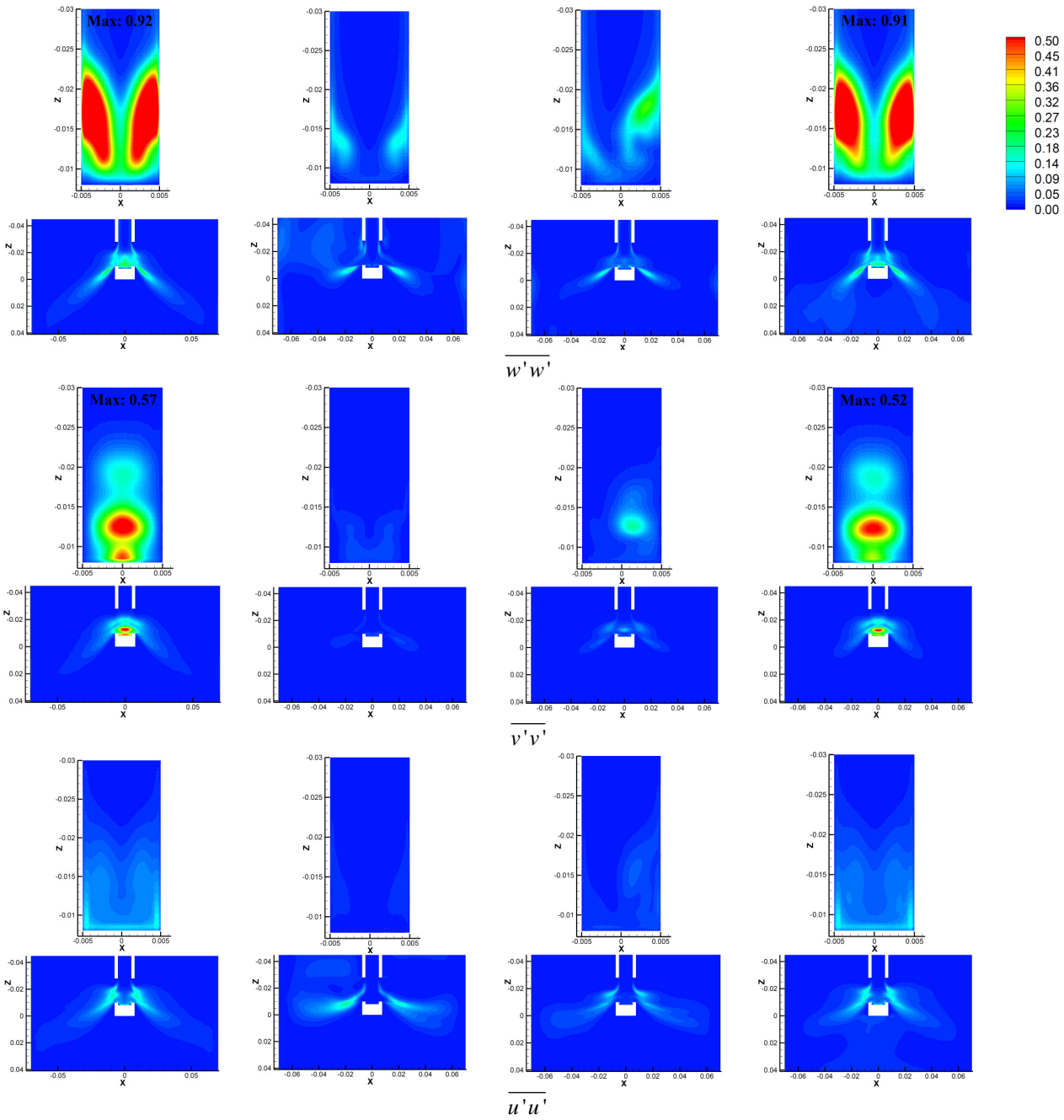

(a) No EMBr (b) 92-mm EMBr (c) 121-mm EMBr (d) Double ruler

Figure 8.13 Resolved Reynolds stresses at mold mid-planes between wide faces (below) and between narrows faces inside nozzle (above) for 4 different cases

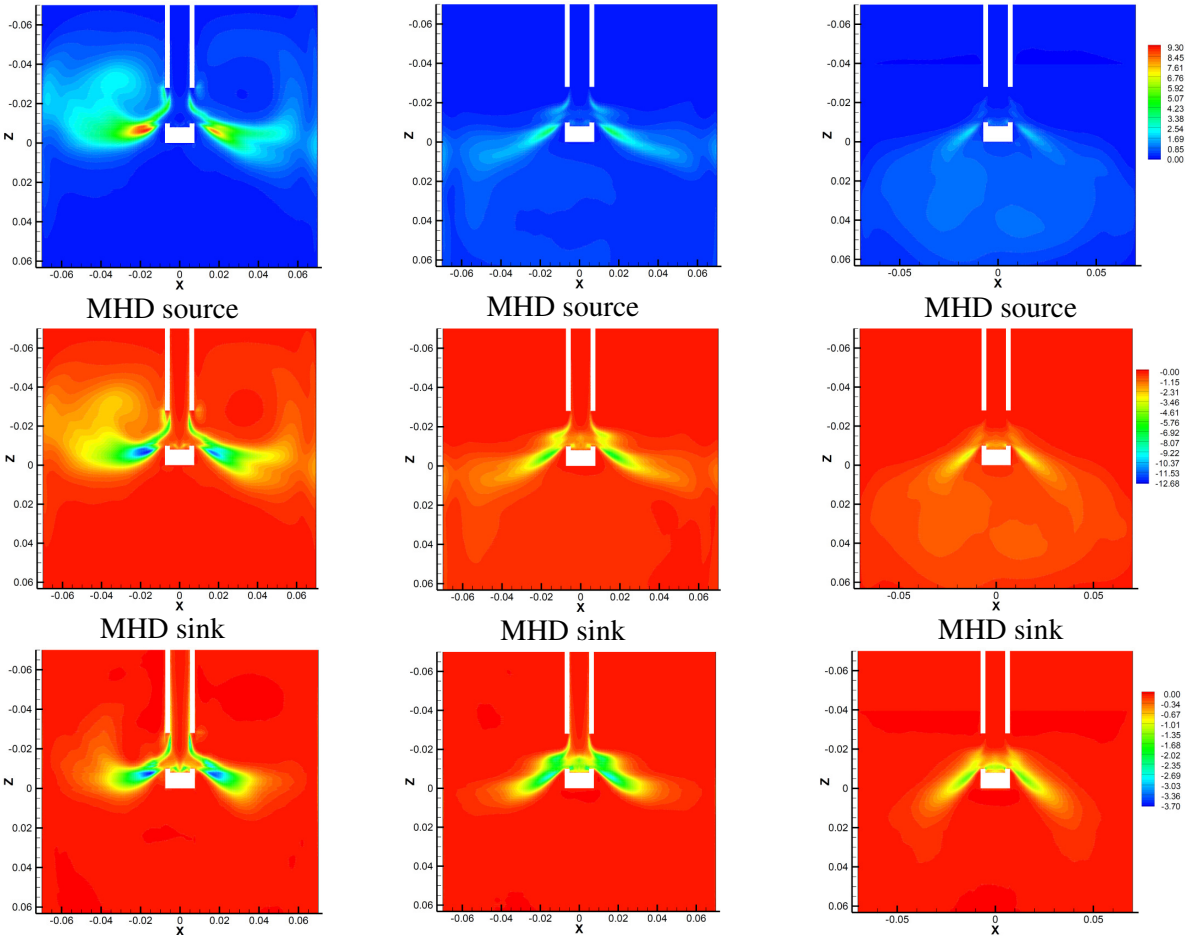

(a) Single-ruler brake at 92 mm (b) Single-ruler brake at 121 mm (c) Double ruler brake

Figure 8.14 Resolved MHD source, sink and net (source+sink) in TKE in different single/double ruler brake cases

8.9. References

1. B. G. Thomas, Fluid flow in the mold, Chapter 14 in Making, Shaping and Treating of Steel, 11th Edition, vol. 5, Casting Volume, Editor: A. Cramb, AISE Steel Foundation, Oct. 2003, Pittsburgh, PA, pp. 14.1-14.41.
2. L.C. Hibbeler, R. Liu, and B.G. Thomas, "Review of Mold Flux Entrainment Mechanisms and Model Investigation of Entrainment by Shear-Layer Instability." Proceedings of the 7th European Conference on Continuous Casting, 27 June - 1 July 2011, Dusseldorf, Germany.
3. Thomas, B. G. and L. Zhang, "Review: Mathematical Modeling of Fluid Flow in Continuous Casting of Steel", ISIJ International, 2001, Vol. 41, No. 10, pp. 1181-1193.
4. Q. Yuan, S. Sivaramakrishnan, S.P. Vanka and B. G. Thomas, Computational and experimental study of turbulent flow in a 0.4 scale water model of a continuous steel caster, Metall. Mat. Trans. B, 2004, vol. 35B, pp. 967-982.
5. Q. Yuan, B. G. Thomas and S. P. Vanka, Study of transient flow and particle transport in continuous steel caster molds: Part I. Fluid flow, Metall Mat. Trans. B, 2004, vol. 35B, pp. 685-702.
6. B. Zhao, B. G. Thomas, S. P. Vanka and R. J. O'Malley, Transient fluid flow and superheat transport in continuous casting of steel slabs, Metall. Mat. Trans. B., 2005, vol. 36B, pp. 801-823.
7. R. Liu, W. Ji, J. Li, H. Shen, and B. Liu, Numerical simulation of transient flow patterns of upper rolls in continuous slab casting moulds, Steel Research Int., 2008, 79, no. 8, pp. 50-55.

8. R. Chaudhary, C. Ji, B. G. Thomas, and S. P. Vanka, Transient turbulent flow in a liquid-metal model of continuous casting, including comparison of six different methods, Metallurgical and Materials Transactions B, In-Press, April 2011.

9. Z.-D. Qian and Y.-L. Wu, Large eddy simulation of turbulent flow with the effects of DC magnetic field and vortex brake application in continuous casting, ISIJ International, 2004, vol. 44, no. 1, pp. 100-107.

10. R. Kageyama and J. W. Evans, Development of a Three Dimensional Mathematical Model of the Electromagnetic Casting of Steel, ISIJ Int., 42, 2, 2002, pp. 163-170.

11. Y. Miki and S. Takeuchi, Internal Defects of Continuous Casting Slabs Caused byAsymmetric Unbalanced Steel Flow in Mold, ISIJ Int., 43, 10, 2003, pp. 1548-1555.

12. K. Timmel, S. Eckert, G. Gerbeth, F. Stefani, and T. Wondrak, Experimental modeling of the continuous casting process of steel using low melting point alloys – the LIMMCAST program, ISIJ International, 2010, 50, No. 8, pp. 1134-1141.

13. K. Timmel, S. Eckert, and G. Gerbeth, Experimental investigation of the flow in a continuous-casting mold under the influence of a transverse, direct current magnetic field, Metall. Mat. Trans. B, 2011, vol. 42, 1, pp. 68-80.

14. K. Timmel, X. Miao, S. Eckert, D. Lucas, and G. Gerbeth, Experimental and numerical modeling of the steel flow in a continuous casting mould under the influence of a transverse DC magnetic field, Magnetohydrodynamics, 2010, vol. 46, 4, pp. 337-448.

15. S. B. Pope, Turbulent Flows, 2000, Cambridge University Press, Cambridge, United Kindom.

16. J. O. Hinze, Turbulence, McGraw-Hill Publishing Company,1975, NewYork.

17. F. Nicoud and F. Ducros, Subgrid-scale stress modeling based on the square of the velocity gradient tensor, Flow, Turbulence and Combustion, 1999, vol. 63(3), pp. 183-200.

18. R. Chaudhary, S.P. Vanka and B.G. Thomas, Direct numerical simulations of magnetic field effects on turbulent flow in a square duct, Phys. of Fluids, 22, 075102, 2010.

19. R. Chaudhary, A.F. Shinn, S. P. Vanka and B. G. Thomas, Direct Numerical Simulations of Transverse and Spanwise Magnetic Field Effects on Turbulent Flow in a 2:1 Aspect Ratio Rectangular Duct, Computers & Fluids, Submitted, Nov. 2010.

20. M. H. Baba-Ahmadi and G. Tabor, Inlet conditions for LES using mapping and feedback control, Computers & Fluids, 38, 6, 2009, pp. 1299-1311.

21. H. Werner and H. Wengle, Large-eddy simulation of turbulence flow over and around a cube in a plate channel, in 8^{th} symposium on turbulent shear flows, 1991, Munich, Germany.

22. A. Sohankar, C. Norberg, and L. Davidson, Low-Reynolds-number flow around a square cylinder at incidence: Study of blockage, onset of vortex shedding and outlet boundary condition, Int. J. for Num. Meth. in Fluids, 26, 1998, pp. 39-56.

23. R. Moreau, Why, How and When MHD Turbulence Becomes Two-Dimensional, Liquid Metal Flows and Magnetohydrodynamics, Progress in Astronautics and Aeronautics, Vol. 84, Edited by H. Branover, P. S. Lykoudis, and A. Yakhot, American Institute of Aeronautics and Astronautics, Inc., New York, 1981.

CHAPTER 9. CONCLUSIONS AND FUTURE SCOPE

This chapter summarizes the findings on each chapter (Section 9.1 to 9.7) followed by overall conclusions and future scope given in sections 9.8 and 9.9 respectively.

9.1. DNS of Magnetic Field Effects on Turbulent Channel and Square Duct Flows

Direct numerical simulations have been performed to investigate the effects of a magnetic field on turbulence in channel and square duct flows. Initially, the code is validated with previous DNS databases and analytical solutions in non-MHD and MHD turbulent channel flows, non-MHD square duct and laminar MHD square duct flows. Subsequently, the simulations in a MHD square duct were performed with two domain sizes (1x1x2π and 1x1x16) and three grids (64x64x128, 80x80x256, and 128x128x512).

The magnetic field altered axial and secondary flows significantly. Secondary flows create strong bulging of axial velocity close to the top and bottom walls. In the regions close to the top and bottom walls, the strong current density perpendicular to the magnetic fields suppresses turbulence (all components of Reynolds stresses) strongly. Close to the side walls the effect of magnetic field is weak due to the current being parallel to field.

Auto-correlation of axial velocity fluctuations suggested that a domain length of ~5D is enough for capturing the longest scales of turbulence. Streaky structures get concentrated and elongated along streamwise direction under the influence of a transverse magnetic field. Streamwise vorticity is suppressed directly by the magnetic field via the first derivative of horizontal velocity and indirectly via second derivatives of Reynolds normal and shear stresses, but more strongly via Reynolds normal stresses ($\overline{u'u'}$, $\overline{v'v'}$). The magnetic field produces a sink

as well as a source to turbulent kinetic energy. Their variations along the bisectors are similar but the sink is stronger and causes a net reduction of turbulence due to a magnetic field. The above behavior of turbulence under magnetic field suggests an immense potential for non-intrusive control of heat, mass and momentum transfer characteristics in these geometries.

9.2. DNS of Transverse and Spanwise Magnetic Field Effects on Turbulent Flow in a 2:1 Aspect Ratio Rectangular Duct

This chapter presents the extension of MHD channel and square duct DNS work in a 2:1 aspect ratio rectangular duct. The calculations are performed by fixing Re_τ=170 with two orientations and two strengths (Ha=6.0 and 8.25) of magnetic field. The results revealed new insights about the effects of magnetic field orientation and strength on turbulence.

Unlike the square duct, the non-MHD 2:1 aspect duct does not have corner bisector symmetry for secondary flows and axial velocity. The secondary flows are focused close to side walls. The vortices of secondary flows are more rounded close to narrow sides and are elongated in the vicinity of the broad sides. As compared to square duct that has two diagonal symmetric vortices, three vortices are observed in every quadrant in non-MHD 2:1 aspect duct.

In the case of a MHD flow in a 2:1 aspect ratio duct, the horizontal magnetic field suppresses turbulence close to side walls and in the core. The vertical magnetic field has an effect close to top and bottom walls and in the core. The effect of magnetic field is much stronger in the case of a vertical magnetic field (i.e. field perpendicular to broader wall) and therefore can be a more effective orientation to suppress turbulence. Similar to non-MHD duct, with a weaker magnetic field, three vortices are observed in every quadrant. Increasing the magnetic field increases the number of vortices.

Both orientations of magnetic field suppress secondary flows with horizontal field giving elongation of the secondary flows close to the side walls and the vertical field giving elongation close to the top and bottom walls. The elongation close to the side walls causes bulging in axial velocity which is not observed close to top and bottom walls perhaps due to the larger width. This bulging in axial velocity was also seen previously in the MHD square duct with a magnetic field. The horizontal magnetic field is more effective in suppressing and reorganizing secondary flows.

The MHD source and sink terms in the TKE budget equation have similar profiles but the sink term is stronger and thus the net effect is the suppression of the turbulence. These terms are of great importance as they can be used to formulate a model for the effect of magnetic field on turbulence for RANS and LES based turbulence models. Application of a magnetic field reduces the formation of the low-speed streaks with the vertical field having a greater effect as compared to the case of a horizontal magnetic field.

Although, this work only considered 2:1 aspect duct but we expect similar behavior at higher aspect ratios perhaps with more secondary flow vortices across the cross-section.

Tailoring the magnetic field to control turbulence, secondary flows, and streaky structures can be of great practical importance in controlling mixing characteristics of the turbulent flow in different regions of a flow domain. Overall, this work gives an idea of the behavior of turbulent flows with two orientations of magnetic fields and supplies a DNS database for future model development through a rectangular 2:1 aspect ratio duct.

9.3. Evaluation of Turbulence Models in MHD Channel and Square Duct Flows

This work evaluates several k-ε and Reynolds stress models for their ability to predict turbulent flow under external magnetic field in channel and square duct. The existing DNS databases were used for evaluations. The additional source terms required to incorporate the effect of magnetic field on turbulence, as proposed by Kenjereš and Hanjalić, were implemented through UDFs in FLUENT. The performance of these models, on the basis of their predictions of mean velocities, RMS of velocity fluctuations, TKE, MHD sources and frictional losses can be summarized as follows:

In both high- and low-Re channel flows, all of the models predicted mean axial velocity reasonably well (within 5% error), given fine-enough grids for grid-independence (EWT and low-Re) or satisfaction of the y+ requirements (SWF and NEWF). However, the TKE was much less accurate, often exceeding 60% overprediction in the core. In high-Re channel flows, models underpredicted near-wall peak turbulence energy whereas in low-Re channel flows, they showed better agreement near the wall but over-predicted values in the core. For the MHD flows, the implementation of the MHD sources improved predictions for low-Re k-ε models. The high-Re models which use the wall treatments did not show much improvement with MHD sources, perhaps due to the lack of MHD effects in the wall formulations.

In the case of low-Re square duct flows, the models tested did not predict the mean axial velocities to a good accuracy (error ranging ~8-30%) because of the secondary flows generated due to turbulence anisotropy. The TKE was overpredicted in the core, often exceeding ~60%, by all models except LB in MHD duct. The effect of turbulence suppression by magnetic field was not properly captured on mean velocity, Reynolds stresses/turbulent kinetic energy and frictional

losses by any single model in a MHD duct, even after inclusion of the MHD sources of turbulence.

For problems involving high-Re, the SKE model offers reasonable accuracy at low computational cost. Adding EWT improves accuracy slightly over standard wall laws, but significantly increases cost. For flows with low-Re number, the Lam-Bremhorst (LB) low-Re k-ε model performed better than the others in both hydrodynamic and magnetic field influenced turbulent flows. Given the need to compute complex industrial flows with efficient computational use, using these 2 models with appropriate changes for magnetic field effects provides a reasonable compromise of accuracy and speed. Finally, the RSM-LPS model with EWT offers similar accuracy with the added ability of capturing turbulence anisotropy and secondary flows, but its computational cost is very high.

9.4. Transient Mold Fluid Flow with Well- and Mountain-Bottom Nozzles in Continuous Casting of Steel

This work combines a three dimensional steady state k-ε turbulence model with PIV and transient impeller velocity measurements to investigate and compare the flow quality produced by well- and mountain-bottom type nozzles into the mold cavity. The predicted velocities and turbulent kinetic energy at the free surface and in the jet region were found matching well with the measurements.

The jet from the well-bottom nozzle is thicker, steeper and more diffusive as compared to mountain-bottom nozzle. The mountain-bottom nozzle produces a thinner jet with low frequency asymmetrical behavior in short time intervals. The frequencies of velocity fluctuations were found to be decreasing from jet to the top free surface. The mountain bottom produced ~50% higher surface velocity than well-bottom. This higher velocity combined with low frequency

surface level variations may be detrimental to the steel quality as it may shear off liquid slag into the steel causing sliver defects in the final steel product. Based upon this work, well-bottom nozzle is recommended over mountain-bottom.

9.5. Effect of Stopper-Rod Misalignment on Fluid Flow in Continuous Casting of Steel

Steady k-ε model and instantaneous velocity measurements performed using impeller velocity probe are used together in a $1/3^{rd}$ scale water model to investigate the effect of stopper-rod misalignment on fluid flow in the nozzle and mold of a continuous casting process. The model predictions matched velocity and turbulent kinetic energy measurements very well and revealed new insights about the effect of stopper rod misalignment on fluid flow in continuous casting.

In case of aligned stopper position, flow field and vortices showed both right-left and front-back symmetries within the standard deviation of measurements. In front misaligned stopper position, flow from bigger opening side at UTN hits the nozzle bottom towards the front before exiting the nozzle ports towards the back side in the mold cavity. This behavior in the nozzle causes front-back asymmetric flow in the mold cavity. Left misaligned stopper-rod causes strong right-left asymmetric flow in the mold. The right side jet is shallower with higher flow rate, so produces higher surface velocity on the right side. The asymmetry in the surface velocity is stronger close to SEN.

Instantaneous vortices form in all cases with similar frequencies on the right and left in the aligned and front-misaligned cases. Turbulence is mainly responsible for these. Left misalignment of stopper generates significantly higher surface velocity on the right thus causing more vortices to form on the left; especially close to SEN.

Overall this study reveals the importance of the stopper rod misalignment in continuous casting. Misaligned stopper-rod causes significant flow asymmetries and increases the formation of detrimental vortices which may entrain liquid slag into molten steel to cause expensive defects.

9.6. Transient Turbulent Flow in a Liquid-Metal Model of Continuous Casting, Including Comparison of Six Different Methods

This work combines various transient (LES, filtered URANS) and steady-state (SKE and RKE) computational models with measurements in a liquid metal GaInSn model to investigate turbulent flow in the nozzle and mold of a typical continuous casting process.

LES predictions of time-averaged horizontal velocity match very well with the measurements, except where limitations in the measurements give unreasonably lower values close to the SEN and narrow face walls. Time and spatial averaging of the LES predictions to match the experimental resolution of <5Hz produces transient velocity histories that match closely with the measurements. Spectral analysis of the LES predictions confirms a large range of velocity fluctuation frequencies near the SEN (up to ~300Hz, for 2 orders of magnitude drop in energy) and close to narrow face (up to ~30Hz, for 2 orders of magnitude drop in energy. The fluctuation energy generally drops with distance from the nozzle, especially at the higher frequencies.

LES-CU-FLOW was the best model, with better accuracy than LES-FLUENT, owing to its higher resolution with a ~5 times finer mesh, and tremendously better computational efficiency, owing to its better numerics and use of a GPU methodology. The “filtered” URANS model performed in between LES and steady RANS, missing the high-frequency fluctuations, but capturing the long-time variations associated with large structures. .The RANS models matched time-averaged velocity closely in the nozzle, but greatly underpredicted turbulence

exiting the ports. This caused mismatches in the mold, especially with turbulence, so caution is needed when using steady RANS models. Among steady RANS models, SKE performed better than RKE.

The flow pattern is a stable, classic double-roll flow pattern, controlled by the strong turbulent nature of the flow structures in the bottom of the nozzle. The resolved Reynolds stresses and TKE show strong fluctuations in vertical velocity ($\overline{w'w'}$) and velocity normal to wide faces ($\overline{v'v'}$) associated with alternating directions of swirl in the bottom of the nozzle, and with wobbling of the jet in the mold. A POD analysis further reveals that the strongest transient flow structures are associated with nozzle bottom swirl and jet wobbling. The modes associated with this swirl contained 22% of the fluctuation energy. To control turbulence in the mold, it is important to control these modes.

9.7. Effect of Electromagnetic Ruler Braking (EMBr) on Transient Turbulent Flow in Continuous Slab Casting using Large Eddy Simulations

The current work studies the effects of electromagnetic braking with the help of a transient large eddy simulation model and ultrasonic Doppler velocimetry measurements in a small scale GaInSn model of continuous casting process. The model predictions matched measurements very well for velocities and overall flow patterns while capturing interesting effects of the braking on transient and time-average flow fields.

Magnetic field suppressed turbulence in the nozzle and mold leading to large scale vortical structures whose axis are aligned with the magnetic field. These vortices show tendency towards 2-D turbulence. Similar behavior was reported by Timmel et al. in their measurements. The suppression of turbulence in the nozzle leads to the suppression of nozzle bottom swirl and its alternation. Due to this reason, the mixing effect in the mold reduces and jet comes out of the

ports as straight laminarized and causing large scale variations in the mold in terms of horizontal velocities. Stronger the magnetic field at the nozzle-bottom well, the larger and long terms transients are generated in the mold. The alignment of magnetic field is important in such cases where a stronger magnetic field is applied at the port and jet regions. The slightly asymmetric magnetic field on right and left when combined with large scale variations in such cases may cause fully biased flow in the mold. As the intensity of magnetic field goes down at nozzle bottom, the flow sustains turbulence and related mixing leading to a more stabilized jet. The jet shows largest scales in 92 mm EMBr case followed by in 121mm EMBr case. The flow in 121mm EMBr location although has smaller scales than 92mm case but due to jet hitting the narrow faces, this case has higher surface velocity. The flow is found to be most stable either with non-EMBr case or with double ruler brake where field is weakest at nozzle bottom and thereby the turbulence suppression is weakest at the nozzle bottom and alternation of swirl sustains mixing leading to a stable jet. The double ruler brake bends the jet in the lower region and causing right-left alternating circulation below nozzle.

Overall, this work suggests the importance of the location and of the strength of electromagnetic braking in continuous casting nozzle and mold. Stronger magnetic field should be avoided at the nozzle bottom and jet regions to avoid large scale variations.

9.8. Overall Summary and Conclusions

This thesis studied turbulent flows in canonical (channel, square and rectangular duct) as well as nozzle and mold geometries of the continuous casting process with and without magnetic field. In the first stage of this thesis, a GPU based CFD code (CU-FLOW) is extended and used to perform direct numerical simulations of the effect of magnetic field on turbulence in channel, square and 2:1 rectangular ducts. Important features of mean flow and turbulence under the

influence of magnetic field are revealed besides providing DNS database for future RANS and LES model development. Thereafter, the various RANS models (k-ε and Reynolds stress transport) models are tested for their performance with DNS databases in channel and the square duct flows with and without magnetic field. This work gave better understanding on the performance of these models in two-wall bounded MHD and non-MHD turbulent flows. This work will be helpful in selecting these models towards their usage in continuous casting as well as in other areas.

In the second stage of the work, the steady-state k-ε model is combined with the PIV and impeller probe velocity measurements in a $1/3^{rd}$ scale water model to study the flow quality coming out of the well and mountain-bottom nozzles. The mountain-bottom nozzle was found more prone to the longtime asymmetries and higher surface velocities. Later, the same k-ε model was extended with water model measurements to analyze the effect of stopper-rod misalignment on the fluid flow in the mold cavity. The misaligned stopper-rod caused flow asymmetry which was more pronounced close to the nozzle. The left misalignment caused higher surface velocity on the right leading to significantly large number of vortices forming behind the nozzle on the left.

Finally, the transient and steady-state models such as LES, filtered URANS and steady RANS models (Standard k-ε and Realizable k-ε) are combined with ultrasonic Doppler velocimetry measurements in a GaInSn model of continuous casting process. The steady RANS and URANS calculations were performed using FLUENT. The LES calculations were performed using CU-FLOW as well as FLUENT. CU-FLOW resolved turbulence more accurately owing to finer mesh and smaller timestep. The CU-FLOW was found more than two orders of magnitude faster than FLUENT. This work revealed new insights on the performance of these models in a

typical continuous casting process. The behavior of instantaneous flows, Reynolds stresses and POD analysis quantified the nozzle bottom swirl and its importance on the turbulent flow in the mold.

The above work is further extended in GaInSn model with the effect of electromagnetic braking to help optimize a ruler type brake and its location for the continuous casting process. LES-CU-FLOW model matched time-average and instantaneous measured velocities for two locations of the brake. This work revealed interesting and new understanding on the effect of magnetic field on turbulent flow in the nozzle and mold of a typical continuous casting process. The magnetic field suppressed turbulence and promoted vortical structures with their axis aligned with the magnetic field. This behavior suggests the tendency towards 2-d turbulence. The stronger magnetic field at the nozzle well and around the jet region created large scale and lower frequency flow behavior by suppressing nozzle bottom swirl and its front-back alternation. As the intensity of magnetic field at nozzle bottom reduced flow become more and more stable. Based on this work, it is advised to avoid a strong magnetic field around the jet and nozzle bottom so as to get more stable and less defect prone flow.

9.9. Future Research

The LES-CU-FLOW may be used to simulate the effect of electromagnetic braking on turbulent flows in a full scale steel caster. The effect of shell solidification can be incorporated by adding mass and momentum sinks in the liquid at the solid-liquid interface. Since solidified steel shell will become part of the computational domain therefore the equation for electric potential needs to be solved in the shell by maintaining continuity of current at the solid-liquid interface. The current work focused on static magnetic fields; however CU-FLOW can also be extended to

time-changing magnetic fields (electromagnetic stirring) by solving a transport equation for the induced magnetic field.

The model considered in CU-FLOW is isothermal and single phase. The code may also be extended for heat transfer and multiphase Lagrangian inclusions and argon gas transports. This way CU-FLOW can be developed as a full 3-d transient heat-multiphase (Argon and inclusion transport)-EMBr turbulent flow simulation code for future calculations in the nozzle and mold of continuous casting process. The LES-CU-FLOW may also be used to perform parametric studies related to SEN depth, nozzle and mold geometries.

The POD analysis at the mold midplane gave deep insights about the behavior of turbulent flow in these systems. This analysis should be extended to other planes or to 3-D, including midplane between narrow faces.

APPENDIX A. USER DEFINED FUNCTIONS (UDFs) FOR FLUENT

A.1 UDF for Mass and Momentum Sink Terms for Shell Solidification

```
/************************************************************************/
/* UDF for specifying a mass and momentum sink terms                    */
/* for shell solidification                                             */
/************************************************************************/
#include "udf.h"
#include "sg.h"
#include "math.h"
#define casting_velocity 0.0273 // Casting speed in m/s
#define wall_id 4  //Solid-liquid interface ID
#define density 7020  //Steel density

DEFINE_SOURCE(mass_source, c, t, dS, eqn)
{
real mass, source, area_face;
int i;
real A[ND_ND];
face_t f;
cell_t cc;
Thread *tf;

  c_face_loop(c,t,i)
 {
          f = C_FACE(c,t,i);
          tf = C_FACE_THREAD(c,t,i);
  if(THREAD_ID(C_FACE_THREAD(c,t,i)) == wall_id )
   {
   F_AREA(A,f,tf);
   area_face = A[1];
   source = -density * casting_velocity * fabs(area_face)/C_VOLUME(c,t);
   dS[eqn] = 0;
         }
  }
   return source;
   return dS[eqn];
}

DEFINE_SOURCE(x_momentum_source, c, t, dS, eqn)
{
 real mass, source, area_face;
int i;
```

```
real A[ND_ND];
face_t f;
cell_t cc;
Thread *tf;

   c_face_loop(c,t,i)
 {
          f = C_FACE(c,t,i);
          tf = C_FACE_THREAD(c,t,i);
  if(THREAD_ID(C_FACE_THREAD(c,t,i)) == wall_id )
   {
   F_AREA(A,f,tf);
   area_face = A[1];
   source = -density * casting_velocity * fabs(area_face)*C_U(c,t)/C_VOLUME(c,t);
   dS[eqn] = -density * casting_velocity * fabs(area_face)/C_VOLUME(c,t);
          }
  }
   return source;
   return dS[eqn];
}

DEFINE_SOURCE(y_momentum_source, c, t, dS, eqn)
{
 real mass, source, area_face;
int i;
real A[ND_ND];
face_t f;
cell_t cc;
Thread *tf;

  c_face_loop(c,t,i)
 {
          f = C_FACE(c,t,i);
          tf = C_FACE_THREAD(c,t,i);
  if(THREAD_ID(C_FACE_THREAD(c,t,i)) == wall_id )
   {
   F_AREA(A,f,tf);
   area_face = A[1];
   source = -density * casting_velocity * fabs(area_face)*C_V(c,t)/C_VOLUME(c,t);
   dS[eqn] = -density * casting_velocity * fabs(area_face)/C_VOLUME(c,t);
          }
  }
   return source;
   return dS[eqn];
}
```

```
DEFINE_SOURCE(z_momentum_source, c, t, dS, eqn)
{
 real mass, source, area_face;
int i;
real A[ND_ND];
face_t f;
cell_t cc;
Thread *tf;

  c_face_loop(c,t,i)
 {
          f = C_FACE(c,t,i);
          tf = C_FACE_THREAD(c,t,i);
  if(THREAD_ID(C_FACE_THREAD(c,t,i)) == wall_id )
   {
   F_AREA(A,f,tf);
   area_face = A[1];
   source = -density * casting_velocity * fabs(area_face)*C_W(c,t)/C_VOLUME(c,t);
   dS[eqn] = -density * casting_velocity * fabs(area_face)/C_VOLUME(c,t);
         }
  }
   return source;
   return dS[eqn];
}
```

A.2 UDF for Eddy Viscosity for "Filtered" URANS Model

```
/************************************************************************************/
/* UDF for specifying eddy viscosity in filtered URANS model                        */
/************************************************************************************/
#include "udf.h"
#include "math.h"

DEFINE_TURBULENT_VISCOSITY(user_mu_t,c,t)
{
  real mu_t,f;
  real filter_width=0.002167; // Largest filter size in whole domain

if(C_K(c,t) !=0.0 && filter_width*C_D(c,t)/pow(C_K(c,t),1.5) < 1.0)
{
f=filter_width*C_D(c,t)/pow(C_K(c,t),1.5);
}
else
{
f=1.0;
}
```

```
if(C_D(c,t) !=0.0)
{
mu_t = f*M_keCmu*C_R(c,t)*C_K(c,t)*C_K(c,t)/C_D(c,t);
}
else
{
mu_t =0.0;
}
  return mu_t;
}
```

APPENDIX B. JET CHARACTERISTICS [Bai et al.]

The liquid velocity magnitude of i[th] cell of the nozzle port, $U_i = \sqrt{(u_l)_i^2 + (v_l)_i^2 + (w_l)_i^2}$

The weighted average liquid velocity at nozzle port in x-direction,

$$\overline{u}_l = \frac{\sum_{i\ (\text{if outflow})} \left[(u_l)_i (\Delta y)_i (\Delta z)_i \right]}{\sum_{i\ (\text{if outflow})} \left[U_i (\Delta y)_i (\Delta z)_i \right]}$$

The weighted average liquid velocity at nozzle port in y-direction,

$$\overline{v}_l = \frac{\sum_{i\ (\text{if outflow})} \left[(v_l)_i (\Delta y)_i (\Delta z)_i \right]}{\sum_{i\ (\text{if outflow})} \left[U_i (\Delta y)_i (\Delta z)_i \right]}$$

The weighted average liquid velocity at nozzle port in z-direction,

$$\overline{w}_l = \frac{\sum_{i\ (\text{if outflow})} \left[(w_l)_i (\Delta y)_i (\Delta z)_i \right]}{\sum_{i\ (\text{if outflow})} \left[U_i (\Delta y)_i (\Delta z)_i \right]}$$

The weighted average turbulent kinetic energy at nozzle port,

$$\overline{k}_l = \frac{\sum_{i\ (\text{if outflow})} \left[(k_l)_i (\Delta y)_i (\Delta z)_i \right]}{\sum_{i\ (\text{if outflow})} \left[U_i (\Delta y)_i (\Delta z)_i \right]}$$

The weighted average turbulent dissipation rate at nozzle port,

$$\overline{\varepsilon}_l = \frac{\sum_{i\ (\text{if outflow})} \left[(\varepsilon_l)_i (\Delta y)_i (\Delta z)_i \right]}{\sum_{i\ (\text{if outflow})} \left[U_i (\Delta y)_i (\Delta z)_i \right]}$$

Vertical jet angle,

$$\theta_{zx} = \tan^{-1}\left(\frac{\overline{w}_l}{\overline{u}_l} \right)$$

Horizontal jet angle,

$$\theta_{yx} = \tan^{-1}\left(\frac{\overline{v}_l}{\overline{u}_l}\right)$$

Average jet speed,

$$U_{jet} = \sqrt{\left(\overline{u}_l\right)^2 + \left(\overline{v}_l\right)^2 + \left(\overline{w}_l\right)^2}$$

Back-flow zone fraction,

$$\eta = \frac{\sum_{i\ (\text{all})}\left[\left(\Delta y\right)_i\left(\Delta z\right)_i\right] - \sum_{i\ (\text{if outflow})}\left[\left(\Delta y\right)_i\left(\Delta z\right)_i\right]}{\sum_{i\ (\text{all})}\left[\left(\Delta y\right)_i\left(\Delta z\right)_i\right]}$$

$\left(\Delta y\right)_i$ and $\left(\Delta z\right)_i$ are the grid spacing of ith cell in y and z directions at the port. $\left(u_l\right)_i$, $\left(v_l\right)_i$ and $\left(w_l\right)_i$ are respectively the velocities of ith cell in x-, y- and z- directions at the port. $\left(k_l\right)_i$ and $\left(\varepsilon_l\right)_i$ are respectively the turbulent kinetic energy and its dissipation rate of ith cell at the port.

APPENDIX C. PROPER ORTHOGONAL DECOMPOSITION IMPLEMENTATION WITH SINGLE VALUE DECOMPOSITION IN MATLAB

The formulations for proper orthogonal decomposition are presented in CHAPTER 7. Here, the MATLAB code used to calculate POD modes, modal coefficients, cumulative energy, and singular values is given.

```
 clear;
 dau=load('matrix2000_92-191_u_92mm_embr.txt');  % files having data in matrix form
 dav=load('matrix2000_92-191_v_92mm_embr.txt');  % rows represent time and column space
 daw=load('matrix2000_92-191_w_92mm_embr.txt');
 mm=193;    % # points in y direction
nn=100;   % # of points in x direction
bb=92;   % starting point in x direction
tt=2000; % # of files in time
t=0.0:0.006:(tt-1)*0.006;
d=zeros(tt,3*mm*nn);
 d(1:tt,1:mm*nn)=dau;
d(1:tt,mm*nn+1:2*mm*nn)=dav;
d(1:tt,2*mm*nn+1:3*mm*nn)=daw;
clear dau;
clear dav;
clear daw;
z2=mean(d);
for j=1:3*mm*nn
```

```
d(:,j)=d(:,j)-z2(j);
end
[u1,s1,v1]=svd(d,'econ');
d1=load('y_coordinate.txt');
for j=1:mm
d2(j)=d1(j*384);
end
for i=1:mm
Y(i)=0.07-d2(i);
end
 d3=load('x_coordinate.txt');
for j=1:385
d4(j)=d3(j);
end
for i=1:nn
X(i)=0.1-d4(bb-1+i);
end
 v11=v1';
dlmwrite('mean_data_final_2000.txt', z2, ' ');
  v22(1:20,:)=v11(1:20,:);
dlmwrite('modal_data_final_2000.txt', v22, ' ');
v33(1,:)=d(1,:)+z2(1,:);
dlmwrite('original_data_final_2000.txt', v33, ' ');
```

```
zz=u1(:,1:1)*s1(1:1,1:1)*v1(:,1:1)';
v44(1,:)=zz(1,:)+z2(1,:);
 dlmwrite('rank1_data_final_2000.txt', v44, ' ');
 zz=u1(:,1:4)*s1(1:4,1:4)*v1(:,1:4)';
 v55(1,:)=zz(1,:)+z2(1,:);
dlmwrite('rank4_data_final_2000.txt', v55, ' ');
zz=u1(:,1:10)*s1(1:10,1:10)*v1(:,1:10)';
v66(1,:)=zz(1,:)+z2(1,:);
 dlmwrite('rank10_data_final_2000.txt', v66, ' ');
zz=u1(:,1:15)*s1(1:15,1:15)*v1(:,1:15)';
v77(1,:)=zz(1,:)+z2(1,:);
dlmwrite('rank15_data_final_2000.txt', v77, ' ');
zz=u1(:,1:100)*s1(1:100,1:100)*v1(:,1:100)';
v88(1,:)=zz(1,:)+z2(1,:);
dlmwrite('rank100_data_final_2000.txt', v88, ' ');
 zz=u1(:,1:400)*s1(1:400,1:400)*v1(:,1:400)';
v99(1,:)=zz(1,:)+z2(1,:);
 dlmwrite('rank400_data_final_2000.txt', v99, ' ');
figure;
s=diag(s1); plot(s,'o'); %semilogy(s1,'o');
xlabel('number'),ylabel('singular value'),title('singular values of z')
dlmwrite('singular_values.txt', s, ' ');
 s3=s.^2/(s'*s);
```

```
sum(1)=0.0;
for i=2:tt
sum(i)=sum(i-1)+s3(i-1);
end
figure
%plot(s3)
hold on
plot(sum(2:tt),'ro')
dlmwrite('cumulative_energy.txt', sum(2:tt), ' ');
c=u1*s1;
figure;
plot(t,c(:,1),'--',t,c(:,2),':',t,c(:,3),'-.',t,c(:,4),'-.');
dlmwrite('time.txt', t, ' ');
dlmwrite('temporal_coefficient1.txt', c(:,1), ' ');
dlmwrite('temporal_coefficient2.txt', c(:,2), ' ');
dlmwrite('temporal_coefficient3.txt', c(:,3), ' ');
dlmwrite('temporal_coefficient4.txt', c(:,4), ' ');
```

APPENDIX D. DERIVATION AND IMPLEMENTATION OF WERNER-WENGLE WALL TREATMENT FOR LES

The Werner-Wengle wall treatment assumes that instantaneous tangential velocity components are in phase with corresponding instantaneous wall shear stress components. This method formulates a relation between instantaneous tangential velocity and corresponding instantaneous wall shear stress in the cell next to the wall by assuming a linear and power law behavior of tangential velocity with the distance from the wall, as follows.

$$u^+ = y^+, \qquad y^+ \le 11.81$$
$$u^+ = A\left(y^+\right)^B, \quad y^+ > 11.81$$

Where, $A = 8.3$, $B = 1/7$, $u^+ = u/u_\tau$, $y^+ = yu_\tau/\nu$, and wall stress $\tau_w = \rho u_\tau^2$.

The linear and power law layers intersection gives normalized distance of intersection point from the wall as, $y^+ = A\left(y^+\right)^B \Rightarrow y^+ = A^{1/(1-B)} = y_i^+ = 11.81$

Now, if the whole cell next to wall is in the linear layer then, $\Delta y^+ \le y_i^+ = 11.81$,

$$u^+ = y^+ \Rightarrow u_p/u_\tau = y_p u_\tau/\nu \Rightarrow \tau_w = \rho u_\tau^2 = u_p \mu / y_p = 2u_p \mu/\Delta y,$$

Where, subscript p denotes the cell center, Δy is the cell thickness or size normal to the wall and u_p is the tangential filtered velocity at the cell center next to the wall.

Now, the tangential filtered velocity in the cell next to the wall can be calculated as,

$$u_p^+ = \frac{1}{\Delta y^+}\int_0^{\Delta y^+} u^+ dy^+ = \frac{1}{\Delta y^+}\int_0^{\Delta y^+} y^+ dy^+ = \frac{A^{2/(1-B)}}{2\Delta y^+} \Rightarrow u_p = \frac{\mu A^{2/(1-B)}}{2\rho\Delta y}$$

Therefore, if $|u_p| \le \frac{\mu}{2\rho\Delta y} A^{2/(1-B)}$, then wall stress is, $|\tau_w| = 2|u_p|\mu/\Delta y$

Now, if whole cell does not falls within linear layer, $\Delta y^+ \ge y_i^+ = 11.81$,

In this case, the tangential filtered velocity is given as,

$$u_p^+ = \frac{1}{\Delta y^+}\int_0^{\Delta y^+} u^+ dy^+ = \frac{1}{\Delta y^+}\left(\int_0^{y_i^+} y^+ dy^+ + \int_{y_i^+}^{\Delta y^+} A\left(y^+\right)^B dy^+\right)$$

$$= \frac{1}{\Delta y^+}\left(\frac{y_i^{+2}}{2} + \frac{A}{1+B}\left(\left(\Delta y^+\right)^{1+B} - \left(y_i^+\right)^{1+B}\right)\right)$$

$$\frac{u_p \Delta y u_\tau}{u_\tau \nu} = \left(\frac{A^{2/(1-B)}}{2} + \frac{A}{1+B}\left(\frac{\Delta y u_\tau}{\nu}\right)^{1+B} - \frac{A}{1+B}A^{(1+B)/(1-B)}\right)$$

Now, using above equation, u_τ can be written in terms of other variables as follows,

$$u_\tau^{1+B} = \frac{1+B}{A}\left(\frac{\nu}{\Delta y}\right)^B u_p + \frac{1-B}{2}\left(\frac{\nu}{\Delta y}\right)^{1+B} A^{(1+B)/(1-B)}$$

With, $\tau_w = \rho u_\tau^2$

$$\left|\tau_w\right| = \rho\left(\frac{1-B}{2}A^{(1+B)/(1-B)}\left(\frac{\nu}{\Delta y}\right)^{1+B} + \frac{1+B}{A}\left(\frac{\nu}{\Delta y}\right)^B \left|u_p\right|\right)^{2/(1+B)}$$

$$\text{for } \left|u_p\right| \geq \frac{\mu}{2\rho\Delta y}A^{2/(1-B)}$$

$$\left|\tau_w\right| = \begin{cases} 2\left|u_p\right|\mu/\Delta y & \text{for } \left|u_p\right| \leq \dfrac{\mu}{2\rho\Delta y}A^{2/(1-B)} \\ \rho\left(\dfrac{1-B}{2}A^{(1+B)/(1-B)}\left(\dfrac{\nu}{\Delta y}\right)^{1+B} + \dfrac{1+B}{A}\left(\dfrac{\nu}{\Delta y}\right)^B \left|u_p\right|\right)^{2/(1+B)} & \text{for } \left|u_p\right| \geq \dfrac{\mu}{2\rho\Delta y}A^{2/(1-B)} \end{cases}$$

Werner-Wengle wall treatment is implemented in CU-FLOW by adding $-\tau_w \Delta x \Delta y$ as a source term in the corresponding momentum equations and equating the corresponding coefficient of viscous terms zero. $\Delta x \Delta y$ is the wall shear tangential area.

APPENDIX E. SPECTRAL ANALYSIS AND CORRELATION

E1. Power Spectrum

The power spectrum ($P(f_k)$) is used to identify frequencies and energy distribution with frequencies in the instantaneous velocity signals. The current work uses the following formulation of power spectrum:

$$P(f_k) = \begin{Bmatrix} |C_k|^2 / n^2, \; k = 0, n/2 \\ \left(|C_k|^2 + |C_{n-k}|^2 \right) / n^2, \; k = 1, ..., n/2 - 1 \end{Bmatrix}$$

Here, the coefficient and frequencies are given as,

$$C_k = \sum_{j=0}^{n-1} V(t_j) e^{i 2\pi f_k t_j}, \; f_k = k / (t_{n-1} - t_0), \; k = -n/2, ...n/2 - 1$$

E2. Auto Correlation

The auto-correlation has been used to calculate required length of the domain to capture longest turbulence scales along homogeneous direction in fully developed turbulent flow, especially in MHD square duct calculations. For a real function in continuous form, the autocorrelation can be written as,

$$R_{ff}(\tau) = \int_{-\infty}^{\infty} f(t) \, f(t + \tau) \, dt$$

In the discrete form, the normalized autocorrelation for velocity fluctuations (w') can be written as,

$$R_{w'w'}(k) = \frac{C_k}{C_0} = \frac{\sum_{i=1}^{n-k} w_i' w_{i+k}'}{\sum_{i=1}^{n} w_i' w_i'}$$

where discrete data points represented by suffix '*i*' can be either in space or in time. Besides, based upon Taylor's frozen flow hypothesis which assumes that turbulence is convected with mean flow, the time and space scales can be used interchangeably when required by converting time to space after multiplying with mean velocity at a particular point.